Nanomechanical Resonators Using Functional Nanowires



Utku Emre Ali
St Anne's College

Supervisor: Harish Bhaskaran

A thesis submitted for the degree of
Doctor of Philosophy

Trinity Term
2022

To the late professor Mustafa Karaman...

Abstract

Nanoelectromechanical systems (NEMS) have seen a surge of active interest in the 21st century. NEMS resonators have been initially employed for mass and force sensing as well as quantum mechanical measurements. With the recent developments in readout techniques at room temperature, NEMS have also proven promising in telecommunications and signal processing applications. Excitingly, NEMS devices operate at the sub-picowatt regime, which is many orders of magnitudes smaller than today's digital signal processing blocks. Thus, nanomechanical signal processing is becoming an exciting area of research, with the aim of developing effective ways for transducing and tuning mechanical resonances.

Currently, active tuning of NEMS is achieved by stress-tuning methods, which rely on the application of net forces to the resonator via electromagnetic fields. However, stress-tuning is volatile, which requires constant electrical stimuli (i.e. quiescent power) to maintain the tuned frequency. Stress-tuning also suffers from reliability issues and alters the quality (Q) factors of the resonators. To overcome these challenges, this thesis investigates a novel technique of tuning nanomechanical resonances by exploiting the Young's modulus change in chalcogenide-based phase-change materials (PCMs). PCMs can be permanently yet reversibly switched between amorphous and crystalline states, which exhibit different elastic properties. This can be employed as a non-volatile tuning mechanism in NEMS resonators. Recent advances have also shown that nanowire configurations offer a more reliable and homogenous phase transition compared to thin-film PCMs. By using nanosecond-fast

electrical pulses for phase-change and employing a piezoresistive readout scheme, the first instance of a non-volatile (power-free) tuning scheme in NEMS has been demonstrated within a range of ~30% using GeTe nanowires. The effect of phase-change on Q factors, phase noise, and piezoresistive gauge factors have also been studied. With non-changing Q factors over 16,000 and a decent phase noise performance, the GeTe nanowires have also been utilised in a frequency-hopping radio transmission. The promises of such a functional resonator are lower power consumption, faster tuning speeds, and better phase noise performance in commercial frequency synthesisers.

To improve the signal-to-noise ratio for real-world applications, a novel transduction scheme for nanowires based on cavity optomechanics has further been demonstrated in this thesis, with transduction gain levels of 1.46 mV nm^{-1} for InP nanowires and 2.02 mV nm^{-1} for GeTe nanowires at an optical probe power < 75 μW. This thesis also investigates theoretically that these gain levels can be further improved by a factor ~200, extending the field of NEMS beyond academia for the first time, with imminent applications in signal processing and telecommunications. To assemble such a functional platform into a hand-held device, a novel pick-and-place technique has also been developed here, integrating single-crystal nanowires with on-chip devices with a placement precision below 1 μm.

Acknowledgements

I would not be able to thank enough to everybody who saw me through good and trying times and helped me get where I am today.

It goes without saying but I am, first and foremost, indebted to Professor Harish Bhaskaran for guiding me throughout my DPhil journey. Thank you, Harish, for being open-minded, observant, and most importantly, patient… not just as a supervisor but also as a friend. I will always appreciate the professional and experimental skills I have learned by merely being a part of your team. I still remember the moments my experiments took a turn for the better upon your valuable suggestions despite my constant attempts to refute them. When I first observed the mechanical resonance or tuned the nanowires, you were always as excited and enthusiastic as me and even modest enough to come down to the lab and join the experiments. Your approval of my work has always meant a lot to me, and I am proud to have had you as my supervisor.

I was very fortunate to get help from and be acquainted with some wonderful people in Oxford. Most importantly, my dearest colleague Yu Shu (舒瑜), with whom I shared the most remarkable moments during my studies. Joining the same research group at the same time, we have always had each other's back for four amazing years and will continue to do so. I feel extremely lucky to have met her at such an important stage of my life, and I think I could never be tired of pronouncing her name "correctly". I will forever cherish our friendship, Yu.

I owe a big "thank you" to the rest of my colleagues, as well. To the one and only Ben Porter, for training me with literally everything in our lab. To Zengguang, for his guidance and friendship since the first day I joined the team. To Nathan, for his invaluable advice on nanofabrication. To Sridevi, whose skills, knowledge, and integrity were consummate. To Mengyun, for generously offering her help. To Bowei, with whom I enjoyed doing experiments the most. To James, the philosopher, for making me think deeper with his ingenious questions (at the most awkward moments). To Eugene, the engineer, whose practicality has always been impressive. To Xuan, the keeper of the photonics setups, for being an amazing lab mate and teacher. To Ghazi, for teaching me to be fearless while testing new devices. To Nipho, whose existence added joy to the whole group. To Sam, my birthday buddy, for the endless selfies. To Tara, for being fun (in her own unique way). To Samarth and Jason, for always being there whenever I needed help or wanted to discuss new ideas. To Luci, the backbone of our team, for diligently managing everything. To Andy, for not only maintaining everything in the lab but also sharing with us from his garden. The list can go on forever, but thanks should also go to Madhav, Wen, Seongdong, Sharizal, Johannes, Méadhbh, Yuhan, Antonios, Kairan, Håvard, Yi, and Kristian.

I'd like to recognise the assistance of our cleanroom managers, Radka and Paul, whose commitment and support have never wavered. I also feel privileged to have worked with Gaurav Modi and Professor Ritesh Agarwal at UPenn, whose expertise on phase-change nanowires has transformed my experiments to a whole new, sophisticated level.

Outside the lab, I must say Oxford's Summertown has a special place in my heart thanks to my amazing landladies who welcomed me to their homes, seeing me as no less than a family member. Penelope Latham, my guardian angel, has the most exquisite taste in anything you can imagine. Like a fairy godmother, she makes everything she touches more beautiful. I really miss waking up in her fabulous house with Cassie's barks. After Penny moved to Northumberland, I stayed with Deborah Bryceson for a year. Deborah is an epitome of academic integrity and has always inspired me with her hardworking side. No wonder I wrote both of my papers in her house. By the way, she makes the best devilled eggs on earth. My third abode was Gülşen Alkan's house. Gülşen is the strongest mother I have ever met. She is always amiable, and I don't think I can ever get bored of spending time with her.

I would like to extend my special thanks to Almalıoğlu family, who not only made my time in Oxford incredibly enjoyable but also were great companions during our hiking adventures in Iceland, Cotswolds, Yorkshire Moors & Dales, South Downs, and Brecon Beacons.

I also acknowledge the financial support from the Scientific and Technological Research Council of Turkey (TÜBİTAK) as well as the Department of Materials at Oxford.

Finally, I would like to dedicate this thesis to my former supervisor, Professor Mustafa Karaman, whose early passing has left an irreplaceable void in our lives. Through us may his legacy live on forever.

Utku Emre Ali

Contents

Abstract ..... **iii**

Acknowledgements ..... **v**

List of figures ..... **xi**

List of tables ..... **xxii**

List of acronyms ..... **xxiii**

List of symbols ..... **xxvi**

1 Introduction **1**

1.1 Motivation 1

1.2 Objective 4

1.3 Outline 5

1.4 Key results and contributions 7

1.5 Statement of originality 8

2 Tunable resonators and phase-change materials: a literature review **9**

2.1 Scaling effects 9

2.2 Micro/nanomechanical resonators 11

2.3 Transduction of nanomechanical resonators 14

2.3.1 Electrical techniques 15

2.3.2 Optical techniques 18

2.4 Stress-tuning of nanomechanical resonators 20

2.5 Introduction to phase-change materials 23

2.6 A tunable phase-change nanowire NEMS 26

3 A novel nanowire pick-and-place technique 28

3.1 Overview 28

3.2 Fabrication of the device chip 29

3.3 Assembly of the nanowires 35

3.3.1 Making of a nanoscale tip 37

3.3.2 Preparation of elastic stamps 41

3.3.3 Nanowire placement 44

3.3.4 Mechanical robustness of the method 48

3.4 Conclusions 50

4 Electrical transduction of devices 52

4.1 Overview 52

4.2 Piezoresistive self-sensing of nanowires 53

4.2.1 Experiment setup 55

4.2.2 Equivalent measurement circuit 58

4.3 Resonance fitting 60

4.4 Validation of the mechanical resonance 66

4.5 Determination of gauge factors 69

4.6 Estimating the drive power 74

4.7 Conclusions 76

5 Electrical tuning of devices 77

5.1 Overview 77

5.2 Phase-change tuning of the mechanical resonance 78

5.2.1 Wide-range frequency tuning 81

5.2.2 Intermediate frequency levels 88

5.3 Non-changing quality factors 95

5.4 Real-time frequency tracking 99

5.4.1 Phase noise measurements 102

5.4.2 Frequency-hopping via phase-change tuning 106

5.5 Conclusions 112

6 Improving the readout by photonic integration 114

6.1 Overview 114

6.2 Integrated photonics 115

6.2.1 Fibre-to-chip coupling 115

6.2.2 Ring resonators 119

6.2.3 Photonic device characterisation 121

6.3 On-chip photonic transduction of a nanowire 124

6.3.1 Cavity optomechanics: theory and simulations 125

6.3.2 Measurement setup 131

6.3.3 Optomechanical device characterisation 134

6.3.4 Estimating the displacement sensitivity 141

6.4 Conclusions 147

7 Conclusions and outlook 149

7.1 Summary of the results 149

7.2 Future work 151

Appendix A: Photonic NEMS assembly 155

Bibliography 158

List of figures

Figure 1.1 A typical RF receiver front-end. Local oscillator (LO) has a fixed frequency that is application-specific and feeds the mixer. Filter indicates a band-pass filter….. 2

Figure 2.1 Nomenclature of micro/nano systems with respect to coupling mechanism between domains. 12

Figure 2.2 First realisation of a MEMS device integrated as a suspended-gate n-channel transistor. A polarisation voltage is applied to G1 while an *a.c.* signal drives G2 (section A – A'). The transverse movement of the rod modulates the channel conductance (section B – B') at the resonance frequency of the rod, providing high-quality bandpass filtering. *Reproduced from [43], with the permission of AIP publishing.* 12

Figure 2.3 Micromachining cornerstones. **a**, First poly-Si cantilever: 25 µm long and 230 nm thick beam suspended 3.5 µm above the Si substrate. © *Electrochemical Society. Reproduced from [54] by permission of IOP publishing Ltd. All rights reserved*. **b**, SEM image showing the vibrations of the first poly-Si electrostatic-comb drive resonator under high vacuum. *Reprinted from [56], with permission from Elsevier.*. 13

Figure 2.4 Exploitation of magnetic and electric fields for NEMS transduction. **a**, Magnetomotive sensing scheme. Vibrations of a nanobeam inside a static magnetic field generates an electromotive force, which is detected by an amplifier. *Reprinted from [14], with the permission of AIP publishing*. **b**, Capacitive transduction of a doubly-clamped Si_3N_4/Al beam with an Al gate. The nanobeam is biased with a *d.c.* voltage.

A sinusoidal gate voltage drives the resonator into motion. *Reprinted (adapted) with permission from [50]. Copyright 2022 American Chemical Society*..... 16

Figure 2.5 SEM image of a SiC nanobeam. A thin layer of gold is deposited on both ends of the resonator for piezoresistive detection (left inset) and electrothermal drive (right inset). *Reprinted from [80], with the permission of AIP publishing*. 17

Figure 2.6 Near-field (evanescent) coupling of nanomechanical resonators to optical microcavities. **a**, A microtoroidal near-field sensor [92]. The light is coupled into the microcavity by a tapered fibre, and an off-chip array of Si_3N_4 beams is interfaced with the cavity using piezo positioners. *Reproduced with permission from Springer Nature*. **b**, CNT-microcavity scheme [93]. A pair of electrical tweezers holds the nanotube over the microdisk cavity. The optical mode within the microcavity is excited by a bare optical fibre. *Reproduced with permission from Springer Nature.* 20

Figure 2.7 Phase-change process. **a**, A highly-energetic, short electrical or optical pulse results in amorphous phase while **b**, a longer and less-energetic pulse leads to crystallisation. *Reproduced from [25] with permission from Springer Nature.* 23

Figure 2.8 Non-thermal, dislocation-based amorphization in phase-change nanowires. **a**, Simulated model of electron charge density in GeTe (Ge, green, Te, tan) [105]. A significant bonding energy difference exists between the short and long bonds. The short bonds have a higher electron density, leading to a stronger bonding. *Reproduced with permission from Springer Nature*. **b**, TEM image (left) of a GeTe nanowire after low-energy electrical pulsing. The image shows a clear dislocation contrast. Diffraction pattern (right) shows spot splitting along the growth direction (<110>) (zone axis: [111]). *Reprinted (adapted) with permission from [36]. Copyright 2022 American Chemical Society.* 25

Figure 2.9 Phase-change NEMS. **a**, Proposed device design by Hosseini et al. showing a free-standing PCM thin-film sandwiched between graphene electrodes. Reproduced from [33] under CC BY 4.0 license. **b**, Proposed device design for this

work. A phase-change nanowire is suspended by two electrodes over a photonic waveguide. 27

Figure 3.1 Nanofabrication process flow regarding the electrical chip. 29

Figure 3.2 CAD file containing the layout of electrodes and alignment markers. 30

Figure 3.3 Optical micrograph of the Au electrodes (yellow) with a gap of 8 µm. 31

Figure 3.4 Nanofabrication process flow regarding the opto-electronic chip. 32

Figure 3.5 The fabricated opto-electronic chip. **a**, Optical microscope image showing a portion of the chip. Si_3N_4 waveguides (green) are aligned with the gaps between the Au electrodes (yellow). **b**, Angled-view SEM image of the grating coupler encircled in **a** with the solid square. **c**, Height data measured by AFM along the dashed line shown in **a**. Height difference between the waveguide (in the middle) and the electrodes (at the sides) is ~102 nm. Gap between the electrodes is measured as 11 µm. 34

Figure 3.6 Optical micrograph of an opto-electronic chip consisting of a microring cavity 35

Figure 3.7 Schematic of conventional nanowire transfer process using the stamp-transfer technique. (1) The PDMS stamp collects a forest of nanowires from the growth substrate. (2) A lithographically-defined polymer window of PMMA (which is a positive-tone resist) facilitates the alignment of the nanowire with the device chip under a light microscope. (3) With simultaneous annealing, the nanowire is contact-printed on the device chip. (4) The PMMA layer is removed in acetone. *Reprinted (adapted) with permission from [128]. Copyright 2022 American Chemical Society.* 36

Figure 3.8 Schematic of the heat-and-pull setup designed for fabricating the nanoscale tips. A polymer filament (PET, thickness: 0.2 mm) is attached on a motorised translation stage and melted on a clean hot surface at 240 ℃. By pulling operation, the melted polymer on the surface instantly cools down and forms a taper. 37

Figure 3.9 A sustainable method to fabricate nanoscale tips. **a**, Snapshots from the heat-and-pull experiment. **b**, Optical microscope image of the resulting polymer tip with a diameter of ~0.6 µm. For clarity, the polymer is placed on a Si wafer. 38

Figure 3.10 Graph showing the characterization of the heat-and-pull setup for various pull lengths and velocities. Increasing pull length and velocity decreases the tip diameter down to sub-micron levels (~0.4 µm). 39

Figure 3.11 Collecting a single nanowire. **a**, Schematic showing a single nanowire picked-up by the tapered polymer tip from a forest of nanowires on the growth substrate. **b**, Top-down optical microscope view of a single GeTe nanowire (diameter: ~300 nm) collected by the nanoscale tip. 40

Figure 3.12 Dome-shaped PDMS stamps. **a**, Upside-down curing of the stamps on a hot plate. **b**, A glass slide containing six PDMS stamps. **c**, Contact angle measurement of one of the stamps. 42

Figure 3.13 Transferring of the nanowire onto the dome-shaped PDMS stamps. **a**, Schematic depicting the transfer process. The nanoscale tip pushes the nanowire towards the stamp. **b**, Optical micrograph of the single GeTe nanowire transferred to the PDMS stamp. 43

Figure 3.14 Alignment of the nanowire on stamp with the device chip. **a**, Illustration of the alignment step. The stamp is upside-down, facing the device chip below. **b**, Top-down view of the alignment process under a light microscope. The nanowire is kept at the focal plane. 45

Figure 3.15 Contact-printing of the nanowire over the device chip with Au electrodes. 46

Figure 3.16 Versatility of the novel nanowire pick-and-place assembly. **a**, Optical microscope image of a GeTe nanowire suspended over Au electrodes. **b**, Optical micrograph of a GeTe nanowire transferred on a 50 nm-thick Si_3N_4 TEM membrane with 2 µm pores. **c**, An angled-view false-colour SEM image of an InP nanowire suspended ~150 nm away from an optical microcavity of Si_3N_4. 47

Figure 3.17 Characterisation of the placement precision. 48

Figure 3.18 An SEM micrograph of the smallest nanowire in diameter (~120 nm) deposited by this technique. Inset shows a zoomed-in SEM image of the nanowire. 49

Figure 3.19 A free-standing InP nanowire before and after performing a lithography step following its deposition. 50

Figure 4.1 Coloured strain map of a doubly-clamped nanowire with a length of L. The dotted line indicates the neutral axis, which is displaced by dc at the maxima of resonant vibrations. The colourbar denotes red for tension, blue for compression, and white for neutral. 54

Figure 4.2 Annotation of the piezoresistive sensing scheme on an actual device used in this thesis. SEM image shows a GeTe nanowire suspended by Au electrodes. Electrical current through the device and mechanical actuation (out-of-plane) are sketched on the image. 54

Figure 4.3 PCB that carries the nanowire devices for resonance measurements in vacuum. 56

Figure 4.4 Piezoresistive measurement setup. Lock-in amplifier drives the piezo actuator at a frequency of ω and detects its frequency response at 2ω reference. Amplification of the drive and readout signals is performed by the HPA and LNA, respectively. 57

Figure 4.5 Schematic of the electrical equivalent of the piezoresistive measurement setup. 58

Figure 4.6 Simplified diagram of the experiment setup showing the ground connections. 59

Figure 4.7 I-V measurements of a GeTe nanowire using a semiconductor analyser. The slope of the fitted line yields a *d.c.* resistance of R = 1.103 kΩ. Inset shows the simplfied experiemental setup. 60

Figure 4.8 Observed resonance peaks from multiple GeTe devices (10 averages, 100 Hz lock-in bandwidth). Individual peaks correspond to the fundamental modes of four different nanowires. Top panel shows the wide range frequency response of the device pointed by the arrow. 61

Figure 4.9 Data shown in Figure 4.8 together with corresponding fits to the modified Lorentzian lineshape given by Eq. 4.10. 64

Figure 4.10 Evolution of the readout for different $V\mathrm{drive}$ levels. 67

Figure 4.11 Evolution of the readout for different $V\mathrm{bias}$ levels. 67

Figure 4.12 Piezoresistive readout at ω and $2\,\omega$ references for the same measurement. 68

Figure 4.13 Calibration of the piezoceramic actuator using contact-mode AFM. **a**, Simplified schematic diagram of the measurement setup. **b**, Surface vibrations of the piezoceramic actuator with respect to the drive amplitude. The piezo element is operated in linear regime. 70

Figure 5.1 A study by Nazeer et al. showing the measured resonance frequencies of a Si cantilever without (black) and with the GST thin-film in amorphous (red) and crystalline (blue) phases. *Reprinted from [32], with permission from Elsevier.* 78

Figure 5.2 Experimental setup for the electrical tuning of GeTe nanowires. 82

Figure 5.3 Nanomechanical tuning of a GeTe nanowire by an electrical pulse. 83

Figure 5.4 Cyclability test of a GeTe nanowire. **a**, Raw experimental data showing the frequency response of the virgin nanowire. **b**, Raw experimental data showing the frequency response of the nanowire amorphized by a 64 pJ pulse. **c**, Evolution of the frequency and the quality factor of the device during 11 phase-change events/cycles. 87

Figure 5.5 Illustration of the dislocation dynamics in 111 plane of a GeTe nanowire, with a Te segment collapsing along the growth direction 110 towards a Ge vacancy cluster. *Reprinted (adapted) with permission from the Supporting Information of [36]. Copyright 2022 American Chemical Society.* 89

Figure 5.6 Concept of polarity-dependent, pulse-driven dislocation generation/annihilation mechanism in phase-change nanowires. The lines denote local antisites, and a thicker line means higher number of defects.s 90

Figure 5.7 Effect of defect generation on the resonance frequency of a GeTe nanowire. The distinctive frequency evolution in the 1st attempt is due to the alternating polarity of pulses (bidirectional pulsing). The polarity is kept constant during the last two attempts (unidirectional pulsing). 91

Figure 5.8 Finite-element analysis to investigate the effect of directional pulsing on the tuning efficiency. 93

Figure 5.9 Effect of growth direction on Q factors. **a**, Variation of Q during tuning cycles for two different nanowires. Odd cycles are crystalline, even cycles are amorphous. **b**, SEM image of the nanowire with non-preferred growth direction after failure. Inset zooms in for showing the increased surface roughness. **c**, SEM image of the the nanowire with preferred growth direction after failure. The nanowire shows no sign of surface roughness unlike the device in **b**..... 98

Figure 5.10 Combined tuning and transduction setups for real-time measurements. 100

Figure 5.11 A simple PLL configuration. The reference signal has a frequency of $f\mathrm{ref}$. 101

Figure 5.12 Interfacing of the NEMS setup with the PLL (subharmonic detection of $f0$)..... 101

Figure 5.13 The concept of phase noise..... 102

Figure 5.14 Open-loop configuration of the PLL setup for phase noise measurements. 103

Figure 5.15 Open-loop phase noise measurements of the resonator in amorphous and crystalline states (solid lines). The dashed lines of the relevant colours show the ultimate (thermomechanical) limit for the phase noise. The black (dashed-dotted) line shows the Johnson noise limit accounting for the device resistance and the non-ideal LNA..... 106

Figure 5.16 Application of phase-change NEMS as a tunable local oscillator in FHSS systems. AM stands for amplitude modulation..... 108

Figure 5.17 Real-time analysis of the frequency hopping sequence and its utilisation in a radio prototype. **a,** Channel statistics suggest $f1$ = 13.067 ± 0.011 MHz, $f2$ = 12.938 ± 0.013 MHz, $f3$ = 12.777 ± 0.014 MHz, and $f4$ = 12.624 ± 0.006 MHz. **b,** Real-time LO frequency tracking data for the largest and longest tuning step, i.e. re-crystallisation. **c,** Transmitted and received audio segments together with the real-time frequency hopping sequence. 110

Figure 6.1 Fibre-to-chip coupling approaches based on **a**, edge coupling (in-plane) [123] (© 2022 IEEE) and **b**, grating couplers (out-of-plane) [173] (© 2022 IEEE). . 116

Figure 6.2 Si_3N_4 waveguide design. **a**, Geometry of the ridge waveguide. **b**, Mode simulations showing the normalised $\mathcal{E}$-field intensity of the (fundamental) TE mode of the waveguide. 117

Figure 6.3 Si_3N_4 grating coupler. **a**, Grating coupler sketch showing the incident laser beam and the apodised Bragg gratings. **b**, Optical micrograph of a fabricated grating coupler. 118

Figure 6.4 Model of a simple ring resonator showing the input and output fields. . 119

Figure 6.5 Fibre-coupled optical measurement setup. 122

Figure 6.6 Optical characterisation of the fabricated devices. **a**, Transmission spectrum of a grating coupler yielding the highest transmission level. **b**, Normalised spectrum of a critically-coupled ring resonator..... 123

Figure 6.7 Transduction concept based on cavity optomechanics. The arrows indicate the direction of the change, i.e. when the nanobeam approaches the cavity, the optical resonance is redshifted, and the transmission is modified. The scales are exaggerated for illustration purposes. 124

Figure 6.8 A slice of the fundamental TE mode of the microcavity along z-axis. ... 126

Figure 6.9 Simulated field intensity showing the nanowire perturbation for various $z0$ values. Increasing the gap ($z0$) leads to a weaker interaction between the nanowire (InP) and the photonic waveguide (Si_3N_4). Light propagates in the positive x-direction,

and the corresponding field intensity plots for each case at x = 0 is given on the right. 129

Figure 6.10 Simulated values using effective-index method. **a**, Change in the effective mode index for various gap ($z0$) values. Dashed lines are guide to the eye. **b**, Comparison of the simulated frequency shift (using $\Delta n\mathrm{eff}$) with the theory. 130

Figure 6.11 Glued fibrearray on the device chip. **a**, Alignment step. **b**, Final assembly. 132

Figure 6.12 Experiment setup for detecting nanomechanical vibrations of an InP nanowire. **a**, Schematic showing the optomechanical measurement setup and **b**, Angled-view false-colour SEM image of the device. 134

Figure 6.13 Normalised optical cavity transmission before (solid line, critical coupling) and after (dashed line) the nanowire deposition. The nanowire introduces additional optical loss to the microcavity, resulting in linewidth broadening. 135

Figure 6.14 Normalised microcavity transmission showing the measurement wavelength $\lambda\mathrm{m}$. Inset shows the normalised slope of a microring cavity numerically obtained from Eq. 6.5. Maximum slope is obtained for a detuning of $\pm\Gamma\mathrm{c}2$. 136

Figure 6.15 Raw experimental data acquired from the InP nanowire with dimensions L = 9.2 μm and D = 150 nm. The finer sweep shows the magnitude and phase response of the resonator. 137

Figure 6.16 Thermomechanical noise spectral density of the resonator with a probe power of 21 μW for various wavelengths. Inset shows the transmission spectrum of the optical cavity with colour-coded wavelength values. Measurement wavelengths and Q factors are further displayed in the same colour as the corresponding readout data, where Lorentzian fits are shown by black solid lines. Goodness of the fits are better than 10%. 138

Figure 6.17 Raw thermomechanical noise data (circles) of the nanowire together with the corresponding Lorentzian fits (solid black lines) for various probe powers.

Increasing optical field intensity softens the resonator (lower resonance frequency) and improves the transduction gain (larger resonance peak). 139

Figure 6.18 Finite element analysis results for the opto-thermo-mechanical effect. **a**, Spatial temperature profile indicating a maximum temperature value of $T\mathrm{max}$ = 25.236 ℃ for the 75-μW probe. **b**, Simulated $T\mathrm{max}$ values for various probe powers. **c**, Measured and simulated change in the mechanical resonance for different probes. Dashed and dotted lines are guide to the eye..... 140

Figure 6.19 Measured displacement noise (left axis) and transduction gain (right axis) for different probes. Dashed and dotted lines are guide to the eye. 142

Figure 6.20 Raw experimental data obtained by increasing the piezo drive voltage, using the 75-μW probe. The left axis shows the readout voltage, and the corresponding displacement value is given on the right axis. Dashed line denotes the critical amplitude ($a\mathrm{crit}$), above which the Duffing nonlinearity kicks in. The resonator shows spring-hardening effect. 143

Figure 6.21 Comparison of the experimental $g\mathrm{om}$ value with the theory (Eq. 4.14) and simulations (Eq. 6.7). At $z0$ = 150 nm, the experiment yields $g\mathrm{om}$ ~75 MHz nm^{-1}.. 145

Figure 6.22 Improvement in the readout amplitude for increasing Q values of the optical cavity. Data points (green circles) are numerically computed, and both axes are normalised to the experimental values, i.e. x-axis by Q = 4,460 and y-axis by 4 mV. Gray line shows the linear fit to the first few data points. The pink circle crosses the 1-dB compression line (pink line) where the readout power drops by 1 dB, i.e. 1-dB compression point. The nonlinearity stems from the Lorentzian (second-order) response of the microcavity (Eq. 6.5). 146

Figure 7.1 Preliminary results regarding the cavity optomechanics of a GeTe nanowire. **a**, False-colour SEM image of the GeTe nanowire (L = 7.5 μm, D = 250 nm) suspended over a microring cavity of Si_3N_4. **b**, Raw experimental data showing the frequency response of the device ($f0$ = 14.609 MHz)..... 152

Figure 7.2 Diagram of the proposed device. 153

List of tables

Table 4.1 Extracted resonance parameters from the fitted curves in Figure 4.9**.** 64

Table 4.2 Length (L) and diameter (D) of the devices used in Figure 4.9**.** 66

Table 4.3 Vibrational amplitude ($a\mathrm{NEMS}$), bias voltage ($V\mathrm{bias}$), *d.c.* resistance (R), and estimated gauge factor (γ) for the devices used in Figure 4.9**.** 72

Table 5.1 Frequency and resistance drift in the amorphous phase. 85

List of acronyms

3D: Three dimensional

5G: Fifth generation

a.c.: Alternating current

AFM: Atomic force microscope

AM: Amplitude modulation

BW: Bandwidth

CAD: Computer-aided design

CMOS: Complementary metal-oxide-semiconductor

CNT: Carbon nanotube

d.c.: Direct current

DAQ: Data acquisition

ESD: Electrostatic discharge

FEM: Finite element method

FM: Frequency modulation

GPS: Global positioning system

GSM: Global system for mobile communications

HPA: High-power amplifier

IC: Integrated circuit

invOLS: Inverse optical lever sensitivity

IoT: Internet of things

LNA: Low-noise amplifier

LO: Local oscillator

MEMS: Microelectromechanical systems

MOMS: Micro optomechanical systems

NEMS: Nanoelectromechanical systems

PCB: Printed circuit board

PCM: Phase-change material

PDMS: Polydimethylsiloxane

PET: Polyethylene terephthalate

PID: Proportional-integral-derivative

PLL: Phase-locked loop

RF: Radio frequency

RIE: Reactive ion etching

RMS: Root-mean-square

SEM: Scanning electron microscopy

SMA: SubMiniature version A

SMU: Source measure unit

SNR: Signal-to-noise ratio

SPICE: Simulation program with integrated circuit emphasis

TE: Transverse electric

TEM: Transmission electron microscopy

TIA: Transimpedance amplifier

UHV: Ultra-high vacuum

USB: Universal serial bus

VCO: Voltage-controlled oscillator

VCVS: Voltage-controlled voltage source

W: Watt

List of symbols

P_0: Effective drive power

W_0: Elastic energy (mechanical)

W_c: Cavity energy (optical)

f_0: Mechanical resonance frequency = $\omega_0/2\pi$

g_{om}: Optomechanical coupling rate

n_{eff}: Effective mode index

ω_c: Optical (cavity) resonance frequency

$\mathcal{E}$: Electric field

C: Capacitance (including subscript versions)

D: Diameter

E: Young's modulus

I: Second moment of area

L: Length

R: Resistance (including subscript versions)

k: (in mechanics) Spring constant

k: (in optics) Imaginary part of the refractive index

m: Mass

n: Real part of the refractive index

q: Electrical charge

t: Thickness

w: Width

$\mathcal{Q}$: Quality factor

α: Decay constant

β: Linear damping coefficient

γ: Piezoresistive gauge factor

η: Viscosity

λ: Wavelength of light

ρ: Mass density

ρ: Mass density

σ: Stress

ω: Angular frequency

ϵ: Permittivity

Chapter 1

Introduction

1.1 Motivation

The need for packing high functionality into relatively small devices has seen a huge surge of interest mainly with the emerging concept of Internet of Things (IoT), which brings us to a new technological era of omnipresent connectivity, computing, and communication [1]. To meet the technical needs of IoT, efforts from academia and endeavours from industry have resulted in leading-edge innovations in various fields from wireless sensors to nanotechnology [2]. At the heart of all these developments in great demand is the communication network between individual devices that can be realised by deploying fashionable telecommunication and positioning protocols such as 5G, GSM, Bluetooth, Wi-Fi, or GPS, all of which require synchronisation, mixing, and filtering of signals (see Figure 1.1). Since massive IoT systems will largely depend on numerous sensor networks with nodes where battery replacements might not be feasible, issues related to power consumption have become even more important [3], [4].

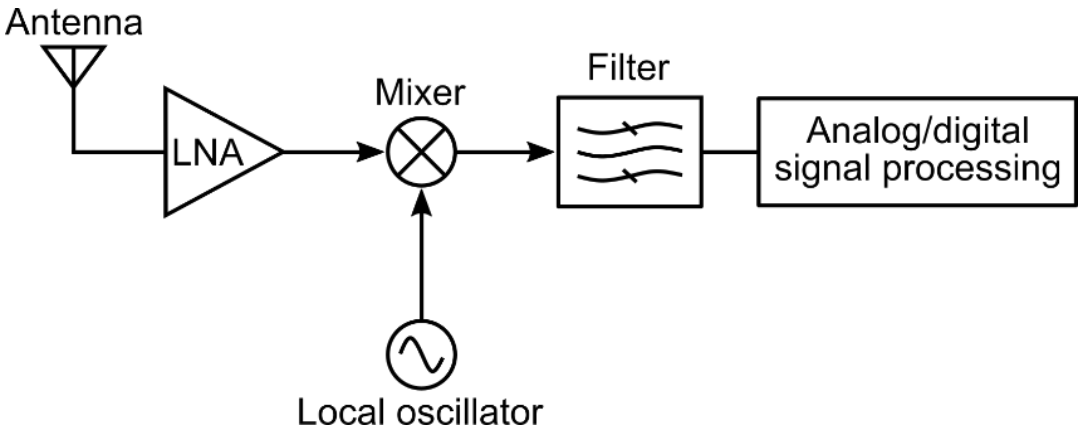


Figure 1.1 A typical RF receiver front-end. Local oscillator (LO) has a fixed frequency that is application-specific and feeds the mixer. Filter indicates a band-pass filter.

Currently, quartz crystal-based oscillators dominate the market by providing the frequency reference required in integrated circuits (ICs) although the quartz crystal itself cannot be monolithically integrated [5]. Integer/non-integer multiples of that reference frequency are then synthesised within a phase-locked loop (PLL) using frequency dividers [6], and such frequency synthesisers are still one of the most power-hungry IC blocks despite ongoing attempts for ultra-low power designs [7]. This method of frequency synthesis further impairs phase noise and tuning speed of the local oscillator [6], [8], both of which constitute a major limitation towards massive IoT connectivity [9].

On the radio frequency (RF) front-end side, voltage-controlled oscillators (VCOs) have the ability to deliver a tunable reference clock. However, VCOs are quite sensitive to process variations since their design relies on resonance tanks consisting of passive on-chip components such as capacitors, inductors, and pn-junction varactors. These components also have low quality ($\mathcal{Q}$) factors [10], [11], thus the VCO blocks dissipate excessive power to compensate the loss in the resonance tank. To achieve low-power operation in such systems, high-$\mathcal{Q}$ microelectromechanical systems (MEMS) have been exploited as tunable resonators [12]. Meanwhile, owing to their extremely-high $\mathcal{Q}$ factors and ultra-low power consumption, nanoelectromechanical systems (NEMS) have the potential to serve as the ultimate building blocks in timing and signal

processing applications with better stability and smaller footprint than their micron-sized counterparts [13]–[15].

Conventionally, tuning of NEMS resonators is achieved by active stress-tuning [16], which is based on continual application of (net) forces through electromagnetic fields (capacitive [17], [18], electrothermal [19], [20], dielectric [21], piezoelectric [22], and magnetomotive [23] tuning). This is analogous to the adjustment of guitar strings using tuning pegs: higher string tension leads to a higher resonance frequency (f_0). However, all stress-tuning methods are volatile, meaning that the frequency reverts to its initial state once the stress generating source is removed. Moreover, stress-tuning dramatically alters surface states and clamping conditions of nanomechanical resonators, which in turn modifies the Q factor for almost an order of magnitude within the tuning range [16], [19]. Here, it should be noted that such modification of Q factors is not desired especially in systems with feedback control such as oscillators due to Barkhausen criterion [24] or filter design where constant selectivity (i.e. constant Q) might be required. Therefore, with Rebeiz's words, "we are still searching for the ideal electronic tuner, nearly 100 years after the invention of radio" [10].

On the other end of the spectrum, chalcogenide-based phase-change materials (PCMs), namely tellurides and antimonides, have been an active area of research over the last two decades [25]. These materials offer rapid structural switching between amorphous and crystalline phases repeatably while retaining their state for many years at room temperature. In addition to displaying high contrast in electrical and optical properties between the two phases [26]–[30], mechanical properties (i.e. Young's modulus) of PCMs also differ upon switching with a contrast of up to 6× [31], [32].

Given the unique availability of such mechanical property modulation in PCMs, a non-volatile (power-free) tuning scheme for nanomechanical resonators using phase-change thin-films has been proposed by H. Bhaskaran and colleagues in 2015, together with the practical challenges pertaining to fabrication, switching, and

transduction [33]. Meanwhile (from 2012 to 2016), R. Agarwal and colleagues have experimentally demonstrated a dislocation-based, non-melting route for amorphization in phase-change nanowires of GeTe and GeSbTe alloys [34]–[37]. Compared to melt-quench processes in thin-films, this non-melting route in nanowires further opens up the possibility for integrating PCMs as free-standing NEMS resonators (which is challenging in thin-film configurations [33]) to create tunability.

Over the years, phase-change nanowires have been further shown to offer lower structural drift that improves stability [38] and ultra-low thermal conductivity that dramatically reduces tuning energy [39], both of which make PCM nanowires even more attractive for robust, low-energy, and power-free tuning of nanomechanical resonators. Furthermore, phase-change processes in PCM nanowires do not affect the surface states and clamping conditions [34], [38], both of which are the most dominant damping mechanisms in NEMS. Thus, it can be surmised that phase-change events in nanowires are not expected to alter the Q factor of nanomechanical resonators unlike conventional stress-tuning mechanisms do as will be discussed in Section 5.3. This being the case, phase-change nanowires seem to be the key to design the ideal tuner by eliminating the need for continuous tuning bias while offering constant and stable Q factors. Thus, the topics covered in this thesis bring to light a new field of study: *phase-change NEMS*.

1.2 Objective

This thesis aims to demonstrate a series of design and fabrication ideas together with novel transduction and tuning mechanisms for mechanical resonators of single-crystal nanowires towards creating the ideal nanomechanical tuner by making use of the unique characteristic of phase-change nanowires (of GeTe). As the dislocation-based amorphization is only available in the electrical domain, GeTe nanowires are tuned via electrical pulses. Initially, the devices are transduced in the electrical domain using

piezoresistive self-sensing owing to its smaller footprint and facile implementation. However, electrical transduction, by its nature, yields readout amplitudes at the microvolt level. Although this is sufficient for testing and characterisation, signal processing applications require much higher amplitudes, i.e. millivolts. Therefore, a more effective way of transducing single-crystal nanowires via cavity optomechanics is also demonstrated in this work.

The fully-integrated nature of these experiments further requires a reliable pick-and-place technique for nanowires with high precision, which is also described in this thesis. Thus, a new phase-change NEMS field via active mechanical property modulation have been introduced here for the first time, step-by-step from design to fabrication, then to experimentation and real-world applications.

1.3 Outline

The chapters of this thesis are organised in the following way:

- **Chapter 2** reviews the literature on the milestones of micro/nanomechanical systems and further criticises the state-of-the-art tuning and transduction schemes for nanomechanical resonators. This chapter also summarises the field of phase-change materials (both thin-film and nanowire configurations) and their applicability as a novel tuning mechanism in nanomechanical systems.
- **Chapter 3** describes the nanofabrication steps (e.g. lithography, evaporation, etching) of the electrical and optical platforms used in Chapters 4-6, together with an entirely new pick-and-place assembly for depositing single nanowires with high accuracy. This assembly further enables, for the first time, the integration single-crystal nanowires of exotic materials into stand-alone on-chip devices, be it electronic or nanophotonic architectures that can readily be packaged.

- **Chapter 4** demonstrates the electrical transduction of phase-change NEMS resonators made of GeTe nanowires. Piezoresistive self-sensing in nanowire devices is explained, and the non-zero phase Lorentzian equation including frequency-doubling effect is derived for the first time in order to determine the resonance parameters, i.e. f_0 and Q. Effect of ground loops on the readout signal as well as calibration of the actuation method are presented.
- **Chapter 5** describes a set of experiments for the electrical tuning of GeTe nanowires. The tuning mechanism is described based on the previous in-situ TEM studies by collaborators at the University of Pennsylvania (refs. [34]–[37]). The relationship between the microstructural evolution and the mechanical resonance is investigated by both finite element method (FEM) models and experimental results. Finally, the uniqueness of the tuning mechanism, i.e. non-volatile tuning of f_0 with non-changing Q factors, is further applied as a tunable local oscillator without the need for frequency dividers, thus solving an engineering problem and paving the way for entirely new applications in communication electronics.
- **Chapter 6** contains a novel optomechanical transduction method for nanowire resonators. Theory of cavity optomechanics is studied and derived for single-crystal nanowires for the first time. The method is demonstrated using InP nanowires owing to their low-loss at telecommunication wavelengths. Displacement sensitivity is analysed in this chapter and compared to the closest examples in literature. The impact of being able to perform fully-integrated transduction of pristine nanowires in the optical domain and ways to improve the readout amplitude further are discussed in terms of real-world applications.
- **Chapter 7** gives a summary of conclusions relying on the experimental findings in this thesis and the contributions to the fields of NEMS, PCMs, nanowires,

and telecommunications. Future work is also presented as an outlook based on preliminary optomechanical measurements of a GeTe nanowire.

1.4 Key results and contributions

This thesis identifies a research gap in tunable resonators and accordingly takes the opportunity to develop unique procedures that experimentally combine the fields of phase-change materials and nanomechanical systems for the first time. Some bullet points below, the key results and new science of the thesis can be listed as follows:

- A novel pick-and-place assembly specifically designed for making functional and disparate devices of single nanowires.
- First time derivation of a non-zero phase Lorentzian curve analytically (including frequency-doubling effect) for resonance fitting.
- Demonstration of non-volatile phase-change tuning of mechanical resonance using GeTe nanowires via electrical pulses within a range of 30%.
- Proof of the accessibility of intermediate frequency levels in GeTe nanowires and its implementation as a tunable local oscillator in a communications system.
- A universal transduction scheme for mechanical resonators of nanowires using photonic microcavities and its experimental and theoretical validation.

The author of this thesis has also contributed to the design and demonstration of the following tools although they are not used in this work:

- Design, simulation, and manufacturing of wideband, low-loss fibre-to-chip optical couplers using the Nanoscribe 3D printer both on organic (PDMS) and inorganic (SiO_2) substrates, which can achieve over 60% coupling efficiency within 1500-1630 nm wavelengths.
- A printed circuit board (PCB) that contains 16 high-power and variable-gain drivers for NiCr-based optical phase shifters.

- A temperature controller for a mini stage to be used in optical measurement setups and the relevant microprocessor programming code.

1.5 Statement of originality

In the light of a comprehensive literature review (Chapter 2), this thesis contains a written set of novel procedures and findings, all of which have been originally obtained by the author within three and a half academic years during DPhil studies at the University of Oxford. Only exception is the synthesis of GeTe and InP nanowires (as described in refs. [36] and [40], respectively), which is performed by the collaborators. However, this collaboration does not undermine the originality of the main work and does only aim to accelerate the advances by utilising the exquisite know-how that is already present in the field.

Chapter 2

Tunable resonators and phase-change materials: a literature review

2.1 Scaling effects

Surrounded by gadgets consisting of billions of micro- and nano-sized devices, the effects of scaling are ubiquitous in daily life. Richard Feynman, a visionary scientist and a Nobel laureate, set the motivation behind scaling during his lecture in 1959 with his famous words: “There’s plenty of room at the bottom” [41]. He also challenged his students for a prize of $1,000 to make an electric motor no larger than 1/64th of an inch on any side. Within a few months, McLellan handcrafted a miniature motor about the size of a grain of sand and said “I’m Bill McLellan, the guy who made it”, confidently showing it to Feynman [42]. McLellan’s achievement thus encouraged the advances in micro/nanomachining and led to the introduction of the first microelectromechanical system (MEMS) in 1965 by Nathanson within less than a decade [43]. Scaling towards nanomechanical systems was later promoted by Michael Roukes in 2001: “The time is ripe for a concerted exploration of nanoelectromechanical systems (NEMS)” [13].

While designing MEMS/NEMS devices, one needs to consider that the physics at the microscale can be quite different, i.e. some effects that are important in macroscopic world may become negligible with scaling, or vice versa. For example, resonance frequency of beams, tubes, or strings linearly increase with scaling. Thus, smaller resonators (i.e. NEMS) offer faster detection speeds with lighter materials.

With scaling, viscous forces can drastically damp the motion of a microscale object moving in a fluid, e.g. in air [44]. For that reason, MEMS/NEMS measurements are usually carried out in vacuum environment (<10^{-3} torr) when high-Q operation is desired [45]. In contrast, gravitational forces become less effective at the microscale as molecular forces (e.g. van der Waals type) start to dominate due to the increased surface-to-volume ratio of devices [46]. Especially in NEMS, the pronounced surface effects further cause surface-related mechanical losses to become one of the most dominant damping mechanisms [14]. As a remedy, ultra-high vacuum (UHV) surface treatment methods [47] or the utilisation of nanotubes/nanowires (due to their perfectly terminated surfaces [14], [38]) has been proven to minimise such damping.

Thermodynamic effects have also been studied in small dimensions. With scaling, the time needed to bring a system into thermal equilibrium by heat diffusion (τ_{th}) becomes smaller since $\tau_{th} \sim x^2$, where x is the Euclidian distance between two points that are subject to heat transfer [48]. This phenomenon is especially crucial in flexural-mode resonators (e.g. doubly-clamped beams) in which mechanical and thermal modes are significantly coupled due to thermoelastic damping (TED) [49].

Electrical properties are another parameter to consider while designing micro/nanoscale devices. For instance, *d.c.* resistance linearly increases with scaling, causing a linear decrease in power dissipation under a constant voltage. Regardless of the decreasing power consumption, current density should be considered especially for smaller cross-sections in order to prevent conductors from melting or burning. Similarly, dielectric strength of an insulator can be easily exceeded with decreasing thickness of capacitors, which causes failure via dielectric breakdown. Here, it is

important to mention that scaling of a capacitor linearly decreases its capacitance; and this constitutes a problem for capacitive transduction of nanomechanical devices, worsening the signal-to-noise ratio (SNR) of the readout as will be seen in Section 2.3.1 [50]. Therefore, precautions must be taken for safe operation and high-fidelity transduction of nanoscale devices.

2.2 Micro/nanomechanical resonators

Vibrations are experienced in many mechanical systems. If not controlled, vibrations can result in catastrophic events such as the tragic collapse of Tacoma Narrows Bridge in 1940 [51]. In some circumstances, vibrations can be deliberately introduced (or even enhanced) in mechanical structures with beneficial effects such as in MEMS/NEMS, Atomic Force Microscopy (AFM), biomechanics, vehicle suspension systems, and energy harvesters [52]. Mathematical modelling of mechanical systems indicates that there are very specific devices which enhance certain vibrational modes while supressing any others. Those systems showing such resonant behaviour are called as mechanical resonators.

A micromechanical resonator has its dimensions in sub-millimetre region. These systems are generally named after their coupling mechanism to either electrical, optical or both domains. As seen in Figure 2.1, if devices are electrically transduced, they are called as microelectromechanical systems (MEMS) whereas their names become micro-opto-electromechanical systems (MOEMS) when all three domains are coupled [53]. In 1965, Nathanson and Wickstrom have demonstrated the very first MEMS device as an electrical band-pass filter (Figure 2.2) [43]. In this scheme, a suspended gold rod forms the gate of an n-channel transistor in a way that application of an *a.c.* voltage to the rod actuates its transverse motion. When the frequency of the *a.c.* signal is in the vicinity of the mechanical resonance of the rod, the amplitude of mechanical vibrations reaches a maximum, and the conductance of the transistor is considerably

modulated at the same frequency due to electrostatic effects. With this establishment, the constraint on designing resonant electronics by only using bulky and low-quality passive circuit components has been relaxed.

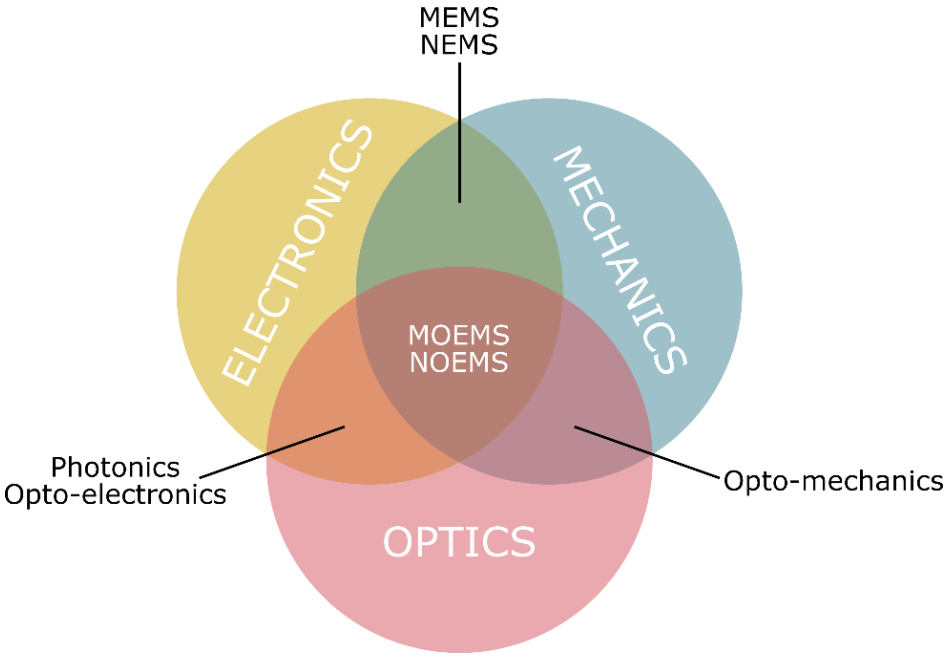


Figure 2.1 Nomenclature of micro/nano systems with respect to coupling mechanism between domains.

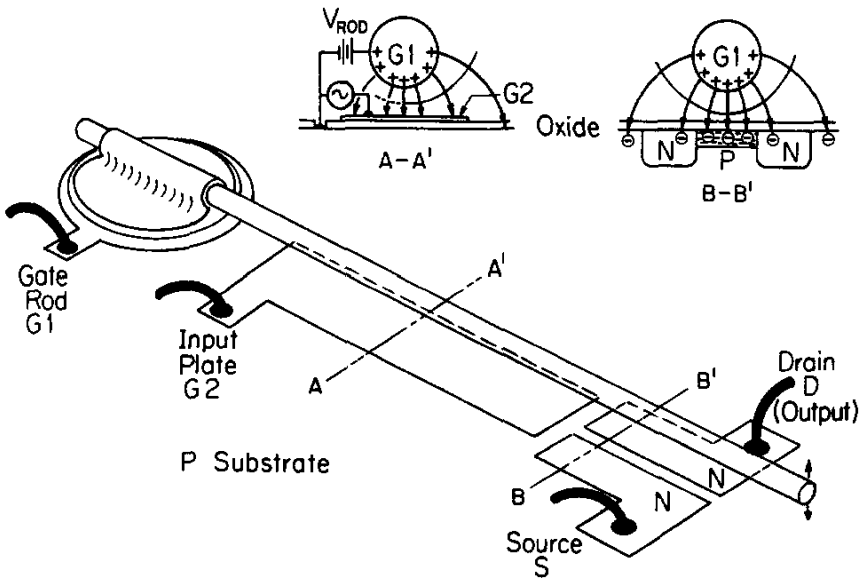


Figure 2.2 First realisation of a MEMS device integrated as a suspended-gate n-channel transistor. A polarisation voltage is applied to G1 while an *a.c.* signal drives G2 (section A – A'). The transverse movement of the rod modulates the channel conductance (section B – B') at the resonance frequency of the rod, providing high-quality bandpass filtering. *Reproduced from [43], with the permission of AIP publishing.*

Subsequently, there have been significant progress in fabrication of MEMS, i.e. surface micromachining. The first integration of poly-Si cantilevers (1983) [54], silicon-to-silicon wafer bonding (1986) [55], and lateral poly-Si resonators as an electrostatic-comb (1990) [56] can be given as examples for such cornerstones (Figure 2.3). No later than 1993, the first commercial monolithic MEMS-based accelerometer with signal conditioning was marketed by Analog Devices [57]. Since then, MEMS devices have been serving as accelerometers [58], gyroscopes [59], pressure sensors [60], band-pass filters [61], and oscillators [62], being expected to reach a market value of $18.2 billion by 2026 [63].

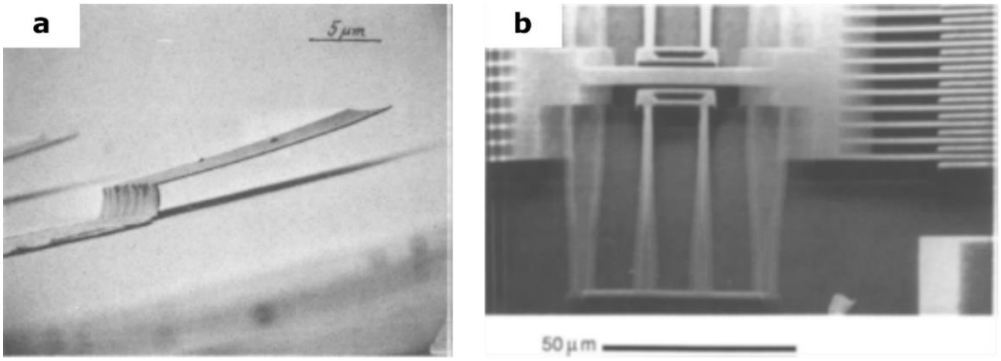


Figure 2.3 Micromachining cornerstones. **a**, First poly-Si cantilever: 25 μm long and 230 nm thick beam suspended 3.5 μm above the Si substrate. © *Electrochemical Society. Reproduced from [54] by permission of IOP publishing Ltd. All rights reserved*. **b**, SEM image showing the vibrations of the first poly-Si electrostatic-comb drive resonator under high vacuum. *Reprinted from [56], with permission from Elsevier.*

As mentioned in Chapter 1, communication electronics rely on synchronisation of pseudorandom clocks, and the communication reliability is a measure of how well these independent clocks within the network are synchronised. In this regard, vibrating MEMS resonators play a key role in providing very precise reference frequencies owing to their high Q factors reported over 10,000 at 1.51 GHz, temperature stability no worse than 0.2 ppm over -45 to 85 ℃, and long-term stability better than 0.5 ppm per year [64], [65]. These values are either comparable to or even better than previously reported values for crystal oscillators [5] and thus, MEMS-based timing applications can meet the needs for better portability, lower power consumption, smaller footprint, and lower cost [64].

The incentive behind further miniaturisation towards nanomechanical resonators is the ability to attain higher resonance frequencies with softer and lighter materials. In other words, NEMS resonators offer faster detection and sensing speeds resulting from the increased resonance frequency while maintaining a far better sensitivity than MEMS. Due to their ultra-low mass and heat capacity, NEMS resonators are capable of counting individual thermal phonons [66] and even sensing below 2 yoctograms (for comparison, a single carbon atom is ~20 yg) [67]. Owing to such superior properties of NEMS, they are frequently utilised in mass spectrometry and AFM. As such, the first application of NEMS resonators dates back to 1999, and not surprisingly, it was an AFM-based data storage media introduced by IBM [68].

Another exciting property of NEMS resonators is their intrinsically-low operating power, which makes them very attractive for signal processing applications. According to Roukes' famous calculation [13], thermal fluctuations in a typical NEMS resonator operating at room temperature are at the attowatt (10^{-18} W) level. Therefore, driving such a resonator even at the picowatt (10^{-12} W) scale will yield an SNR of a million. Even when a million of these devices are operated simultaneously as an ensemble for mechanical signal processing, e.g. in a nanomechanical filter bank, the total power consumption will only be around a microwatt. This value is several orders of magnitude smaller than the power levels of conventional digital filter banks with similar complexity. Furthermore, extremely-high Q factors of NEMS resonators over a million [15] and the tuning capability of both f_0 and Q [16] further facilitates the proliferation of NEMS resonators in signal processing and time-keeping applications in the future.

2.3 Transduction of nanomechanical resonators

As the resonator dimensions get smaller, the transduction mechanism becomes elusive. Especially for some exciting applications such as bio-detection in liquid buffers or observation of quantum mechanical effects, the detection sensitivity has to be

pushed below 1 fm $Hz^{-1/2}$ [69]. In this section, various transduction methods for nanomechanical systems will be represented, with a focus on electrical and optical domains.

2.3.1 Electrical techniques

At the very early stages of NEMS (in 1990s), electromagnetic (Lorentz) forces have first been introduced for actuation and detection of nanobeams successfully [70]. In this method, the resonator is placed in a static magnetic field while an alternating current from a network analyser is passing through the resonator. The alternating current generates a Lorentz force over the resonator and drives it into motion. As the resonator vibrates, an electromotive force is generated between its terminals, which can then be detected by the network analyser (Figure 2.4a). However, the need for superconductor magnets (at cryogenic temperatures) to create the required large magnetic fields (1-10 Tesla) restricts the potential applications of this technique.

At cryogenic temperatures, atomic point contacts have also been demonstrated as precision transducers for NEMS, yielding displacement noise levels as good as 2.3 fm $Hz^{-1/2}$ [71], [72]. Exploiting single electron transistors for motion detection has likewise enhanced the displacement sensitivity in NEMS measurements, down to 2 fm $Hz^{-1/2}$ [73]. However, such techniques also have limited applications due to the requirement of sub-kelvin temperatures.

For room-temperature detection of nanomechanical motion, electrostatic (capacitive) effects have been highly exploited. In this technique, the resonator forms a capacitor with a gate electrode. As seen in Figure 2.4b, under a *d.c.* bias voltage V_g, the motion of the resonator induces an additional electric current due to the change in capacitance ($\Delta q = V_g \times \Delta C$), which can be sensed by a low-noise amplifier. Here, it should be noted that the capacitance of a typical doubly-clamped beam resonator is around 10^{-17} F whereas a measurement setup (composed of cables and contact pads) constitutes a

huge parasitic load of ~10^{-11} F. This makes capacitive transduction of NEMS almost impractical at high frequencies due to the reduced bandwidth. However, there are various examples of capacitive readout schemes for NEMS that exploit special techniques to extend the measurement bandwidth.

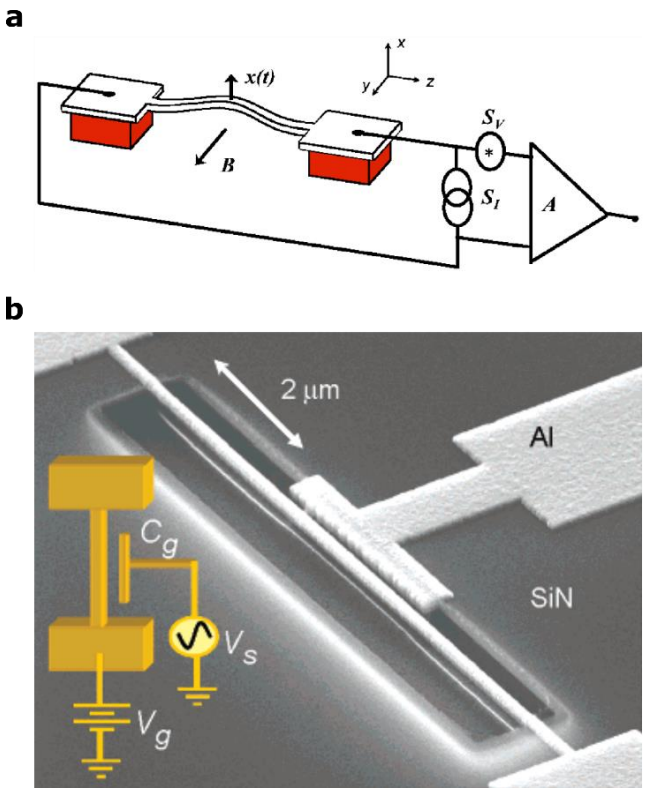


Figure 2.4 Exploitation of magnetic and electric fields for NEMS transduction. **a**, Magnetomotive sensing scheme. Vibrations of a nanobeam inside a static magnetic field generates an electromotive force, which is detected by an amplifier. *Reprinted from [14], with the permission of AIP publishing*. **b**, Capacitive transduction of a doubly-clamped Si_3N_4/Al beam with an Al gate. The nanobeam is biased with a *d.c.* voltage. A sinusoidal gate voltage drives the resonator into motion. *Reprinted (adapted) with permission from [50]. Copyright 2022 American Chemical Society*.

In 2006, Truitt et al. have shown capacitive transduction of doubly-clamped beams using impedance matching networks [50]. By determining the lumped parameter model of the resonator, they designed an off-chip LC network to reduce the reflected power (due to impedance mismatch) in the vicinity of the resonance frequency, enhancing the readout signal. A similar method have later been utilised in a graphene NEMS platform (this time with a π-matching network) [74].

A year later, Verd et al. (2007) have integrated a submicron-sized cantilever with a complementary metal-oxide-semiconductor (CMOS) circuitry on a single chip, significantly reducing the footprint of the measurement system [75]. They estimated the input capacitor of the CMOS amplifier to be at the femtofarad scale. Thus, this method inherently offers a much larger measurement bandwidth as the amplifier acts as a buffer between the resonator and the highly capacitive experiment setup. Using this method, in 2014, a self-sustained oscillator (NEMS + CMOS) has also been implemented, making monolithic time-keeping devices of NEMS a possibility [76].

Instead of tweaking the measurement bandwidth by impedance matching or monolithic integration, alternatively the readout signal can be mixed down to frequencies below the cut-off frequency of the experiment. In 2004, Sazonova et al. have capacitively transduced a semiconducting carbon nanotube (CNT) by biasing both the resonator and the gate electrode with *a.c.* signals [18], which is dissimilar to the scheme in Figure 2.4b. In addition, the signal applied to the nanotube is selected at a slightly different frequency from the gate drive, with a frequency difference of $\Delta\omega$ (a few kHz). Since the current through the nanotube is the multiplication of these two signals, the resulting Δq is mixed down to $\Delta\omega$. Consequently, the readout signal can be detected by a lock-in amplifier with its reference set to $\Delta\omega$. It is worth noting that the down-mixing method is not only limited to capacitive transduction but also applicable to other methods such as AFM-based techniques [77], interferometric methods [78], and piezoresistive detection [79].

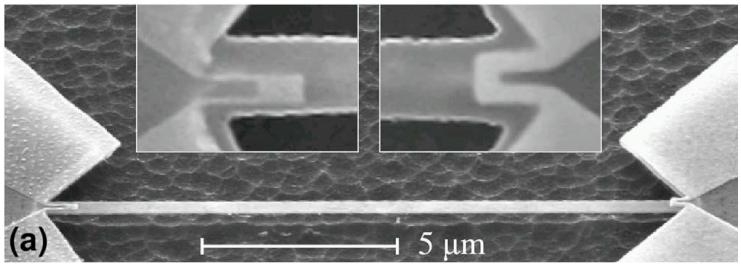


Figure 2.5 SEM image of a SiC nanobeam. A thin layer of gold is deposited on both ends of the resonator for piezoresistive detection (left inset) and electrothermal drive (right inset). *Reprinted from [80], with the permission of AIP publishing*.

Piezoresistivity, i.e. the change in electrical resistance due to mechanical strain, is another viable method for NEMS transduction. Since a mechanical resonator continuously experiences dynamic strain due to vibrations, its electrical resistance is proportionally modified [81]. This modification can then be converted to a readout signal by using either a *d.c.* or an *a.c.* bias [82], offering a robust detection of nanomechanical motion with displacement sensitivities as good as 39 fm $Hz^{-1/2}$ in ambient conditions (i.e. room temperature and 1 atm) [83].

Traditionally, a piezoresistive loop is patterned on the resonator surface (typically a metal thin-film) to harness the net strain (Figure 2.5). However, with further scaling of devices, this approach becomes impractical due to the stringent nanofabrication requirements. On the other hand, in doubly-clamped beams, there exists a non-zero net strain due to the elongation of the device. Although this effect is less pronounced, it is possible to obtain a good SNR by implementing special techniques such as down-mixing methods [79] or differential readout [84]. Thus, the applicability of piezoresistive sensing has further been expanded to lithographically-defined Si nanobeams [84], leading to large-scale integration of self-sensing NEMS resonators of doubly-clamped beams at very high frequencies for the first time.

2.3.2 Optical techniques

As a common way to read out NEMS at room temperature, interferometric transduction via free-space optics have been introduced and first applied to submicron-sized resonators by Carr et al. in 1998 [85]. The main drawback of this method is the difficulty of focusing and aligning the micron-sized light spot onto nanoscale devices at the far-field. Thus, sub-wavelength dimensions of NEMS devices impair the displacement sensitivity, which remains around pm $Hz^{-1/2}$ level in this method [86]. A better confinement of the optical mode can be achieved by near-field plasmonic interactions, which can bring the detection limit down to 6 fm $Hz^{-1/2}$ for a beam power of ~1-2 mW

[87]. Despite this high sensitivity, the requirement of metallic surfaces in plasmonic devices limits the range of materials that can be used for fabrication.

Another way to improve near-field optical interactions is to use integrated photonics. One approach relies on the idea of suspending a portion of photonic structures such as waveguides [88], Mach-Zehnder interferometers [89], and microcavities [90]. In all these examples, mechanical displacement of the free-standing portion (i.e. the NEMS resonator) modifies the mode index and induces a phase and/or an amplitude shift. Especially in high-finesse cavities, such optomechanical coupling becomes extremely strong and can yield displacement sensitivities as good as 0.45 fm $Hz^{-1/2}$ at mW-level optical powers [90].

Instead of suspending the photonic structure itself, evanescent field coupling can also be exploited to transduce NEMS. This can be either done by fabricating a nanomechanical beam next to a photonic element (which limits the applicable material range) [89], [91] or aligning the photonic device with an off-chip NEMS resonator (which requires precise positioning) [92], [93]. In both cases, the resonator acts as a scatterer and perturbs the evanescent tail of the optical mode guided inside the photonic waveguide.

The detection sensitivity can be significantly improved in the case of an optical cavity. One such example is given in Figure 2.6a, where Anetsberger et al. (2009) have coupled doubly-clamped Si_3N_4 beams to a toroidal microcavity illuminated by a tapered optical fibre. The authors aligned the devices by means of piezoelectric positioners, reaching a shot noise-limited displacement sensitivity of 0.57 fm $Hz^{-1/2}$ for a 65 µW probe [92]. Ten years later, Barnard et al. (2019) have measured real-time vibrations of a CNT resonator using a similar method (as illustrated in Figure 2.6b) but obtained a displacement noise as large as 700 fm $Hz^{-1/2}$ due to the much smaller diameter of the CNT [93]. Even though these methods enable the transduction of exotic NEMS resonators, they still constitute a technological challenge due to the need for optimum

conditions such as precise alignment of both resonators and input fibres with the optical cavities. Thus, monolithic integration of these methods is a necessity.

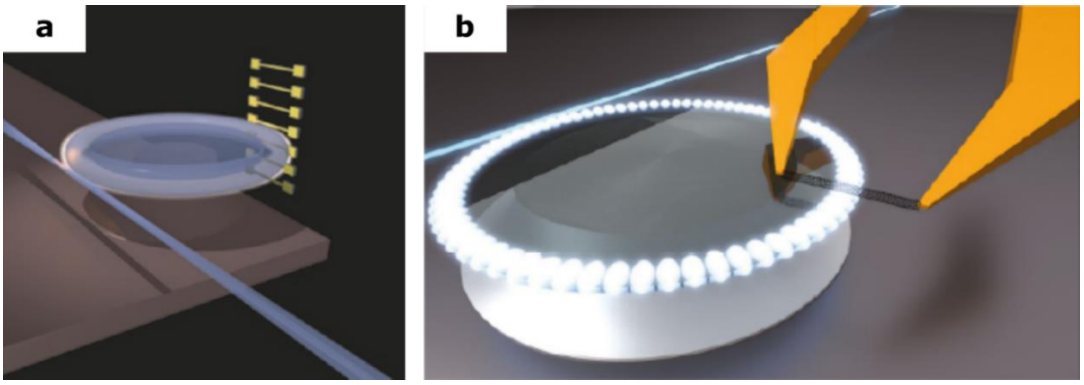


Figure 2.6 Near-field (evanescent) coupling of nanomechanical resonators to optical microcavities. **a**, A microtoroidal near-field sensor [92]. The light is coupled into the microcavity by a tapered fibre, and an off-chip array of Si_3N_4 beams is interfaced with the cavity using piezo positioners. *Reproduced with permission from Springer Nature*. **b**, CNT-microcavity scheme [93]. A pair of electrical tweezers holds the nanotube over the microdisk cavity. The optical mode within the microcavity is excited by a bare optical fibre. *Reproduced with permission from Springer Nature.*

All in all, there is a tremendous amount of ongoing research to develop novel NEMS transduction techniques that are also universal (i.e. material-independent). A scalable, fully-integrated motion sensor that can achieve excellent displacement sensitivities over a large measurement bandwidth is the ultimate goal of NEMS researchers, and so is the ability to achieve such a performance routinely [69], [94].

2.4 Stress-tuning of nanomechanical resonators

With the incentive of making large-scale NEMS devices, reliable and wide-range tuning of f_0 has gained importance not only in signal processing applications (short-term tuning) but also for correcting post-fabrication variations, changing operation regimes, and compensating for ageing of devices (long-term tuning) [19], [20]. It is well-known from the continuum mechanics that application of mechanical stress to a beam alters its resonance frequency [95]. This is not dissimilar to changing the tension of guitar strings, e.g. under a tensile stress of σ, the frequency increases linearly with $\sqrt{\sigma}$ [20]. As such, active stress-tuning of mechanical resonance can readily be implemented in-

situ via electromagnetic fields at the nanoscale, and some of the most common techniques are investigated in this section in terms of tuning range and Q factor variation.

Gate-induced electrostatic forces have been widely used for stress-tuning of NEMS devices. One advantage of this technique is its facile implementation to a wide range of configurations as long as the resonator is non-insulating, e.g. InP [96] and SnO_2 [97] nanowires, CNTs [18], graphene flakes [17], SiC beams [98], and MoS_2 nanoribbons [99]. However, the capacitive nature of this method leads to additional mechanical damping and can decrease Q factors by more than 50% due to loaded$-Q$ effect [98], [100]. This aspect further gains importance in low-mass resonators such as nanotubes and monolayers, which already suffer from low Q factors at room temperature. Furthermore, the tuning range is typically below 15% and is limited by the pull-in voltage threshold, over which the resonator irreversibly snaps in and fails [98].

Stress-tuning can also be performed through dielectric gradient forces, which is a generalised version of capacitive tuning, i.e. it does not require a conductive media. This universal tuning scheme has enabled the use of high-Q dielectric materials such as Si_3N_4 in tunable NEMS for the first time. The method has been first demonstrated by Unterreithmeier et al. (2009), yielding a tuning range of ~1% in doubly-clamped Si_3N_4 beams with Q factors over 100,000 [21]. In 2012, using a similar design, Rieger et al. have increased the tuning range to 5% for a tuning voltage below 10 V [101]. Similarly to capacitive tuning, the authors also reported a 2-3× degradation of Q factors within the tuning range.

Another prevalent technique is electrothermal tuning, where Joule heating leads to thermal expansion and modifies the mechanical tension of the resonator. This method has been first demonstrated in NEMS by Jun et al. (2006) using Al-SiC nanobeams [20]. They observed a tuning range of ~10% prior to the device failure for a *d.c.* heating power below 40 μW, while the Q factors degraded by 8%. To achieve a higher tuning

range in this method, superior thermal expansion coefficients and higher strain limits are a necessity. As such, Ye et al. (2018) have shown a record tuning range of ~310% with tri-layer graphene flakes for *d.c.* power levels exceeding 6 mW (together with a 10-fold variation in Q factors) [19]. Given that electrothermal tuning suffers from high power dissipation and variation of Q factors, the applicability of this method to low-power and reliable designs becomes problematic.

Piezoelectric materials have also been exploited for stress-tuning of NEMS due to their ability to convert electric fields into mechanical strain. Compared to other methods, anisotropic nature of piezoelectricity is a major advantage, enabling adjustable tuning slopes (and signs) with decent linearity. However, fabrication challenges, slow response times, and small tuning ranges (<< 1%) restrict the proliferation of this method in tunable NEMS and require further investigation [22], [102], [103].

Overall, active stress-tuning has proven to be a viable way to alter the resonance frequency of nanomechanical resonators; however, there are several drawbacks. Firstly, one needs continuous electrical stimuli to maintain the tuned frequency. Such volatility inevitably adds to the overall power dissipation of the system, and no active tuning mechanism today can offer a non-volatile solution. In addition, the need for high tuning voltages (typically 5-30 V range) raises reliability issues at the nanoscale and further hinders the compatibility of these techniques with current CMOS devices (which operate at ~1 V [104]). Finally, the variation of Q factors is not desired in sensing and signal processing applications that require a robust feedback loop such as control systems, frequency-tracking, and local oscillator design [20]. All these concerns further encourage the NEMS community to discover novel techniques for tuning the mechanical resonance with ultra-low or no tuning power as well as minimal perturbation to Q factors.

2.5 Introduction to phase-change materials

Chalcogenide-based phase-change materials (PCMs), e.g. GeTe, GeSbTe (GST), and AgInSbTe (AIST), have the ability to reversibly switch between an amorphous and a crystalline phase in solid state. Owing to the distinct bonding nature and geometry between these two phases [105]–[107], PCMs offer a high contrast in their physical properties such as electrical conductance [108], refractive index [28], and Young's modulus [31]. Thus, PCMs have pioneered the development of three generations of optical storage technology (i.e. CD, DVD, and Blu-ray) [25], multi-level memory devices for in-memory computing [29], [109], reflective displays [28], and smart coatings [110].

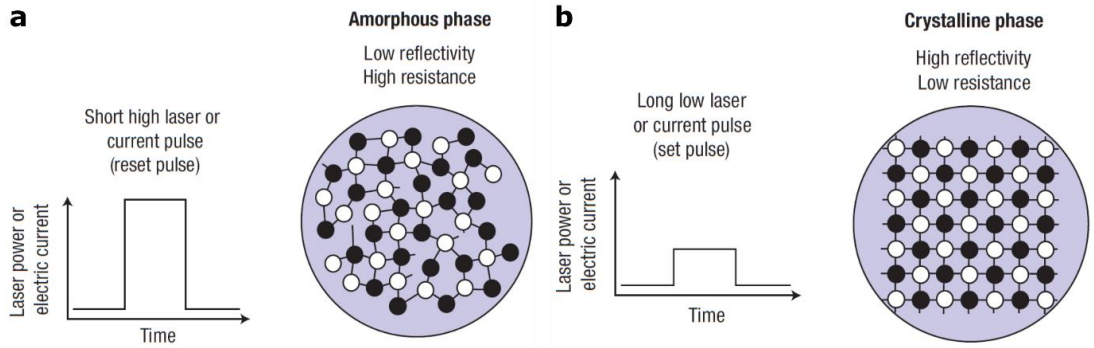


Figure 2.7 Phase-change process. **a**, A highly-energetic, short electrical or optical pulse results in amorphous phase while **b**, a longer and less-energetic pulse leads to crystallisation. *Reproduced from [25] with permission from Springer Nature.*

Crystal structure of PCM thin-films can be switched by controlling heating and cooling rates by means of electrical or optical pulses [25]. Applying a short and high-energy pulse melts the material and rapidly cools it down (melt-quenching). This leads to a covalently bonded amorphous solid that lacks long-range order (Figure 2.7a). On the other hand, a relatively slow and less energetic pulse can raise the temperature of the material below the melting point but above the glass-transition temperature, resulting in a resonantly bonded crystalline state (Figure 2.7b). In the electrical domain, crystallisation process is initiated via threshold switching, whereby the material goes under an electronic breakdown above a threshold field and forms a conductive filament prior to the nucleation of the crystalline phase [111]. As such, structural switching of

PCMs can be performed with cyclability rates up to a trillion, and most remarkably, PCMs retain their phases at room temperature for decades [112].

To shed more light on the phase-change process, in 2011, Kolobov et al. have studied the directional bond energy hierarchy in crystalline GeTe caused by the rhombohedral distortion in the lattice, i.e. Peierls distorted with resonance bonding, which results in three long and three short bonds with different electron densities (Figure 2.8a) [105]. Consequently, the resonantly bonded crystalline state becomes very fragile in a way that even low-energy disruptions to the longer (weaker) bonds can completely destroy the ordered phase and initiate amorphization without melting. Here, to effectively trigger this non-thermal process, the input energy should only excite the appropriate vibrational modes of the crystal, and this has been previously performed by using coherent phonons [113] and/or polarised lasers [114]. Recently, the use of carrier-wind force (via electrical pulsing) to selectively destroy the subsystem of weaker bonds has been demonstrated in phase-change nanowires of GST [34] and GeTe [36]. Here, the nanowire configuration is the ideal system of choice owing to its single-crystal structure and one-dimensional (1D) electron flow, both of which are unavailable in thin-films. As seen from Figure 2.8b, the high dislocation contrast and the spot splitting along the nanowire growth direction indicate the directional destruction of long-range order in the electrical domain, making nanowires a greener alternative to thin-films.

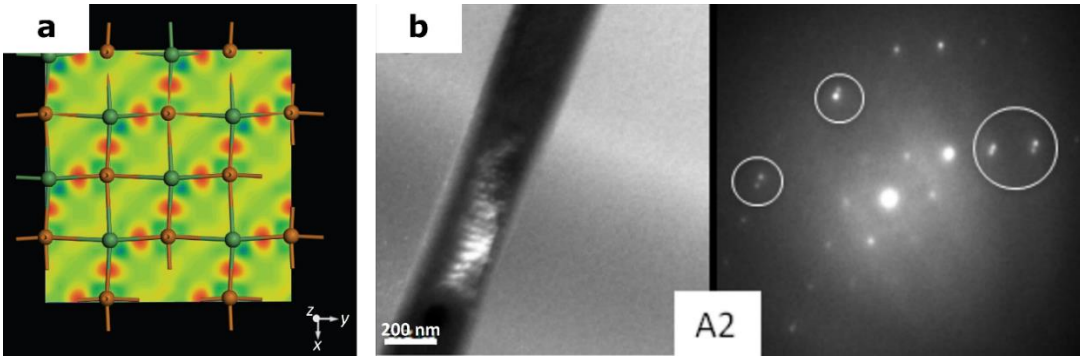


Figure 2.8 Non-thermal, dislocation-based amorphization in phase-change nanowires. **a**, Simulated model of electron charge density in GeTe (Ge, green, Te, tan) [105]. A significant bonding energy difference exists between the short and long bonds. The short bonds have a higher electron density, leading to a stronger bonding. *Reproduced with permission from Springer Nature*. **b**, TEM image (left) of a GeTe nanowire after low-energy electrical pulsing. The image shows a clear dislocation contrast. Diffraction pattern (right) shows spot splitting along the growth direction (<110>) (zone axis: [111]). *Reprinted (adapted) with permission from [36]. Copyright 2022 American Chemical Society.*

Stress-related reliability issues in PCMs have also been widely studied. In 2001, both Njoroge et al. and Pedersen et al. have observed a volume reduction of 5-10% in thin-films of Te alloys after crystallisation [115], [116]. Such a dramatic volume change between the two phases causes excessive stress build-up upon switching, leading to delamination failure [117] and formation of amorphous domes [115]. The latter issue further manifests itself over long periods of time as behavioural drift in electrical [118], optical [119], mechanical [120], and thermal [121] properties. This is a consequence of inefficient stress relaxation in thin-films and can be engineered by utilising high surface-to-volume ratio materials such as nanowires. As demonstrated by Mitra et al. in 2010, phase-change nanowires can relax the stress more effectively due to their large surface area, resulting in an extremely low drift in amorphous phase compared to that of thin-films [38]. Therefore, phase-change nanowires offer not only ultra-low energy switching but also superior reliability, which makes them a highly sought-after candidate for future designs.

2.6 A tunable phase-change nanowire NEMS

It is well-known that phase-change materials offer distinct mechanical properties between the two phases. By using PCM-coated Si cantilevers, both Won et al. (2012) and Nazeer et al. (2015) have observed an increase in Young's modulus (E) of PCM thin-films upon crystallisation with a contrast of up to 6 [31], [32]. In 2015, Hosseini et al. have suggested exploiting this unique property of PCMs as a tunable NEMS framework, where $f_0 \propto \sqrt{E}$ [33]. The authors simulated the mechanical resonance behaviour of the device consisting of a PCM thin-film sandwiched between two graphene electrodes (Figure 2.9a). Their results suggested that this structure could be operated as a tunable NEMS resonator covering the whole GSM band (800 MHz to 1.9 GHz). This method of tuning is also power-free owing to its non-volatile nature, i.e. no voltage/current bias is needed to maintain the tuned frequency.

However, at the device level, the design in Figure 2.9a poses some practical challenges. Firstly, PCM thin-films require melt-quenching for amorphization, and this is not feasible in free-standing systems such as NEMS. Also, crystallisation in the electrical domain occurs via random formation of conductive filaments in thin-films, which prevents homogeneous crystallisation. On the other hand, phase-change nanowires do not suffer from these issues, and they further offer paramount structural stability and require much lower switching energy. Thus, utilisation of PCM nanowires as a tunable NEMS resonator can serve as the ultimate tuner.

The proposed device design is given in Figure 2.9b. Here, a phase-change nanowire is suspended over a photonic waveguide, and the electrodes on both sides enable electrical access to the device. Furthermore, tuning and readout of this device can be simultaneously done in electrical and optical domains owing to the versatility of PCMs, thus elucidating its feasibility for exciting applications in IoT systems and many other opto-electro-mechanical frameworks. As such, the feasibility of this scheme will be

investigated in the following chapters, with an emphasis on developing novel tuning and transduction schemes for nanowire NEMS using exotic materials.

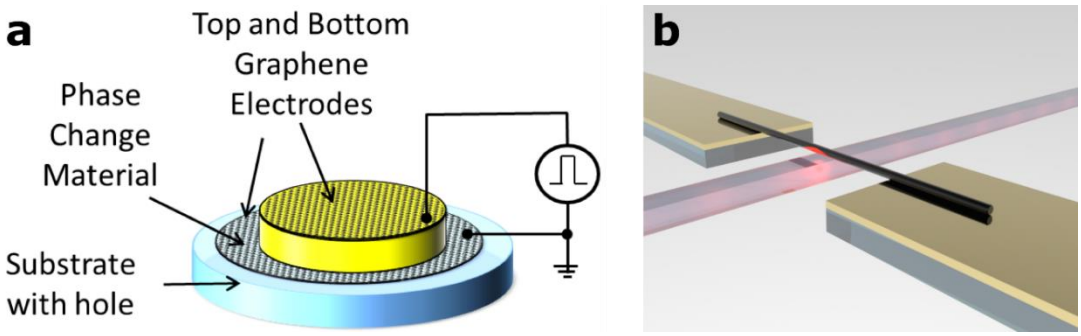


Figure 2.9 Phase-change NEMS. **a**, Proposed device design by Hosseini et al. showing a free-standing PCM thin-film sandwiched between graphene electrodes. Reproduced from [33] under CC BY 4.0 license. **b**, Proposed device design for this work. A phase-change nanowire is suspended by two electrodes over a photonic waveguide.

Chapter 3

A novel nanowire pick-and-place technique

The findings presented in Chapters 3 & 6 have been published in:

Utku Emre Ali, He Yang, Vladislav Khayrudinov, Gaurav Modi, Zengguang Cheng, Ritesh Agarwal, Harri Lipsanen, Harish Bhaskaran, *"A Universal Pick-and-Place Assembly for Nanowires",* Small 2201968 (2022). DOI: 10.1002/smll.202201968

3.1 Overview

As discussed earlier, this work aims to study tuning and transduction characteristics of phase-change nanowire resonators. To achieve this, firstly, a functional platform that enables electrical or optical access to a doubly-clamped, free-standing nanowire has to be fabricated. Given the nanoscale dimensions of these devices, the fabrication of such platforms has been performed in a cleanroom facility, using standard and reliable micro/nanofabrication steps. As such, the top-down fabrication of the functional platform (i.e. the device chip) is described in Section 3.2. Since depositing CVD-grown, single-crystal nanowires on these micro/nanoscale platforms is challenging, the steps regarding a novel pick-and-place assembly for nanowires are given in Section 3.3.

3.2 Fabrication of the device chip

Step-by-step fabrication of the electrical platform is summarised in Figure 3.1. To start with, a 10×10 mm^2 piece is diced from a Si wafer, which contains a 3 µm-thick oxide layer (SiO_2) and a thin layer of Si_3N_4 (0.33 µm) on top. Prior to the lithography process, wet cleaning of the sample is performed in an ultrasonic bath for 10 minutes with acetone and then isopropyl alcohol. Later, the bare chip is spin-coated with a positive-tone electron-sensitive resist (AR-P 6200.09). The spin-coating is performed for 45 seconds at 4000 rpm, followed by a soft bake for 3 minutes at 150 ℃.

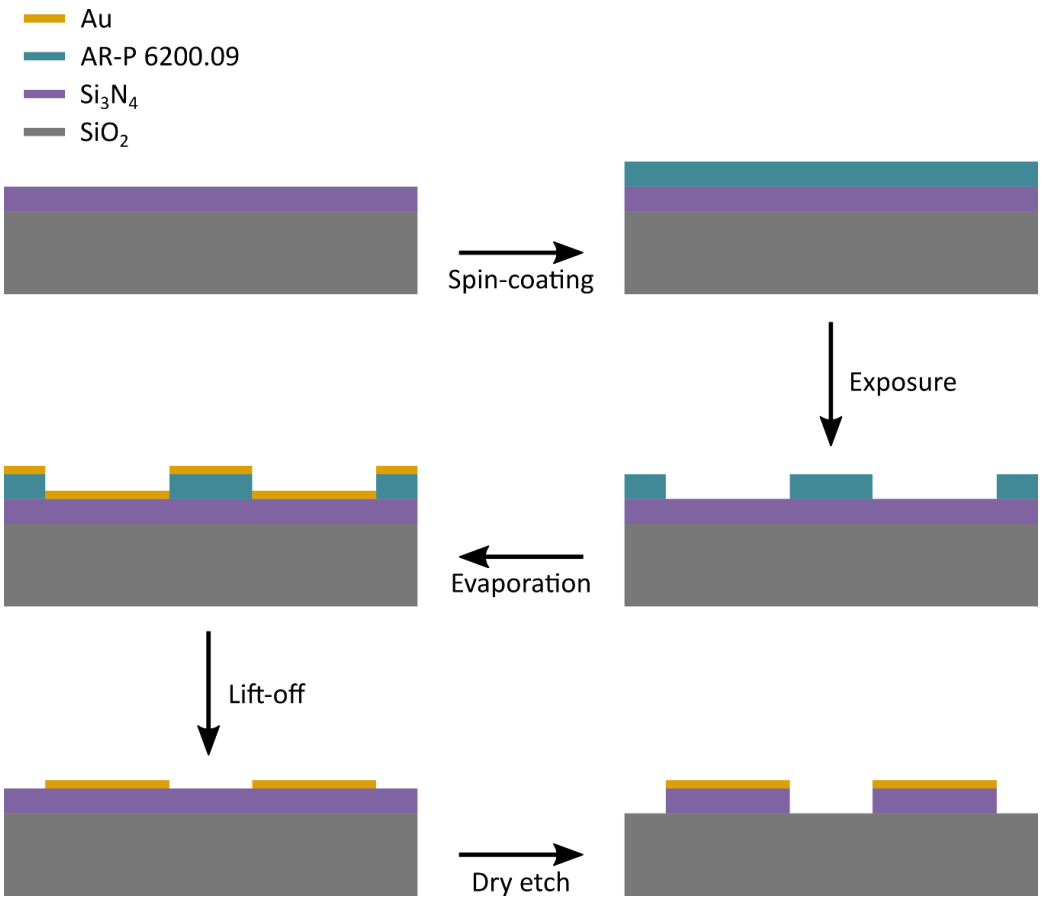


Figure 3.1 Nanofabrication process flow regarding the electrical chip.

To create the patterns, a computer-aided design (CAD) file is generated using Python programming language together with the open-source gdsHelpers library (Figure 3.2) [122]. Then, the electrodes and markers are patterned within a single electron-beam lithography step, using JEOL 5500FS (50 kV) lithography system. Given the large

feature sizes (over 1 µm) in this step, conventional photolithography has also been attempted but it increased the surface roughness at the electrode edges, impairing electrical contacts to the nanowire. The beam current is set to a high value of 10 nA. Exposure dose is carefully chosen as 180 µC cm^{-2}. Following the patterning, the resist is developed in AR 600-546 and methyl isobutyl ketone (MIBK) for 30 and 15 seconds, respectively, and the sample is rinsed in isopropyl alcohol for 15 seconds to remove any residue. This process yields a mask thickness of ~200 nm, as measured by a profilometer. Subsequently, 95 nm-thick Au electrodes are deposited by thermal evaporation with a 5 nm of Cr adhesion layer. For not disturbing the vacuum level inside the evaporation chamber, the deposition rate is chosen as 0.2 nm per second. After the deposition, the chip is immersed in mr-Rem 700 remover for 3 hours (at 70 ℃) to lift off the AR-P 6200.09 mask. At the end of 3 hours, a pipette is used to agitate the remover solution for thoroughly separating the metal layer from the non-patterned areas. Following the rinsing of the chip with acetone and isopropyl alcohol, the metallisation step is completed.

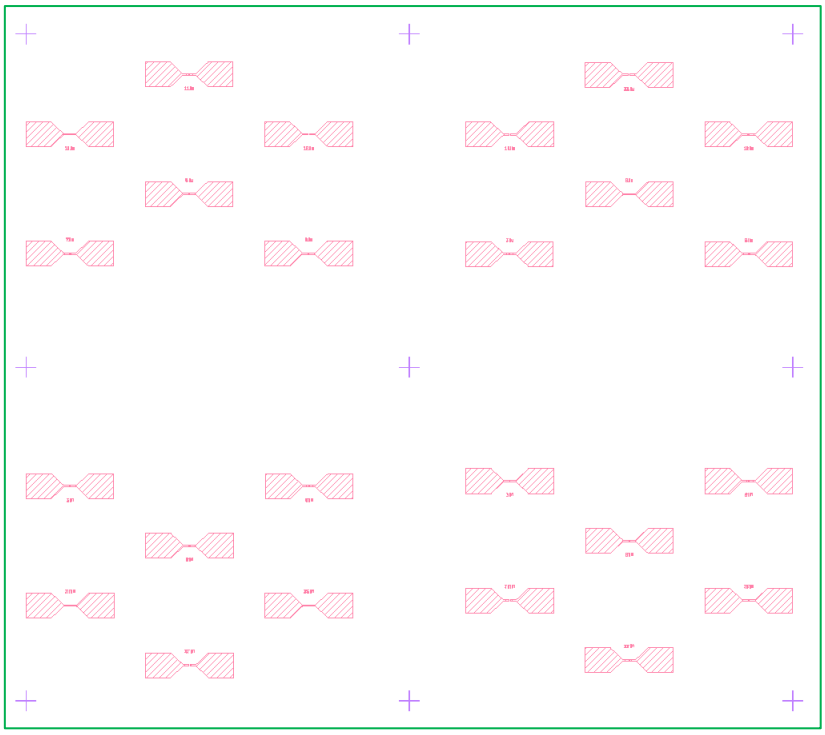


Figure 3.2 CAD file containing the layout of electrodes and alignment markers.

To create deeper trenches for secure suspension of the nanowires, the Si_3N_4 thin-film is further etched anisotropically by reactive ion etching (RIE, Oxford 80 Plasmalab). Here, the electrodes deposited in the previous step act as a hard mask during the etching process. The RIE recipe utilises CHF_3 (50 sccm), Ar (10 sccm), and O_2 (2 sccm) gases under a chamber pressure of 25 mbar and a plate temperature of 20 ℃. The RF power for plasma generation is set to 100 W, yielding an etch rate of approximately 22 nm per minute. Thus, by fully removing the Si_3N_4 layer, trenches deeper than 400 nm in total are created. The resulting electrical platform can be seen in Figure 3.3.

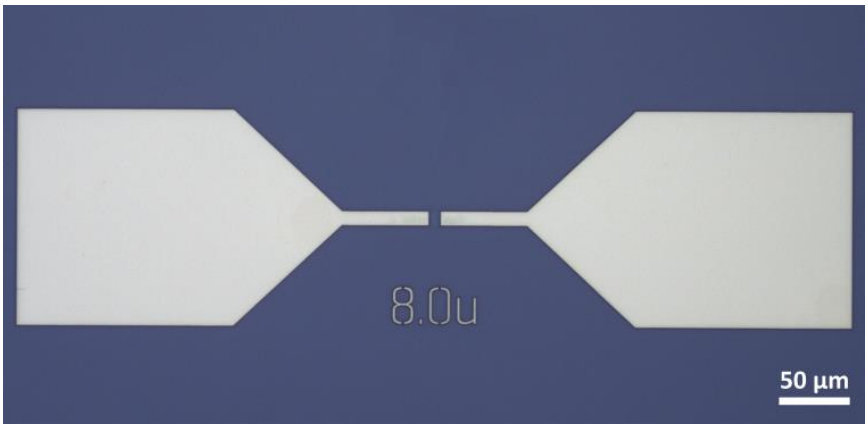


Figure 3.3 Optical micrograph of the Au electrodes (yellow) with a gap of 8 µm.

Fabrication of the opto-electronic chip is depicted in Figure 3.4. Here, it should be noted that the opto-electronic chip requires two lithography steps, the first of which is the metallisation and performed similarly to the fabrication of the electrical chip. Global alignment markers are deposited during the metallisation step in order to facilitate the second lithography step.

To pattern the photonic waveguides of Si_3N_4 in the second lithography step, the sample is spin-coated again. Spin-coating process consists of two stages. In the first step, the chip is coated with an adhesion promoter (TI Prime) at 4000 rpm for 20 seconds and soft-baked on a hot plate at 120 ℃ for 2 minutes. The promoter is for enhancing the adhesion between the chip surface and the negative-tone resist in the following step.

The sample is then spin-coated with a negative-tone electron-sensitive resist (ma-N 2403) for 3700 rpm for 60 seconds. Soft-baking of ma-N 2403 is performed at 90 ℃ for 2 minutes. This whole process results in a resist thickness of approximately 300 nm, which is enough to fully etch the 330 nm-thick Si_3N_4 layer.

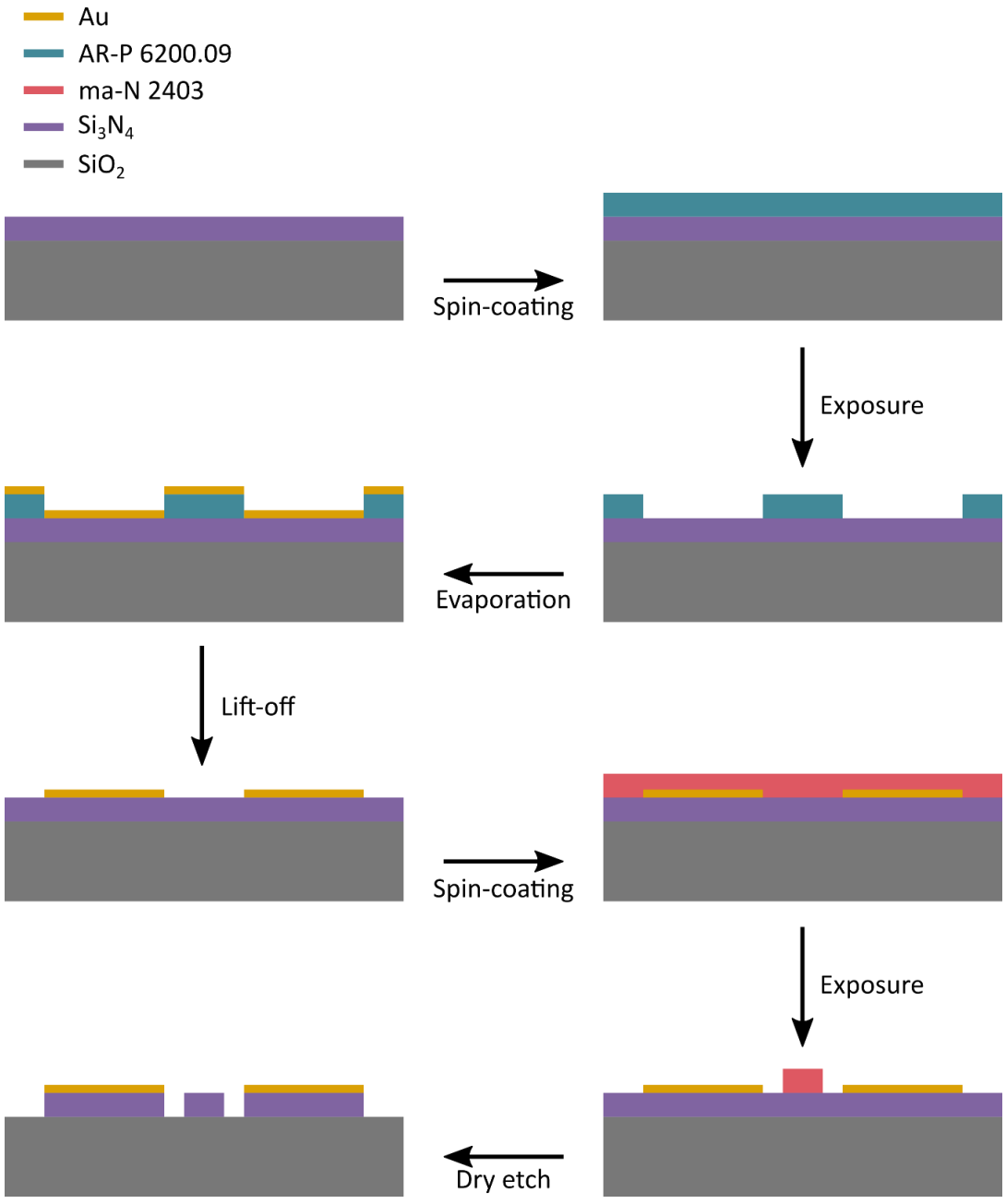


Figure 3.4 Nanofabrication process flow regarding the opto-electronic chip.

In the second electron-beam lithography step, global alignment markers (cross-shaped) are used to align the waveguide patterns with the electrodes in a way that the

waveguides sit in the middle of the gap between the electrodes. The beam current is selected as 100 pA given that the minimum feature size in this step is around 80 nm. A dose of 220 μC cm^{-2} is used to expose the patterns. Following the exposure, the resist is developed in Microposit MF-319 for 75 seconds, and then the sample is rinsed in deionised water. To further increase the etch resistance and mechanical stability of the resist, the sample is hard-baked on a hot plate at 90 ℃ for 10 minutes. Hard-baking also helps smooth out the sidewall roughness of the waveguides during RIE by reducing the imperfections of the resist patterns [123].

The RIE is performed in the same way as done for the electrical chip. Following the etching, the sample is immersed in mr-Rem 700 remover for 3 hours (at 70 ℃) to get rid of the ma-N 2403 mask and then rinsed in acetone and isopropyl alcohol. Thus, the fabrication is completed. Figure 3.5a shows an optical microscope image of the resulting chip (i.e. the proposed design in Figure 2.9b), and the SEM image in Figure 3.5b zooms into the grating couplers [124]. To confirm that the electrodes are higher than the waveguides, AFM topography of the nanowire suspension area (i.e. the gaps between the electrodes) is obtained. According to the height data in Figure 3.5c, the electrodes have a thickness of ~102 nm, which is in good agreement with the value set during the thermal evaporation step. This height difference further enables secure suspension of the nanowire while allowing for evanescent field interactions between the nanowire and the waveguide.

As discussed in Section 2.3.2, optical cavities dramatically improve the detection sensitivity when used as a NEMS transducer. For that reason, ring resonators of Si_3N_4 have also been fabricated to form a microcavity as seen in Figure 3.6. Similarly to the design in Figure 3.5a, grating couplers are designed to couple light into the devices, and thick Au electrodes facilitate the suspension of the nanowires.

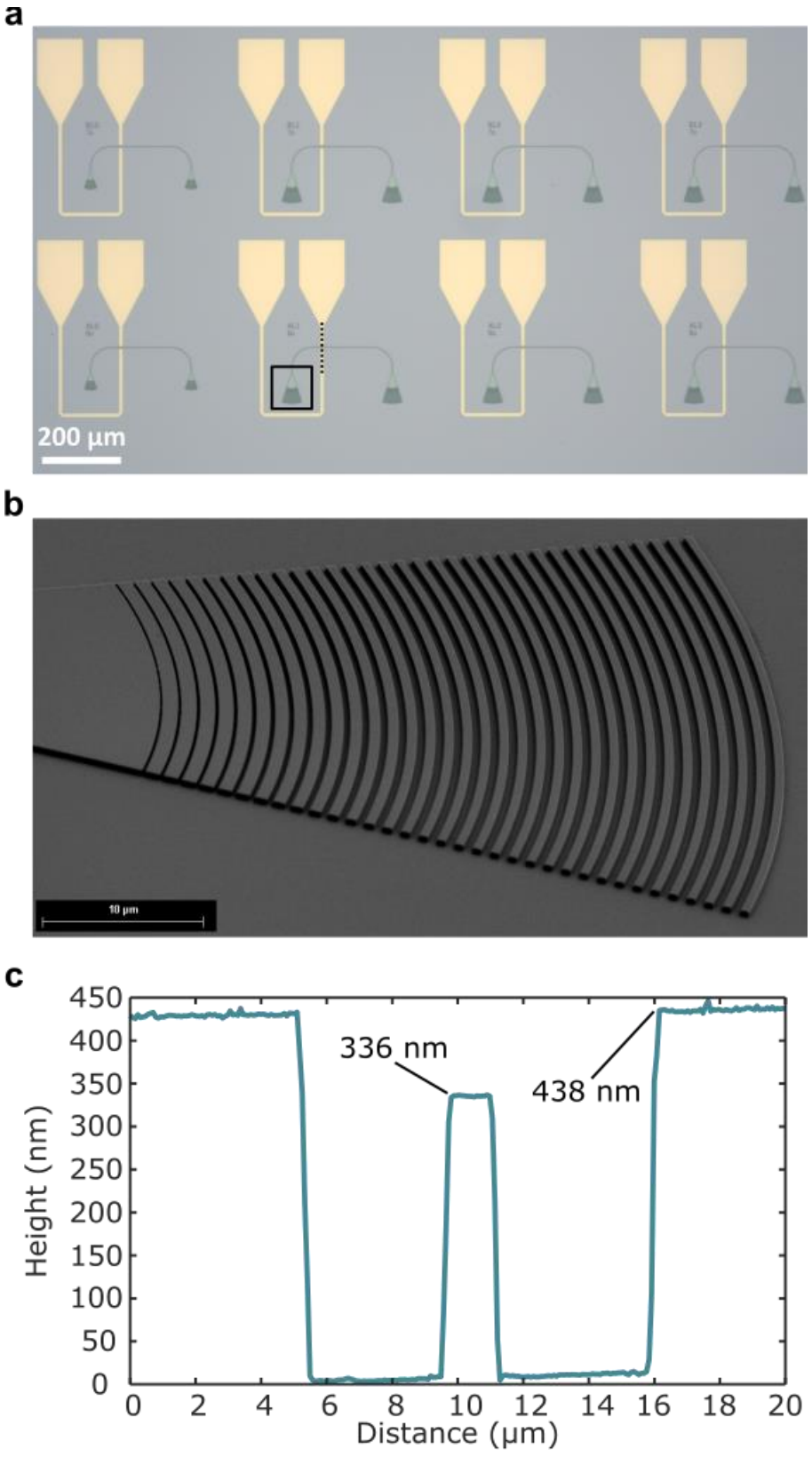


Figure 3.5 The fabricated opto-electronic chip. **a**, Optical microscope image showing a portion of the chip. Si_3N_4 waveguides (green) are aligned with the gaps between the Au electrodes (yellow). **b**, Angled-view SEM image of the grating coupler encircled in **a** with the solid square. **c**, Height data measured by AFM along the dashed line shown in **a**. Height difference between the waveguide (in the middle) and the electrodes (at the sides) is ~102 nm. Gap between the electrodes is measured as 11 µm.

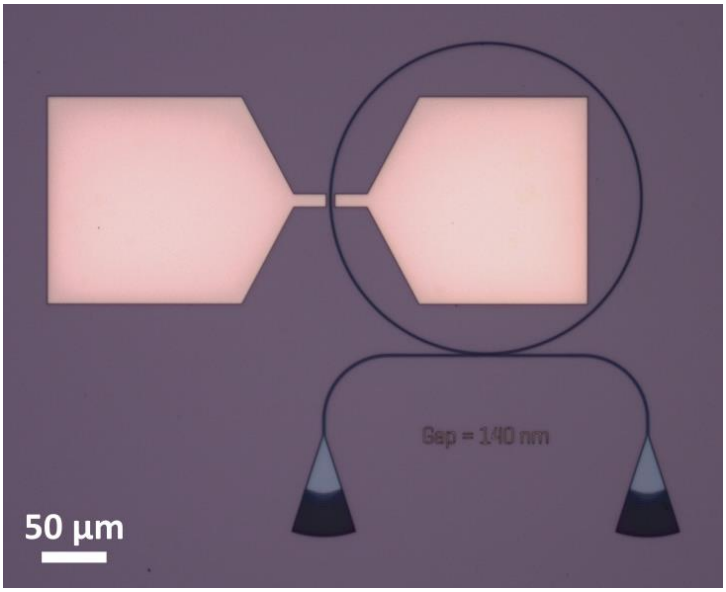


Figure 3.6 Optical micrograph of an opto-electronic chip consisting of a microring cavity.

3.3 Assembly of the nanowires

Owing to their fascinating electrical [125] and optical [126] properties, nanowires have been successfully employed as functional devices in the fields of nanoelectronics and nanophotonics for almost two decades. However, integration of nanowires at the physical device level still remains challenging. Reliable integration becomes even more elusive when it comes to handling individual nanowires with high precision. This has so far been a limiting factor for creating disparate devices of exotic nanowires.

Some approaches for the assembly of 1D nanostructures can be listed as stamping method [127], [128], solution drop-dry technique [129], AFM-based manipulation [130], lithographic alignment [131], localised growth of nanowires at predetermined nucleation points [132], and the Langmuir-Blodgett process [133]. To date, only the stamp-transfer technique allows for a material-independent methodology together with the ability to control placement density and orientation [125]. Thus, if it can be improved in a way to enable single nanowire manipulation, it has the potential to be a universal tool for nanowire deposition. Fundamentally, stamping technique is a bottom-up approach, meaning that it enables placement of functional nanowires after the

fabrication of the device chip. Therefore, it could enable mass-production of nanowire devices even in applications that may be sensitive to nanowire growth conditions or solvents.

A summary of stamping technique is given in Figure 3.7 [128]. In this technique, nanowires are collected from a growth substrate using an intermediate medium termed stamp. Here, the stamp material is chosen transparent and elastic in order to facilitate the alignment step, after which it is contact-printed on the device substrate. A major disadvantage of this method is the lack of control over the number of the picked-up nanowires from the growth substrate. In general, the stamp collects a “forest” of nanowires in a random fashion, which dramatically increases fabrication complexity (e.g. additional lithography steps as seen in Figure 3.7). This reduces reproducibility especially for applications that require a single nanowire. In addition, the stamps are conventionally designed with relatively flat surfaces [128], thus they have to be perfectly parallel to the device substrate, leaving no headroom for tilt misalignment and even hindering the whole process. In this section, these two major issues have been addressed, leading to the development of a new set of tools that allow the stamping method to reach its full potential by significantly increasing single nanowire placement precision and reproducibility.

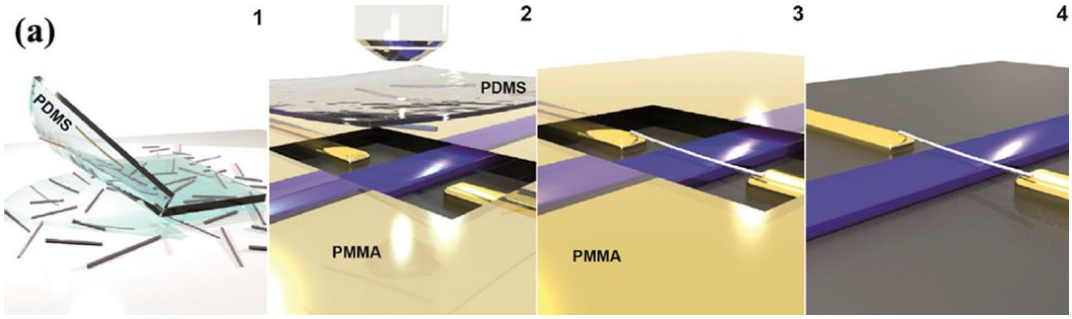


Figure 3.7 Schematic of conventional nanowire transfer process using the stamp-transfer technique. (1) The PDMS stamp collects a forest of nanowires from the growth substrate. (2) A lithographically-defined polymer window of PMMA (which is a positive-tone resist) facilitates the alignment of the nanowire with the device chip under a light microscope. (3) With simultaneous annealing, the nanowire is contact-printed on the device chip. (4) The PMMA layer is removed in acetone. *Reprinted (adapted) with permission from [128]. Copyright 2022 American Chemical Society.*

3.3.1 Making of a nanoscale tip

As mentioned earlier, additional lithography steps are needed in the stamping technique due to the problem of randomly collecting hundreds of nanowires in a small area. To mitigate this issue, one has to perform a cleaner picking-up step by being able to transfer individual nanowires from the growth substrate onto the stamp. Although there are examples of manipulating single nanowires/nanotubes with tungsten tips [134], AFM probes [130], and microtweezers [93], these methods have not been implemented in stamping techniques before. Besides, chemical processes involved in the fabrication of such tools prolong the overall nanowire transfer process and are not sustainable. Such inorganic tips further have high stiffness values, posing a risk of indenting the nanowires as well as damaging the stamp. On the other hand, it is well-known that soft materials are less abrasive and adhere better to rigid surfaces due to their viscoelasticity allowing them to spread around surfaces [46], [135]. Thus, organic polymers are investigated in this section as a substitute for conventional nanoscale tips.

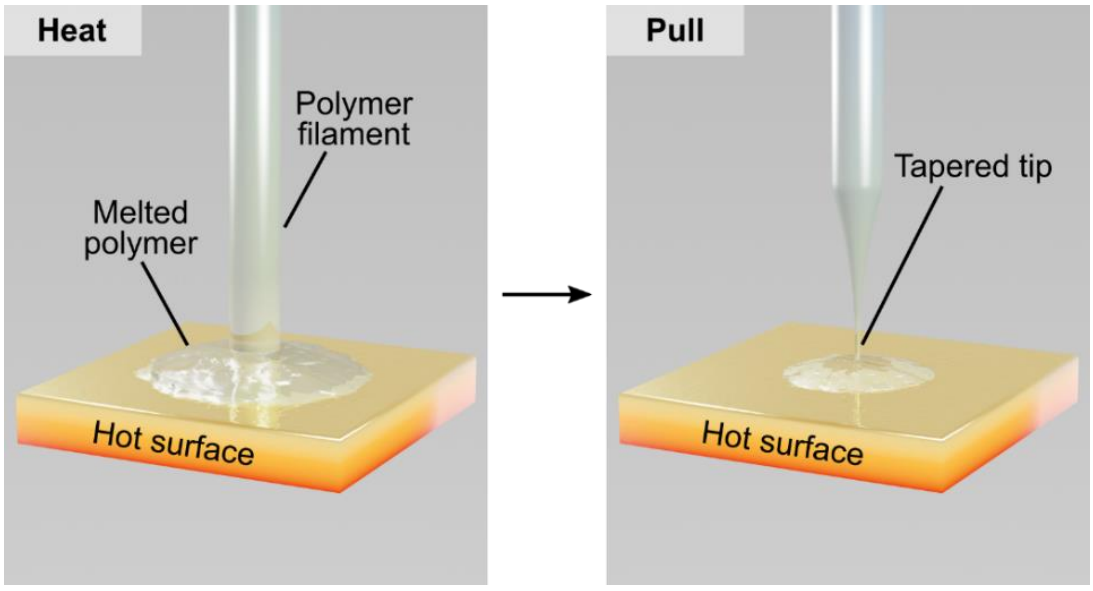


Figure 3.8 Schematic of the heat-and-pull setup designed for fabricating the nanoscale tips. A polymer filament (PET, thickness: 0.2 mm) is attached on a motorised translation stage and melted on a clean hot surface at 240 ℃. By pulling operation, the melted polymer on the surface instantly cools down and forms a taper.

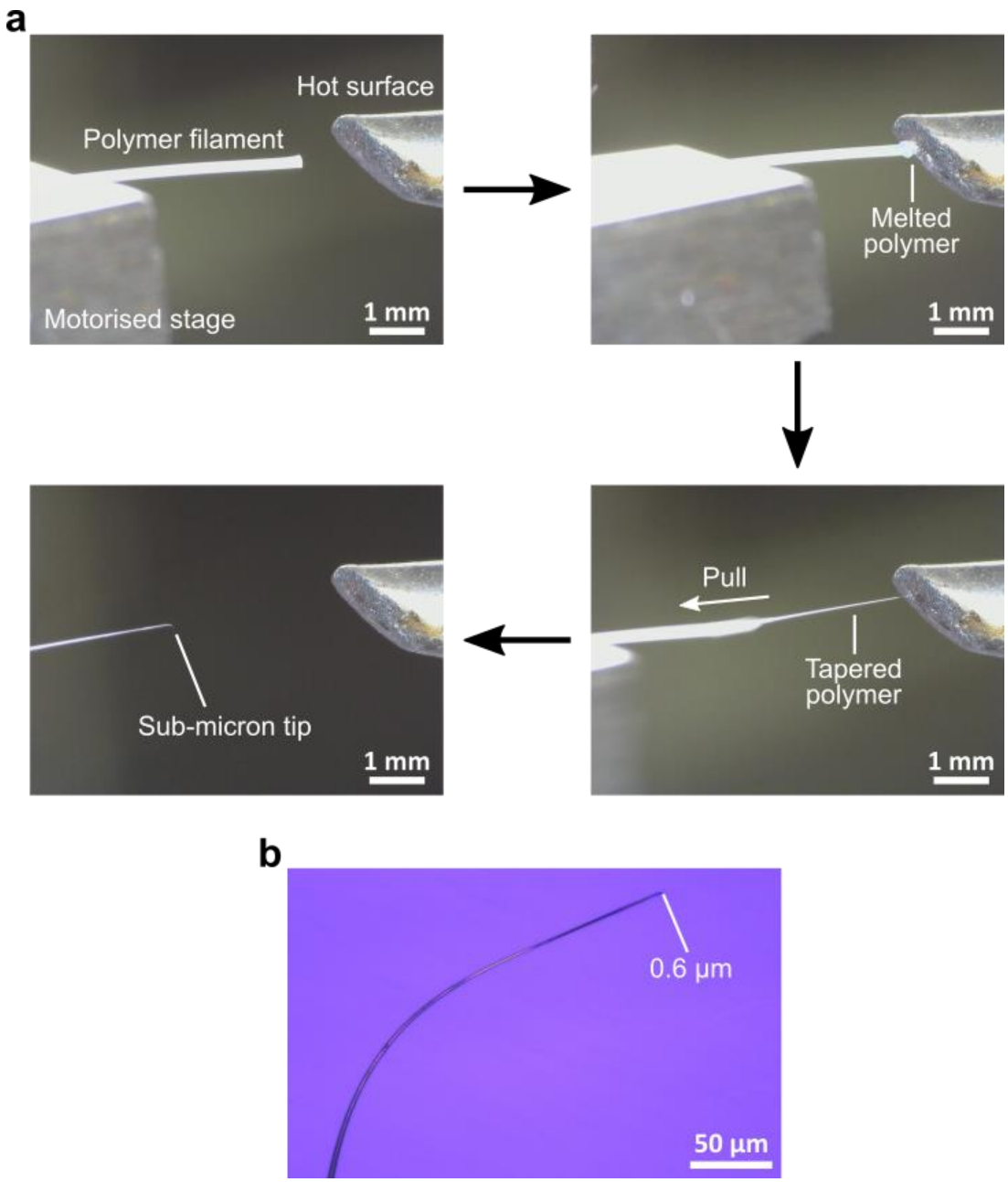


Figure 3.9 A sustainable method to fabricate nanoscale tips. **a**, Snapshots from the heat-and-pull experiment. **b**, Optical microscope image of the resulting polymer tip with a diameter of ~0.6 µm. For clarity, the polymer is placed on a Si wafer.

To start with, a commercially-available PET monofilament (from Goodfellow) is selected. Using the purpose-built heat-and-pull setup depicted in Figure 3.8, the diameter of the monofilament is tapered from 0.2 mm down to sub-micron levels. In order to control pull length and velocity, the monofilament is fixed on a 1D motorised stage (PI L-511). The hot surface is formed using a temperature-controlled soldering iron tip, and its temperature is set to 240 ℃. By bringing the polymer into close contact

with the hot surface, the monofilament is melted. When the filament is pulled away from the hot surface, the liquid polymer cools down and forms a taper. This whole process is further recorded as a video clip, and some snapshots from that video are given in Figure 3.9a together with the zoomed-in optical micrograph of the resulting nanoscale tip in Figure 3.9b.

The thickness of the tapered tip mainly depends on the pulling parameters. Experimental data in Figure 3.10 shows a clear trend that increasing pull length and velocity decreases the tip diameter. The minimum diameter (~0.38 µm) is obtained with a pull length of 12 mm and a velocity of 7 mm/s. Thus, this is the first example of a polymer tip with sub-micron diameter [136], and its fabrication does not involve lithography steps unlike inorganic nanoscale tips. Therefore, using this process, one can match the dimensions of a polymer monofilament with those of nanowires and perform a cleaner picking step.

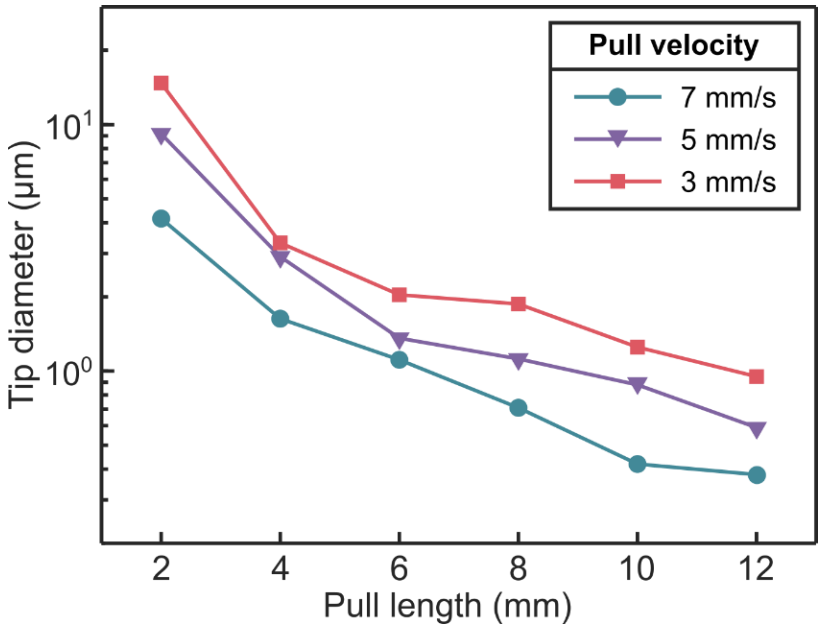


Figure 3.10 Graph showing the characterization of the heat-and-pull setup for various pull lengths and velocities. Increasing pull length and velocity decreases the tip diameter down to sub-micron levels (~0.4 µm).

Figure 3.11a depicts the picking-up of a single nanowire using the sub-micron tip. When the separation between the tip and the nanowire is reduced (e.g. below ~10 nm),

the nanowire jumps into contact with the tip due to the enhanced van der Waals forces overcoming the weaker interactions between smooth, crystalline nanowire surfaces [46]. To demonstrate this concept, the nanoscale tip is mounted on a 5-axis micromanipulator. Under a light microscope, with the growth substrate (of GeTe nanowires) sitting on the microscope stage, the tip is brought into close contact with one of the nanowires.

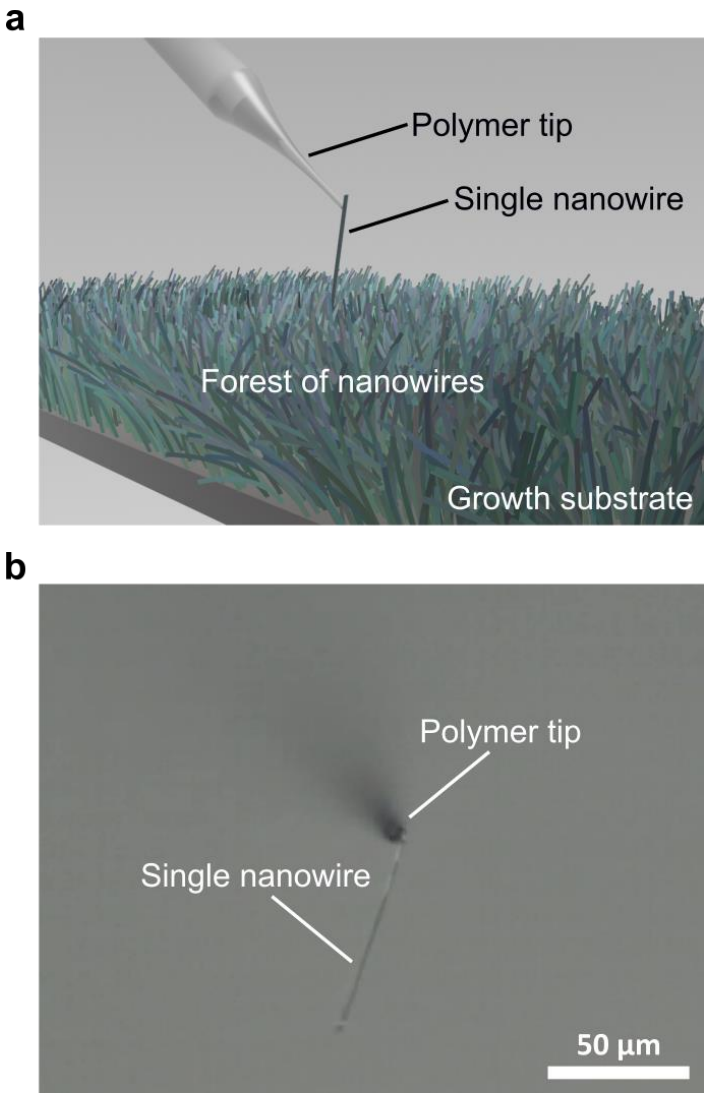


Figure 3.11 Collecting a single nanowire. **a**, Schematic showing a single nanowire picked-up by the tapered polymer tip from a forest of nanowires on the growth substrate. **b**, Top-down optical microscope view of a single GeTe nanowire (diameter: ~300 nm) collected by the nanoscale tip.

As seen in Figure 3.11b, the tip is able to collect a single GeTe nanowire with a diameter of ~200 nm. It has been further observed that the resulting *ad hoc* tool can

pick up single nanowires with diameters of 120-400 nm as long as the tip diameter is below ~2 μm, substantially relaxing the parameters for the heat-and-pull process. From experience, the reproducibility of the picking-up step has been determined to be better than 80%.

3.3.2 Preparation of elastic stamps

Although the nanowire collected by the nanoscale tip can be directly placed on the device chip, such a placement will not be precise due to the extremely small contact area between the tip and the nanowire. As such, even a tiny perturbation to the tip-nanowire system will dramatically affect the nanowire's orientation and position, and this is not desired especially when the placement area is restricted such as in nanophotonic devices. For that reason, the nanowire has to be placed on an intermediate medium in order to have better control over the orientation. As previously mentioned, this intermediate medium is called as 'stamp', which is a transparent and elastic organic polymer. The transparency is crucial during the alignment to be able to see the device chip below, and the elasticity is necessary for minimal or no damage to the device chip during the placement.

Conventionally, the stamps are made of PDMS and fabricated by either drop-casting or spin-coating methods. Both techniques result in a flat stamp that hampers the placement precision as previously discussed. For that reason, the PDMS stamps designed in this work are cured in a way that the resulting stamp has a circular, dome shape. Then, if the nanowire is placed at the centre of this dome-shaped stamp, it is intuitive that the portion of the stamp with the nanowire will touch the device chip first, thus leading to a precise nanowire transfer.

To prepare the stamps, the two-part liquid kit (SYLGRAD 184) is used with a mix ratio of 10:1 as suggested by the manufacture, without performing de-airing. Glass slides (with a thickness of ~1.5 mm) are cleaned with ethanol, and the elastomer mixture is

carefully transferred onto the glass slide surface forming circular droplets with diameters of 2-3 mm. The glass slides are kept upside-down throughout the whole process, preventing the liquid mixture from spreading out. Note that further research is needed to determine how different surface treatment methods on the glass slide affect the droplet size and shape. To cure the stamps, the glass slides are placed on a hot plate (at 90 ℃) facing down and cured for 90-120 minutes (Figure 3.12a). One of the resulting glass slides with six cured stamps can be seen in Figure 3.12b. When not used, the stamps can be stored at room temperature for at least 6 months, without losing their ability as a transfer medium.

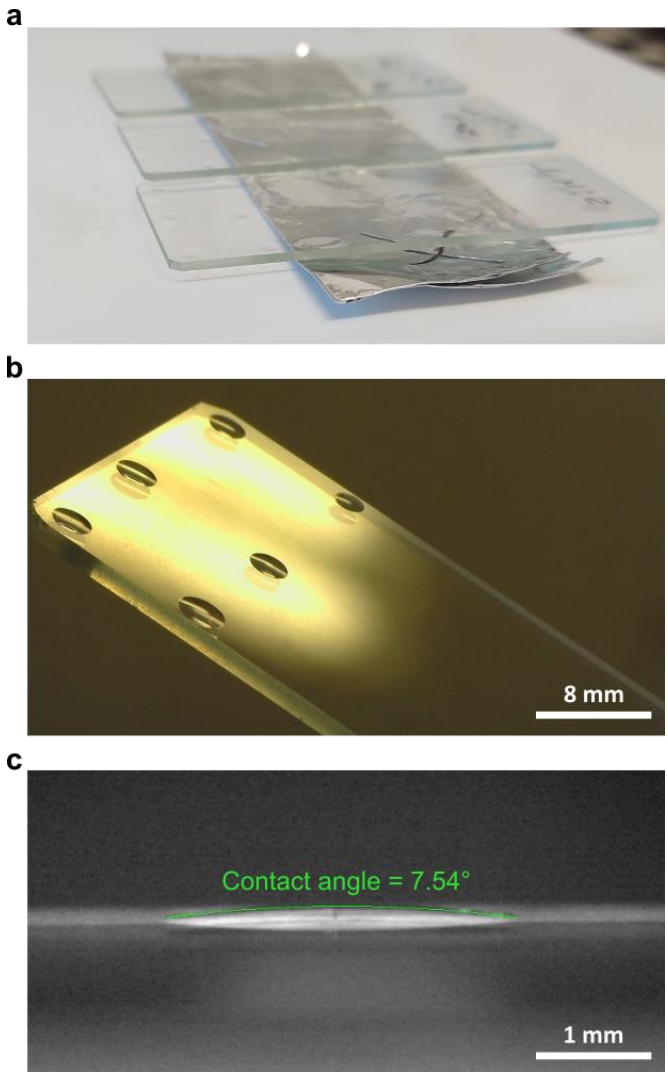


Figure 3.12 Dome-shaped PDMS stamps. **a**, Upside-down curing of the stamps on a hot plate. **b**, A glass slide containing six PDMS stamps. **c**, Contact angle measurement of one of the stamps.

To confirm the circular shape of the stamps, contact angle measurements are performed on the cured PDMS droplets using an open-source software DropSnake as explained in [137]. As seen in Figure 3.12c, the measured contact angle is 7.54 degrees. Even though there are reported examples of circular PDMS stamps, they necessitate complicated processes such as micro-stamping [138] or vacuum curing [139]. Therefore, the method described here offers facile manufacturing of such stamps while maintaining a decent dome shape.

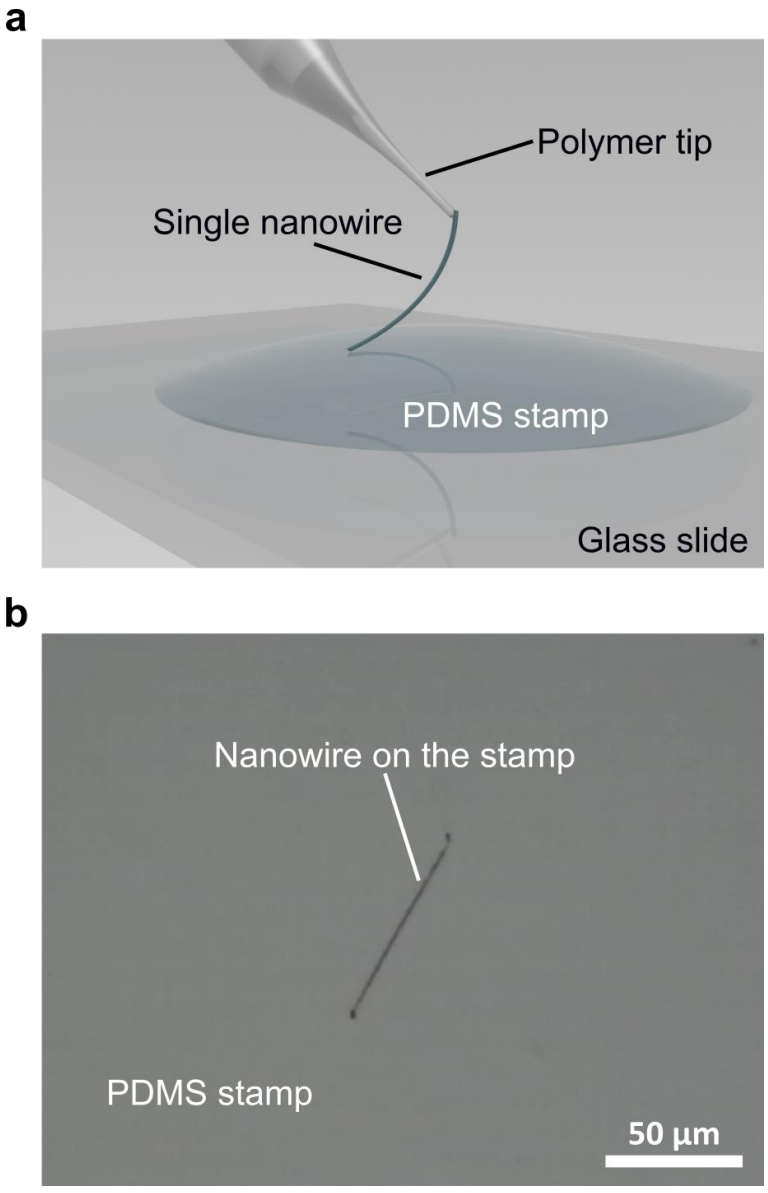


Figure 3.13 Transferring of the nanowire onto the dome-shaped PDMS stamps. **a**, Schematic depicting the transfer process. The nanoscale tip pushes the nanowire towards the stamp. **b**, Optical micrograph of the single GeTe nanowire transferred to the PDMS stamp.

The single nanowire picked-up in the previous step can now be transferred onto the centre of the stamp. Initially, the stamp is placed on the 3D-movable microscope stage such that the highest point of the stamp remains in the focal plane. Note that the nanoscale tip carrying the single nanowire is still attached on the 5-axis micromanipulator. Then, the tip is slowly brought into focus while being aligned with the centre of the stamp underneath. Here, the nanowire starts bending as it approaches to the stamp (Figure 3.13a) and eventually adheres to the surface. As such, Figure 3.13b shows the optical micrograph of a single GeTe nanowire transferred onto the centre of the PDMS stamp.

3.3.3 Nanowire placement

To start the nanowire placement process, the glass slide carrying the nanowire is fixed on a 3-axis micromanipulator with the nanowire facing downwards. Meanwhile, the device chip is placed on the microscope stage. This configuration is depicted in Figure 3.14a. Top-down optical microscope image in Figure 3.14b shows the nanowire-stamp combination aligned with the on-chip electrodes. As seen, the nanowire is in the focal plane whereas the device chip is out-of-focus.

Following the alignment, the PDMS stamp is contact-printed on the device by slowly bringing the device chip into focus while the nanowire being kept at the focal plane. Separation of the stamp from the device chip is done by lowering the microscope stage with a simultaneous dragging movement along the nanowire growth axis. To make sure the contact-printing is successful, this manoeuvre is crucial and further eliminates the requirement for heating the device substrate traditionally required to overcome the strong mechanical interlocking between the stamp and the nanowire [128]. A visual summary of the contact-printing technique is also provided in Figure 3.15 with optical microscope images. The distinctive peeling effect is a result of the dome shape of the stamp combined with the dragging movement.

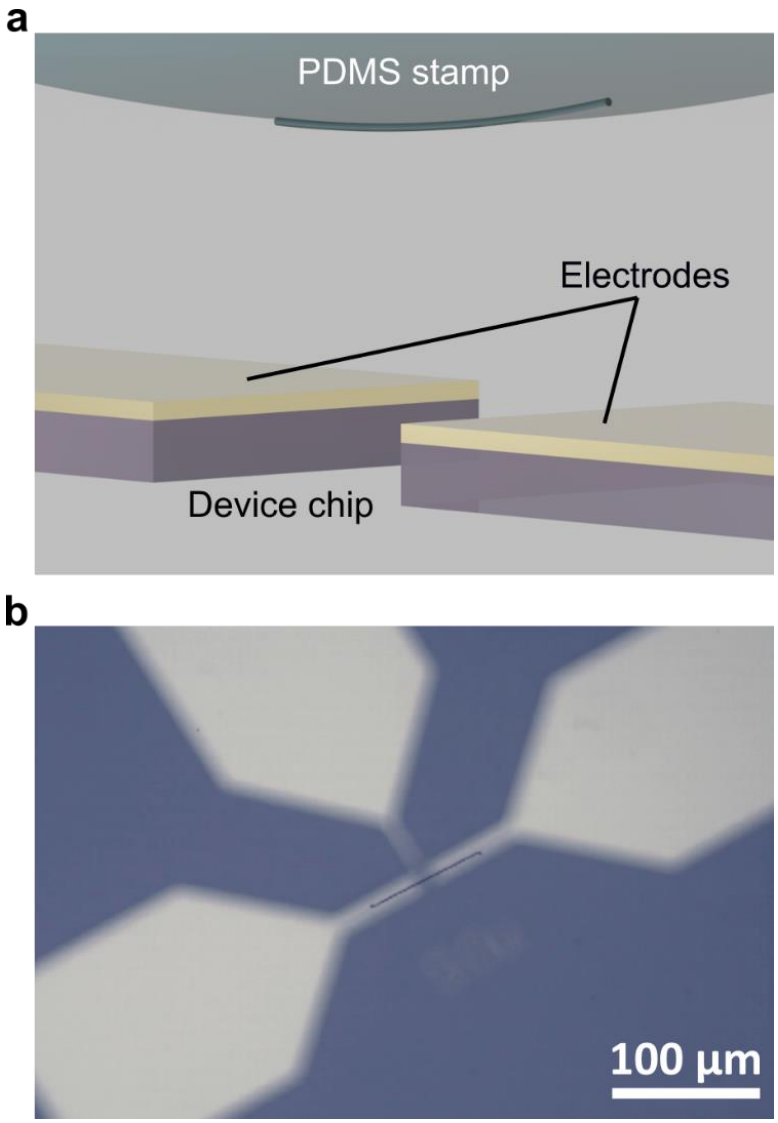


Figure 3.14 Alignment of the nanowire on stamp with the device chip. **a**, Illustration of the alignment step. The stamp is upside-down, facing the device chip below. **b**, Top-down view of the alignment process under a light microscope. The nanowire is kept at the focal plane.

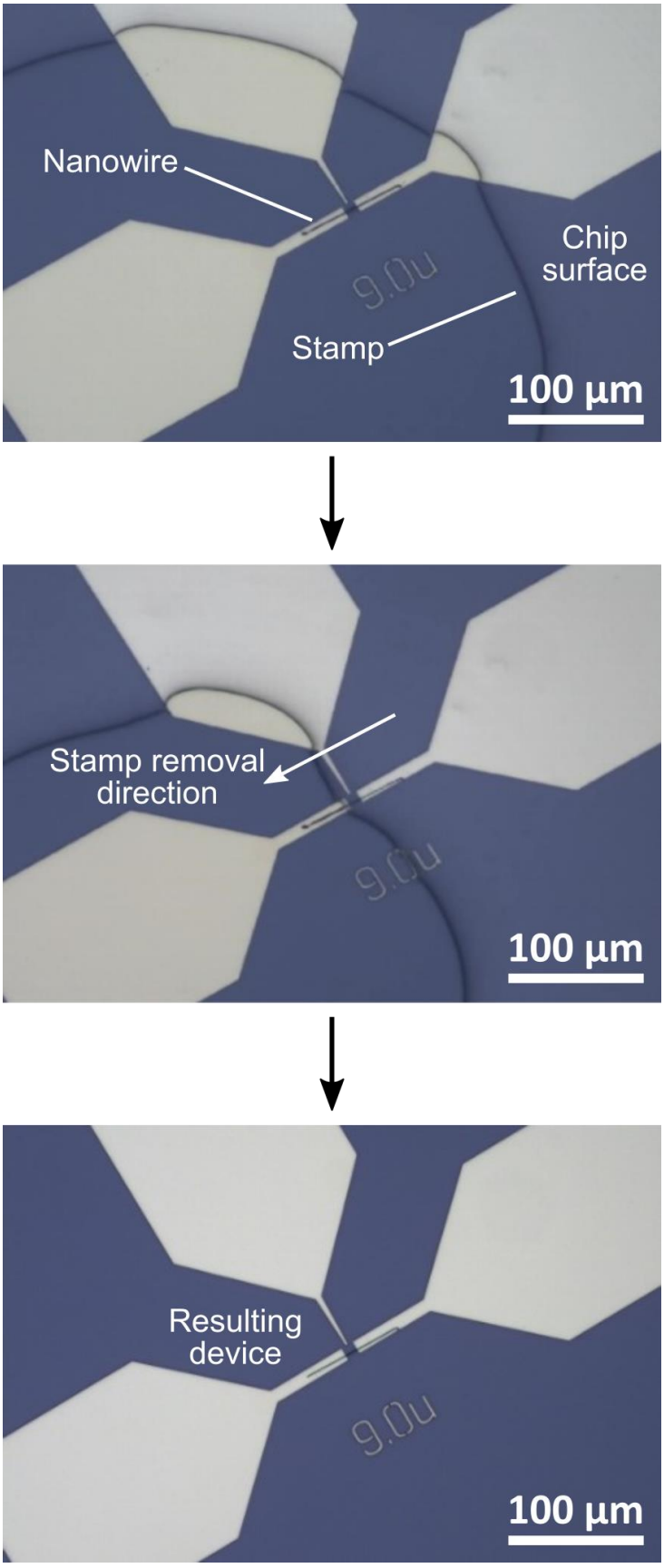


Figure 3.15 Contact-printing of the nanowire over the device chip with Au electrodes.

To demonstrate the versatility of this method, InP and GeTe nanowires are deposited on different patterned substrates such as electrodes (Figure 3.16a), 50 nm-thick TEM membranes (EM Resolutions SN100-A50MP2Q05, Figure 3.16b), and nanophotonic devices (Figure 3.16c). At this point, it should be noted that the ability to transfer single nanowires over optical microcavities in a suspended fashion and even on TEM membranes without damaging the ultra-thin substrate showcases the delicacy of this method. Most importantly, eliminating the need for additional lithography steps while maintaining the placement precision significantly reduces the duration of the stamping process and retains the pristineness of the nanowires. Such developments are further exciting for the NEMS community as the technique described here has enabled fully-integrated nano-optomechanical measurements of single-crystal nanowires for the first time via evanescent field coupling, and this will be seen in Chapter 6.

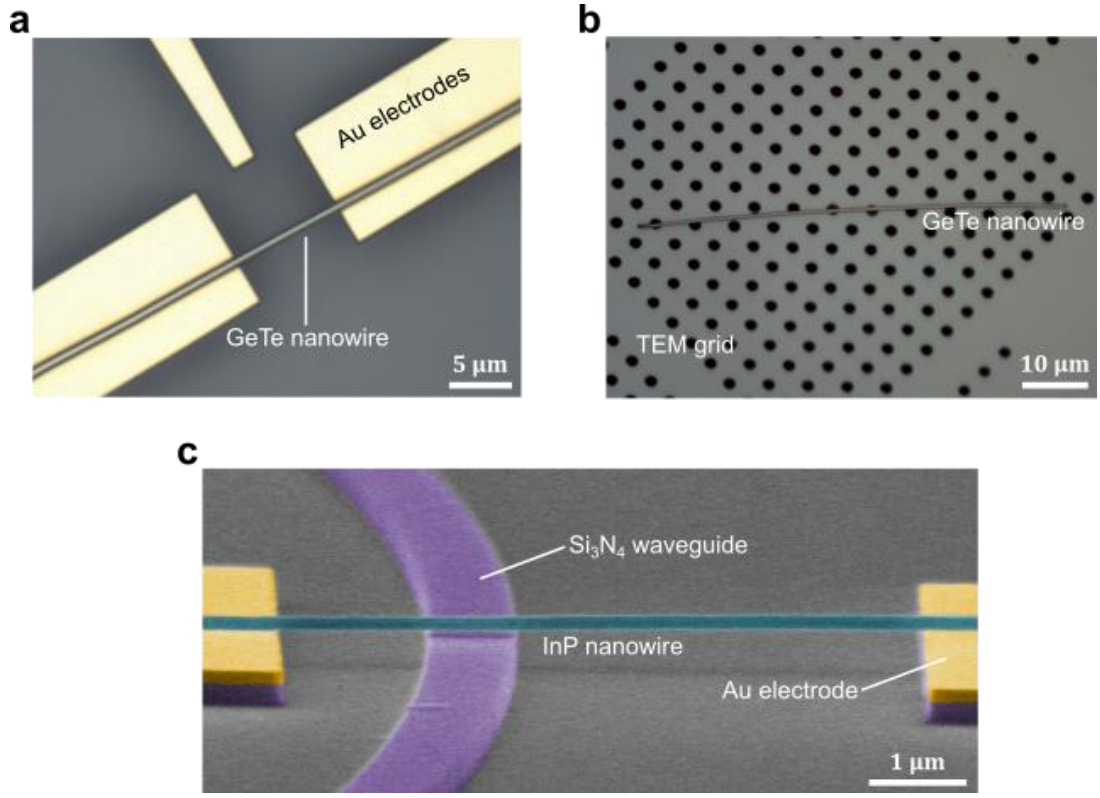


Figure 3.16 Versatility of the novel nanowire pick-and-place assembly. **a**, Optical microscope image of a GeTe nanowire suspended over Au electrodes. **b**, Optical micrograph of a GeTe nanowire transferred on a 50 nm-thick Si_3N_4 TEM membrane with 2 µm pores. **c**, An angled-view false-colour SEM image of an InP nanowire suspended ~150 nm away from an optical microcavity of Si_3N_4.

It is also important, at this point, to investigate the placement precision of this technique. Such quantitative analysis of the placement precision has been performed using 25 different nanowire devices. The target position and orientation have been compared to those of the obtained devices. Figure 3.17 illustrates this concept, where the orientation of the nanowire is misaligned by the angle θ and its final position L' deviates from the middle of the electrode ($L/2$) by an amount of ΔL.

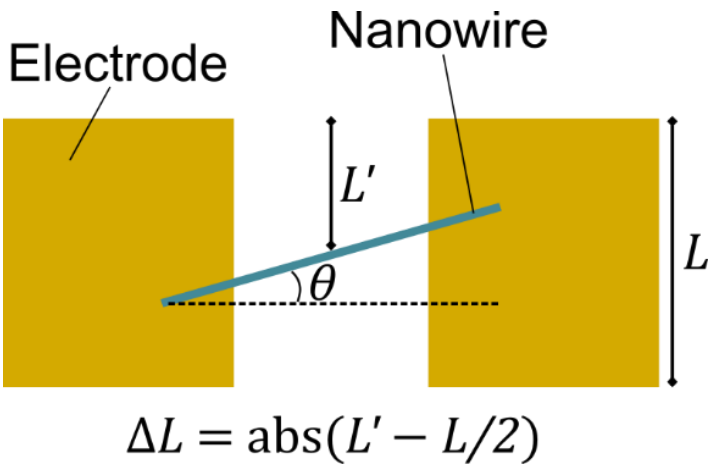


Figure 3.17 Characterisation of the placement precision.

The analysis yields a mean angle inaccuracy of θ = 1.2° (with $\theta_{\max}$ = 3.6°) and a mean placement error of ΔL = 0.6 µm ($\Delta L_{\max}$ = 1.9 µm). In comparison, commercially available alignment systems (e.g. wafer bonders and mask aligners) offer θ < 0.5° and ΔL < 2 µm. Both of these values favourably compare to the results presented in this chapter. It should also be noted that in this work only manual nanopositioners without a rotation stage have been used. Thus, using motorised stages with rotation capability in the xy-plane has the potential to improve the placement precision even further.

3.3.4 Mechanical robustness of the method

During three years of DPhil studies, more than 300 nanowires have been deposited on various chips. Amongst all those devices, the nanowire with the smallest diameter transferred by this method can be seen in Figure 3.18. The nanowire is suspended by electrodes and has a diameter of 120 nm as estimated from the SEM image. It is

important to mention that the lower limit of diameter strongly depends on the resolution of optical microscopy. Also note from Figure 3.18 that the stamping process has not damaged the nanowire despite its small diameter, i.e. no breakage has been noted.

At this point, it should also be mentioned that the lower limit for the nanowire diameter in this method is not only limited by the mechanical robustness of the nanowire but also restricted by the resolution of optical microscopy. Especially for photonics applications, this limit needs to be pushed below 100 nm, and this can be achieved in future by using novel metalens structures with ultrahigh numerical aperture [140].

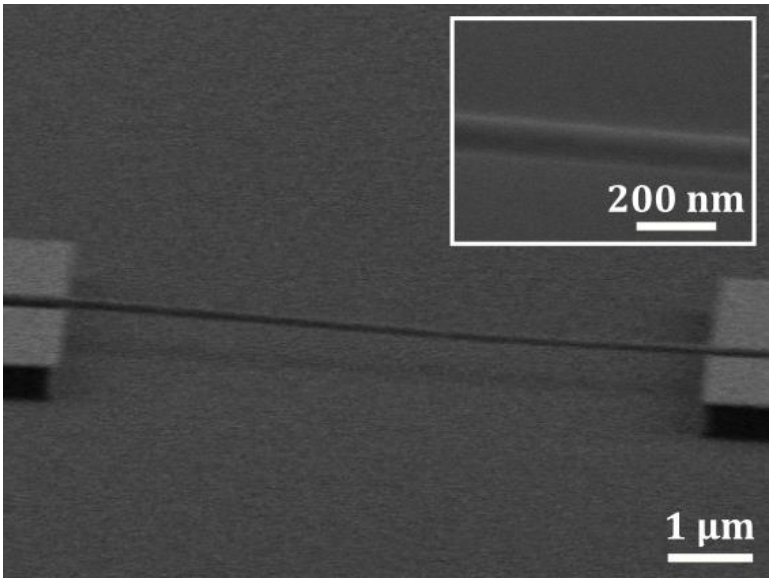


Figure 3.18 An SEM micrograph of the smallest nanowire in diameter (~120 nm) deposited by this technique. Inset shows a zoomed-in SEM image of the nanowire.

It has been also observed that annealing of the final device chip (e.g. at 150 ℃ for 10 minutes) considerably improves the adhesion between the nanowire and the substrate/electrodes, i.e. by enabling the diffusion of Au atoms from the electrodes into the nanowires [128]. Although the actual mechanism by which the adhesion improves is not verified, an additional lithography step has been performed on the device seen in Figure 3.19 to show the improvement in adhesion. The device chip carrying an InP nanowire is spin-coated with a negative-tone resist (ma-N 2403) as described in Section 3.2. Subsequent patterning and development of the resist resulted in the

clamped device given in Figure 3.19 (right), without any noticeable shift in the nanowire's position. Furthermore, the suspended nanowire has survived this process, showing the high mechanical stability offered by this technique as well as enabling the use of exotic nanowires in liquid buffers [141].

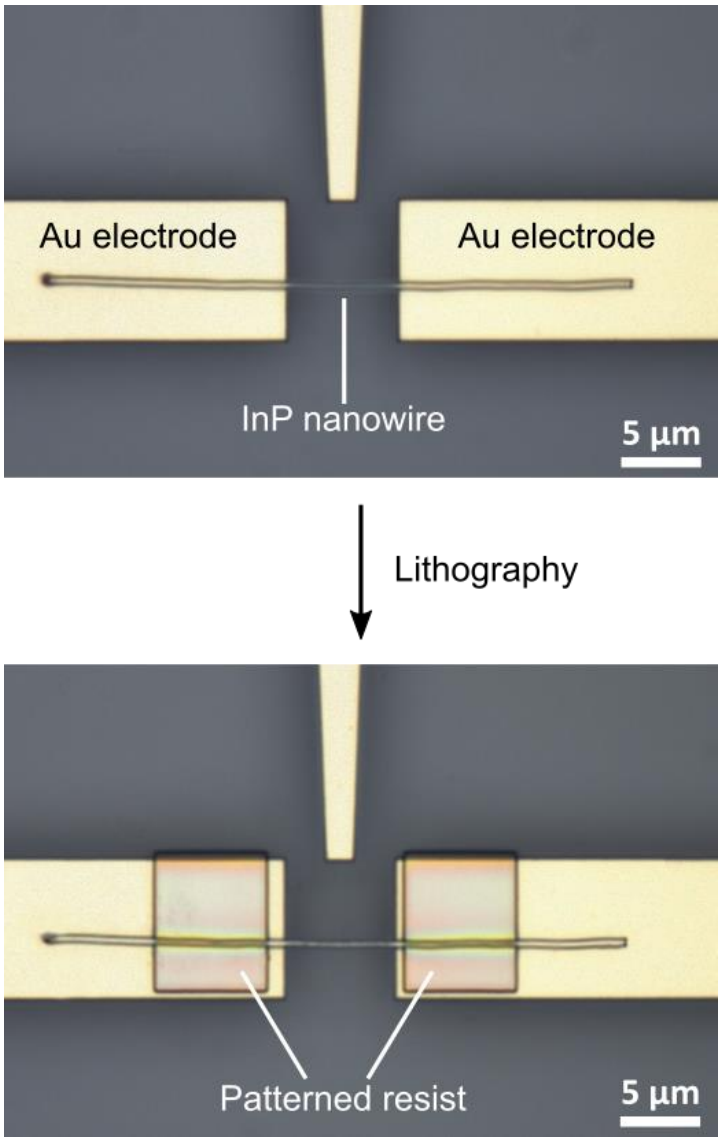


Figure 3.19 A free-standing InP nanowire before and after performing a lithography step following its deposition.

3.4 Conclusions

In this chapter, fabrication of functional nanowire devices used in this work has been summarised. In the first section, a step-by-step guide for fabricating the on-chip

platforms is provided. These platforms enable electrical and/or optical access to the nanowires. In the second section, a novel and universal method has been described for depositing single nanowires on various substrates ranging from nanophotonic devices to ultra-thin TEM membranes. This method comprises of a modified pick-and-place assembly with the introduction of an additional picking step to conventional stamp-transfer techniques.

The picking step is performed using the first example of nanoscale polymer tips, which facilitate the transfer of single nanowires. Individually picked-up nanowires are then transferred onto dome-shaped PDMS stamps and contact-printed on the fabricated devices. The whole process takes less than 3 minutes by only using manual micromanipulators, with the promise of full-scale automation if motorised stages are used. With this assembly, a placement precision of ~0.6 µm has been achieved. Thus, the stamping technique reaches its full potential with the modifications presented here, offering a more accurate solution for single nanowire placement with better reproducibility (~80%) while eliminating the need for additional lithography steps required in conventional methods. The technique is also mechanically robust. Therefore, the pick-and-place method described here facilitates effortless integration of single nanowires of exotic materials in applications that were previously seen as cumbersome or even impractical, spanning a wide range from TEM studies to in-situ electrical, optical, and mechanical characterisation.

Chapter 4

Electrical transduction of devices

The findings presented in Chapters 4 & 5 have been published in:

Utku Emre Ali, Gaurav Modi, Ritesh Agarwal, Harish Bhaskaran, *"Real-time nanomechanical property modulation as a framework for tunable NEMS",* Nature Communications 13, 1464, (2022). DOI: 10.1038/s41467-022-29117-7

4.1 Overview

In this chapter, a series of experimental methods has been explored in order to transduce nanomechanical vibrations of GeTe nanowires electrically. The transduction has been performed piezoresistively, and a detailed investigation of the experiment setup is given in Section 4.2. A non-zero phase Lorentzian including frequency-doubling effect has been derived in Section 4.3. Besides, Section 4.4 describes a guide for experimentally validating nanomechanical resonances. As this is the first-time investigation of dynamic properties of a phase-change nanowire, Young's modulus and piezoresistive gauge factor estimations have been presented in Sections 4.4 and 4.5. Finally, Section 4.6 describes the effective drive power required for NEMS operation, together with the importance of the actuation method.

4.2 Piezoresistive self-sensing of nanowires

Piezoresistive sensing of nanomechanical motion has been previously discussed in Section 2.3.1. Briefly, a mechanical resonator dynamically experiences strain, which modifies its own electrical resistance. This effect is termed piezoresistivity, and the piezoresistance coefficient is defined as the fractional change in resistivity of a material per unit tension [81]. It is a common transduction method specifically for NEMS because piezoresistive effects enhance with scaling while other readout techniques become less practical. For instance, piezoresistance coefficient of p-type Si nanowires along $\langle 111 \rangle$ axis reaches up to $3{,}550 \times 10^{-11}$ Pa^{-1} while the bulk value for Si is as low as 94×10^{-11} Pa^{-1} [142].

Another extensively used parameter in piezoresistive sensing is the gauge factor (γ), which is defined as:

$$\gamma = \frac{\Delta R/R}{\varepsilon} \tag{4.1}$$

Here, R is the *d.c.* resistance of the device, ΔR is the absolute resistance change, and ε is the strain. If the geometric variations are neglected, one can obtain the unitless parameter γ by multiplying the piezoresistance coefficient with the Young's modulus along the relevant axis [143]. As such, with a Young's modulus of 169 GPa for Si nanowires [84], the relative resistance change ($\Delta R/R$) can be as high as 60% even for a minuscule strain of 0.01%.

To elaborate on mechanical strain in nanowires, one needs to have a closer look at the strain dynamics of flexural-mode vibrations in a doubly-clamped beam. To this end, FEM simulations have been performed in COMSOL Multiphysics® environment, and the resulting strain map is given in Figure 4.1. Here, compressive and tensile stresses cancel each other out along the neutral axis. Therefore, transverse displacement of the resonator effectively results in zero resistance change [79].

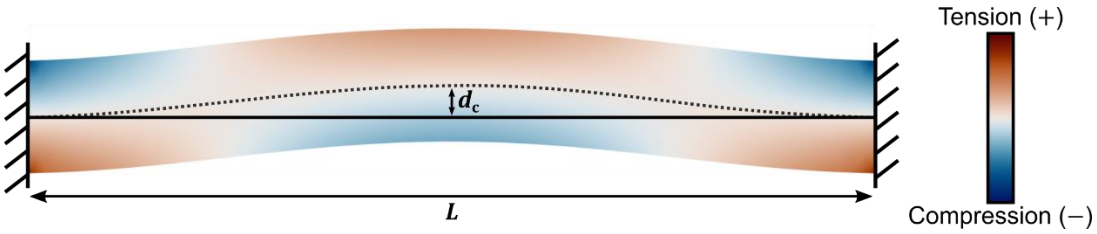


Figure 4.1 Coloured strain map of a doubly-clamped nanowire with a length of L. The dotted line indicates the neutral axis, which is displaced by d_c at the maxima of resonant vibrations. The colourbar denotes red for tension, blue for compression, and white for neutral.

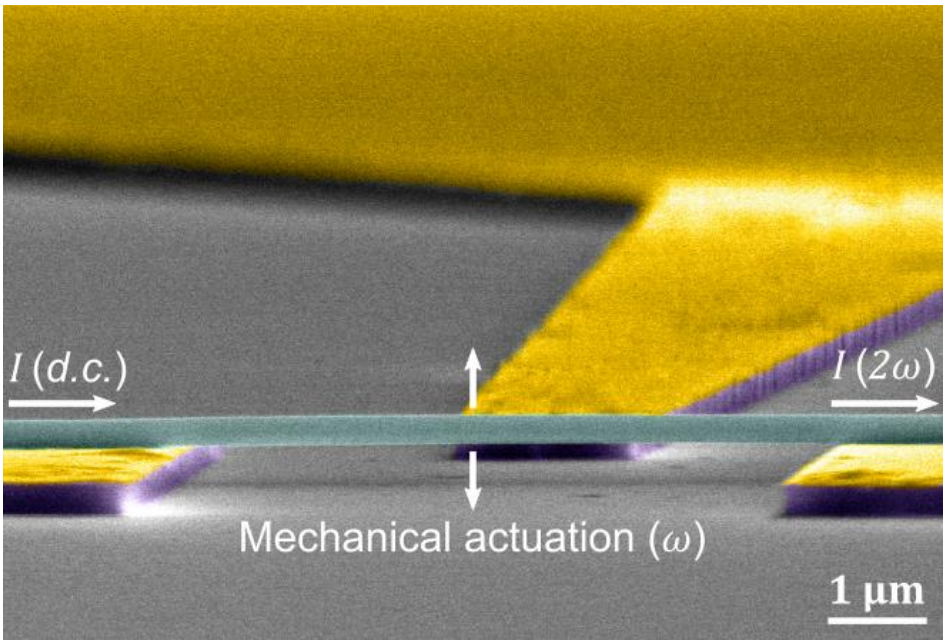


Figure 4.2 Annotation of the piezoresistive sensing scheme on an actual device used in this thesis. SEM image shows a GeTe nanowire suspended by Au electrodes. Electrical current through the device and mechanical actuation (out-of-plane) are sketched on the image.

On the other hand, elongation of the device causes a non-zero net strain, and this can be approximated as,

$$\varepsilon = 2\left(\frac{d_c}{L}\right)^2 \qquad 4.2$$

where d_c is the displacement at the centre of the nanowire and L is the nanowire length at rest. Although the amount of lengthening is almost negligible for a NEMS device operating in linear region (e.g. d_c ~1 nm), this effect becomes a feasible readout technique with the enhancement of piezoresistive effect in nanowires [79], [142]. It should also be noted from Eq. 4.2 that the strain is a quadratic function of displacement, hence the readout has to be performed at 2ω where ω is the mechanical actuation frequency, as depicted in Figure 4.2. Considering such frequency-doubling effect, the piezoresistive measurement setup is described in the following section.

4.2.1 Experiment setup

The measurements are performed inside a room temperature vacuum chamber at pressures below 10^{-5} torr, with a custom-built Faraday cage around the instruments. The nanowires are actuated via direct mechanical coupling using a piezoceramic shaker. Here, the device chip is electrically isolated by a thin piece of glass and mounted on the actuator, which is then fixed on a vacuum-compatible PCB (Figure 4.3). Top plate of the piezo crystal is grounded to minimise the capacitive damping in the NEMS devices, thus improving their mechanical performance. SMA connectors are soldered into electrical pads on the PCB. Device electrodes are contacted to the electrical pads via wirebonding (Kulicke & Sofa 4523 Wire Wedge Bonder) using 25 µm-thick Al:Si (99:1) bond wires.

At this point, it is crucial to mention that GeTe exhibits metallic conduction in the crystalline phase owing to the high concentration of Ge vacancies (~10^{19} cm^{-3}, p-type

doping) [144]. Thus, while working with such metallic devices, extreme electrostatic discharge (ESD) precautions must be taken. Otherwise, these nanowires are especially vulnerable to electrical shocks and can be easily damaged. One way to prevent ESD damage to the devices is to keep all electrical connections at the same voltage level (i.e. the ground) while handling. Thus, the shorting caps seen in Figure 4.3 (grey-coloured) have been kept on the SMA connectors whenever possible. Other precautions may include proper grounding of instruments in the experiment setup as well as wearing ESD-safe clothing and grounded wrist straps.

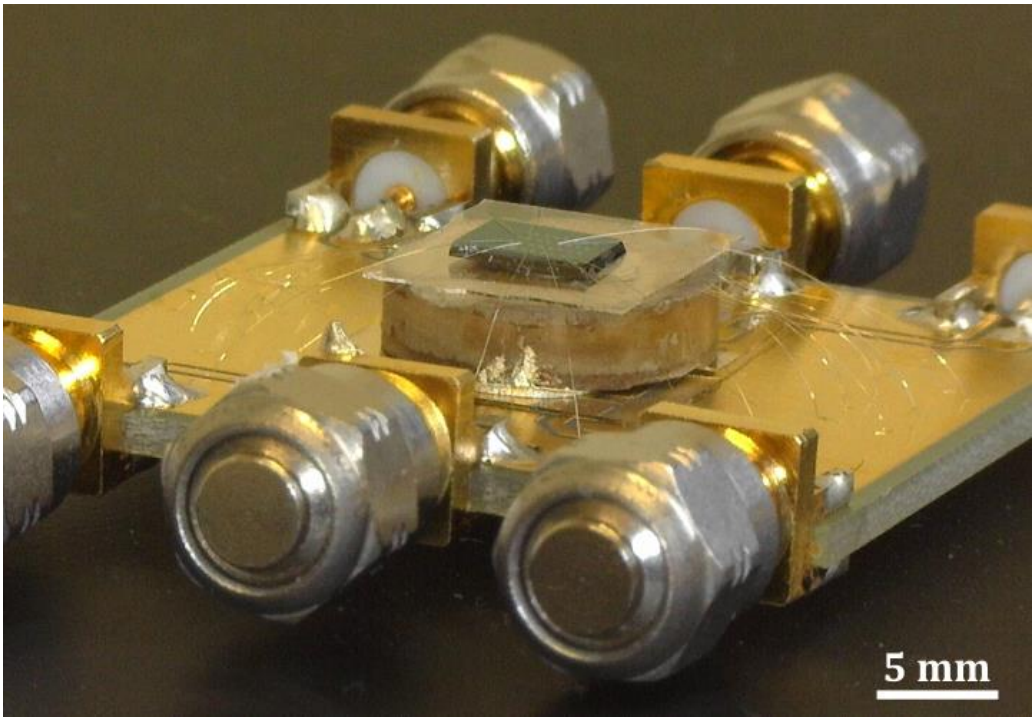


Figure 4.3 PCB that carries the nanowire devices for resonance measurements in vacuum.

Figure 4.4 shows the measurement setup for the piezoresistive self-sensing of a doubly-clamped nanowire resonator. To be more specific, the resonator is a GeTe nanowire and externally actuated by a piezoceramic crystal. The drive signal (V_{drive}) is outputted from a lock-in amplifier (Zurich Instruments HF2LI) at a frequency of ω and amplified by a high-power amplifier (HPA, Mini Circuits LZY-22+). Note that the HPA drives the bottom plate of the piezo actuator while its top plate is grounded, as previously explained.

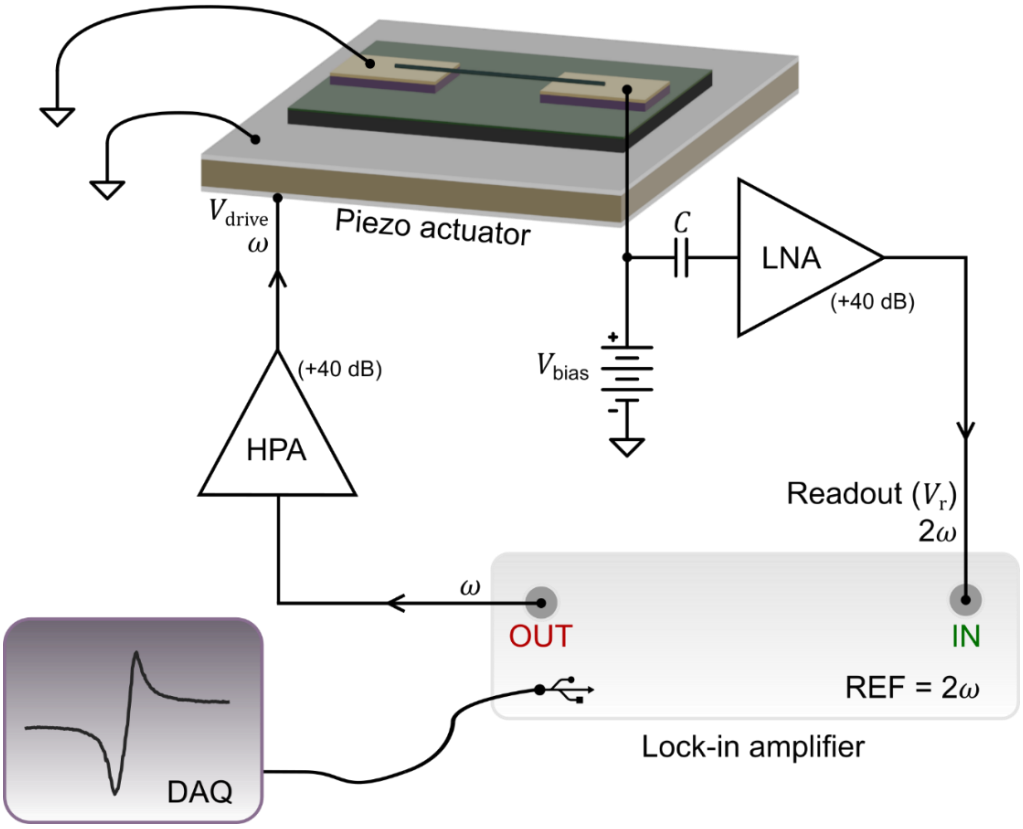


Figure 4.4 Piezoresistive measurement setup. Lock-in amplifier drives the piezo actuator at a frequency of ω and detects its frequency response at 2ω reference. Amplification of the drive and readout signals is performed by the HPA and LNA, respectively.

For the piezoresistive detection, a *d.c.* bias voltage (e.g. V_{bias} = 100 mV) is applied to the nanowire from a battery (for low-noise operation). Dynamic vibrations of the nanowire modify its own electrical resistance (R) due to the piezoresistive effect. Thus, under a *d.c.* bias, a piezoresistive *a.c.* signal is generated. The *a.c.* signal is then coupled to a low-noise amplifier (LNA, MITEQ AU-1442) through a coupling capacitor (Crystek DC Block 300 kHz – 3 GHz). The amplified signal (i.e. the readout) is routed into the lock-in amplifier with its demodulation reference set to 2ω. Here, setting the lock-in reference to 2ω is crucial due to the aforementioned frequency-doubling effect in doubly-clamped beams. The lock-in parameters are manipulated using LabOne software from Zurich Instruments. Data acquisition (DAQ) is performed via universal serial bus (USB) interface.

4.2.2 Equivalent measurement circuit

Before commenting on any experimental data, it is important to analyse electrical equivalent of the experiment setup, which is schematised in Figure 4.5. Here, the *d.c.* bias source has a potential of V_{bias} and an internal (source) resistance of R_{s}. The resonator is modelled as a time-varying resistor R', i.e. $R' = R + \Delta R$, where R is the *d.c.* resistance of the nanowire as previously mentioned, and ΔR is the time-varying resistance change due to piezoresistivity.

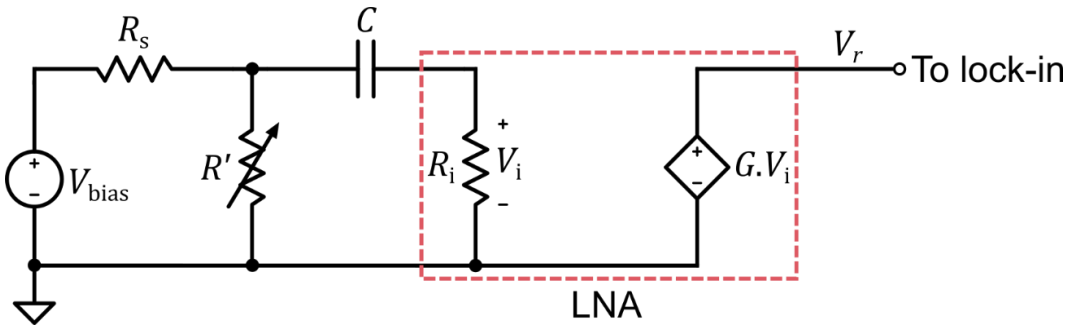


Figure 4.5 Schematic of the electrical equivalent of the piezoresistive measurement setup.

The voltage across the resonator is routed into the LNA through a coupling capacitor C. The LNA is sketched as a voltage-controlled voltage source (VCVS) with an input resistance R_{i} and a gain G. The amplified signal ($V_{\mathrm{r}} = G.V_{\mathrm{i}}$) is subsequently inputted to the lock-in amplifier. By setting $R \gg R_{\mathrm{s}} = R_{\mathrm{I}}$ and assuming C is ideal within the measurement bandwidth, the sinusoidal amplitude of the readout (V_{r}) becomes:

$$V_{\mathrm{r}} = GV_{\mathrm{bias}}R_{\mathrm{i}}\frac{R_{\mathrm{s}} \parallel R}{R_{\mathrm{i}} + R_{\mathrm{s}} \parallel R}\left(\frac{1}{R_{\mathrm{s}} + R} - \frac{1}{R_{\mathrm{s}} + R + \Delta R_{\mathrm{max}}}\right)$$
$$\approx \frac{1}{2}GV_{\mathrm{bias}}R_{\mathrm{i}}\left(\frac{1}{R_{\mathrm{s}} + R} - \frac{1}{R_{\mathrm{s}} + R + \Delta R_{\mathrm{max}}}\right) \qquad 4.3$$

Here, ΔR_{max} is the absolute resistance change at the maximum displacement d_{c}. The expression in Eq. 4.3 has also been confirmed using an electrical circuit simulator, e.g. SPICE (Simulation Program with Integrated Circuit Emphasis), via transient analyses using the schematic in Figure 4.5.

A critical aspect while designing an electrical experiment is the ground loops. A ground loop occurs when there is more than one path to the ground node, and this is indeed the case for the experiments here (Figure 4.6). Although one may expect that all ground nodes should be at the same potential, this is practically impossible due to non-zero impedance of connection cables. At high frequencies, this leads to capacitive and inductive crosstalk between instruments/devices. Such crosstalk further manifests itself as a frequency-dependent background signal [18], [73] (as will be seen in the next section) and noise sources, suppressing the desired piezoresistive readout signal. Therefore, ground loops must be avoided.

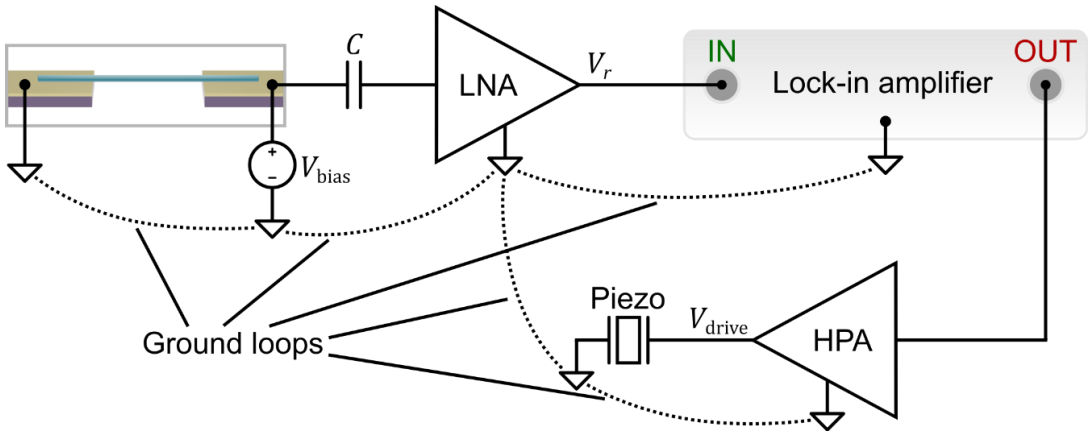


Figure 4.6 Simplified diagram of the experiment setup showing the ground connections.

Especially in instrumentation such as NEMS measurements, utilising differential readout [84] and/or down-mixing techniques [18], [79] has proven to be an effective way to avoid ground-related crosstalk as well as noise. However, these methods require additional mixers, phase shifters, and power splitters in the experiment, complicating the setup. Thus, they have not been implemented in this thesis.

Another way to reduce the effect of ground loops is to keep all the instruments as closely to the ground node as possible. This involves using short connection cables between the instruments. This method has been adopted in this work. For further improving the performance, monolithic integration is a viable option as previously reviewed in Section 2.3.1.

4.3 Resonance fitting

To verify the electrical conduction, current-voltage (I-V) characteristics of the devices have been measured. Here, it is useful to mention that to improve electrical contacts to the nanowires, device chips are annealed on a hot plate at 150 ℃ for 10 mins following the nanowire deposition. Using a semiconductor analyser (Keysight B1500A), I-V curve of a GeTe nanowire has been acquired by sweeping the *d.c.* current from 0 to 100 μA. Experimental data is given in Figure 4.7 together with an inset showing the simplified measurement diagram. Linear fit to the data yields a *d.c.* resistance of R = 1.103 kΩ.

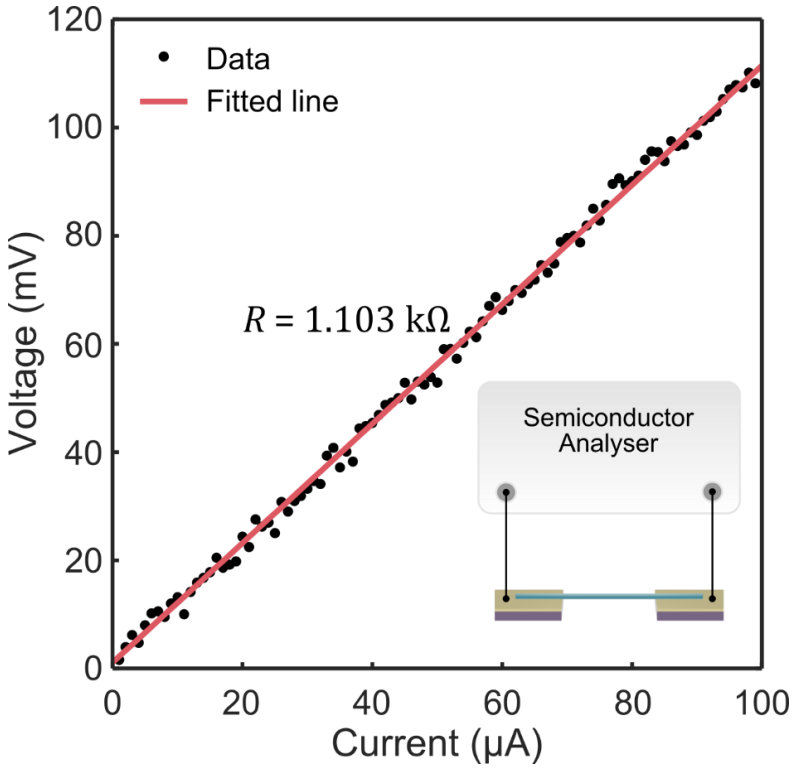


Figure 4.7 I-V measurements of a GeTe nanowire using a semiconductor analyser. The slope of the fitted line yields a *d.c.* resistance of R = 1.103 kΩ. Inset shows the simplfied experiemental setup.

Once the electrical conduction is verified, the piezoresistive current generated by the resonance vibrations can be measured using the lock-in amplifier following the procedure described in Section 4.2.1. The readout results are taken in vacuum at room temperature. As such, the readout voltage V_r is plotted as a function of the drive

frequency ($\omega = 2\pi f$) for four different GeTe devices (Figure 4.8). Wide-range frequency sweep of one of the devices can also be seen in the top panel of Figure 4.8. Note that there is a sharp resonance peak in each plot with a slowly changing (linear) background, which has been previously observed in NEMS measurements by Knobel and Cleland [73] as well as Sazonova et al. [145].

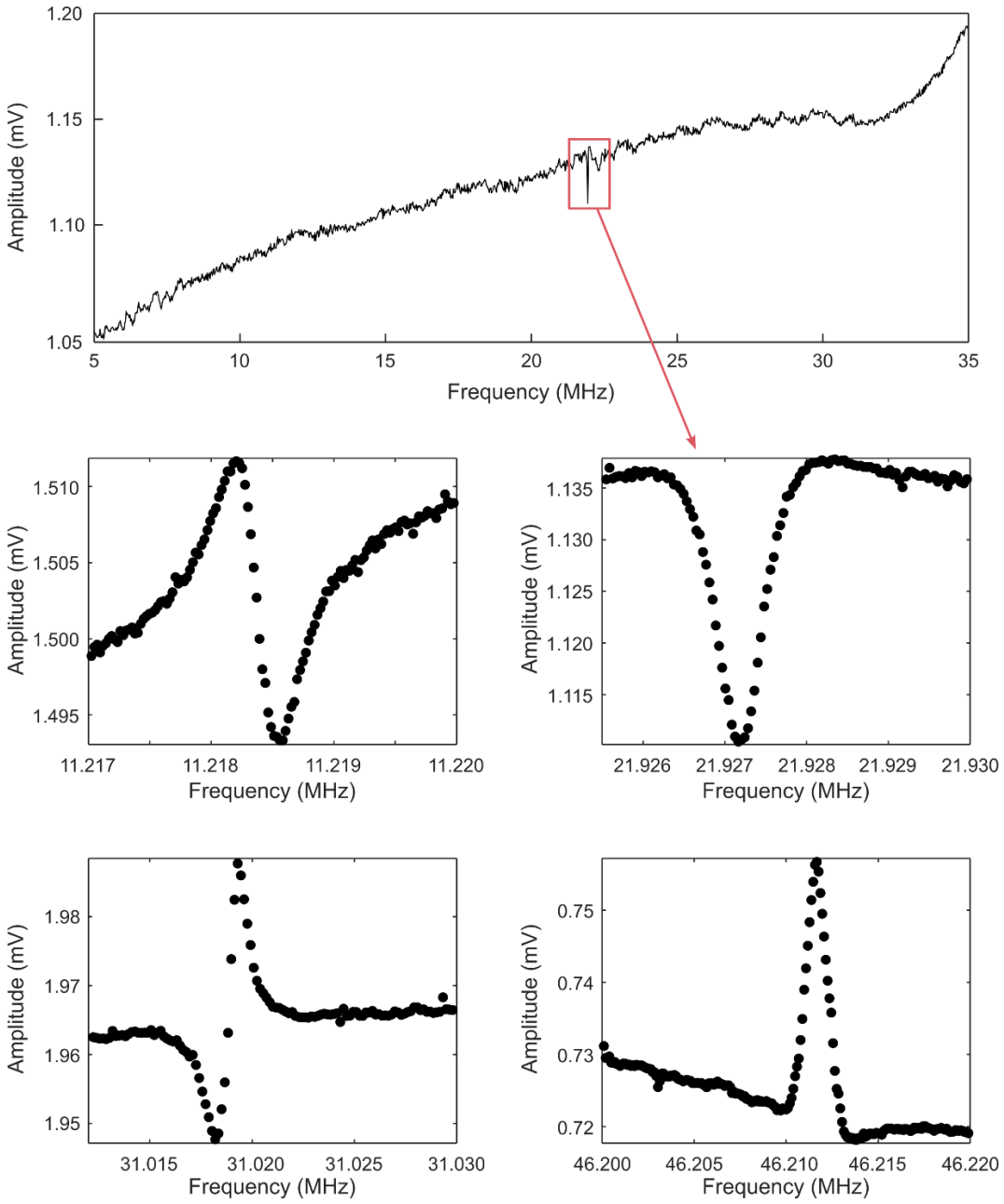


Figure 4.8 Observed resonance peaks from multiple GeTe devices (10 averages, 100 Hz lock-in bandwidth). Individual peaks correspond to the fundamental modes of four different nanowires. Top panel shows the wide range frequency response of the device pointed by the arrow.

This background further modifies the resonance lineshape, hence making it impractical to fit a Lorentzian curve to the experimental data. Thus, it is necessary to analytically derive a suitable Lorentzian equation in order to evaluate resonator performance, i.e. to determine f_0 and Q. To that end, the differential equation governing the motion of a damped harmonic oscillator driven by a sinusoidal force is given below.

$$m\frac{d^2x}{dt^2} + \beta\frac{dx}{dt} + kx = F_0 e^{i\omega t} \tag{4.4}$$

Here, x is the displacement, m is the mass, β is the damping coefficient, k is the linear spring constant while F_0 and ω are the amplitude and the angular frequency of the driving force, respectively. For $\beta^2 \ll 4mk$, let $Q = m\omega_0/\beta$ be the quality factor and $\omega_0 = \sqrt{k/m}$ be the angular resonance frequency of the oscillator ($\omega_0 = 2\pi f_0$). In steady sinusoidal state, the solution to Eq. 4.4 is in the form of,

$$x = x_0 e^{i(\omega t + \varphi_0)} \tag{4.5}$$

where the frequency dependent amplitude x_0 and phase φ_0 of the displacement are:

$$x_0 = \frac{F_0/m}{\sqrt{(\omega_0^2 - \omega^2)^2 + (\omega_0\omega/Q)^2}} \tag{4.6a}$$

$$\varphi_0 = -\tan^{-1}\left(\frac{\omega_0\omega/Q}{\omega_0^2 - \omega^2}\right) \tag{4.6b}$$

In nanowire resonators, frequency-doubling effect takes place due to the symmetric elongation of devices, as discussed in Section 4.1. Therefore, the piezoresistive signal $V_{\mathrm{pz}}(\omega)$ becomes proportional to the square of the displacement $\left(V_{\mathrm{pz}}(\omega) \propto x^2\right)$. As given in Eq. 4.7, $\left|V_{\mathrm{pz}}(\omega)\right|$ follows the Lorentzian lineshape, i.e. not the square-root of the Lorentzian as in the case of cantilevered beams.

$$\left|V_{\mathrm{pz}}(\omega)\right| \propto \frac{1}{(\omega_0^2 - \omega^2)^2 + (\omega_0\omega/Q)^2} \tag{4.7}$$

As seen from the data in Figure 4.8, in addition to $V_{\mathrm{pz}}(\omega)$, there is also a frequency dependent background signal, which will be denoted by $V_{\mathrm{bg}}(\omega)$. Within a small frequency interval, i.e. for $Q \gg 1$, the measurement background can be linearised as follows,

$$V_{\mathrm{bg}}(\omega) = (A + B\omega)e^{i\Delta\varphi} \tag{4.8}$$

with the fitting parameters A and B, and the phase $\Delta\varphi$. Here, $\Delta\varphi$ stems from the non-zero delays within the experiment due to connection cables and parasitic device capacitances. Thus, $V_{\mathrm{bg}}(\omega)$ is a result of both the crosstalk from the drive signal (Figure 4.6) and the electrical background of the experiment. At this point, it is crucial to state that the drive signal contains not only the ω component but also its higher-order harmonics, e.g. 2ω, 3ω, 4ω, …, due to the total harmonic distortion (THD) of the HPA. Therefore, even though the readout is performed at 2ω, the crosstalk from the drive signal still contributes to $V_{\mathrm{bg}}(\omega)$.

By following a similar procedure previously described by Sazonova [145], the overall lock-in readout $V_{\mathrm{r}}(\omega)$ can be written as the addition of the two physical quantities:

$$\begin{aligned} V_{\mathrm{r}}(\omega) &= V_{\mathrm{pz}}(\omega) + V_{\mathrm{bg}}(\omega) \\ &= x_0^2 e^{i2\varphi_0} + (A + B\omega)e^{i\Delta\varphi} \end{aligned} \tag{4.9}$$

By substituting x_0 and φ_0 from Eq. 4.6a into Eq. 4.9 and simplifying, the magnitude response of the readout, i.e. $|V_{\mathrm{r}}(\omega)|$, can be obtained as,

$$|V_{\mathrm{r}}(\omega)| = A + B\omega + K(\omega_0^2/Q)^2 \frac{\cos\left(\Delta\varphi + 2\tan^{-1}\left(\frac{\omega_0\omega/Q}{\omega_0^2 - \omega^2}\right)\right)}{(\omega_0^2 - \omega^2)^2 + (\omega_0\omega/Q)^2} \tag{4.10}$$

where K is the amplitude contribution to the piezoresistive readout from the nanowire for $|A| \gg K$. Figure 4.9 shows the experimental data previously given in Figure 4.8 together with the best fits to them. Curve fitting has been performed in MATLAB using

Eq. 4.10. The goodness of the fits is better than 1.5% (root-mean-square-error), and Table 4.1 summarises the extracted performance parameters of the resonators, i.e. f_0, Q, and K).

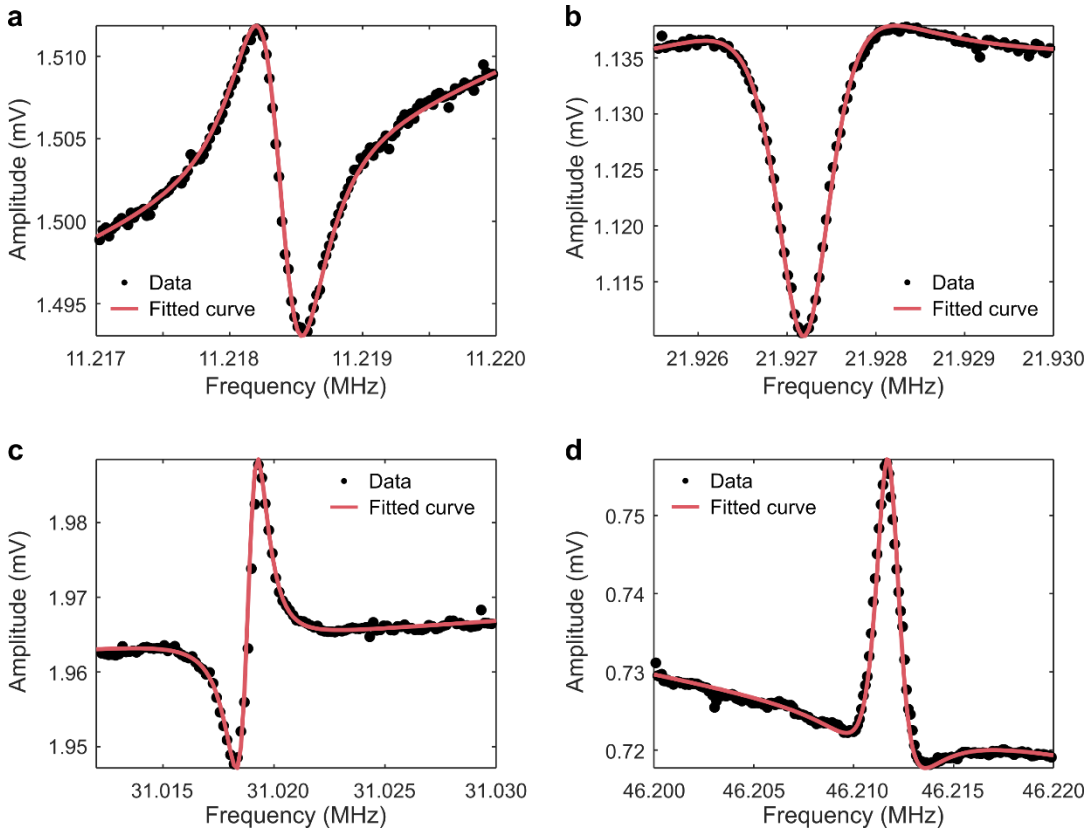


Figure 4.9 Data shown in Figure 4.8 together with corresponding fits to the modified Lorentzian lineshape given by Eq. 4.10.

Table 4.1 Extracted resonance parameters from the fitted curves in Figure 4.9**.**

	f_0	Q	K
Figure 4.9a	11.2184 MHz	18,100	15.46 μV
Figure 4.9b	21.9272 MHz	17,700	24.09 μV
Figure 4.9c	31.0189 MHz	18,900	31.93 μV
Figure 4.9d	46.2118 MHz	20,300	33.32 μV

One remarkable observation made from Table 4.1 is the unprecedented Q factors of these nanowires, and this is attributed to the fully-mechanical nanowire transfer process with no wet chemistry involved. For comparison, the Q values measured in this work are higher than those of previously reported high-Q resonators of doubly-clamped nanowires at room temperature [146], [147] and also comparable to those of cantilevered nanowires [148]. Moreover, this comparison can be extended to time-keeping MEMS devices with Q > 10,000 [64], paving the way for the intended application of phase-change NEMS, i.e. inherently tunable timekeeping and filtering solutions, as described in Chapter 1.

From the measured resonance frequencies, it is also possible to estimate the Young's modulus of GeTe nanowires in the crystalline phase (E_{cry}). It is well-known from Euler-Bernoulli beam theory that the resonance frequency of a doubly-clamped beam can be calculated using the following formula [149]:

$$\omega_0 = 2\pi f_0 = \frac{22.373}{L^2}\sqrt{\frac{EI}{\rho A}} \qquad 4.11$$

Here, L is the length, E is the Young's modulus, I is the second moment of area, ρ is the mass density, and A is the cross-section of the beam. For circular slender bodies such as nanowires, the second moment of area is given as $I = \pi D^4/64$, where D is the diameter.

Length and diameter of the nanowires used in Figure 4.9 are estimated via SEM and tabulated in Table 4.2. It is also useful to note that the mass density of GeTe in the crystalline state is 6060 kg m^{-3} [150]. Thus, by substituting the f_0, L, D, and ρ values into Eq. 4.11, E_{cry} can be calculated as 86 ± 4 GPa, which is in good agreement with the previously reported values for GeTe (i.e. 77 GPa) [151].

Table 4.2 Length (L) and diameter (D) of the devices used in Figure 4.9**.**

	L	D
Figure 4.9a	9.0 µm	280 nm
Figure 4.9b	7.0 µm	320 nm
Figure 4.9c	5.7 µm	300 nm
Figure 4.9d	5.0 µm	340 nm

4.4 Validation of the mechanical resonance

As seen in the previous section, readout signals from the NEMS devices can be as small as tens of microvolts. This being the case, distinguishing nanomechanical resonance peaks from environmental noise sources becomes elusive. Some of these noise sources may include radio signals, line noise, and electrical crosstalk. Even though the resonance measurements in this thesis have been performed in a Faraday cage, such interferences might not be suppressed completely due to the existence of ground loops and lengthy connection cables. To confirm whether a measured resonance peak belongs to the NEMS resonator, the behaviour of the peak under different experimental conditions should be investigated.

An increase in the drive level should increase the resonance peak amplitude. In Figure 4.10, frequency response of a GeTe nanowire (L = 8 µm, D = 250 nm) is given for two different V_{drive} values (V_{bias} = 300 mV). As can be seen from this wide-range frequency sweep (1 to 20 MHz), the resonance peak is distinctive, and its amplitude increases for increasing V_{drive}. This method is particularly effective for distinguishing spurious peaks from mechanical resonances, i.e. increasing V_{drive} eventually suppresses the noise peaks while enhancing the amplitude of the NEMS peak. Also note from Figure 4.10 that the change in the background signal is not linearly proportional to the drive amplitude. This difference needs to be investigated further. Potential cause might be the deformation in the chip assembly with increasing amplitudes at high frequencies.

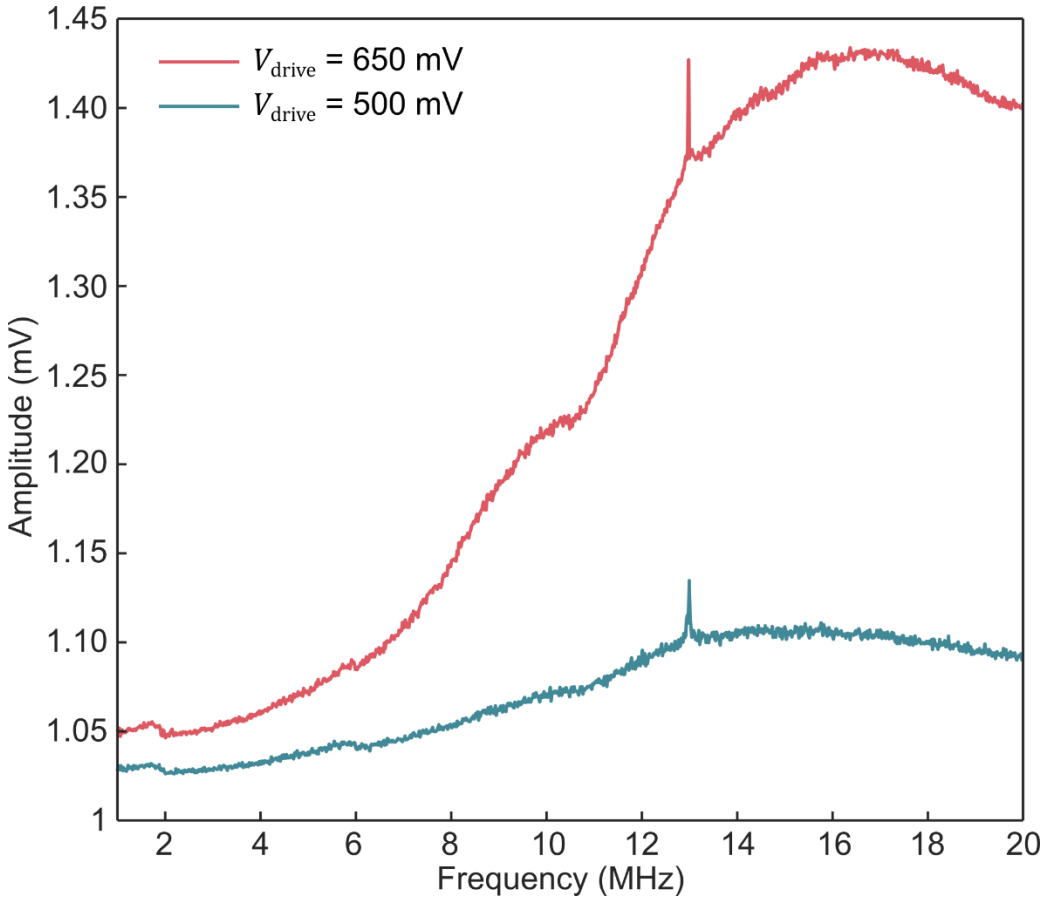


Figure 4.10 Evolution of the readout for different V_{drive} levels.

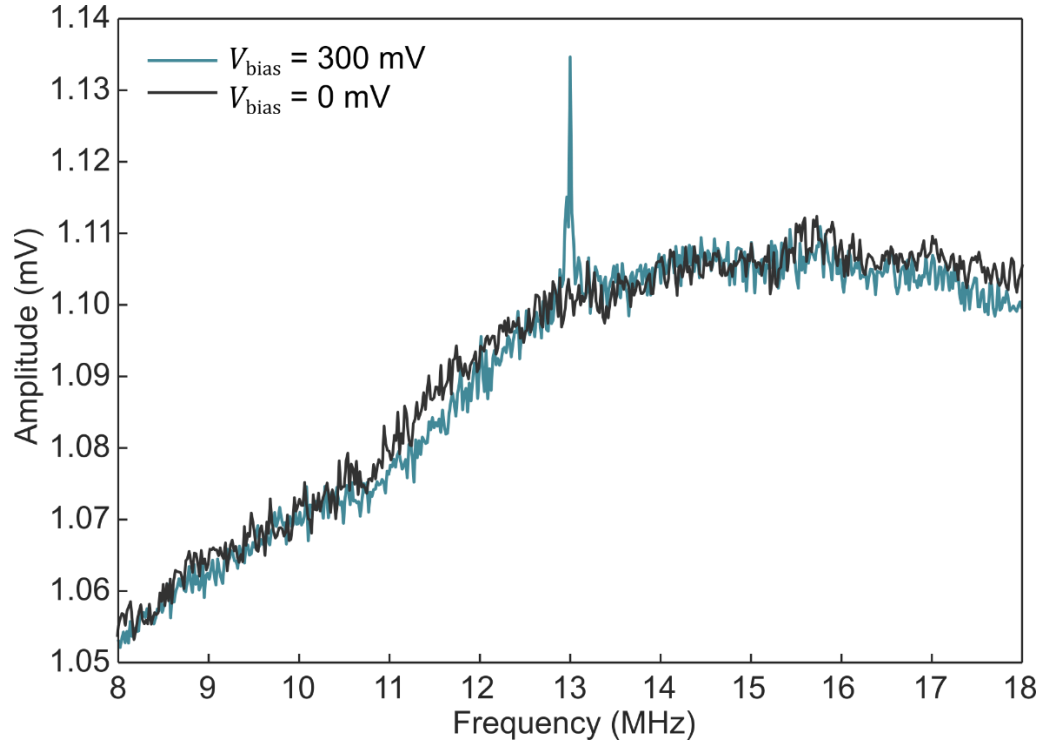


Figure 4.11 Evolution of the readout for different V_{bias} levels.

At this point, only examining the effect of V_{drive} is not sufficient to rule out the possibility of an unintentional electrical resonance such as a parasitic LC tank formation within the setup or bulk acoustic modes of the piezoceramic shaker. To that end, measurements should be performed for different V_{bias} values, as well. This is to ensure that the resonance peak is piezoresistive. As such, the measured readout signals for two V_{bias} levels are given in Figure 4.11 (V_{drive} = 500 mV). Here, the data suggests that the resonance peak disappears for zero bias (V_{bias} = 0), and this is an anticipated response from a piezoresistive transduction scheme.

It is also worthwhile to display the readout signals demodulated at both ω and 2ω references. The data in Figure 4.12 has been obtained for the same nanowire by simultaneously activating two lock-in demodulators, with their references set to ω and 2ω. As seen from the plots, the 2ω reference yields the resonance peak while the ω reference shows no sign of a peak. This further validates the frequency-doubling effect in nanowires as discussed before. It should also be noted that the electrical background is much higher at ω because the crosstalk from the drive signal is expected to be the highest at ω.

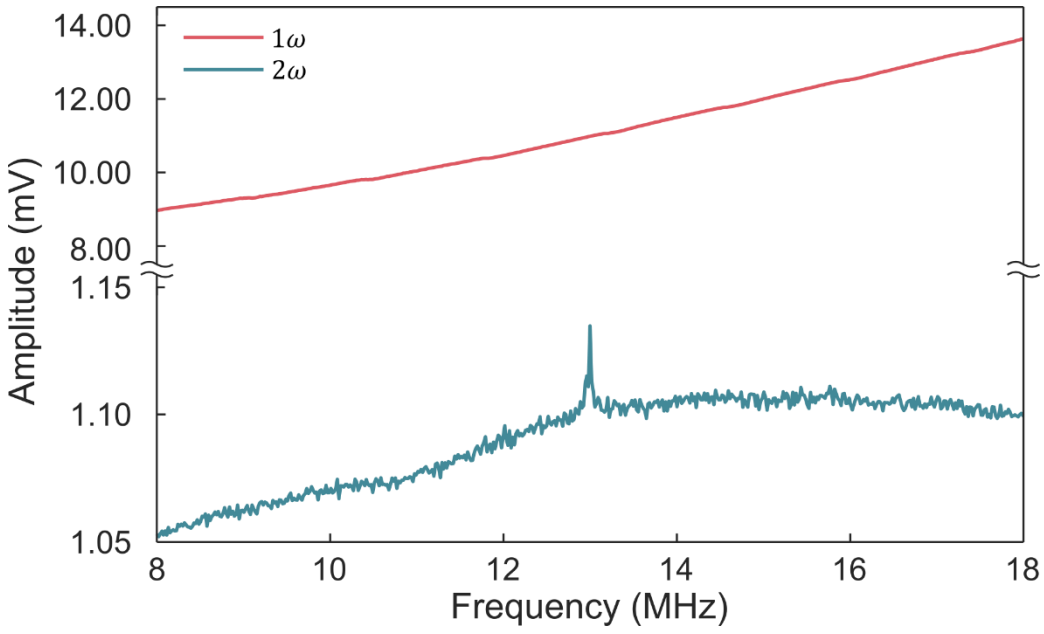


Figure 4.12 Piezoresistive readout at ω and 2ω references for the same measurement.

Overall, it is crucial to obtain the readout signal from a NEMS device under various V_{drive} and V_{bias} levels. Intuitively, increasing both parameters should result in a larger peak amplitude. Otherwise, the peak is very unlikely to be a NEMS resonance. One should also repeat the same measurement more than once. If the peak parameters (amplitude, phase, or shape) differ under the same experimental conditions, it can be concluded that the peak is spurious.

4.5 Determination of gauge factors

Although amorphous GST thin-films exhibit ultra-high piezoresistive gauge factors (~338) [152], the effect has not been explored in phase-change nanowires before. As mentioned earlier, piezoresistivity improves with scaling – and especially in nanowires due to their increased surface-to-volume ratio [142].

To calculate the gauge factor of GeTe nanowires, vibrational amplitude of the NEMS devices (a_{NEMS}) has to be determined for a given drive voltage (V_{drive}). One way to determine a_{NEMS} is to measure the amplitude of surface vibrations of the piezoceramic shaker (a_{surf}). Since direct mechanical coupling is used to actuate the devices here, the following relation holds true for $Q \gg 1$:

$$a_{\mathrm{NEMS}} = Q \times a_{\mathrm{surf}} \qquad 4.12$$

To this end, the piezoceramic actuator has been calibrated using contact-mode AFM measurements. The AFM system used in this experiment is Asylum MFP-3D, and the measurement setup is depicted in Figure 4.13a. It is important to note from the setup that the AFM cantilever is placed on top of the device electrodes, i.e. not on the piezo surface. Thus, the mechanical losses between the boundaries (actuator-chip-nanowire) have been considered for this experiment. In other words, the measurand a_{surf} in the experiment is the effective actuation amplitude experienced by the NEMS device.

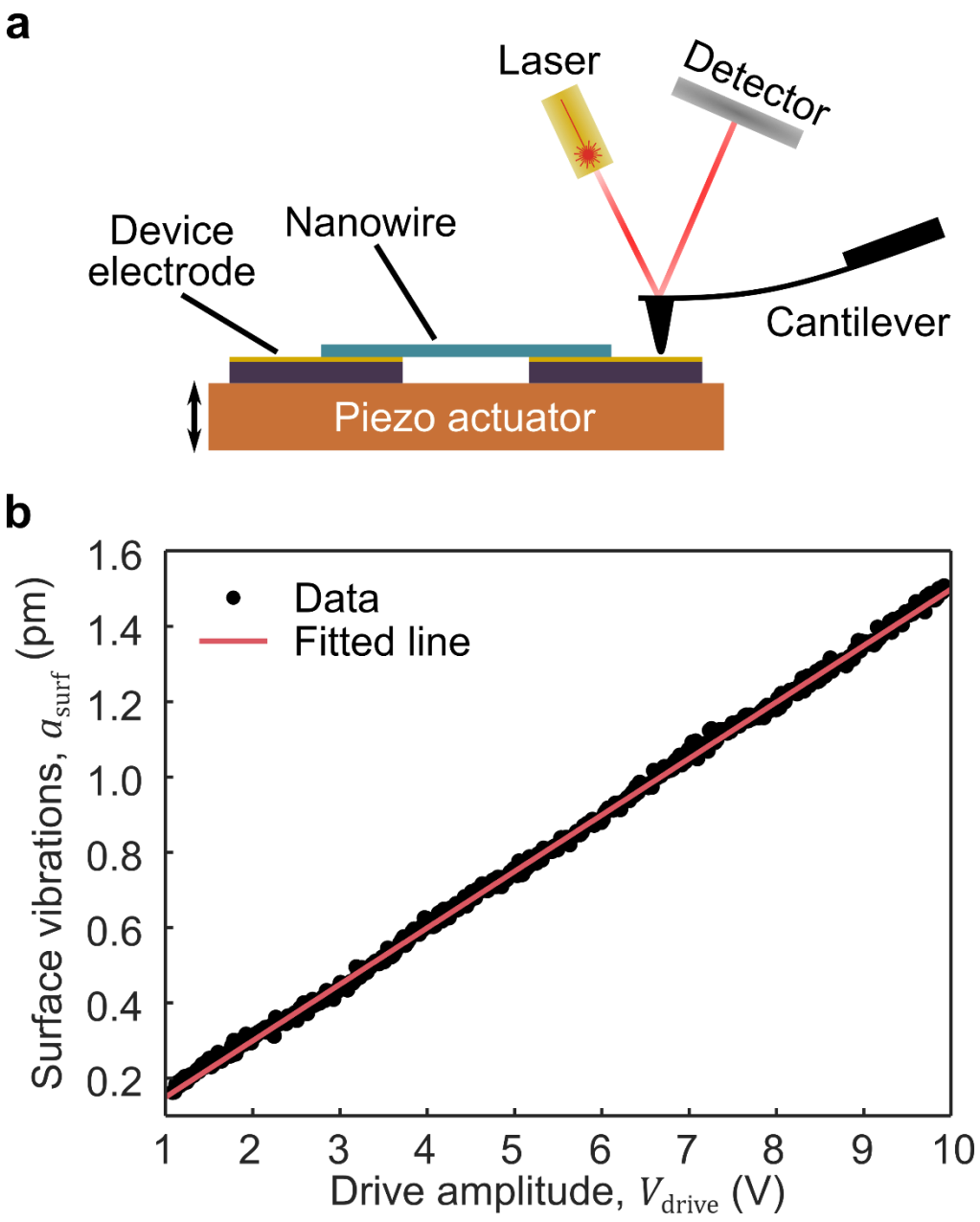


Figure 4.13 Calibration of the piezoceramic actuator using contact-mode AFM. **a**, Simplified schematic diagram of the measurement setup. **b**, Surface vibrations of the piezoceramic actuator with respect to the drive amplitude. The piezo element is operated in linear regime.

Lorentzian fit to the thermal spectrum of the AFM probe (BudgetSensors® Contact-G cantilever) yields a resonance frequency f_{cant} = 11.98 kHz and a quality factor Q_{cant} = 61. Spring constant of the cantilever is calibrated as 0.188 N m^{-1}, with an inverse optical lever sensitivity (invOLS) of 238.63 nm V^{-1}. The AFM system is then interfaced with the lock-in amplifier. Here, the lock-in output drives the piezo shaker whereas the lock-in input reads out the photodetector signal from the AFM interface (open-loop configuration). To improve the noise performance of the measurement, average signal count is set to 1,000. Furthermore, the drive frequency is chosen as f_{cant} to mechanically amplify the readout signal by Q_{cant}. Thus, a_{surf} can be simply determined by scaling the photodetector signal by invOLS / Q_{cant}. It should be mentioned that the invOLS calibration in this experiment accounts for the root-mean-square (RMS) conversion done by the lock-in amplifier, hence a_{surf} is not the RMS displacement but the sinusoidal amplitude of displacement.

Figure 4.13b shows the data obtained by sweeping the lock-in output from 1 to 10 V (at 11.98 kHz) while simultaneously recording the detector output. Linear fit to the data suggests that the piezo shaker stays in linear region even at the highest drive amplitude in this experiment (i.e. 10 V). From the fitting results, the slope is found as ~0.15 pm V^{-1}, and the goodness of the fit remains within 1.2%.

For V_{drive} < 1 V, the photodetector signal becomes undetectable due to the noise floor of the experiment, thus a_{surf} needs to be extrapolated for lower drive levels. Provided that V_{drive} is below 1 V for the NEMS measurements in this work, subsequent gauge factor estimations have been performed with extrapolated values of a_{surf}. For example, the data in Figure 4.9b has been obtained with V_{drive} = 550 mV, which yields a_{NEMS} = 1.46 nm for a Q value of 17,700 (Eq. 4.12). At the maxima of flexural-mode vibrations, the displacement at the centre of the GeTe nanowire becomes $d_{\mathrm{c}} = a_{\mathrm{NEMS}}$. Therefore, the combination of Eqs. 4.1 and 4.2 yields:

$$\Delta R_{\max} = 2R\gamma\left(\frac{a_{\mathrm{NEMS}}}{L}\right)^2 \qquad 4.13$$

From here, one can solve for γ by substituting $\Delta R_{\max}$ into Eq. 4.3. Note from Table 4.1 that the peak height K (= $V_{\mathrm{r}}/\sqrt{2}$) for that device is measured as 24.09 μV under V_{bias} = 150 mV. With a *d.c.* resistance of R = 0.83 kΩ, the gauge factor of the device can be estimated as 19.5. As such, the same procedure has been repeated for all the devices in Figure 4.9, and the results are listed in Table 4.3. Consequently, the gauge factor of GeTe nanowires in the crystalline phase is estimated as γ_{cry} = 19.3 ± 0.9. Gauge factor in the amorphous phase (γ_{amo}) will be revealed in the next chapter, upon amorphization of the devices.

Table 4.3 Vibrational amplitude (a_{NEMS}), bias voltage (V_{bias}), *d.c.* resistance (R), and estimated gauge factor (γ) for the devices used in Figure 4.9**.**

	a_{NEMS}	V_{bias}	R	γ
Figure 4.9a	1.35 nm	300 mV	1.48 kΩ	20.5
Figure 4.9b	1.46 nm	150 mV	0.83 kΩ	19.5
Figure 4.9c	1.38 nm	150 mV	0.79 kΩ	18.3
Figure 4.9d	1.22 nm	120 mV	0.61 kΩ	18.8

It should be noted that the uncertainty in γ_{cry} directly arises from the deviation of γ values estimated in Table 4.3, which is primarily attributed to the variation of nanowire diameters and crystal defects in different devices [142], [153]. On the other hand, the uncertainty in the measurements (< 0.1%) is negligible compared to this deviation, thus ignored during the estimations. This is due to the improved SNR obtained by averaging (> 100 times) in AFM and lock-in measurements while determining individual parameters, i.e. error is 1/SNR.

It is also useful to investigate the dependency of γ_{cry} on V_{bias}. To that end, the gauge factor of the device in Figure 4.9b has been calculated for different values of V_{bias}. The

gauge factor decreased for the increasing bias voltage, e.g. γ = 20.6 for V_{bias} = 100 mV, γ = 19.5 for V_{bias} = 150 mV, and γ = 18.2 for V_{bias} = 200 mV. Such degradation of gauge factor has been previously observed in other semiconducting materials at elevated temperatures [153], i.e. Joule heating in this case. Even though a detailed study of gauge factors is beyond the scope of this thesis, further investigation is needed to understand the mechanism behind this observation.

From these results, the following observations can be made. Firstly, the gauge factors measured here are gigantic for a material that exhibits metallic conduction as metals typically have gauge factors of ~1-3 [83]. This is mainly attributed to the high concentration of Ge vacancies (p-type doping), making the gauge factor of crystalline GeTe nanowires comparable those of doped semiconductors (~30 for p-type SiC and ~50 for p-type Si) [84], [153]. Moreover, decreasing the length of the devices can dramatically increase the readout efficiency for similar drive levels (see Eq. 4.2 or 4.13). The reduced length also increases the resonance frequency (Eq. 4.11). Combined with the high gauge factors in the metallic state, this behaviour compensates for the signal loss in high-frequency designs, facilitating impedance matching even at elevated working frequencies. Lastly, to further enhance the readout amplitude V_{r}, a low-noise transimpedance amplifier (TIA) could be used due to their high input resistance provided that V_{r} is proportional to R_{i} (Eq. 4.3).

It is also important to note that all the measurements in this chapter have been performed within the linear region of operation of NEMS devices, meaning that the drive levels are set to produce $a_{\mathrm{NEMS}} < a_{\mathrm{crit}}$. Here, a_{crit} is the critical amplitude for the onset of Duffing nonlinearity. For cylindrical beams under no residual tension, the critical amplitude is given as [154]:

$$a_{\mathrm{crit}} = \sqrt{\frac{D^2}{\sqrt{3}Q}} \qquad 4.14$$

Thus, to confirm the linear region of operation, a_{crit} values calculated by Eq. 4.14 can be compared with a_{NEMS} values of the relevant devices in Table 4.3. The beams have also been driven in the non-linear regime, all showing Duffing nonlinearity with spring-hardening effect.

4.6 Estimating the drive power

As discussed in Section 2.2, driving levels for NEMS devices are usually at the sub-picowatt level. To validate this claim, effective drive power required by the GeTe nanowires can be calculated. To this end, it is essential to determine the energy of the resonator during fundamental mode vibrations due to harmonic strain variations. When modelled as a spring-mass system, energy stored in an oscillating doubly-clamped beam with a displacement amplitude d_{c} is simplified to Hooke's law relation:

$$W_0 = \frac{1}{2} m_{\mathrm{eff}} \omega_0^2 d_{\mathrm{c}}^2 \tag{4.15}$$

Here, m_{eff} is the effective mass of the resonator at the fundamental mode and compensates for the effect of non-uniform displacement along the beam (e.g. see the mode shape of a deflected beam in Figure 4.1). Thus, the required drive power to maintain oscillations at ω_0 with constant amplitude can be calculated as [155]:

$$P_0 = \frac{\omega_0}{Q} W_0 \tag{4.16}$$

To determine an estimate for the effective drive power, effective mass of the device in Figure 4.9b has been calculated via FEM analyses in COMSOL Multiphysics® environment, by performing the following volume integration over the deflected beam:

$$m_{\mathrm{eff}} = \iiint_V \rho \frac{x^2}{d_{\mathrm{c}}^2} dV \tag{4.17}$$

To reiterate, here, V is the volume of the suspended portion of the nanowire, x is the displacement while ρ and d_c is the mass density and the displacement at the centre of the nanowire, respectively. Thus, m_{eff} of the device in Figure 4.9b is computed as 1.356×10^{-15} kg. FEM analyses for the first eigenmode further yield the relation between m_{eff} and m for doubly-clamped nanowires as given by Eq. 4.18. For d_c = 1.46 nm, the effective drive power required by the device can be estimated as P_0 = 0.21 pW, paving the way for ultra-low power applications as mentioned earlier, e.g. for mechanical signal processing [13].

$$\frac{m_{\text{eff}}}{m} = 0.3965 \tag{4.18}$$

It should be noted that the actual drive power (i.e. active power) dissipated at the output of the HPA is much higher than P_0. To elaborate, the peak current required by the piezoceramic shaker is given as,

$$I_{\text{peak}} = \pi f C_{\text{piezo}} V_{\text{pp}} \tag{4.19}$$

where f is the drive frequency, C_{piezo} is the capacitance of the piezo crystal, and V_{pp} is the peak-to-peak drive amplitude. Neglecting the loss factor of the piezoceramic actuator, i.e. assuming a purely capacitive load, I_{peak} is only dissipated by the output resistance of the HPA, which is 50 Ω.

For a typical load of C_{piezo} = 1 nF with V_{pp} = 1 V and f = 20 MHz, I_{peak} becomes 63 mA, which leads to a power dissipation of ~0.2 W. This is approximately twelve orders of magnitude higher than P_0 since the power is applied to the whole chip, which makes piezo actuation inherently inefficient regardless of its easy implementation. Therefore, for practical/commercial NEMS applications in future, more effective (i.e. more localised) actuation techniques should be utilised such as capacitive [18], dielectric [21], or electrothermal [80] drive.

4.7 Conclusions

In this chapter, experimental methods for piezoresistively transducing the nanowire NEMS resonators of GeTe are explained. A comprehensive design and characterization of the measurement setup is given together with an electrical equivalent of the setup and explanation of the ground loops. Following the electrical characterisation of the nanowires, their mechanical resonance spectra have been measured using a lock-in amplifier and external (piezo) actuation. To determine the resonance parameters (f_0 and Q), the need for deriving a new non-zero phase Lorentzian has been mentioned. Here, the Lorentzian includes the frequency-doubling effect, which is due to symmetrical elongation of the nanowire during flexural-mode vibrations.

Dynamic properties of GeTe nanowires have been explored for the first time in this chapter. From f_0 values of four different nanowires with various length and diameter, the Young's modulus of crystalline GeTe is estimated as 86 GPa. Using the peak amplitude values of the readouts, the gauge factor in the crystalline phase is also calculated as 19.3. The latter experiment further requires the calibration of the piezoceramic actuator, which has been performed using contact-mode AFM measurements. From this calibration, an estimate for the effective drive power for NEMS resonators is found to be less than a picowatt. Coupled with the Q factors over 16,000, these nanowires can pave the way for mechanical timing and signal processing applications in the future.

Chapter 5

Electrical tuning of devices

The findings presented in Chapters 4 & 5 have been published in:

Utku Emre Ali, Gaurav Modi, Ritesh Agarwal, Harish Bhaskaran, *"Real-time nanomechanical property modulation as a framework for tunable NEMS",* Nature Communications 13, 1464, (2022). DOI: 10.1038/s41467-022-29117-7

5.1 Overview

Chapter 5 introduces a novel platform for tunable NEMS via direct mechanical property modulation. The tuning is performed via electrical pulses, which leads to a dislocation-based route for amorphization in these nanowires. Section 5.2 investigates in detail the non-volatile tuning mechanism upon electrical pulses. In this section, long-term stability of the tuned frequency has also been investigated in the amorphous phase. Effect of phase-change tuning on mechanical Q factors is explored in Section 5.3. Real-time frequency tracking has been performed in Section 5.4, where short-term stability of the nanomechanical resonance in amorphous and crystalline states has been studied. A real-world application idea for such tunable resonators has also been demonstrated in this section for the future of telecommunication electronics.

5.2 Phase-change tuning of the mechanical resonance

As explained in Section 2.5, PCMs offer distinct electrical, optical, and mechanical properties when switched between their amorphous and crystalline phases. The changes in their electrical and optical properties have been exploited for a wide range of applications from data storage and in-memory computing to reflective displays, metasurfaces, and smart coatings. However, their mechanical properties have largely gone unexploited, even in device research.

Conventionally, resonating microcantilevers are commonly employed to determine the mechanical properties of thin-films. By measuring the resonance frequency of the microcantilever before and after the thin-film deposition, the Young's modulus of the film can be determined. As such, the mechanical properties of PCM thin-films have also been measured using Si microcantilevers. An example is given in Figure 5.1.

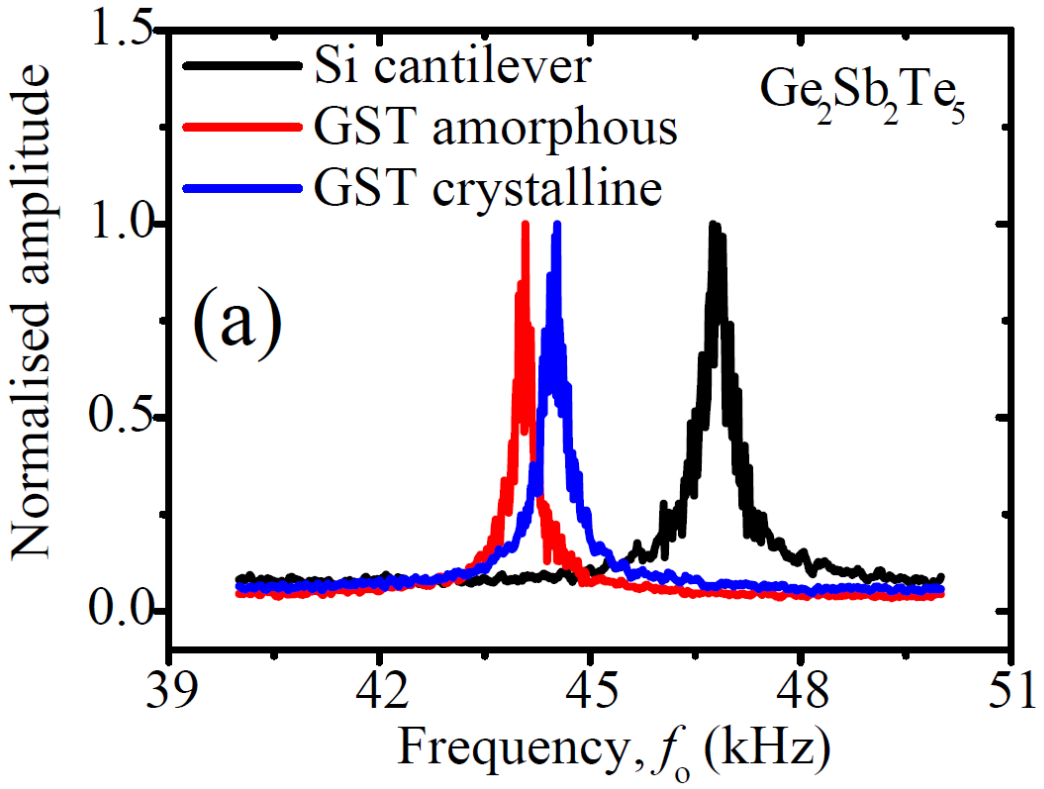


Figure 5.1 A study by Nazeer et al. showing the measured resonance frequencies of a Si cantilever without (black) and with the GST thin-film in amorphous (red) and crystalline (blue) phases. *Reprinted from [32], with permission from Elsevier.*

In this work by Nazeer et al. [32], the resonance frequency of a 3 µm-thick Si cantilever was initially measured. Following the sputter-deposition of a 200 nm-thick $Ge_2Sb_2Te_5$ (GST) film on the cantilever, its resonance frequency decreased by about 2 kHz. Here, it should be noted that the sputtering results in an amorphous thin-film. In order to crystallise the material, the GST-coated Si cantilever was annealed on a hot plate at 150 ℃ for 15 minutes. As seen from Figure 5.1, crystallisation process increased the resonance frequency by ~500 Hz. From here, the authors further estimated a Young's modulus contrast of about two (calculated as $E_{\mathrm{crys}}/E_{\mathrm{amo}}$). Using the same technique, Won et al. (2012) have also shown a dramatic change in the Young's modulus of PCM thin-films, with a contrast of up to 6-fold for decreasing thin-film thicknesses [31].

From Figure 5.1, one can notice that the frequency shift remains less than 1% regardless of the significant Young's modulus change, where $f_0 \propto \sqrt{E}$ (Eq. 4.11). This is mainly due to the larger thickness of the Si base compared to that of the GST film. In addition to this small tuning range, the tuning process is not practically reversible in such a design, i.e. re-amorphization and re-crystallisation of the GST-cantilever system may require 100s of Volts due to the thick Si base [33].

To harness a wider tuning range from the high Young's modulus contrast, Hosseini et al. have suggested using a graphene membrane as the support [33], which was previously shown in Figure 2.9a. As the PCM thin-film constituted a much larger volume in the overall structure in their design, the authors claimed a theoretical tuning range over the whole GSM band (800 MHz to 1.9 GHz). However, fabrication of such a structure has so far remained challenging.

Furthermore, as have discussed in Section 2.6, conventional phase-change processes in thin-films require filamentation for crystallisation and melt-quenching for amorphization, both of which limit the applicability of thin-films as free-standing systems, e.g. resonant NEMS devices. Firstly, in electrical switching, the filamentation

process prevents homogenous crystallisation in thin-films, i.e. crystallising the whole cross-section is not feasible. Secondly, a suspended device should not be melted; otherwise, it will collapse. Therefore, it is evident that thin-film configurations are not practical to demonstrate active (i.e. dynamic, reversible, and repeatable) phase-change tuning in NEMS resonators.

On the other hand, it has been long assumed that amorphization of PCMs starts with melting, which is then followed by rapid cooling of the material at rates higher than 10^9 K s^{-1} [25]. This requires pulse durations of tens of nanoseconds (e.g. in optical storage media). With the incentive of achieving higher switching speeds, studies with bulk PCMs using femtosecond laser pulses have shown that amorphization can also occur in sub-picosecond regime with much lower energies than that required for melting [114]. Later, it has been unambiguously explained that this is due to the unique presence of resonance bonds in crystalline PCMs, which creates Peierls-like distortion in the lattice consisting of longer (weaker) and shorter (stronger) bonds such as Ge-Te bonds [105], [156]. With the selective excitation of the weaker bonds (e.g. by using polarised light [114]), the crystal loses long-range order and forms an amorphous solid. Thus, these findings have strengthened the concept of a lattice-distortion-triggered amorphization process in single-crystal PCMs. Such non-melting route for amorphization could further eliminate the aforementioned issue of collapsing in suspended devices such as NEMS.

An ideal platform to study and visualise this phenomenon at the device level in the electrical domain can be nanowires [34]. Unlike polycrystalline thin-films, nanowires do not suffer from grain boundaries owing to their single-crystal lattice, thus carrier transport and structural dynamics are only affected by the variations in the lattice. Therefore, electrical properties of PCM nanowires are highly correlated to the microstructural changes caused by amorphization/crystallisation pulses. This further enables probing structural evolution by simply reading out the electrical resistance as

demonstrated by previous in-situ TEM studies using GST nanowires in 2012 [34] and GeTe nanowires in 2014 [36].

A brief description of this non-conventional (i.e. dislocation-based) switching characteristics of phase-change nanowires in the electrical domain will be given in the following sections. Excitingly, such a property could facilitate active and reliable frequency tuning of NEMS at the device level through phase-change switching. Thus, the main focus in the following experiments will be on modulating the Young's modulus of suspended GeTe nanowires for frequency tuning applications while determining relevant performance parameters such as frequency tuning range, change in Q-factors, repeatability, tuning energy, and speed.

5.2.1 Wide-range frequency tuning

GeTe nanowires have been used in this work owing to its simpler (binary) chemical composition and well-understood atomic structure compared to other PCM alloys such as GST and AIST. The schematic used to inject pulses into the nanowires is given in Figure 5.2. Here, the bias tee (Mini Circuits ZFBT-4R2GW+) combines the pulse generator (Tektronix AFG3151C) and the source measure unit (SMU, Keithley 2410 SourceMeter).

To determine the amorphization parameters, 50-ns pulses with increasing amplitudes are applied to the nanowire while its *d.c.* resistance being monitored by the SMU with a bias voltage of 10 mV. After each pulse, the nanowire is reset to its virgin (crystalline) state via Joule annealing (~50 µA *d.c.* from the SMU) until a lower resistance state is observed, i.e. the duration is trivial. Here, it is worth noting that Joule annealing is a valid and practical method to homogenously crystallise phase-change nanowires as annealing drives the system closer to its thermodynamic equilibrium state, which is the (lower-energy) crystalline state with fewer dislocations [35]. To determine the amorphization pulse amplitude, the amplitude is increased by 0.1 V steps starting from

0.5 V until the electrical resistance is increased by at least two orders of magnitude. Such an increase in the *d.c.* resistance is the signature of amorphization in nanowires.

For the device given in Figure 4.2 (L = 7 µm, D = 300 nm), initial *d.c.* resistance is measured as 1.15 kΩ. Using the piezoresistive measurement setup in Figure 4.4, the resonance parameters are determined from the Lorentzian fit as f_0 = 20.3658 MHz and Q ≈ 16,700 (see Figure 5.3). Using the method described in the previous paragraph, amorphization pulse parameters are determined for this device as 50 ns – 1.2 V, which increases the *d.c.* resistance to 0.16 MΩ.

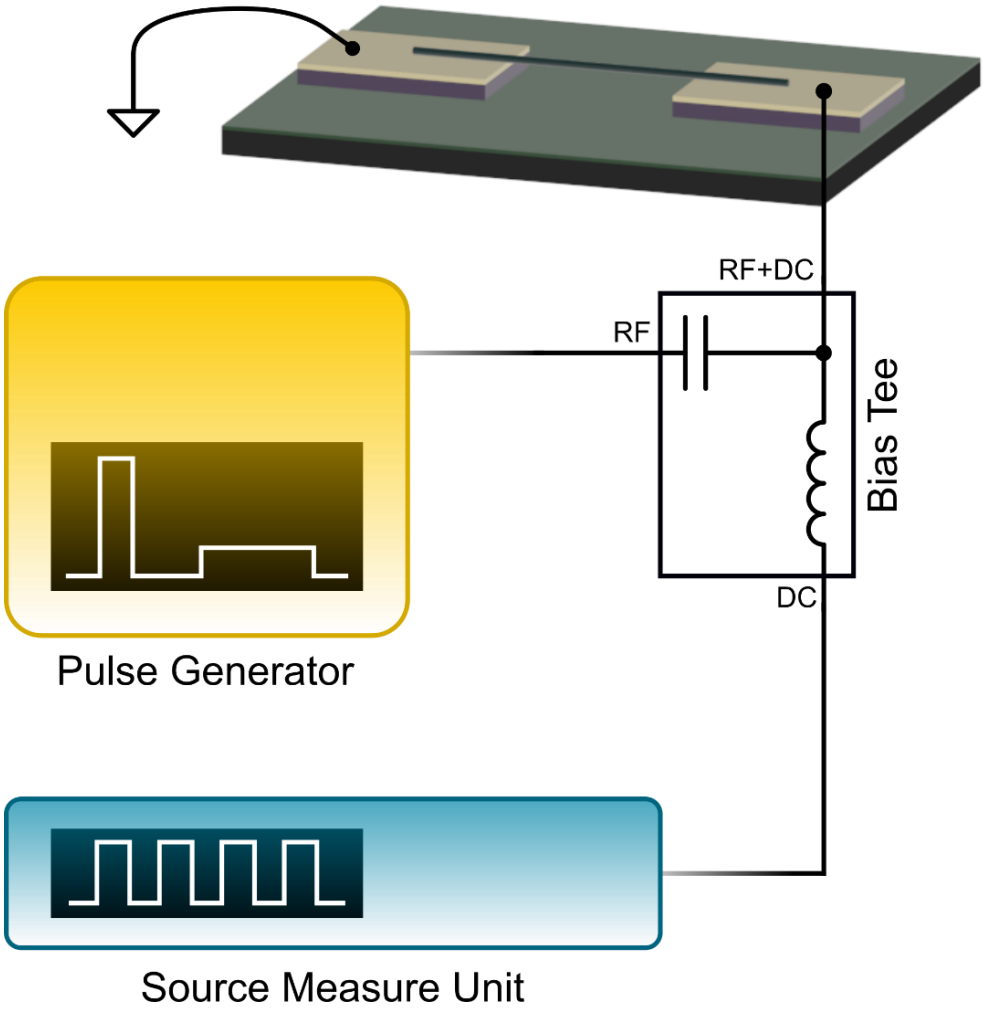


Figure 5.2 Experimental setup for the electrical tuning of GeTe nanowires.

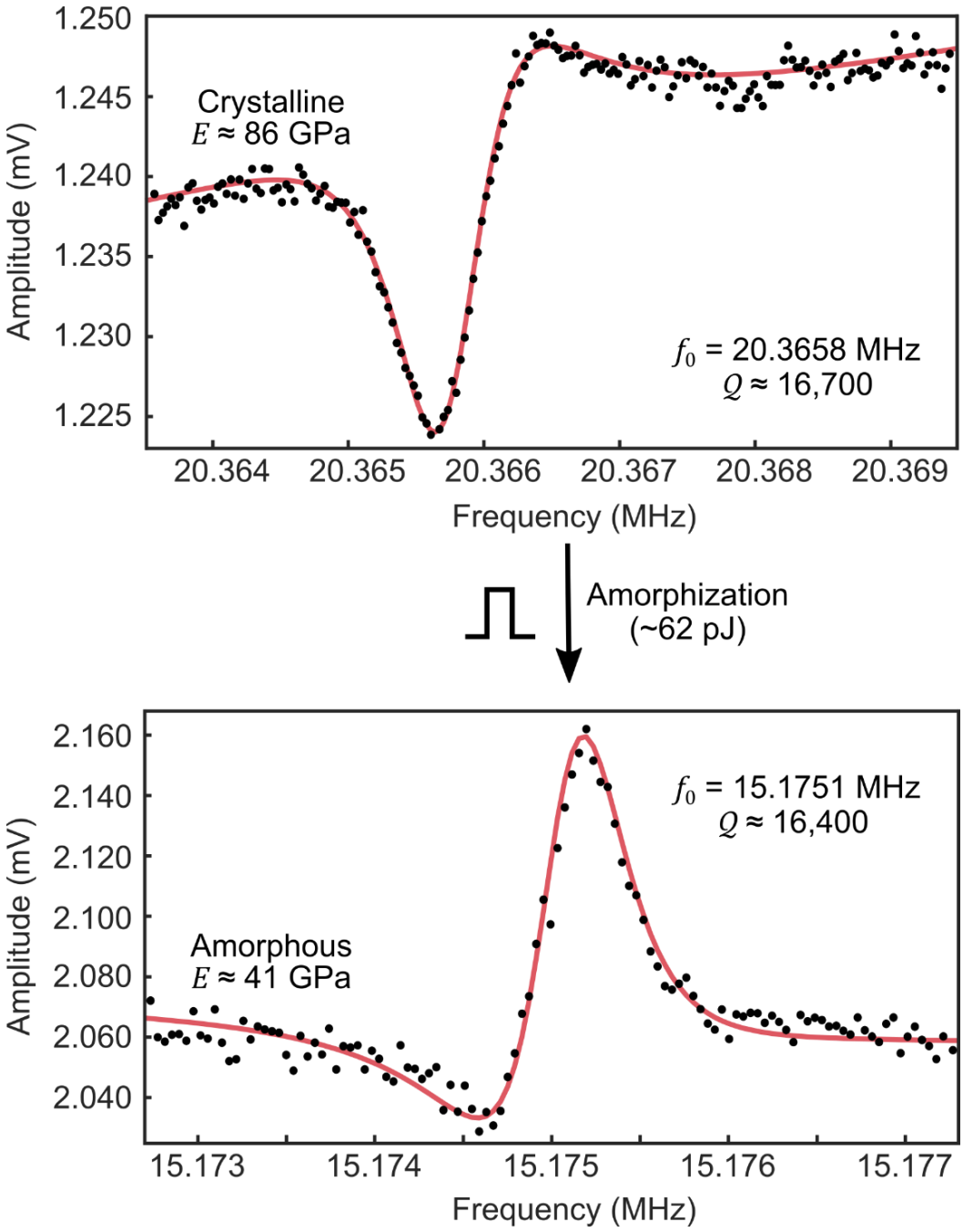


Figure 5.3 Nanomechanical tuning of a GeTe nanowire by an electrical pulse.

Remarkably, following the amorphization of the nanowire as seen in Figure 5.3, the mechanical resonance is tuned by 26% down to f_0 = 15.1751 MHz while its Q (≈ 16,400) remains almost intact (the explanation on non-changing Q factors will be given in Section 5.3). Assuming a constant resonator mass and a density of 5600 kg m^{-3} in the amorphous phase [150], this accounts for an effective softening in the Young's modulus of 52% (from 86 GPa to 41 GPa). Compared to the GST-coated Si cantilever in Figure 5.1, where the tuning range was less than 1%, the relative tuning in the GeTe nanowire is significantly higher. This is mainly because the suspended portion of the NEMS resonator in this thesis is fully comprised of a phase-change material, i.e. no mechanical base/support is required unlike in thin-film-based designs [32], [33]. Thus, the changes in Young's modulus can be entirely harnessed in nanowire configurations as their amorphization does not require melting.

More crucially, no tuning power is required after the tuning event because the phase change is non-volatile, making this work particularly suitable for low-power applications such as mobile and satellite communications. From the data in Figure 5.3 and using a similar procedure in Section 4.5, the gauge factor of the nanowire can also be estimated as γ_{amo} = 1,100. This exhibits more than a two-fold increase compared to the previously reported values for amorphous thin-film PCMs (~338) [152] and comparable to those of crystalline Si nanowires (~5000) [142]. Such enhancement in nanowires is primarily attributed to their increased surface-to-volume ratio. Besides, γ_{amo} is higher than γ_{cry}. This is owing to the metal-to-insulator transformation of the material upon amorphization [36], [106].

It should be noted that the resonance lineshape changes after amorphization, from a resonance dip to a resonance peak. Remembering the derived non-zero phase Lorentzian given in Eq. 4.10, this shape is determined by the phase of the electrical background ($\Delta\varphi$). For the data in Figure 5.3, for example, $\Delta\varphi$ rises from 35˚ to 140˚ when switched from crystalline to amorphous. Such a change in $\Delta\varphi$ is expected;

because firstly, the experiment has a different electrical background response at different frequencies, and secondly, the modified *d.c.* resistance of the nanowire impacts the electrical background (i.e. A and B coefficients in Eq. 4.10) due to the changing (capacitive) time constants of the measurement setup.

To study long-term stability in the amorphous state, the tuned resonance frequency and electrical resistance of the device in Figure 5.3 have been tracked for 5 days with intervals of approximately 24 hours (±0.5 h). The drift of electrical resistance in chalcogenide glasses has been well established and predominantly explained by structural relaxation dynamics causing mobility gap to increase over time (by trapping mobile holes in the case of GeTe). The resistance drift model follows the power rule, i.e. t^{α}, where t is the time. From the fitting results to the data in Table 5.1, the exponent α is found as 0.007, which is in good agreement with the reported values for GeTe nanowires ($0.002 < \alpha < 0.009$) [38].

Table 5.1 Frequency and resistance drift in the amorphous phase.

	Day 0	Day 1	Day 2	Day 3	Day 4
R [kΩ]	160.16	173.32	173.84	174.64	175.36
f_0 [MHz]	15.1751	15.1786	15.1847	15.1910	15.1959

On the other hand, the drift of the resonance frequency has not been previously studied in chalcogenide glasses. The data in Table 5.1 suggests a monotonic increase in f_0 over time. Although this could be due to the temperature fluctuations in the measurement chamber or the stress relaxation within the substrate, there is another factor that might explain this phenomenon. The hypothesis is that the increase in f_0 can be attributed to the pronounced drift of viscosity (η) of the material that also impacts its Young's modulus [120].

As described by Gemant in 1941 [157], Young's modulus of glasses is proportional to their viscosity, i.e. $E \propto \log_{10}(\eta)$. Given that the viscosity of PCMs linearly increase over

time due to bimolecular relaxation kinetics [120], one can estimate a frequency shift of about 4.8 kHz per day for this device, which is sufficiently non-volatile for practical requirements. For example, the typical frequency switching speeds required in frequency-hopping systems are smaller than 0.4 seconds, as described in 47 CFR § 15.247 [158]. To explicitly determine a viscosity value, however, a better-controlled experiment is necessary for future studies, e.g. more data points at different ambient temperatures are required while accounting for the substrate relaxation over longer periods of time (similar to the study by Kalb et al. [120]).

It is also worth mentioning that, to date, there is no single work presenting experimental data for both E and η mainly because of the contrasting temperature requirements in relevant experiments, i.e. lower temperatures for determining E and higher temperatures for η measurements. For instance, it takes more than a year to measure room-temperature viscosity of glasses even with the current technological capabilities due to extremely high viscosity levels (~10^{17}-10^{23} Pa s) at temperatures well below the glass transition temperature [159]. In contrast, this problem could turn into simply sensing the long-term drift of the resonance frequency of high-Q NEMS devices, where $f_0 \propto \sqrt{E} \propto \sqrt{\log_{10}(\eta)}$. However, it is crucial to take temperature fluctuations and substrate relaxation into account during such a measurement as discussed earlier.

To further confirm the findings on the tuning range and Q factors, another device with similar dimensions has been tested (L = 7 µm, D = 280 nm). Upon amorphization by a ~64 pJ pulse (50 ns – 3.5 V), the resonance frequency of this device decreased from 19.1583 MHz (14.5 kΩ) to 13.2158 MHz (1.82 MΩ) while its Q factor slightly increased from 18,100 to 18,800 (see Figure 5.4a,b). For re-crystallisation, Joule annealing is adopted. Thus, the device was cycled between amorphous and crystalline states ~5 times (a total of 11 phase-change events), and the results are shown in Figure 5.4c. The higher electrical resistance in this device is attributed to the poorer electrical contacts between the nanowire and the Au electrodes.

From the cyclability test, the mean and standard deviation of the resonance frequencies are calculated as: f_{cry} = 19.65 ± 0.46 MHz in the crystalline state and f_{amo} = 13.60 ± 0.28 MHz in the amorphous state. These results yield a significant ratio of $\overline{f}_{\mathrm{cry}}/\overline{f}_{\mathrm{amo}}$ = 1.45. On the other hand, the quality factors have only shown minor changes (Q = 19,210 ± 1,034), with no evident correlation to the crystallinity. Remarkably, the deviation in the Q factor is approximately 5%, and this remains much smaller than stress-tuning methods, where the Q changes almost an order of magnitude within the tuning range.

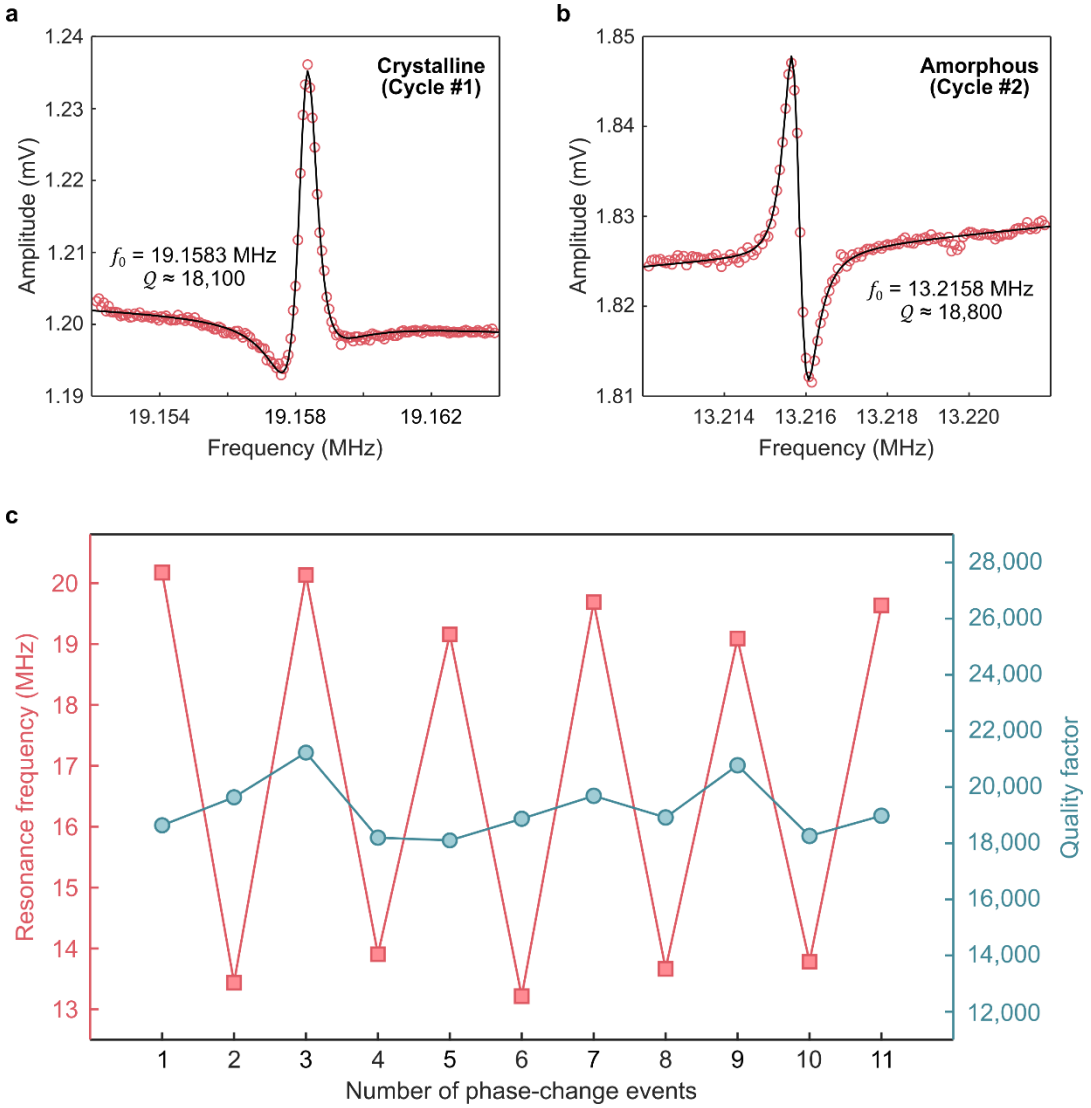


Figure 5.4 Cyclability test of a GeTe nanowire. **a**, Raw experimental data showing the frequency response of the virgin nanowire. **b**, Raw experimental data showing the frequency response of the nanowire amorphized by a 64 pJ pulse. **c**, Evolution of the frequency and the quality factor of the device during 11 phase-change events/cycles.

Relying on the data in Figure 5.4, one can also evaluate spectral tuning performance of the device. Note that crystalline-to-amorphous transformation is the most energy consuming phase transition. Consequently, the tuning energy required per unit Hertz can be calculated as low as ~10.6 aJ Hz^{-1}. In comparison with the theoretical values approximated for thin-film phase-change NEMS resonators [33], this is a 3-fold improvement, which can be attributed to the availability of a non-melting route in phase-change nanowires [37], [105].

5.2.2 Intermediate frequency levels

So far, it has been shown that switching the nanowire between fully amorphous and fully crystalline states can tune the mechanical resonance within a range over 30%. This naturally brings up an interesting question: is it possible to obtain intermediate frequency levels? Unlike thin-film configurations, one can access non-volatile intermediate states in phase-change nanowires reliably along the amorphization pathway [37]. This is owing to the availability of a dislocation-based amorphization mechanism via vacancy condensation in single-crystal nanowires.

Briefly, 50-ns pulses used in the previous section abruptly nucleate the amorphous phase by vigorously accumulating and moving the existing defect sites in the nanowire. Such defect jamming process in phase-change nanowires has first been demonstrated by Nam et al. in 2012 [34]. In order to understand the dislocation dynamics better, Nukala et al. (2014) injected less energetic pulses with durations of 20 ns into GeTe nanowires, so they could controllably accumulate the defects [36]. Note that the most easily formed intrinsic defects in GeTe are Ge vacancies, with a density of ~10^{19} cm^{-3} [144]. With the application of electrical pulses, Ge vacancies condense to from vacancy loops in $\{111\}$ planes as these planes contain only one type of atom.

Here, it is crucial to choose the nanowire growth direction such that the vacancy clusters can easily glide along the carrier-wind force created by electrical pulses. As

such, the authors chose ⟨110⟩ direction as the growth axis. Upon further pulsing, the crystal activates $(111)[1\bar{1}0]$ slip system – which is one of the most easily triggered slip systems in GeTe – and vacancy loops start to propagate and dissociate by leaving antisite defects behind (see Figure 5.5). If the mobility of the dislocation loops decreases during this propagation, e.g. by encountering a defect of a different kind [37], other slip systems can be activated, including the ones that are not in the growth direction. This dramatically increases the local disorder via defect jamming, which in turn nucleates the amorphous phase.

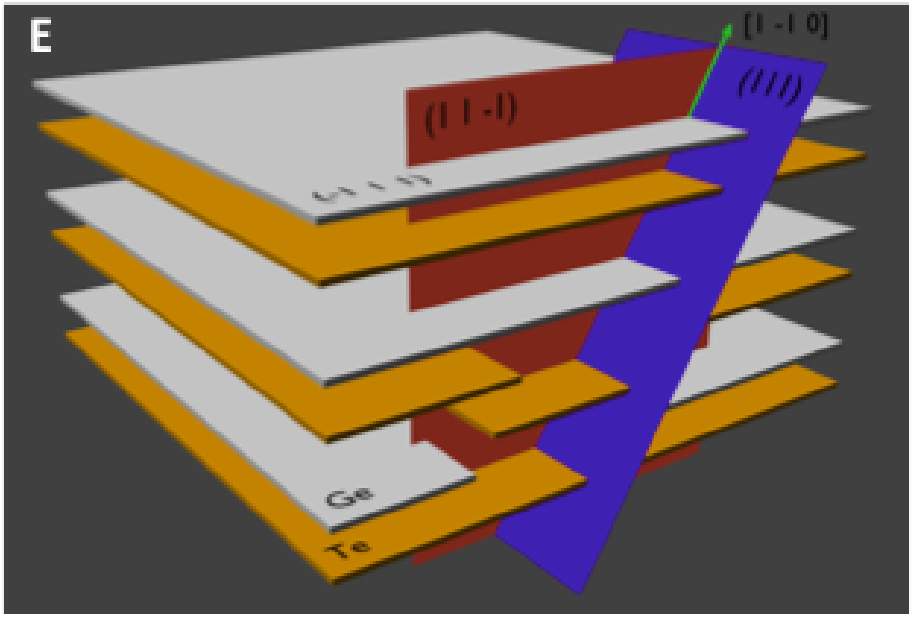


Figure 5.5 Illustration of the dislocation dynamics in $(\bar{1}11)$ plane of a GeTe nanowire, with a Te segment collapsing along the growth direction ⟨$1\bar{1}0$⟩ towards a Ge vacancy cluster. *Reprinted (adapted) with permission from the Supporting Information of [36]. Copyright 2022 American Chemical Society.*

It is insightful to mention that to activate the $(111)[1\bar{1}0]$ slip system in perfect (defect-free) GeTe, the required energy levels are estimated as 340 mJ m^{-2} by density functional theory calculations [36]. This is even lower in GST (~10 mJ m^{-2}) owing to the presence of van der Waals bonds between unit cells [34]. On the other hand, in other covalently-bonded systems such as Si, these energy levels can be as high as 1500 mJ m^{-2}, which demonstrates the unique availability of such electrically-driven structural modification in phase-change alloys [34].

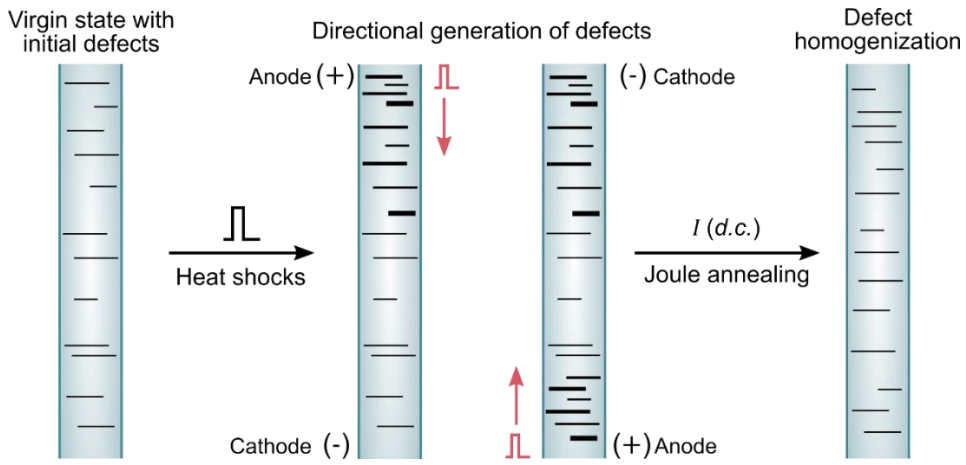


Figure 5.6 Concept of polarity-dependent, pulse-driven dislocation generation/annihilation mechanism in phase-change nanowires. The lines denote local antisites, and a thicker line means higher number of defects.s

The main trigger behind this process is the carrier-wind force. Given that the carrier transport occurs via holes in GeTe, the defects are more likely to be generated near the positive electrode [34]–[36]. Therefore, as previously demonstrated, directional generation of vacancy loops is also possible [34], [39]. In practice, this can be simply done by changing the polarity of pulses. Moreover, the crystallinity can be restored via Joule annealing (direction-independent) [35], [37]. Thus, the overall concept is depicted in Figure 5.6.

In the light of previous findings in the literature, this work investigates the impact of structural modification on the effective Young's modulus for the first time in phase-change nanowires. To that end, resonance frequency of a GeTe nanowire (L = 7 µm, D = 250 nm) has been recorded while injecting low-energy pulses (20-ns each) with increasing amplitudes into the device. As an indicator of microstructural evolution of defects, the *d.c.* resistance of the nanowire is monitored using a source measure unit, which further helps avoid uncontrolled amorphization [34]–[36]. Whenever a significant change is observed in the *d.c.* resistance, the resonance frequency and the resistance of the nanowire has been recorded. The resulting data for this experiment is shown in Figure 5.7, with three distinct resistance regions: state **A** (< 5 kΩ), state **B** (10-15 kΩ), and state **C** (> 20 kΩ).

Initially, the virgin nanowire had a resonance frequency and a resistance of 17.205 MHz and 3.40 kΩ, respectively (beginning of the 1st attempt). During this 1st experiment, the polarity of pulses was alternated while the amplitude was gradually increased at each step (bidirectional pulsing). As such, the exact sequence of pulses used in this experiment was +0.1 V, -0.2 V, +0.3 V, -0.4 V, +0.5 V, -0.6 V, +0.7 V, -0.8 V and +0.9 V. After the first few pulses (state **A**), only marginal shifts were observed in the measurands, i.e. resonance frequency and *d.c.* resistance. The hypothesis here is that the annealing of electrical contacts nanometrically alters the anchoring conditions of the nanowire, which in turn might modify the surface states and the residual stress of the nanowire by either helping more Au atoms diffuse into the device or treating its surface in high vacuum [14], [16]. Thus, for the sake of clarity, the focus will on the pronounced change between states **B** and **C** from this point onwards.

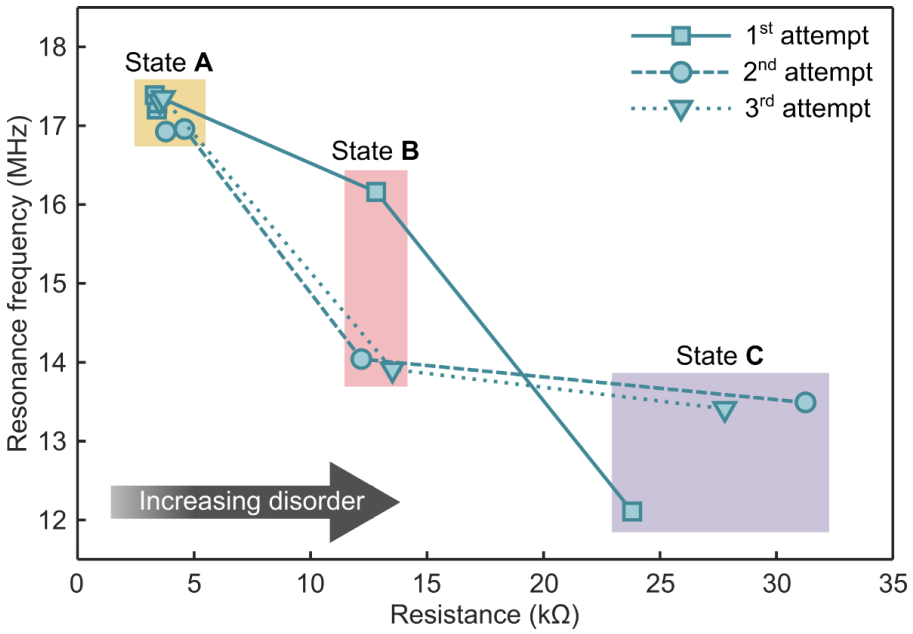


Figure 5.7 Effect of defect generation on the resonance frequency of a GeTe nanowire. The distinctive frequency evolution in the 1st attempt is due to the alternating polarity of pulses (bidirectional pulsing). The polarity is kept constant during the last two attempts (unidirectional pulsing).

The first significant increase in the resistance was observed with a -0.8 V pulse (to 12.82 kΩ). This amplitude level is comparable to those in the literature [37], and such a change in electrical properties is a sign of microstructural modification [34], [36].

Importantly, the resulting resonance frequency is tuned down to 16.161 MHz, which is attributed to the increasing disorder in the nanowire's lattice. The effect is similar to the amorphization case, meaning that the generation of Ge vacancy loops leads to the relaxation of the lattice, softening the effective Young's modulus. Here, note that the long-range order is still crystalline [36]. The next pulse (+0.9 V) increased the resistance to a higher value of 23.80 kΩ, with further tuning of the resonance frequency down to 12.108 MHz. At this stage, no further pulses were applied in order to prevent an unintentional amorphization [37], [105]. To annihilate the defects, the device was annealed by passing a *d.c.* current (~5 μA) through. Thus, the nanowire state was restored back to 16.926 MHz and 3.53 kΩ (state **A**).

In the subsequent experiments (2nd and the 3rd attempts) on this device, the polarity of pulses was kept the same (unidirectional pulsing). The amplitude of pulses was changed from +0.1 to +0.7 V with increments of 0.1 V. These experiments have been performed to study the difference between unidirectional and bidirectional pulsing. During the 2nd attempt, the first considerable shift occurred with a +0.6 V pulse, which moved the nanowire into the state **B** (14.041 MHz and 12.18 kΩ). The following +0.7 V pulse further tuned the nanowire into the state **C** (13.490 MHz and 31.25 kΩ). By annealing (5 μA *d.c.*), the device was recovered once again to state **A**. In the 3rd attempt, the device switched into the states **B** (13.911 MHz and 13.16 kΩ) and **C** (13.412 MHz and 27.78 kΩ) with the application of +0.6 and +0.7 V pulses, respectively.

These experiments reveal some compelling outcomes. Firstly, Joule annealing can thermally erase the memory of the nanowire, reverting the resonance frequency and the resistance very close to the virgin state. This corroborates previous findings in the literature, i.e. thermal instability of the intermediate states [35]–[37]. At room temperature, however, intermediate states have stability levels over 3 years, thus still enabling non-volatile operation [37].

Surprisingly, the tuning efficiency in Figure 5.7 is comparable to the wide-range tuning experiments (Figure 5.3 and Figure 5.4). Here, it is useful to state that the amorphous region in GeTe nanowires is around ~100 nm in length [37]. Therefore, the findings here further confirm that the phase-change tuning is mostly a result of the structural modification described in Figure 5.6 rather than amorphization itself. This also means that the application of 50-ns pulses is a direct way to amorphise the nanowire while contributing to the intermediary dynamics.

The most remarkable result in Figure 5.7 is that the 1st attempt (bidirectional pulsing) leads to a different evolution of resonance frequency compared to the subsequent two experiments (unidirectional pulsing). Meanwhile, in all three attempts, the evolution of resistance is relatively invariant. At this point, the hypothesis is that the resistance is only affected by the number of produced defects whereas the resonance frequency also depends on their distribution along the nanowire. Thus, these experiments extend the knowledge of the defect generation mechanism.

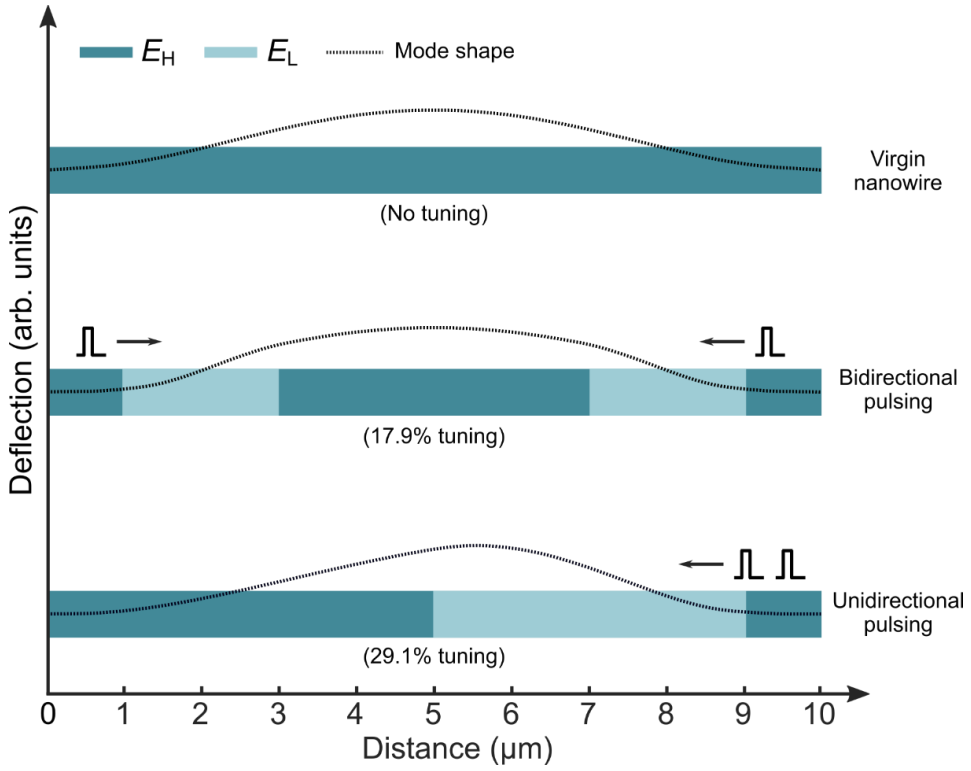


Figure 5.8 Finite-element analysis to investigate the effect of directional pulsing on the tuning efficiency.

In a broader sense, unidirectional pulses alter the nanowire lattice only near the anode, affecting both the resonance frequency and the mode shape more dramatically. Therefore, unidirectional pulsing results in a higher amount of tuning for a similar number of added defects (see state **B** in Figure 5.7). The corresponding finite-element analysis (using COMSOL Multiphysics®) for this case is given in Figure 5.8. The simulations have been performed with a 10 µm-long GeTe nanowire (D = 250 nm). Unaffected regions are considered as fully-crystalline with $E_{\mathrm{H}} = E_{\mathrm{crys}}$ = 86 GPa. The modified (softer) segments of the nanowire lattice are assumed to be 4 µm-long in total, with a lower Young's modulus value of E_{L} = 14 GPa. These values have been estimated from the previous literature [31], [34] to yield similar results to the experimental findings in this work. Also note from Figure 5.8 that the softer portion is equally split on both sides of the nanowire (2 + 2 µm) in the case of bidirectional pulsing.

The simulations yield a resonance frequency of 8.36 MHz for the virgin nanowire. The resonance frequency drops to 6.86 MHz (17.9% tuning) in bidirectional pulsing and to 5.92 MHz (29.1% tuning) in unidirectional pulsing. Referring back to the state **B** in Figure 5.7, the experiments and the simulations both suggest a higher tuning efficiency for unidirectional pulsing for a similar level of defect concentration. It can also be seen from Figure 5.8 that the change in the mode shape is more noticeable in the case of unidirectional pulsing.

Interestingly, the frequency points in the state **C** indicate that the tuning efficiency of unidirectional pulsing decreases as more pulses are injected into the device. Here, it is helpful to mention that the carrier flow in nanowires is one-dimensional, which is analogous to the traffic flow on a crowded highway [34]. According to the analytical model by Lighthill and Whitham describing traffic flow [160], there is a trend that the cars suddenly decrease their mean velocity while entering a congested region. In contrast, the cars can recover their speed only at a much slower rate as they leave the

congested area. Furthermore, this rate is affected by the history of the congestion: the rate decreases if the concentration of vehicles increases.

In GeTe nanowires, bidirectional pulsing leads to a more uniform distribution of the added defects in state **B**. To make an analogy to the traffic flow model, the state **B** of the 1st attempt has a lower amount of electronic congestion on either side of the nanowire. Thus, the carriers from subsequent pulses can propagate through the material more easily and create dislocations more effectively. This corresponds to a superior tuning range as seen from the state **C** of the 1st attempt. The upshot of having such control over the evolution of mechanical resonance is that a single device may produce endless number of tuning profiles with adequate adjustment of the pulsing pattern. Further, each of these pulses takes only 20 ns. This is potentially enabling for unique applications in spread spectrum communications provided that the reproducibility of individual frequency levels as well as the number of cycles are significantly improved in future studies. The applicability of phase-change tuning will be explored in more detail in Section 5.4.2.

5.3 Non-changing quality factors

It has been shown in the wide-range tuning experiments that the Q factors are not influenced by the phase-change events, namely amorphization and re-crystallisation. The variation of Q remains below 5.3% over a broad frequency tuning range of 30%, with no dependence on the crystallinity. Compared with the stress-tuning methods, where quality factors can vary more than an order of magnitude, this is another advantage of phase-change tuning especially in signal processing applications as discussed in Chapters 1 and 2. In this section, the reasons behind this observation will be investigated.

Surface effects and clamping conditions are known to be the most dominant factors in determining the Q of NEMS resonators [16]. This is mainly due to the increased

surface-to-volume ratio of the nano-sized devices. Thus, any change in the resonator's surface conditions or anchoring points directly modifies the quality factor, i.e. $Q^{-1} \approx Q_{\mathrm{clamp}}^{-1} + Q_{\mathrm{surface}}^{-1}$, where Q_{clamp} and Q_{surface} are the clamping-limited and surface-limited quality factors, respectively.

Clamping conditions have been widely studied in micro/nanomechanical systems using the two-dimensional elasticity theory, where Q_{clamp} is approximately given by $(L/D)^3$ in doubly-clamped beams [14], [45], [161], [162]. With the typical device dimensions in this study, this imposes an upper limit of ~30,000 to the Q. Given the measured Q factors are between 16,000 and 21,000 here, the dominance of clamping losses is obvious. On the other hand, it is less straightforward to derive an analytical model for the surface-related losses. Thus, Q_{surface} is usually surmised from experiments [161].

In the light of the experimental findings, it can be hypothesised that the effect of phase-change tuning on both the surface and the clamps should be minimal. To elaborate, it has been demonstrated by previous studies that phase-change events take place in the suspended region, away from the electrical contacts [34], [37]. There are two main reasons for that. Firstly, electric current at the electrode-nanowire interface prefers to flow through the electrode as it is metallic. Secondly, the electrodes – which act as a heatsink – are away from the suspended portion of the nanowire, making it more susceptible to thermal activities. Given that the phase-change is a thermal process, it is self-evident that the clamped segments of the nanowire remain intact upon switching. It can thus be concluded that the clamping conditions between amorphous and crystalline phases should not differ.

Variation of surface tension is also negligible in phase-change nanowires as the stress build-up after amorphization can be easily relaxed at their large surface [38]. In contrast, in PCM thin-films, random formation of amorphous domes via melt-quenching

dramatically modifies the surface stress while raising some reliability issues such as delamination failure or elevated drifting behaviour [38]. Note that the initial residual stress of the nanowire is also expected to be negligible as the nanowire deposition is performed at room temperature (Chapter 3). Given the efficient stress relaxation in phase-change nanowires, this further facilitates the effective Young's modulus calculations (Eq. 4.11) in both phases.

Although the variation of surface tension and clamping conditions has proven to be insignificant in phase-change nanowires, the effect of dislocation-based amorphization on the surface states should be studied in more detail. To this end, nanowires with different growth directions have been measured. As explained in the previous section, GeTe prefers to activate $(111)[1\bar{1}0]$ slip system. To ensure the Ge vacancy clusters glide along the nanowire axis, the growth direction has to be selected carefully in a way that the carrier-wind force facilitates this glide. Otherwise, a non-preferred growth direction, i.e. any direction that is parallel to the family of $\{111\}$ planes such as $\langle\bar{1}1\bar{1}\rangle$, can result in defects randomly moving towards the surface and creating dangling bonds, which in turn degrade the Q factor.

Due to process variations during the growth, there is 15-20% chance of synthesising nanowires with a non-preferred growth direction, i.e. the yield of a preferred growth remains above 80%. The probability here has been estimated from experience during the experiments in this thesis as well as by Ritesh Agarwal and colleagues. This being the case, data for Q factor variation in both cases, i.e. preferred and non-preferred growth directions, is given in Figure 5.9a. The data for the preferred direction case is taken from Figure 5.4. The non-preferred direction case was witnessed while experimenting on another device, whose Q factor degraded gradually down to ~500 after each amorphization pulse (even cycles) and could not be recovered by Joule annealing (odd cycles). Furthermore, the device failed after the eighth cycle.

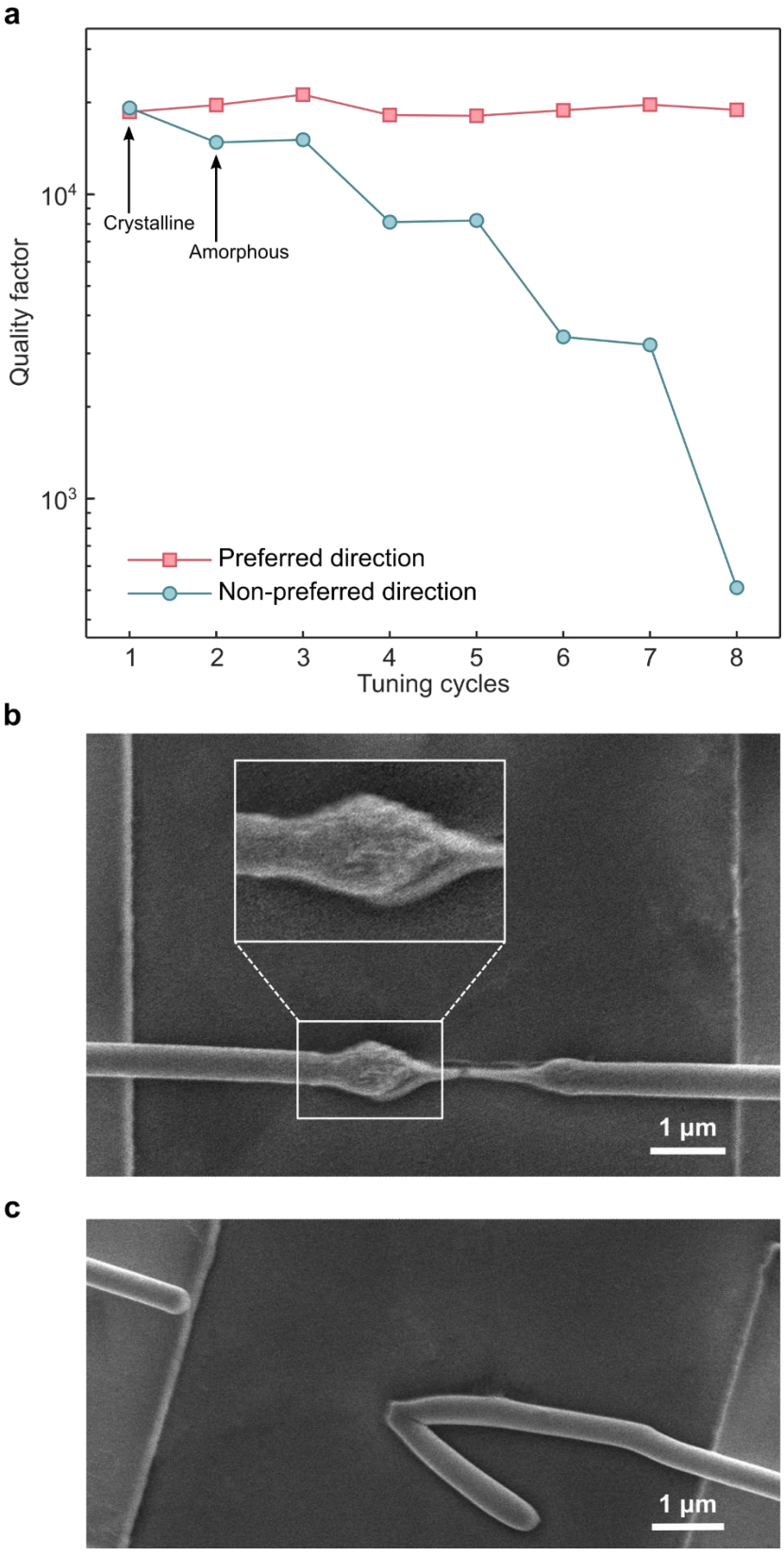


Figure 5.9 Effect of growth direction on Q factors. **a**, Variation of Q during tuning cycles for two different nanowires. Odd cycles are crystalline, even cycles are amorphous. **b**, SEM image of the nanowire with non-preferred growth direction after failure. Inset zooms in for showing the increased surface roughness. **c**, SEM image of the the nanowire with preferred growth direction after failure. The nanowire shows no sign of surface roughness unlike the device in **b**.

The failed device was then imaged under an SEM (Figure 5.9b). As seen, the centre of the suspended portion is tapered down and broken with lumps formed on each side. Inset of Figure 5.9b further shows a zoomed-in image of the lefthand side portion. The image suggests an extremely rough surface. This is a signature of the non-preferred growth direction, whereby the defects escape to the free surface.

Figure 5.9c shows the SEM image of the device with preferred growth direction, which failed after 11 phase-change events (the device in Figure 5.4). From this image, it can be seen that there is no obvious region with increased surface roughness. Besides, the device failure occurred at the anchoring point, i.e. the edge of the electrode. Given that this device had higher contact resistance (refer to Section 5.2.1), the failure is more likely to be caused by ESD rather than a microstructural issue. It could also be hypothesised that the region where this device is bent might be amorphous due to the lower E, however, further study is required to support this. Overall, combined with the findings Figure 5.9a, this further validates the dominance of surface effects in NEMS. Therefore, if the nanowire growth direction is chosen carefully, the defects can be dissociated and annihilated before reaching the surface, preserving the Q factor during the phase-change events.

5.4 Real-time frequency tracking

Up to this point, long-term behaviour of phase-change NEMS devices have been investigated by switching between the transduction (Figure 4.4) and the tuning (Figure 5.2) setups manually. However, this is not robust enough to capture short-term response of the resonators such as real-time frequency tracking or transient dynamics of phase-change tuning. Thus, the need for combining these measurement setups is obvious. Figure 5.10 shows the schematic of the combined measurement setup, which utilises an RF switch (Mini Circuits ZFSWA-2-46). The RF switch stays in state ‘1’ by default, enabling piezoresistive sensing. For electrical tuning, the switch is transiently

brought to state ‘2’, which connects the pulse generator directly to the nanowire. The switch is controlled by another pulse generator (Tektronix AFG3102C).

For real-time frequency tracking, phase-locked loop (PLL) configuration of the lock-in amplifier is utilised. Briefly, PLLs try to match the frequency and phase of a reference signal with the frequency and phase of a loop oscillator. A negative feedback loop in frequency domain is essential for PLLs, and the loop consists of a phase detector, a loop filter (low-pass), and a voltage-controlled oscillator (VCO). If the generation of integer/non-integer multiples of the reference signal is desired such as in frequency synthesis, frequency dividers (by N) can be added to the feedback path and/or the feedforward path. As such, a simple logic diagram of a PLL-based frequency synthesiser is given in Figure 5.11.

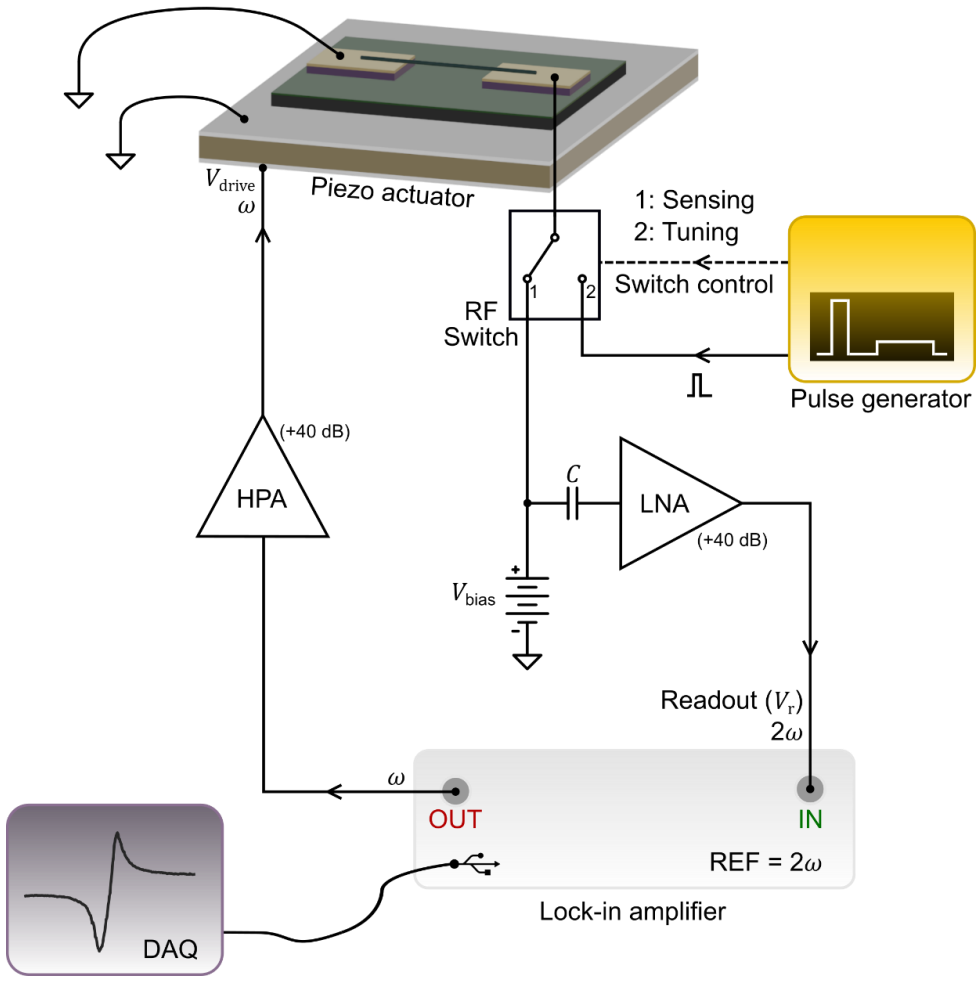


Figure 5.10 Combined tuning and transduction setups for real-time measurements.

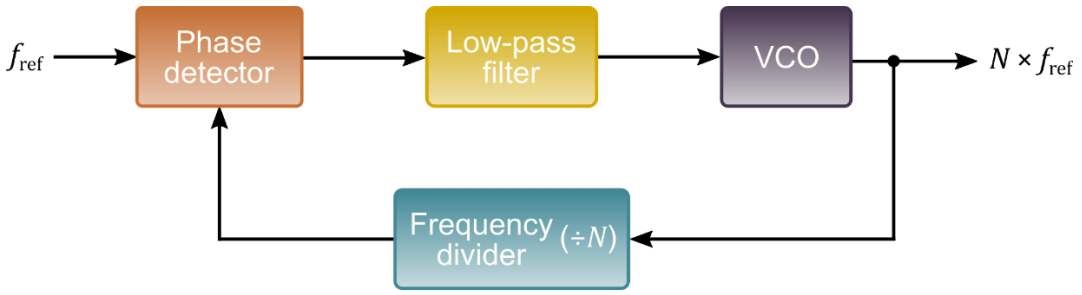


Figure 5.11 A simple PLL configuration. The reference signal has a frequency of f_{ref}.

The loop filter sets the PLL bandwidth, which determines how fast the output frequency tracks the reference, i.e. larger bandwidth leads to faster locking. The lock-in software by Zurich Instruments offers an advisor functionality to determine the required feedback parameters for a given bandwidth. Here, the feedback parameters are in digital domain, hence the calculation optimises the PID coefficients. This PLL module further offers a feature called subharmonic detection, which forces the PLL to lock into half the reference frequency. Given the frequency-doubling effect, this significantly facilitates frequency tracking directly from the piezoresistive readout.

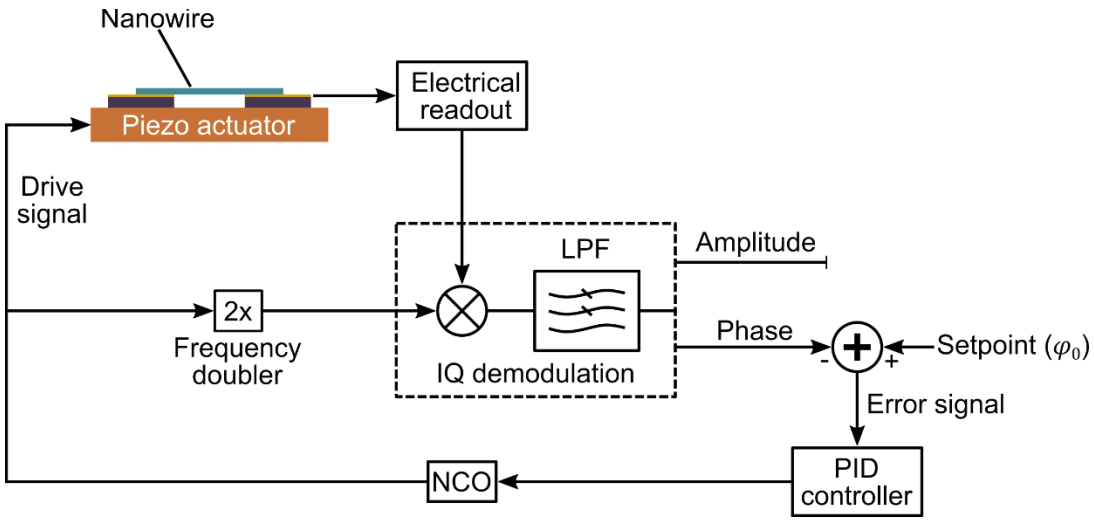


Figure 5.12 Interfacing of the NEMS setup with the PLL (subharmonic detection of f_0).

A simplified diagram that interfaces the NEMS resonator with the PLL (with the subharmonic detection enabled) is depicted in Figure 5.12. Electrical readout from the resonator is demodulated by the lock-in amplifier. As a result of the IQ demodulation, the output is in the polar form, i.e. amplitude and phase. The PID controller takes the

phase output from the demodulator and tries to match it with a predetermined setpoint φ_0, minimising the error. The controller achieves this by adjusting the numerically-controlled oscillator (NCO) – which is the digital version of a VCO. The NCO then drives the NEMS resonator via piezo actuation. Note that the reference signal to the demodulator is at double the ferquency of the NCO. This is known as subharmonic detection, which compensates for the frequency-doubling effect. Consequently, the NCO output follows the the mechanical resonance of the NEMS device. Such combinations of mechanical resonators with PLLs have been widely used in literature from characterising phase noise [91] to designing frequency synthesisers [12].

5.4.1 Phase noise measurements

Phase noise is a measure of short-term stability of a frequency reference and commonly denoted by dBc Hz^{-1} (decibels below the carrier per Hertz) [163]. For example, if the signal from a local oscillator has excessive phase noise, it fluctuates more around the oscillation frequency and interferes with other carriers in the vicinity, resulting in an inferior demodulation performance.

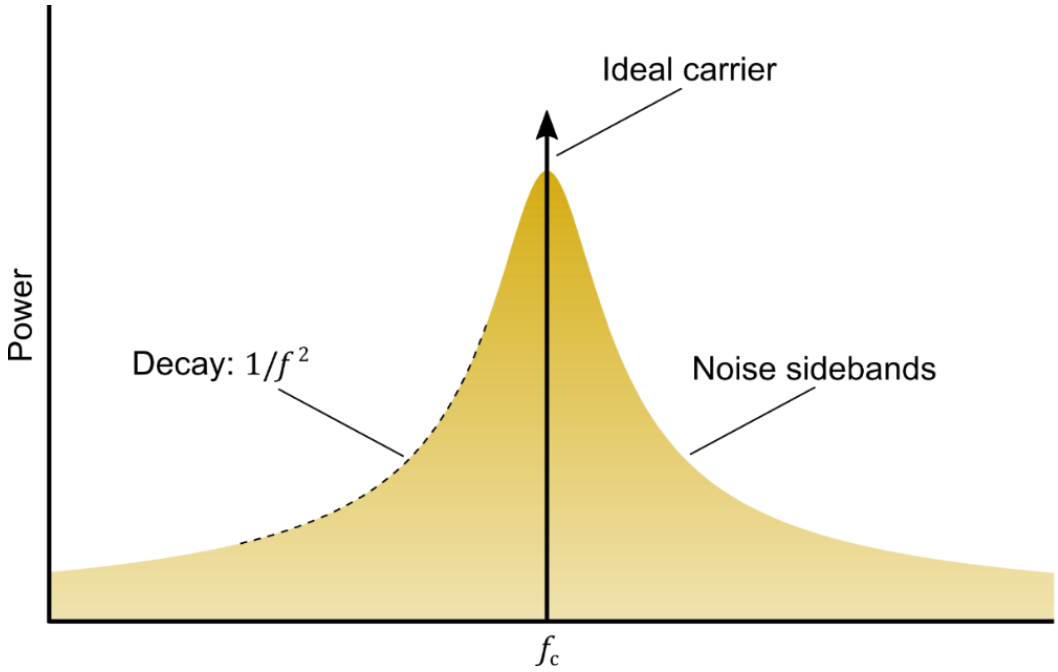


Figure 5.13 The concept of phase noise.

The frequency response of a carrier with phase noise is further depicted in Figure 5.13. Here, the carrier frequency (f_c) is from a mechanical resonator, and the noise sidebands ideally follow the Lorentzian with $1/f^2$ decay, where f is the offset frequency from f_c. Such Lorentzian behaviour arises when the noise is purely thermomechanical [14]. In practice, however, there are additional sources of noise such as electrical noise from instruments and devices as well as environmental noise, e.g. temperature fluctuations. As a result, the actual resonance spectrum deviates from the Lorentzian and may contain spurious frequency components.

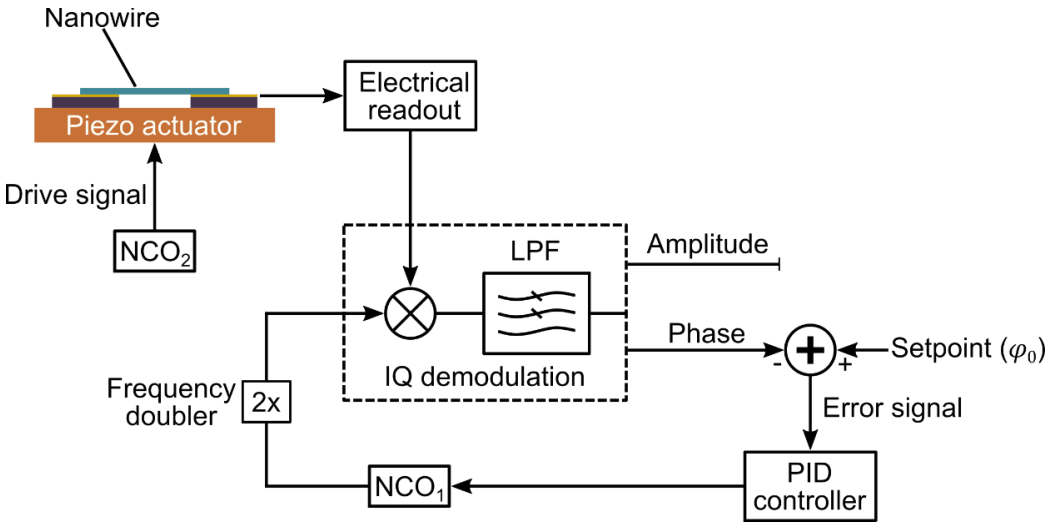


Figure 5.14 Open-loop configuration of the PLL setup for phase noise measurements.

Note that the setup in Figure 5.12 is ideal for creating a local oscillator as the feedback loop further stabilises the resonator dynamics [24]. However, if one wants to measure intrinsic (thermomechanical) phase noise behaviour of a resonator, a slight modification is needed. To that end, a new setup is designed to break the feedback loop by exploiting two independent NCOs within the lock-in amplifier (see Figure 5.14). NCO_1 is locked into the resonance frequency via subharmonic detection while the resonator is manually driven by NCO_2. This way, the resonator is actuated at a constant frequency, so the true phase characteristics of the device can be revealed. Note that the phase noise of the NCOs within the lock-in system is significantly lower than that of a typical NEMS resonator as provided in the datasheet [164], thus HF2LI

is suitable for characterising thermomechanical phase noise. It should also be mentioned that such open-loop measurements using the this lock-in system have been successfully performed in the NEMS literature before [91].

Prior to the measurements, determination of the loop bandwidth of the PLL is crucial. A large bandwidth will lead to excessive noise leakage into the measurement while a lower value may not be fast enough to capture the required phase noise information. At this point, an approximation can be made from Eq. 5.1, which gives the ultimate phase noise $S_\varphi(f)$ attainable from a high-Q NEMS resonator:

$$S_\varphi(f) = \frac{k_\mathrm{B}T}{4P_\mathrm{c}Q^2}\left(\frac{f_\mathrm{c}}{f}\right)^2 \qquad 5.1$$

Here, k_B is the Boltzmann constant, T is the temperature, and P_c is the carrier power [155]. Note that the carrier frequency f_c is the same as mechanical resonance f_0. According to the stringent GSM requirements, phase noise of a frequency reference should be better than -120 dBc Hz^{-1} at 1 kHz offset [64]. By substituting typical values obtained during the experiments with GeTe nanowires (e.g. f_0 = 20 MHz, Q = 19,000, and P_c = 1.6 nW) into Eq. 5.1, the device can theoretically achieve -120 dBc Hz^{-1} even at 500 Hz offset. Therefore, the loop bandwidth of the PLL is chosen as $f_{\mathrm{cut-off}}$ = 500 Hz.

For the measurements, a 7 µm-long GeTe nanowire (D = 240 nm) is used. Resonance frequency of the nanowire is measured as f_{cry} = 16.662 MHz (Q = 19,200) in the crystalline phase and f_{amo} = 11.190 MHz (Q = 19,000) in the amorphous phase. By following the step-by-step procedure given below, phase noise of the resonator has been obtained:

i. From the measured resonance spectrum, phase of the electrical readout at f_0 is determined in order to define the PLL setpoint.

ii. NCO_2 is driven at f_0 to yield P_c = 1.6 nW (on a 1Ω resistor), and NCO_1 is made sure to lock into the same frequency using the PLL setup in Figure 5.14.

iii. Phase of the relevant demodulator is recorded for 20 seconds at a sampling rate of 28.782 kHz. Alternatively, one can record the frequency of NCO_1 or the phase error from the PLL.

iv. Power spectral density of the (mean) phase data is calculated in MATLAB via *pwelch* function, using a Hanning window.

v. The resulting spectrum is divided by two and plotted in $10\log_{10}(\cdot)$ scale in accordance with the IEEE Std 1139-2008, i.e. $\mathcal{L}(f) = S_\varphi(f)/2$.

Subsequently, the phase noise $\mathcal{L}(f)$ of the device is given in Figure 5.15, together with the thermomechanical and white (Johnson) noise limits (Eq. 5.1). As expected, white noise sources dominate the resonator's phase noise behaviour, leaving around 30 dB of headroom for improvement in the experiment, e.g. the noise matching between the resonator and the external circuitry can be revisited [163]. In terms of Johnson noise, it is worth noting that the equivalent resistance seen at the LNA input, i.e. $R_s \parallel R$ (from Figure 4.5), is ~50 Ω in both amorphous and crystalline states (R_s = 50 Ω and $R \gg R_s$), leading to a noise voltage of 1 nV $Hz^{-1/2}$ at the LNA input. Given that the noise figure of the LNA is 1 dB (from the datasheet of MITEQ AU-1442), this translates into a noise power of -108 dBm at the lock-in input within 1-Hz bandwidth. As P_c is -75 dBm, this gives rise to a phase noise of -33 dBc Hz^{-1} at f = 1 Hz, which substantiates the headroom and shows the importance of white noise sources [165].

In the crystalline state, the noise spectrum shows $1/f^3$ dependency at lower frequencies due to flicker noise ($1/f$) [163], which is associated with the *d.c.* current ($I_{\mathrm{noise}} \propto {I_{\mathrm{DC}}}^{0.5}$) [166]. This is anticipated because the *d.c.* current is higher in the crystalline state under the same bias voltage. The spurious component at 50 Hz is a result of the power line noise, which can be avoided by using battery-powered

components in the experiment. In addition, the effect of the PLL bandwidth (PLL BW) can be seen at higher frequencies, manifesting itself as a knee at $f_{\mathrm{cut-off}}$ = 500 Hz.

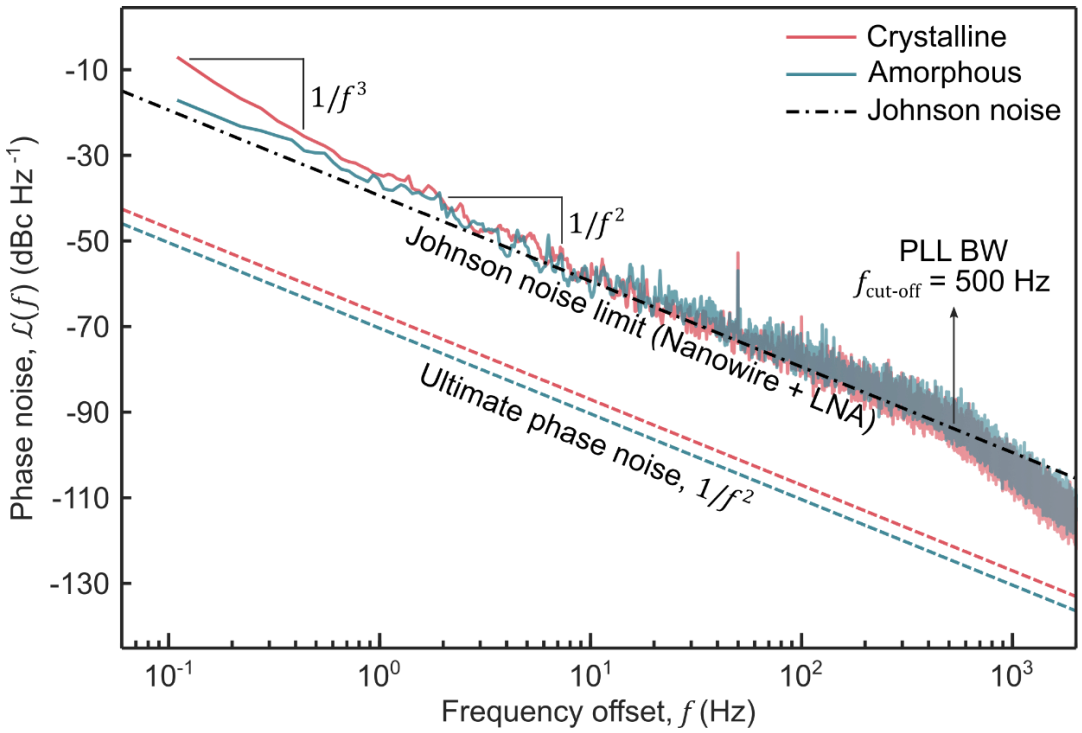


Figure 5.15 Open-loop phase noise measurements of the resonator in amorphous and crystalline states (solid lines). The dashed lines of the relevant colours show the ultimate (thermomechanical) limit for the phase noise. The black (dashed-dotted) line shows the Johnson noise limit accounting for the device resistance and the non-ideal LNA.

Overall, the phase noise of the device compares favourably to quartz crystal oscillators as well as Si nanowires and graphene oscillators in both states [17], [64], [165]. Excitingly, the carrier power level used in these measurements (P_c = 1.6 nW) shows a significant improvement of at least 6 orders of magnitude compared to quartz-based oscillators [5]. Combined with non-volatile tunablity and non-changing Q factors of the phase-change nanowires, such a performance can open up new possibilities in communication technologies, which will be elaborated in the next section.

5.4.2 Frequency-hopping via phase-change tuning

Traditionally, frequency synthesis is achieved by feeding a constant and stable reference clock from a quartz-based local oscillator (LO) into a PLL. Integer/non-

integer multiples of that reference is then generated via frequency dividers (counters) placed on the feedback and the feedforward paths as discussed previously. Although this method of frequency synthesis is the mainstream technology in today's telecommunication electronics, it constitutes major concerns for future applications [6], [8].

Quartz crystals are bulky, which raises integration and power consumption issues. Besides, they are non-tunable, requiring frequency dividers in the PLL loop. At this point, it is crucial to state that the use of frequency dividers on the feedback path impairs the phase noise, i.e. the phase noise is multiplied by the integer divider N (see Figure 5.11) [8]. Such frequency multiplication further prolongs the lock time as the feedback loop has to wait for the frequency dividers to finish counting. In effect, this lowers the PLL bandwidth and reduces the tuning speed [8]. Therefore, just by eliminating the frequency dividers, one can improve both the phase noise performance and the tuning speed.

Elimination of frequency dividers requires a modification to the frequency reference. Indeed, the need for an inherently-tunable reference source with non-changing performance parameters is evident. In the light of the experimental findings in the previous sections, phase-change nanowires seem to be one of the best candidates for designing such frequency synthesisers. To that end, the combined tuning and transduction setup in Figure 5.10 is interfaced with the PLL setup in Figure 5.12. The PLL bandwidth is selected as 30 kHz during these experiments for faster locking. The resulting LO with tunable NEMS reference is schematised in Figure 5.16. In this configuration, the RF switch still serves as an isolator between the setups. When the tuning of f_0 is desired, the switch is momentarily brought to state '2' for 1 µs, and a tuning pulse is injected into the device. At the end of 1 µs, the device is brought back to state '1' for subharmonic detection of f_0. The generated LO frequency ($f_{\mathrm{LO}} = f_0$) is then inputted to a frequency-hopping spread spectrum (FHSS) radio prototype. Note

that in this experiment, the NEMS device only acts as a local oscillator, and the AM modulation is performed by an external mixer that multiplies the NEMS readout with the data signal (i.e. audio).

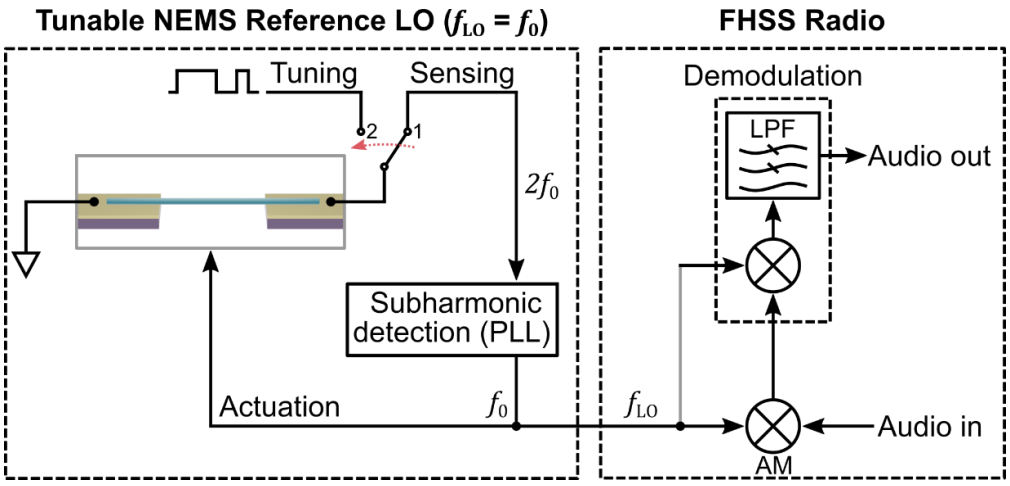


Figure 5.16 Application of phase-change NEMS as a tunable local oscillator in FHSS systems. AM stands for amplitude modulation.

Spread spectrum communications dates back to 1903, when the basic idea was patented by Nikola Tesla [167]. In essence, the concept relies on expanding the actual bandwidth of radio signals beyond what is necessary to transmit data while offering significant benefits in supressing interference (e.g. multiple access, multipath fading, and hostile jamming) and assisting GPS [168]. One way to spread the spectrum of radio signals is to rapidly change its carrier frequency in a pattern that is known to both transmitter and receiver. This technique is known as FHSS, and it has seen a renewed interest mainly with the intention to proliferate massive IoT networks [9]. Here, phase-change NEMS could be enabling in unprecedented ways by reducing design complexity, power consumption, and tuning (hopping) speed, thus reviving FHSS systems that strongly depend on frequency synthesis.

The LO is designed using a GeTe nanowire (L = 8 µm, D = 250 nm) as a tunable frequency reference, which has f_0 = 13.083 MHz in its virgin state. Before starting the experiment, the *d.c.* bias current across the nanowire was switched off, and the LO lost track of the reference frequency, validating the nanomechanical resonance. For

hopping the transmission channel, 20 ns – 500 mV pulses were used for softening the nanowire, and 250 ns – 500 mV pulses were used for re-crystallisation. In accordance with 47 CFR § 15.247 regulations [158], the period between two tuning pulses was set to 400 ms. Here, one re-crystallisation pulse follows three softening pulses in each cycle. As such, within a total of four cycles, 16 frequency levels have been obtained. To characterise the levels, the LO frequency has been tracked in real-time with a sampling period of ~2.17 µs (minimum value attainable from the lock-in amplifier). Analysis of 16 frequency levels results in four distinct frequency channels (f_{1-4}) as seen in Figure 5.17a, with a maximum frequency deviation of ±14 kHz for channel f_3.

From the real-time tracking data, the tuning speed can also be estimated. Figure 5.17b shows the data for a re-crystallisation step, which is the largest and longest tuning step in this experiment. To reiterate, the RF switch connects the pulse generator to the nanowire for only 1 µs. Thus, the tuning pulse was applied between point **a** and point **b**, meaning that the LO frequency jumped from one state to the other within one sampling period (~2.17 µs). Compared to the state-of-the-art PLL synthesizers, this is an order of magnitude improvement in tuning speed, significantly reducing system cost and complexity [6].

For data transmission through the FHSS radio, a four-second segment of Guglielmo Marconi's speech given on 14 December 1930 (*SA 27/9/1 Side B by Essex Record Office*) is chosen. The audio sample was reproduced with a sampling rate of 8 kHz and up-converted (i.e. amplitude modulation) using a double-balanced mixer (Mini-Circuits ZLW-1-1+). Coherent demodulation was performed by the lock-in amplifier, with its demodulation bandwidth set to 88.39 kHz. To prevent aliasing, the received signal was sampled at 460.53 kHz. Finally, the demodulated signal was decimated to its original sampling rate (~8 kHz). As shown in Figure 5.17c, the LO frequency could be switched by dynamically changing the phase of the nanowire, which allows reliable transmission of the audio signal through four distinct channels.

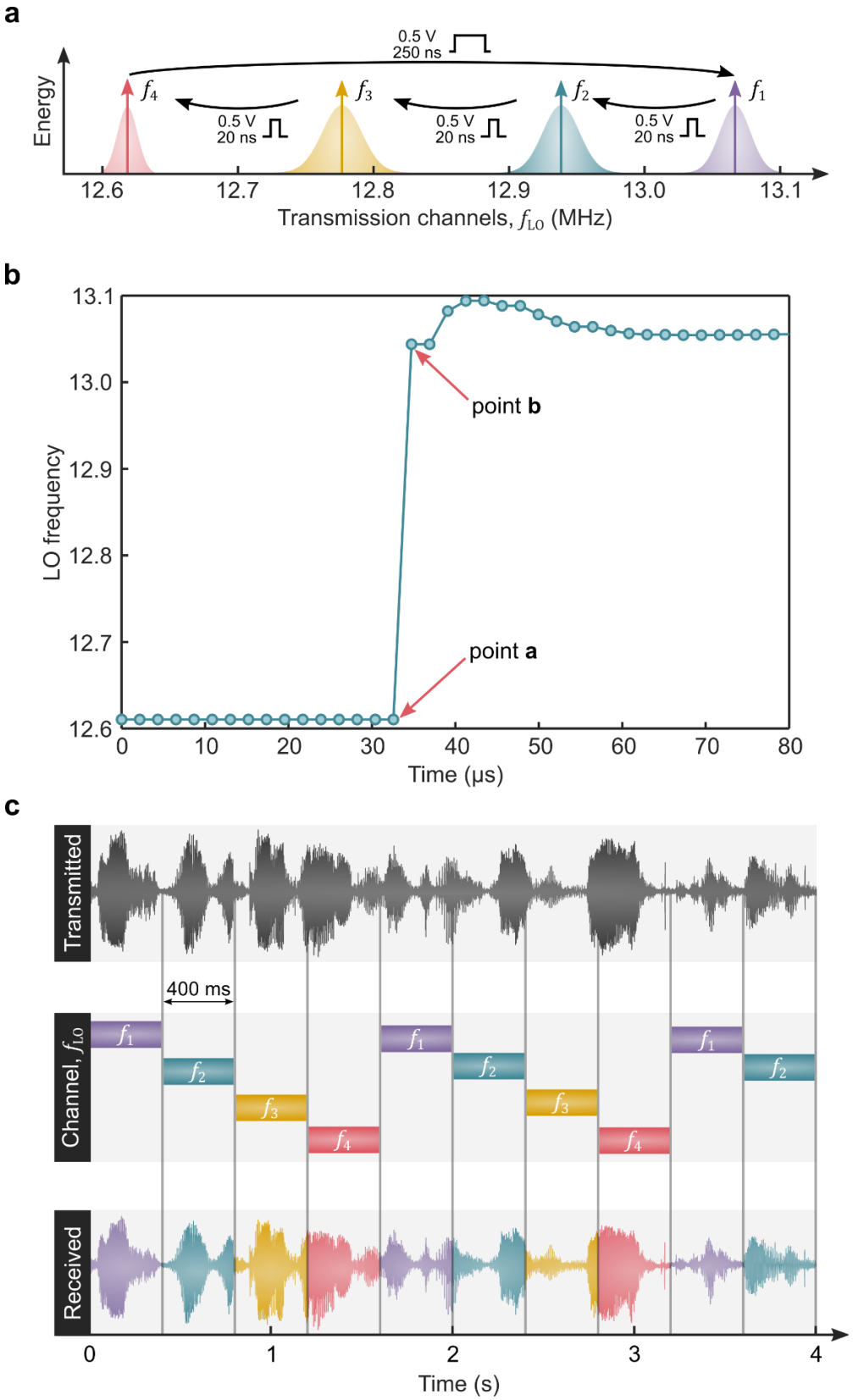


Figure 5.17 Real-time analysis of the frequency hopping sequence and its utilisation in a radio prototype. **a,** Channel statistics suggest f_1 = 13.067 ± 0.011 MHz, f_2 = 12.938 ± 0.013 MHz, f_3 = 12.777 ± 0.014 MHz, and f_4 = 12.624 ± 0.006 MHz. **b,** Real-time LO frequency tracking data for the largest and longest tuning step, i.e. re-crystallisation. **c,** Transmitted and received audio segments together with the real-time frequency hopping sequence.

Remarkably, the experiment here demonstrates the feasibility of using phase-change NEMS in order to solve an engineering problem by eliminating the need for frequency dividers. In a real-world scenario, however, some improvements are needed. For example, the configuration in Figure 5.16 uses the same LO frequency at both ends of the communication channel for the sake of simplicity. In practice, transmitter and receiver will be using two different nanowires as reference due to the lack of physical contact. Thus, synchronisation of these frequencies is crucial. To this end, practically identical nanowires (of similar f_0) can be employed on both sides. For further frequency trimming, high-energy ion irradiation can be utilised to introduce permanent defects into the nanowires without affecting their unique structural evolution dynamics [37].

It can also be noticed that the tuning resolution in this experiment is much finer than the results in Figure 5.7. This is due to the differences between experimental methods. Note that in Figure 5.7, the resonance frequency is recorded whenever a significant change is observed in the *d.c.* resistance. Here, the hypothesis based on the former TEM studies on GeTe nanowires is that each heat shock sent into the nanowire causes a structural modification but not a measurable modification to the electrical states [35], [36]. Therefore, some of the intermediate frequency points may have been disregarded during the experiments in Figure 5.7. This is further promising in terms of achieving a continuous tunability within the wide tuning range without even amorphising the nanowire.

Using the findings in Figure 5.17a, one can show the feasibility of obtaining 30 intermittent frequency levels (with an estimated channel spacing of 130 kHz), which even satisfies the current requirements for the low-rate wireless area networks (the IEEE 802.15.4 standard). At this point, it should be mentioned that the minimum transmission power required by the IEEE 802.15.4 standard is -3dBm. On the other hand, the carrier power used in this study is -75 dBm, corresponding to an amplification

requirement of over 70 dB, which is one of the biggest obstacles hindering the proliferation of NEMS in integrated circuits. Also note that increasing the drive power is not a viable solution in NEMS due to their limited dynamic range (Eq. 4.14). Thus, this gain difference should be compensated by either using a cascade of amplifiers (which impairs the phase noise) or improving the transduction gain via an alternative readout method. To show the feasibility of the latter, a fully-integrated photonic transduction scheme will be presented for single-crystal nanowires for the first time in Chapter 6, which could completely mitigate the abovementioned gain requirement.

Finally, the cyclability of the devices used in this thesis is not sufficient for commercialisation, i.e. the maximum number of frequency states obtained from a single device was 16, which was during the experiment in Figure 5.17. This should be addressed in future work. Perhaps, encapsulating the nanowires in an ultra-thin dielectric layer (e.g. via atomic layer deposition) or investigating different alloys could mitigate this issue.

5.5 Conclusions

To conclude, a novel tuning technique for NEMS resonators has been demonstrated in this chapter, using phase-change nanowires of GeTe. With the application of nanosecond-fast electrical pulses, it has been shown that the effective Young's modulus of GeTe nanowires can be actively modulated, which in turn tunes the mechanical resonance. The tuning range is over 30% between amorphous and crystalline phases, and no power is required to maintain the tuned frequency as the tuning mechanism is non-volatile. Multi-frequency operation has also been demonstrated via a dislocation-based, non-melting route achieved by injecting 20-ns electrical pulses into the nanowire.

Owing to the unique phase transformation dynamics, the high Q factors of these nanowires do not change upon phase-change, which is a great advantage over

traditional stress-tuning schemes, enabling constant selectivity and consistent phase noise performance at any frequency state. A giant piezoresistive gauge factor of 1,100 has also been unveiled in the amorphous state, further facilitating monolithic integration of these devices. Moreover, these devices offer a novel way of frequency synthesis, eliminating the need for frequency dividers in PLL synthesisers. This could simultaneously reduce the system complexity, power consumption, and tuning speed. If the cyclability of these devices are improved to meet the commercial standards, phase-change NEMS can be the ultimate building blocks in mechanical signal processing applications.

Chapter 6

Improving the readout by photonic integration

The findings presented in Chapters 3 & 6 have been published in:

Utku Emre Ali, He Yang, Vladislav Khayrudinov, Gaurav Modi, Zengguang Cheng, Ritesh Agarwal, Harri Lipsanen, Harish Bhaskaran, *"A Universal Pick-and-Place Assembly for Nanowires",* Small 2201968 (2022). DOI: 10.1002/smll.202201968

6.1 Overview

Previous chapters have demonstrated, for the first time, a non-volatile tuning method in NEMS enabled by phase-change nanowires of GeTe. However, real-world applications require much higher signal power levels as discussed earlier. To that end, Chapter 6 investigates the feasibility of further improving the readout amplitude in nanowire systems via photonic integration. As such, Section 6.2 summarises the field of integrated photonics together with the design and characterisation of grating couplers and microring cavities for telecommunication wavelengths. By interfacing an InP nanowire (lossless at these wavelengths) with the photonic elements, Section 6.3 develops a theory for the cavity optomechanics of dielectric nanowires and presents experimental results regarding the displacement sensitivity and transduction gain.

6.2 Integrated photonics

The popularity of photonics has begun with the replacement of electrical wires with optical fibres in telecommunications technology [169]. Photons are massless and chargeless particles and not subject to capacitive/inductive effects unlike electrons. Therefore, photons at different wavelengths can be multiplexed through the same medium with negligible crosstalk, enabling massive parallelisation. In the late 1980s, first integrated photonic devices on a silicon-on-insulator (SOI) platform were introduced by Soref and Lorenzo, with the capability of working at telecommunication wavelengths (1.3–1.6 µm) [170]. Since then, SOI devices have been employed in various applications, some of which include low-loss waveguides, photonic crystals, microring resonators, high-speed modulators, and photodetectors [123], [171], [172]. Such wide-spread use of SOI platforms is owing to the high refractive index and ultra-low loss of silicon in telecommunication bands. However, when low-loss operation is needed in the visible spectrum, silicon nitride and aluminium nitride platforms are highly preferred owing to their large bandgaps that enable low-loss operation at wavelengths ranging from deep-UV to far-IR [172].

As important as the design of these highly-functional devices, interfacing them with off-chip light sources and photodetectors has also been intensely studied. In the next section, these coupling techniques will be elaborated, together with the performance of the fabricated devices.

6.2.1 Fibre-to-chip coupling

One of the persistent challenges in integrated photonics is the coupling of light guided in a fibreoptic cable from and into a nanoscale device, mainly because of the large mode mismatch between them. A decent coupler should maintain a low insertion loss over a wide bandwidth. Commonly, there are two approaches when designing photonic couplers: in-plane and out-of-plane methods. In-plane coupling is based on inverse

tapers that delocalise the optical mode at the edge of the chip (Figure 6.1a). To enlarge the mode-field size of the rectangular waveguide, a larger over-cladding core is added over the waveguide taper. This method is called as edge coupling, which can achieve insertion losses below 0.5 dB over a wide wavelength range [173]. However, edge coupling suffers from tedious fabrication and alignment steps, thus making it harder to characterise large-scale devices repeatably.

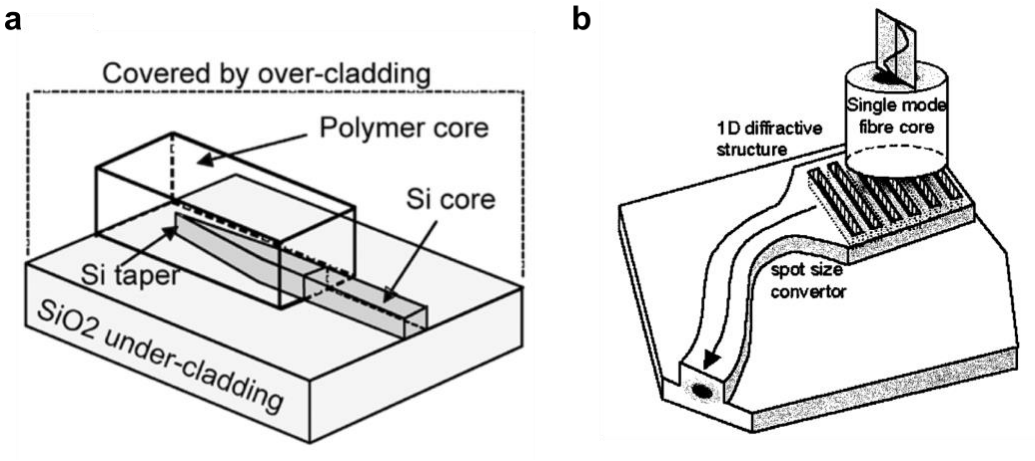


Figure 6.1 Fibre-to-chip coupling approaches based on **a**, edge coupling (in-plane) [123] (© 2022 IEEE) and **b**, grating couplers (out-of-plane) [173] (© 2022 IEEE).

Out-of-plane coupling techniques mainly make use of Bragg gratings with periodic refractive index perturbations, e.g. Si-gap-Si alternations, which minimise mode mismatch at certain wavelengths and incident angles [173] (Figure 6.1b). Grating couplers can offer high density integration because they can be placed anywhere on the chip, speeding up wafer-scale testing. Using CMOS-compatible fabrication techniques, it is possible to achieve an insertion loss of ~5 dB within a few 10-nm bandwidth [174]. Recently, hybrid approaches based on 3D direct laser writing have become popular. Gehring et al. have demonstrated near-adiabatic out-of-plane mode converters (1.8 dB loss) using IP-Dip resist in Nanoscribe on a silicon nitride platform that can operate over 0.8-1.7 µm wavelengths [175]. This method combines the practicality of gratings with the low-loss and wideband operation of edge couplers, facilitating rapid prototyping and packaging of functional photonic components.

Given the aim in this chapter is to develop a transduction technique for nanowires, the couplers have been made of fully-etched Bragg gratings for facile fabrication in a single lithography step. Though, the use of 3D-printed couplers is also encouraged for future work. Silicon nitride is selected as the photonic platform owing to its lower refractive index at telecommunication wavelengths (n_{SiN} ~ 2), yielding a stronger evanescent field compared to silicon (n_{Si} ~ 3.5). Thus, the geometry has been chosen as fully-etched (ridge) waveguide ($n_{\mathrm{waveguide}}$ = 2) with no cladding (n_{vacuum} = 1) over a SiO_2 substrate ($n_{\mathrm{substrate}}$ = 1.46) as shown in Figure 6.2a.

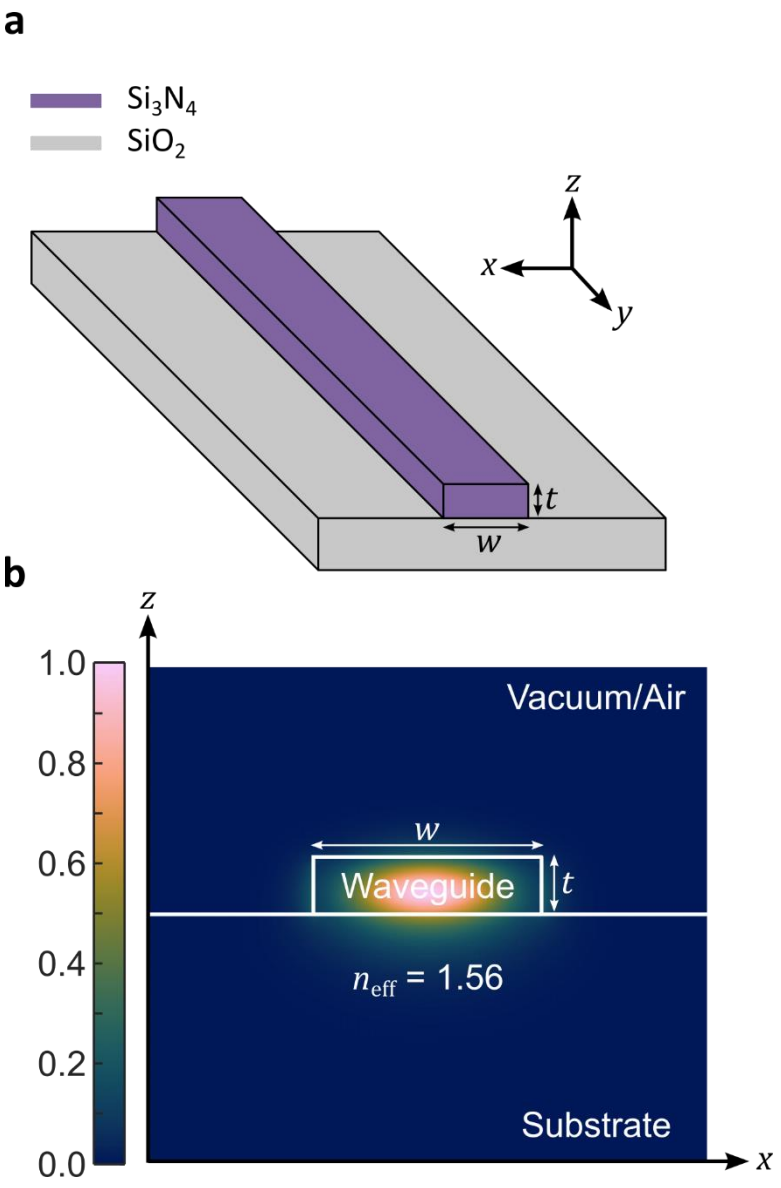


Figure 6.2 Si_3N_4 waveguide design. **a**, Geometry of the ridge waveguide. **b**, Mode simulations showing the normalised $\mathcal{E}$-field intensity of the (fundamental) TE mode of the waveguide.

Gratings have been optimised through a fabrication-based approach rather than using FEM analysis. To pick an optimisation range for the grating period, Bragg condition have been used:

$$\Lambda = \frac{\lambda_C}{n_{\text{eff}} - \sin\theta_i} \tag{6.1}$$

Here, Λ is the grating period, λ_C is the centre wavelength, n_{eff} is the effective mode index, and θ_i is the incident angle. Using mode simulations in Lumerical (Figure 6.2b), n_{eff} has been calculated as 1.56 at the fundamental (transverse electric, TE) mode with a width of w = 1.3 µm and a thickness of t = 0.33 µm. The incident light will be delivered by a fibre-array equipped with SMF-28 fibres that have a polishing angle of 8º (see Figure 6.3a), hence θ_i = 12º in air.

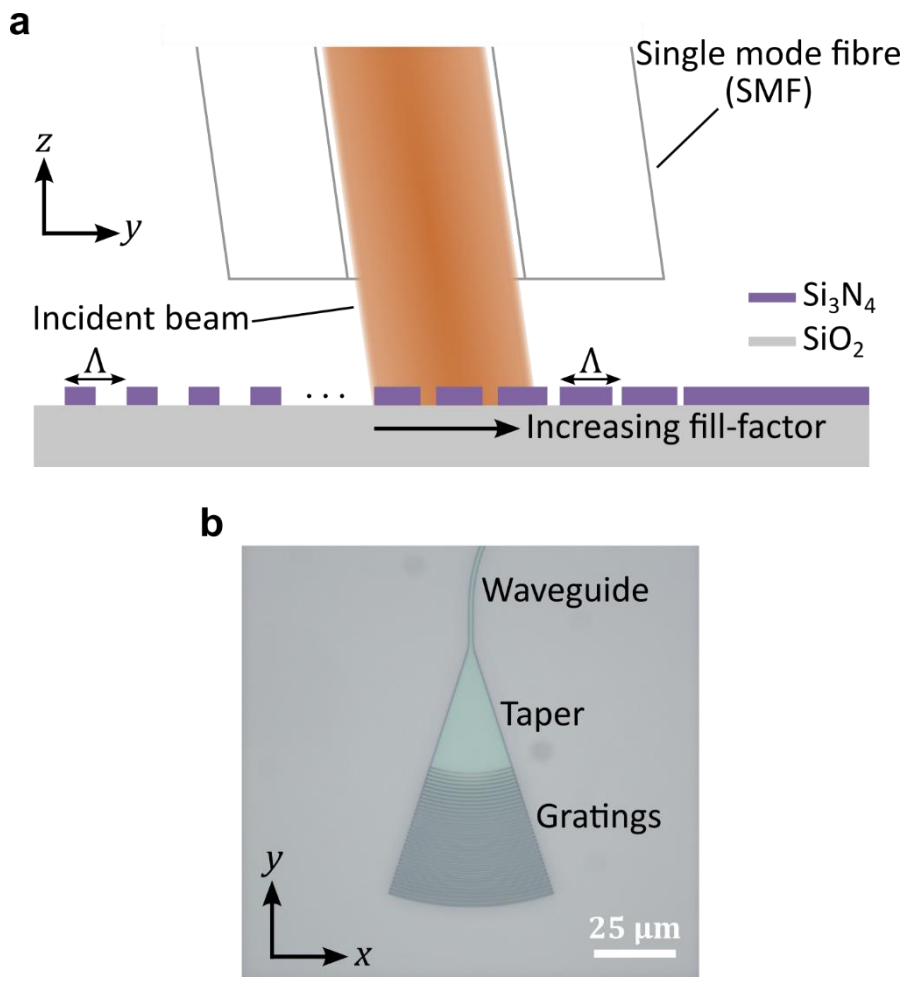


Figure 6.3 Si_3N_4 grating coupler. **a**, Grating coupler sketch showing the incident laser beam and the apodised Bragg gratings. **b**, Optical micrograph of a fabricated grating coupler.

By setting λ_C = 1550 nm, the grating period Λ is determined as approximately 1.14 µm. To optimise the grating parameters, Λ of the fabricated devices is varied from 1.0 to 1.3 µm. Given that the mode field diameter of SMF-28 fibres is around 10 µm, the grating number is selected as 34 for easy the alignment. For all devices, the fill-factor is kept at 55% for the first 18 gratings, and it is linearly increased to 95% (Figure 6.3b) in accordance with the former design examples based on such apodisation [109]. The devices are fabricated using the methods described earlier in Section 3.2, and characterisation results will be given in 6.2.3 .

6.2.2 Ring resonators

Ring resonators consist of two coupled waveguides where the output of one of the waveguides is fed back to its input, forming a ring-shaped cavity. When the phase of the light travelling through the ring is an integer multiple of 2π radians, constructive interference occurs, which in turn enhances the field within the cavity. Such a device offers periodic resonances at specific wavelengths that can meet this phase criterion. Any scatterer nearby a ring resonator affects the resonance condition, making it an excellent candidate to transduce nanomechanical vibrations on a chip.

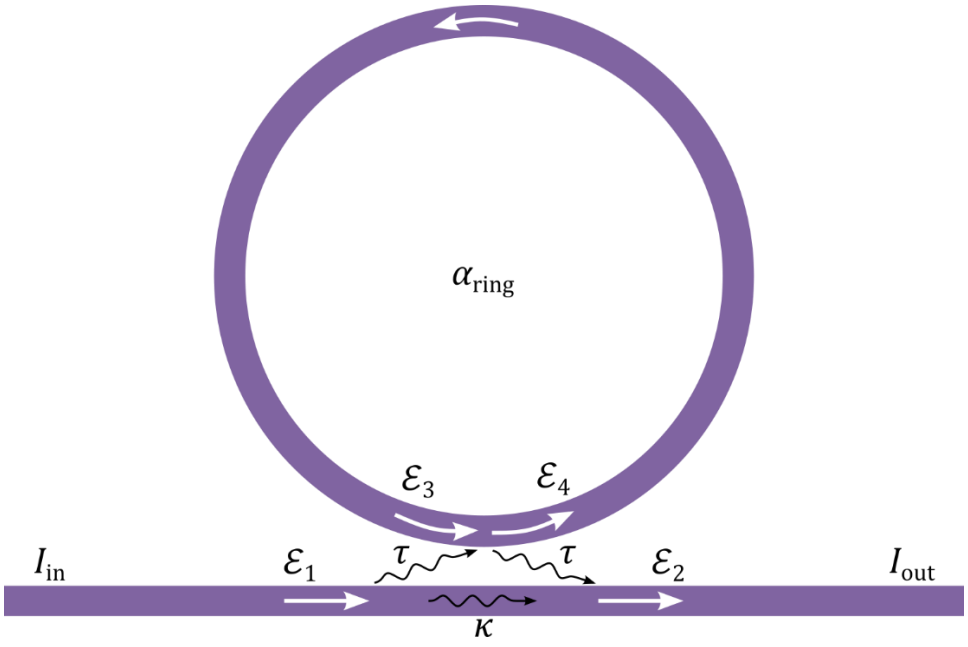


Figure 6.4 Model of a simple ring resonator showing the input and output fields.

Mathematical modelling of ring resonators is performed using scattering parameters owing to their similarity to directional couplers [176]. As given in Figure 6.4, the input field $\mathcal{E}_1$, the output field $\mathcal{E}_2$, and the circulating fields $\mathcal{E}_{3,4}$ can be related to each other through a series of coefficients. Here, τ and κ are the cross-coupling and self-coupling coefficients, respectively, while α_{ring} is the (amplitude) attenuation coefficient of the ring, where $\tau,\ \kappa,\ \alpha_{\mathrm{ring}} \in \mathbb{R}$. By using power conservation and reciprocity properties, the relation between the fields can be written as,

$$\begin{pmatrix} \mathcal{E}_2 \\ \mathcal{E}_4 \end{pmatrix} = \begin{pmatrix} \kappa & i\tau \\ i\tau & \kappa \end{pmatrix} \begin{pmatrix} \mathcal{E}_1 \\ \mathcal{E}_3 \end{pmatrix} \tag{6.2}$$

with the condition of $\kappa^2 + \tau^2 = 1$. There is also a direct relation between the circulating fields $\mathcal{E}_3$ and $\mathcal{E}_4$:

$$\mathcal{E}_3 = e^{-\alpha_{\mathrm{ring}} L} e^{i\theta} \mathcal{E}_4 = a e^{i\theta} \mathcal{E}_4 \tag{6.3}$$

Here, a is the attenuated field amplitude within one round-trip length $L = \pi D_{\mathrm{R}}$, where D_{R} is the ring diameter, and $\theta = \omega t_{\mathrm{R}}$ is the phase of the field at the end of L with $t_{\mathrm{R}} = n_{\mathrm{eff}} L / c_0$ being the round-trip time (c_0 is the speed of light in vacuum).

In order to find the normalised transfer characteristics of the resonator, $\mathcal{E}_1$ can be set to unity. Then, the output field $\mathcal{E}_2$ becomes:

$$\mathcal{E}_2 = \frac{\kappa - a e^{i\theta}}{1 - a\kappa e^{i\theta}} \tag{6.4}$$

This leads to a transmitted intensity I_{out} at the output:

$$I_{\mathrm{out}} = |\mathcal{E}_2|^2 = \frac{\kappa^2 + a^2 - 2\kappa a \cos\theta}{1 + \kappa^2 a^2 - 2\kappa a \cos\theta} \tag{6.5}$$

The resonance condition is periodically met for $\cos\theta = 1$, and I_{out} approaches to zero acting as a notch-type (bandstop) filter at a series of frequencies. Furthermore, for $\kappa = a$, critical coupling occurs when I_{out} drops to zero at the cavity resonance ω_{c}, meaning

that all the input power is circulated inside the ring. This dramatically increases the phase sensitivity of the resonator since any scatterer in the vicinity of the ring affects I_{out} by altering the coupling condition (see Section 6.3 for more details).

Note that the transmission curve in Eq. 6.5 is in the form of a Lorentzian dip that facilitates the determination of the $\mathcal{Q}$ factor, which is an important performance parameter of the ring related to its sensitivity. It is also convenient to determine the $\mathcal{Q}$ directly from the design parameters. By definition, $\mathcal{Q}$ is the ratio of the stored energy to the energy lost per cycle. From Eq. 6.3, it can be seen that the intensity of the circulating field $|\mathcal{E}_3|^2$ is diminished by a^2 after each round-trip. Since the power loss is equal to the energy loss per unit time, one can show that:

$$\mathcal{Q} = \omega_{\mathrm{c}} \frac{t_{\mathrm{R}}}{1 - e^{-2\alpha_{\mathrm{ring}} L}} \approx \frac{\omega_{\mathrm{c}} t_{\mathrm{R}}}{2\alpha_{\mathrm{ring}} L} \qquad 6.6$$

Similarly to the optimisation of the grating parameters, a fabrication-based method is adopted to achieve critical coupling. To that end, the ring radius is kept constant at a value of 120 µm while the gap between the ring and the waveguide is varied between 100-200 nm. The corresponding measurement results will be presented in the next section.

6.2.3 Photonic device characterisation

The fabricated devices, i.e. simple waveguides and ring resonators with grating couplers, have been characterised using a fibre-coupled optical measurement setup given in Figure 6.5. The devices are excited by a bench-top tunable laser source (Santec TSL-550) with 5 pm tuning steps within 1500-1630 nm. The laser light is polarised using a 3-paddle controller (Thorlabs FPC032) to yield the maximum transmission. Here, it should be noted that the waveguides are optimised to support the TE mode. The transmitted light intensity through the device is detected by a photodetector (Newport 1811-FC), and the resulting electrical signal is recorded by the

computer. As such, the spectral response of the fabricated devices has been characterised within the available wavelength range of 1500-1630 nm by measuring the optical transmission.

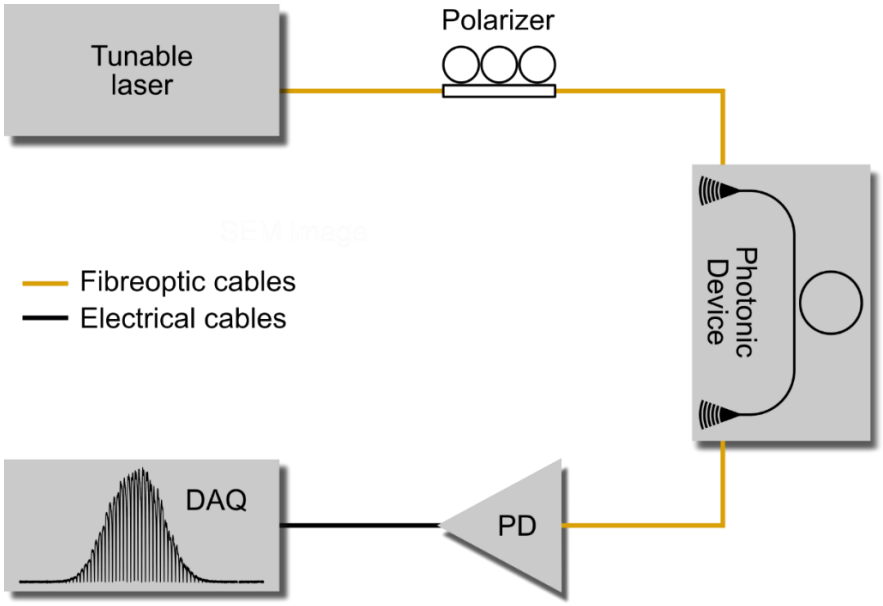


Figure 6.5 Fibre-coupled optical measurement setup.

Out of 64 simple waveguides, the highest transmission has been achieved for a grating period of Λ = 1.175 µm. As seen in Figure 6.6a, the device can achieve a maximum transmission over 5%, which translates into an insertion loss of 6.4 dB per coupler. The 1-dB bandwidth of the coupler has been measured as 52 nm (1529-1581 nm) around a centre wavelength of λ_C = 1556 nm. Both the bandwidth and the insertion loss are comparable to those values in the literature [173], [174]. It is useful to mention that in this work, insertion losses as high as ~12 dB per coupler have also been measured for the same grating parameters, due to the process variations.

As for the ring resonators, critical coupling condition has been met at a physical gap of 170 nm between the waveguide and the microring. The resulting spectrum of one of the critically-coupled resonators is given in Figure 6.6b. From Lorentzian fitting data, the Q factors of the critically-coupled ring resonators have been found to be around 5,000-7,000.

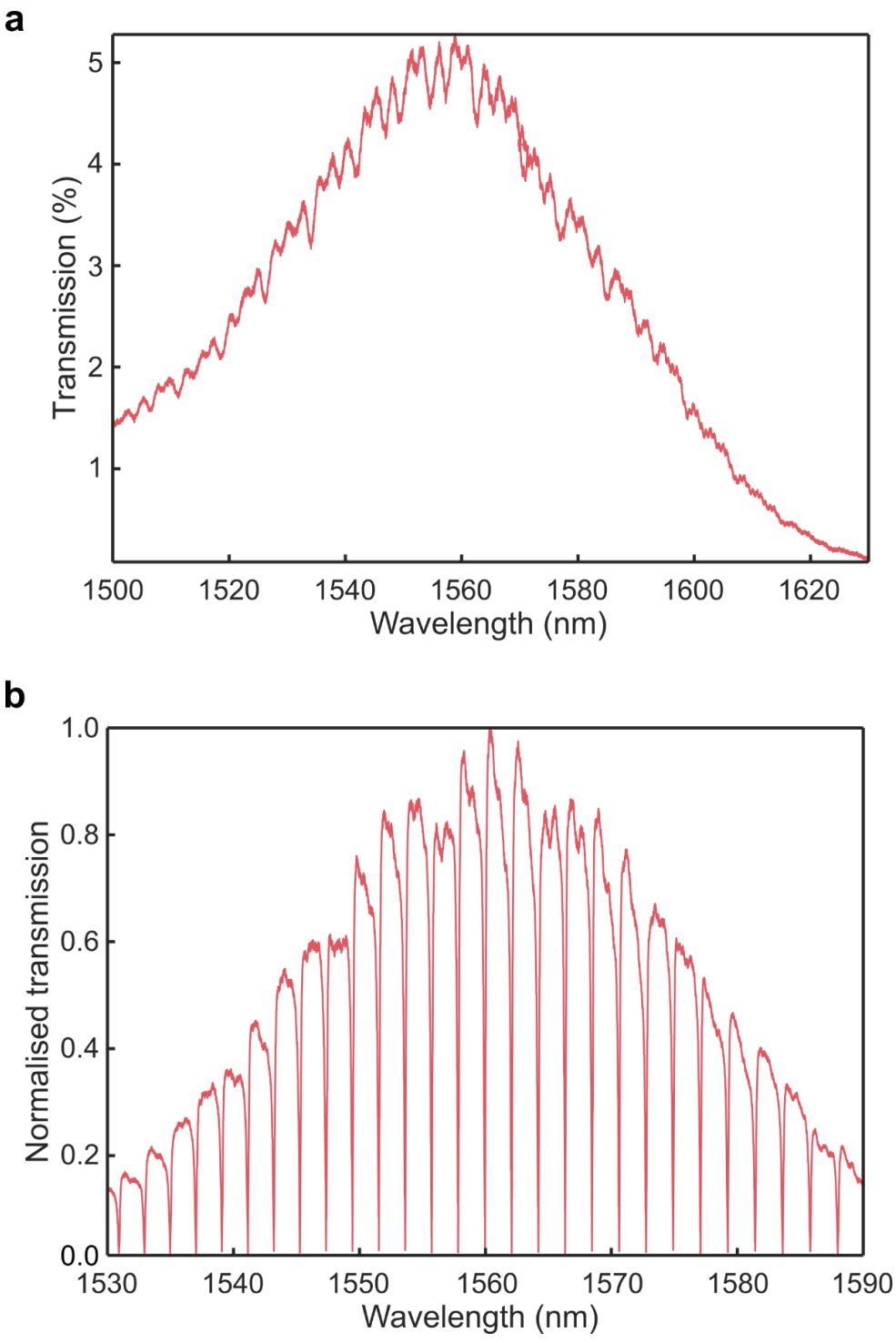


Figure 6.6 Optical characterisation of the fabricated devices. **a**, Transmission spectrum of a grating coupler yielding the highest transmission level. **b**, Normalised spectrum of a critically-coupled ring resonator.

6.3 On-chip photonic transduction of a nanowire

In principle, any scatterer or perturbation nearby a photonic device (usually a cavity) can be inherently transduced as a change in the intensity of light due to evanescent-field interactions. When the scatterer is a mechanical beam, this concept is termed cavity optomechanics. Vibrations of the nanomechanical beam causes a phase and/or amplitude shift within the optical cavity, which can then be sensed as a small intensity change at the output. Assume the nanobeam is made of a dielectric material whose optical losses are negligible at the wavelength of interest, i.e. $n_{\mathrm{nano}} > 1$ and $k_{\mathrm{nano}} \sim 0$. Then, it alters the effective mode index of the ring by lengthening the path length of the guided light within the cavity, which in turn redshifts the optical resonance by $\Delta\omega_{\mathrm{c}}$. As such, the idea behind optomechanical coupling is depicted in Figure 6.7.

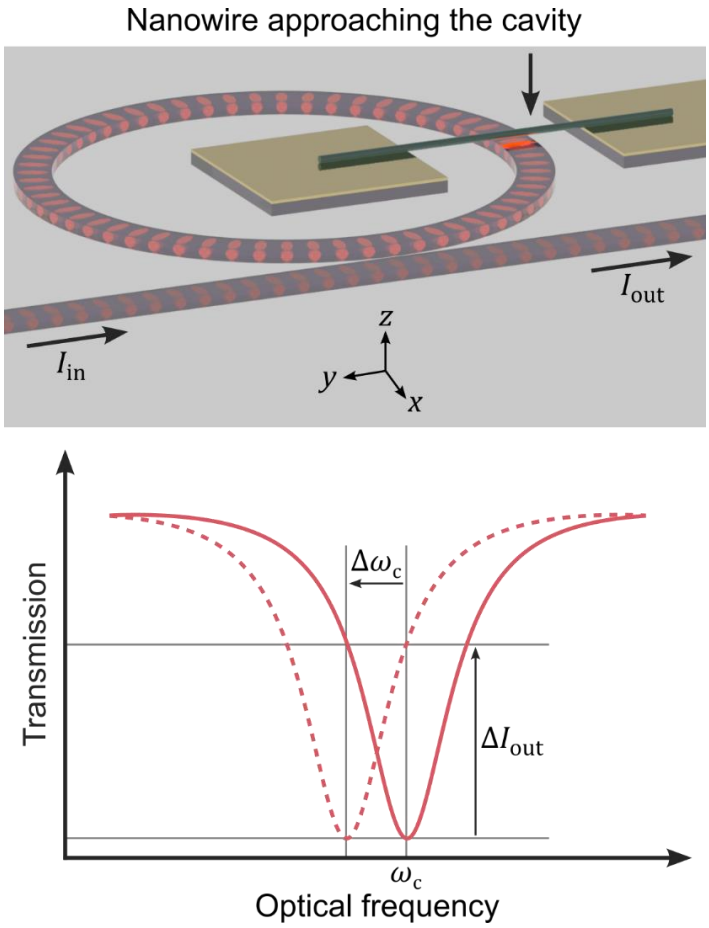


Figure 6.7 Transduction concept based on cavity optomechanics. The arrows indicate the direction of the change, i.e. when the nanobeam approaches the cavity, the optical resonance is redshifted, and the transmission is modified. The scales are exaggerated for illustration purposes.

Experimentally, when the cavity is excited at a constant wavelength, oscillations of the nanomechanical beam can be detected by simply measuring the change in the output field intensity (ΔI_{out}). Although it seems straightforward, evanescent coupling between the nanobeam and the microcavity should be investigated before discussing the experimental results. The configuration used in this work is a doubly-clamped nanowire suspended over Au pads, ~150 nm away from a microring cavity. For the sake of simplicity, InP nanowires will be examined both theoretically and experimentally owing to their near-zero loss at telecommunication wavelengths, i.e. $\tilde{n}_{\mathrm{InP}} = n_{\mathrm{InP}} + ik_{\mathrm{InP}}$ = 3.17+ i0.004 [177]. Transduction results of lossy GeTe nanowires ($\tilde{n}_{\mathrm{GeTe}}$ = 6.86+i1.18 in the crystalline phase [128]) will also be presented in the final chapter as part of future work (Section 7.2). This is to show the universality of the measurement technique. It should also be mentioned that this is the first example of a fully-integrated optical transduction scheme for single-crystal nanowires, which has been enabled by the novel pick-and-place assembly presented in Chapter 3.

6.3.1 Cavity optomechanics: theory and simulations

It is crucial to study how the microcavity resonance conditions are affected by external perturbations. It has been previously explained using Eq. 6.5 that resonance criterion is satisfied for $\cos\theta$ = 1. Thus, the cavity resonances (ω_{c}) appear at integer multiples of $2c_0/D_{\mathrm{R}}n_{\mathrm{eff}}$. As the speed of light and the ring radius are constant, ω_{c} can only be modified by the variations in the effective mode index.

$$\frac{\Delta\omega_{\mathrm{c}}}{\omega_{\mathrm{c}}} = -\frac{\Delta n_{\mathrm{eff}}}{\Delta n_{\mathrm{eff}} + n_{\mathrm{eff}}} \approx -\frac{\Delta n_{\mathrm{eff}}}{n_{\mathrm{eff}}} \qquad 6.7$$

The physical meaning of Eq. 6.7 is that any perturbation to the effective mode index of the microring proportionally redshifts the optical resonance spectrum by the relative change in the effective mode index. Therefore, one needs to study the influence of nanomechanical vibrations on n_{eff}. A common way to determine such a coupling relation is to use numerical simulations [88], [91] although it is also encouraged to

derive an analytical approximation [92], [93]. To start with, the evanescent field amplitude along z-axis (outside the waveguide) can be written as:

$$|\mathcal{E}_z| = \xi \mathcal{E}_{\max} e^{-\alpha z} \qquad 6.8$$

Here, the reference plane (z = 0) has been chosen at the cavity/vacuum interface, $\mathcal{E}_{\max}$ is the maximum electric field amplitude inside the cavity, $\xi\mathcal{E}_{\max}$ is the field amplitude at the cavity/vacuum interface, and α is the evanescent decay constant.

$$\alpha^{-1} = \left(\frac{\lambda}{2\pi}\right) \Big/ \sqrt{n_{\text{eff}}^2 - 1} \qquad 6.9$$

From Eq. 6.9 [92], one can find the decay length of the evanescent field as ~200 nm for λ = 1500 nm. This value has been further confirmed using mode simulations in Lumerical, and a slice of the corresponding field intensity in z-direction is given in Figure 6.8. From here, ξ has been estimated as ξ^2 = 0.404.

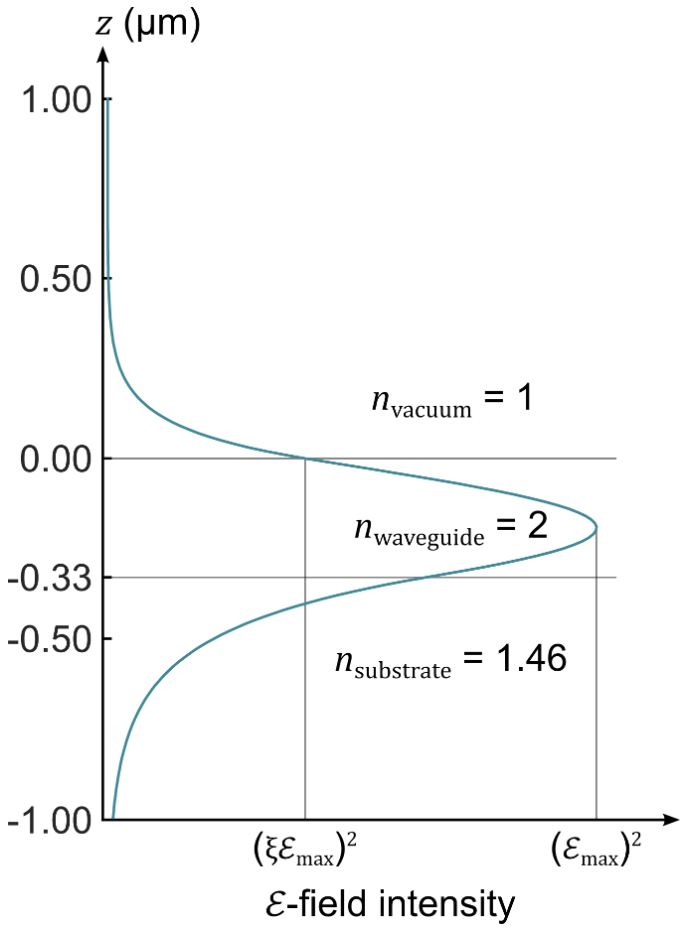


Figure 6.8 A slice of the fundamental TE mode of the microcavity along z-axis.

Once the evanescent field characteristics are determined, the effect of the nanowire vibrations on the cavity resonance can be approximated using cavity perturbation theory [178]. This theory investigates the modified resonance conditions of an electromagnetic cavity in the presence of an external perturbation, say, a small object such as a nanowire nearby the cavity. The basis of the perturbation is rooted in energy considerations, i.e. the nanowire extracts some energy out of the cavity, decreasing the optical resonance frequency. Let $|\mathcal{E}_r|$ be the field amplitude circulating inside the cavity. Then, the energy stored in the unperturbed cavity becomes,

$$W_{\mathrm{c}} = \frac{1}{2}\iiint_{\mathrm{cav}} \epsilon_0 \epsilon_{\mathrm{r,cav}} |\mathcal{E}_r|^2 \,\mathrm{d}V = \frac{1}{2}\epsilon_0 \mathcal{E}_{\max}^2 V_{\mathrm{cav}} \qquad 6.10$$

where ϵ_0 is the vacuum permittivity while $\epsilon_{\mathrm{r,cav}}$ and V_{cav} are the relative permittivity and the effective mode volume of the microring cavity, respectively. Likewise, the energy perturbation due to the nanowire is given as:

$$dW_{\mathrm{c}} = \frac{1}{2}\iiint_{\mathrm{nano}} \epsilon_0 \epsilon_{\mathrm{r,nano}} |\mathcal{E}_r|^2 \, dV - \frac{1}{2}\iiint_{\mathrm{nano}} \epsilon_0 |\mathcal{E}_r|^2 \,\mathrm{d}V \qquad 6.11$$

Here, $\epsilon_{\mathrm{r,nano}} = n_{\mathrm{nano}}^2$ is the relative permittivity of the nanowire. In Eq. 6.11, the first term is the evanescent field energy stored inside the nanowire whereas the second term is the amount of vacuum energy replaced by the nanowire. Assume the nanowire has a diameter of D and is placed above the cavity at a distance of z_0, i.e. the gap between the nanowire and the waveguide is z_0. With the assumption that $|\mathcal{E}_r|$ is homogenous along the microring, dW_{c} can be simplified as:

$$dW_{\mathrm{c}} = \frac{1}{2}\epsilon_0 (n_{\mathrm{nano}}^2 - 1) \frac{\xi^2 \mathcal{E}_{\max}^2 e^{-2\alpha z_0} e^{-\alpha D}}{\alpha} w \int_{-D/2}^{D/2} \sinh\left(2\alpha\sqrt{D^2/4 - x^2}\right) \mathrm{d}x \qquad 6.12$$

To reiterate, w is the waveguide width. The integral can be numerically calculated, e.g. in MATLAB, for particular D values. Therefore, the relative resonance shift given in Eq. 6.7 can be rewritten in terms of known physical quantities to a first-order approximation where $\Delta\omega_c/\omega_c \approx -(dW_c/W_c)/2$ [92].

$$\Delta\omega_c = -\frac{\omega_c}{2}(n_{nano}^2 - 1)\frac{\xi^2 e^{-2\alpha z_0} e^{-\alpha D}}{\alpha}\frac{w}{V_{cav}}\int_{-D/2}^{D/2} \sinh\left(2\alpha\sqrt{D^2/4 - x^2}\right) dx \qquad 6.13$$

From Eq. 6.13, it is also possible to define a new parameter called optomechanical coupling rate g_{om}, which corresponds to the cavity resonance shift with respect to small fluctuations in nanowire's position around z_0, i.e. $g_{om} = \partial\omega_c/\partial z_0$.

$$g_{om} = \omega_c(n_{nano}^2 - 1)\xi^2 e^{-2\alpha z_0} e^{-\alpha D}\frac{w}{V_{cav}}\int_{-D/2}^{D/2} \sinh\left(2\alpha\sqrt{D^2/4 - x^2}\right) dx \qquad 6.14$$

Eq. 6.14 contains noteworthy information for designing optomechanical experiments. For example, g_{om} can be improved by using a smaller cavity, a higher optical resonance frequency, a smaller nanowire/cavity gap, and a nanowire with a higher refractive index or a larger diameter. Note that increasing the field intensity inside the cavity does not affect g_{om} as ξ remains constant for a given design. However, higher input (probe) powers do improve the readout amplitude by yielding a larger ΔI_{out}.

As mentioned earlier, the relation based on n_{eff} in Eq. 6.7 can also be used to estimate $\Delta\omega_c$ via FEM simulations. To that end, frequency domain analysis has been performed in COMSOL Multiphysics® using an InP nanowire (D = 150 nm) placed over a straight waveguide, which is excited at a wavelength of λ = 1500 nm. Corresponding optical field intensity profiles for three different gap (z_0) values (0 nm, 150 nm, and 500 nm) can be seen in Figure 6.9. A slice of the field profile at x = 0 has also been given for each case. Note that the perturbation from the nanowire is significantly enhanced for

a smaller gap, i.e. the nanowire pulls the guided mode out of the waveguide more effectively when the gap is small. Such mode-pulling behaviour manifests itself as a secondary (perturbative) maxima as can be seen from the intensity plots in Figure 6.9.

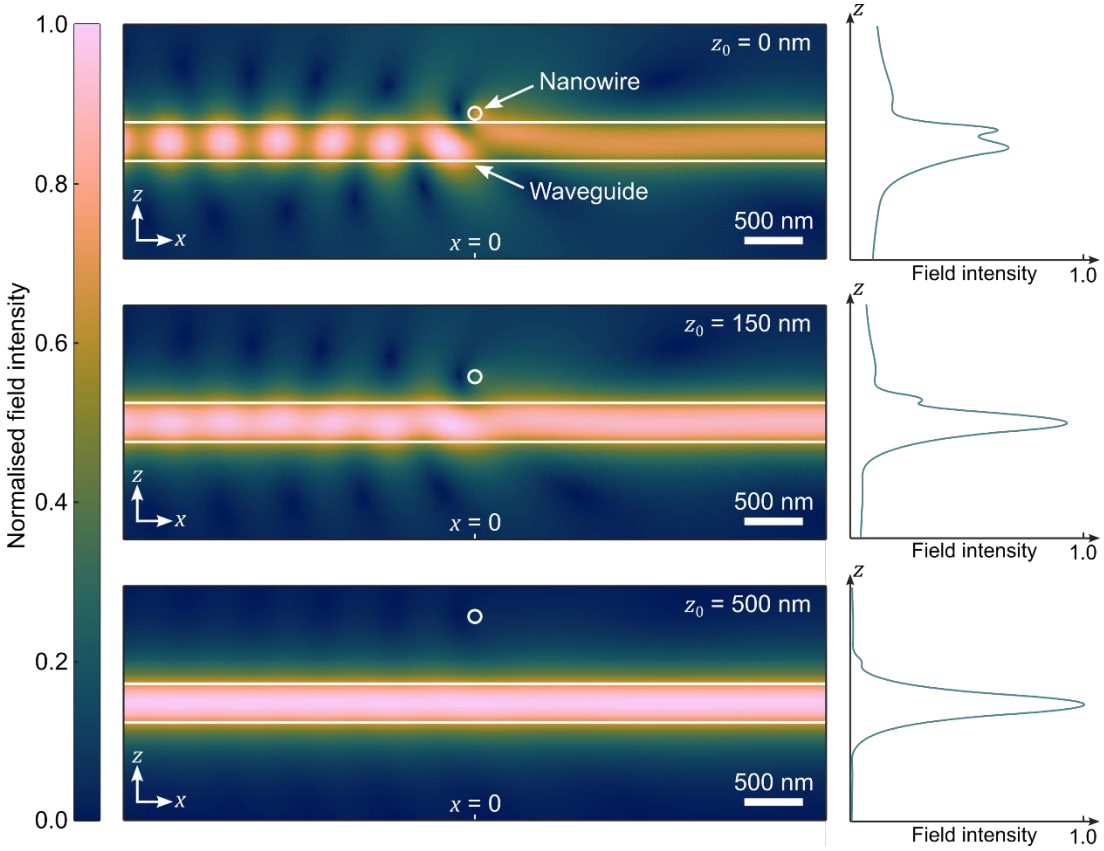


Figure 6.9 Simulated field intensity showing the nanowire perturbation for various z_0 values. Increasing the gap (z_0) leads to a weaker interaction between the nanowire (InP) and the photonic waveguide (Si_3N_4). Light propagates in the positive x -direction, and the corresponding field intensity plots for each case at x = 0 is given on the right.

To examine the effect of mode-pulling on n_{eff}, the simulation has been repeated for eleven z_0 values between 0 to 500 nm with 50 nm increments. Computed n_{eff} values are appropriately scaled using the mode volumes, and the resulting Δn_{eff} is provided in Figure 6.10a. It can be seen that the value of Δn_{eff} decreases exponentially for increasing gap values. Given that $\Delta\omega_{\mathrm{c}} \propto \Delta n_{\mathrm{eff}}$, such an exponential behaviour substantiates the theoretical approximations in Eq. 6.13. Generally speaking, this is due to the exponential decay of the evanescent field, which regulates the interaction strength between the microcavity and the nanowire.

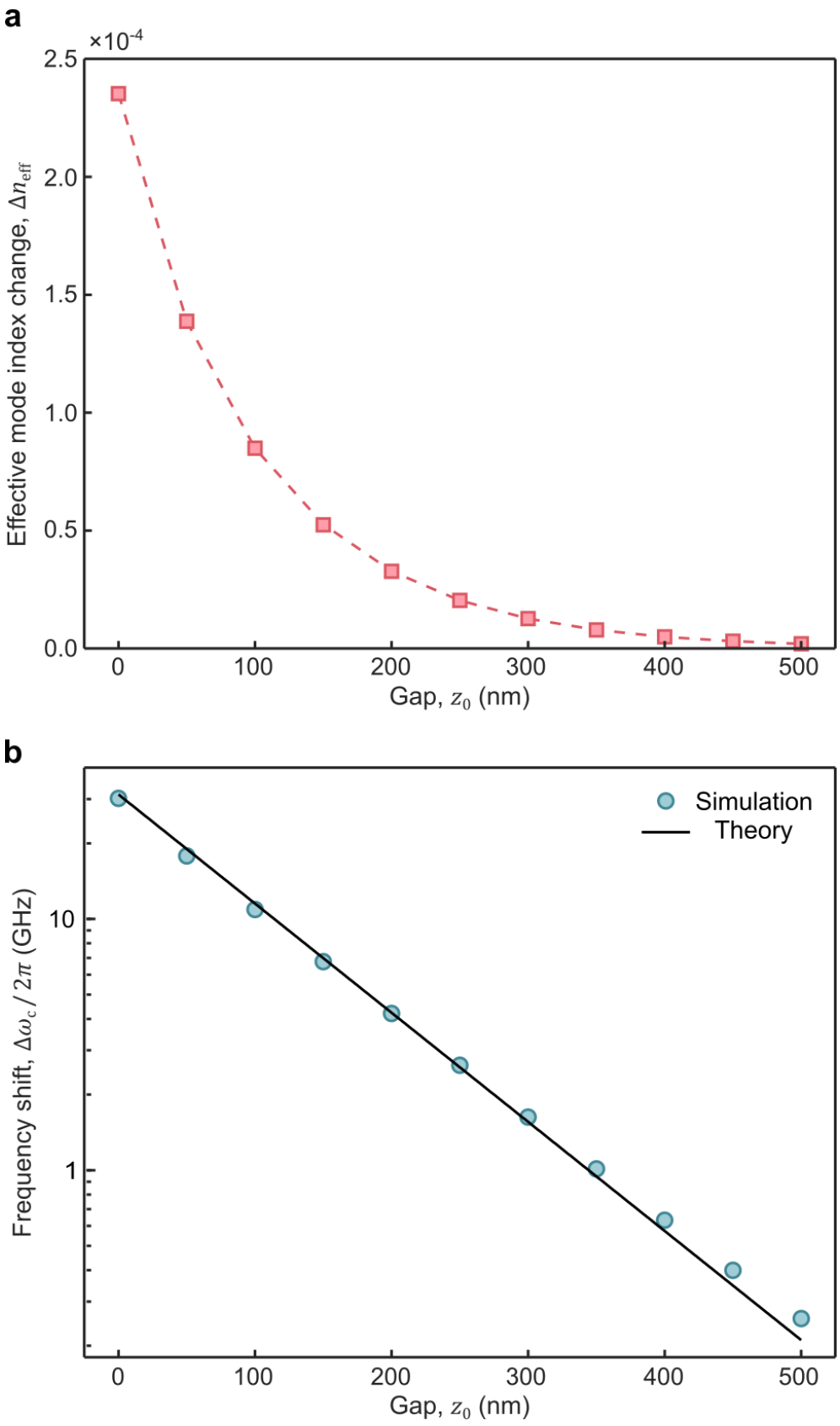


Figure 6.10 Simulated values using effective-index method. **a**, Change in the effective mode index for various gap (z_0) values. Dashed lines are guide to the eye. **b**, Comparison of the simulated frequency shift (using Δn_{eff}) with the theory.

These Δn_{eff} values have further been inserted into Eq. 6.7 in order to calculate the absolute frequency shift ($\Delta\omega_{\mathrm{c}}/2\pi$), and a comparison of the simulated results with the theory (Eq. 6.13) is provided in Figure 6.10b. They both compare favourably within 2% of agreement, where the simulated values slightly deviate from the pure exponential behaviour of the theory. For lower z_0 values, this is attributed to the first-order perturbation approximation [92]. For increasing values of z_0, the slope of the simulated curve, which yields g_{om}, gets weaker. This is mainly due to the limited simulation tolerance compromising the accuracy of the results as the nanowire gets farther away from the cavity.

6.3.2 Measurement setup

Similarly to the piezoresistive transduction scheme, optomechanical experiments take place inside a room-temperature vacuum chamber. Although all-electrical measurements are straightforward to perform in vacuum by means of wirebonding, this is not the case for photonic transduction as there does not exist a de facto method of bonding optical fibres to on-chip devices.

Typically, several micromanipulators are placed inside the vacuum chamber to align the devices with fibres. However, this often requires a meticulous vibration isolation system given that the individual micromanipulators have different weight and shape for practical reasons. Even if identical micromanipulators can be used, their mounting points will still differ, leading to spatial variations of experimental conditions. Moreover, to accommodate all the equipment, a relatively large chamber has to be deployed, which intensifies vacuum fluctuations and thus worsens damping-related nanomechanical noise. Therefore, it is important to make a vacuum-compatible, hand-held assembly that can readily incorporate a fibre-coupled optomechanical device on a single chip. To this end, a process of gluing the fibrearray to the device chip has been developed.

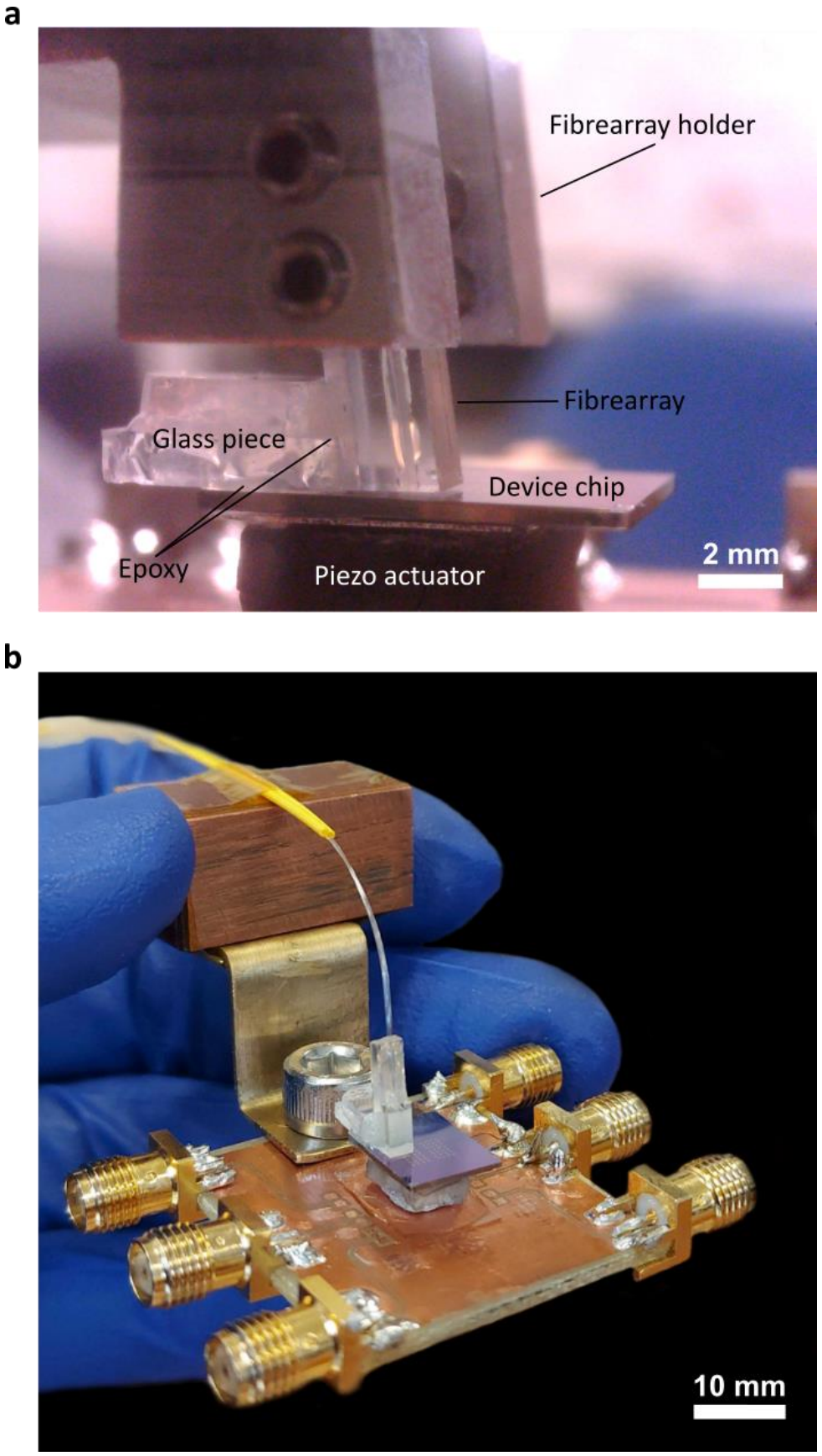


Figure 6.11 Glued fibrearray on the device chip. **a**, Alignment step. **b**, Final assembly.

The annotated alignment setup is given in Figure 6.11a. Initially, the two-channel fibrearray (from SQS Vlaknova optika a.s.) is glued to a piece of glass using epoxy resin (Araldite Rapid Drying Epoxy Resin). After curing this structure for 2 hours at room temperature, the fibrearray is fixed on a purpose-built holder and aligned with the device chip underneath using the optical measurement setup in Figure 6.5. Here, the alignment is optimised to yield the maximum transmission. It should be noted that the couplers offer a relaxed alignment tolerance of ~5 µm in the xy-plane and ~100 µm in z-axis (accounting for a 1 dB loss window). Once the alignment is finished, the device chip is lowered, and a small drop of epoxy resin is casted on the bottom side of the glass piece that faces the chip. Then, the device chip is carefully brought back to its initial position. Note that this step disperses the epoxy droplet around the glass piece, forming a thin adhesive interface between the chip and the glass. The presence of the glass piece further ensures a physical gap between the fibrearray and the chip while keeping the resin from being spread over the device of interest. After curing the epoxy overnight, the gluing step is completed, and the final assembly can be seen in Figure 6.11b (see Appendix A for further details).

Mechanical actuation of the resonator is performed using a piezoceramic shaker. As previously discussed, the top plate of the piezo is grounded, and the actuation signal is applied to the bottom plate using a PCB with SMA connectors. Due to the small dimensions of the vacuum chamber, fibreoptic cables are mechanically fixed on a copper block in order to protect the non-jacketed areas from breaking (Figure 6.11b). This also reduces optical bending losses.

Figure 6.12a summarises the optomechanical transduction setup. For this experiment, the same optical components as in Figure 6.5 have been used. Briefly, polarised light from the tunable laser is coupled into the photonic device inside the vacuum chamber via fibre feedthroughs. Output light from the device is converted to electrical signals using the low-noise photodetector (PD), which is then fed into the lock-in amplifier.

Note that the lock-in amplifier also actuates the vibrational (out-of-plane) mode of the nanowire by driving the piezo shaker through the HPA. Thus, the readout can be obtained within the desired frequency band by sweeping the actuation frequency. As such, the measurement results will be given in the next section for the device whose SEM image is given in Figure 6.12b (L = 9.2 µm and D = 150 nm).

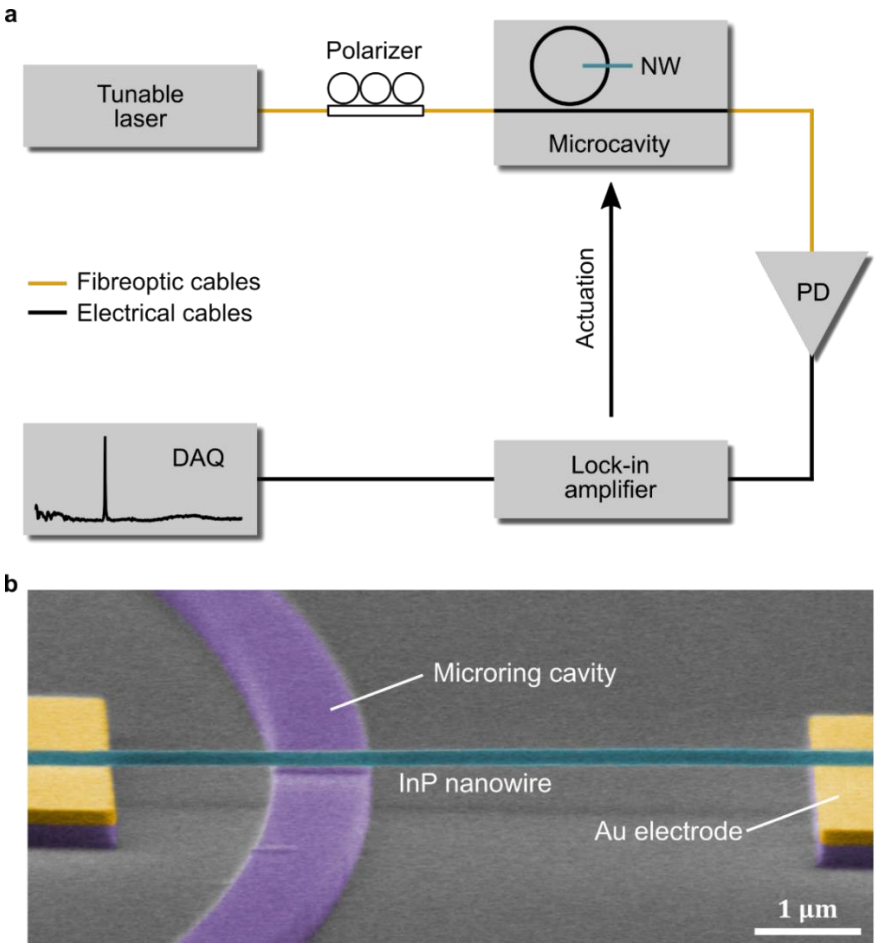


Figure 6.12 Experiment setup for detecting nanomechanical vibrations of an InP nanowire. **a**, Schematic showing the optomechanical measurement setup and **b**, Angled-view false-colour SEM image of the device.

6.3.3 Optomechanical device characterisation

Although theoretical analysis has been performed in frequency domain, experimental results will be presented with respect to the wavelength of light due to practicality reasons. However, corresponding calculations in the frequency domain will be given when necessary.

Prior to the optomechanical measurements, spectrum of the microring cavity has been obtained with and without the nanowire in order to validate the evanescent field interactions. Before the nanowire deposition, the unperturbed cavity was critically coupled and had a resonance wavelength of 1505.73 nm as shown by the solid line in Figure 6.13. With the introduction of the nanowire, the optical resonance is redshifted to 1505.90 nm (the dashed line in Figure 6.13). This corresponds to a frequency shift of 22.5 GHz, which is approximately 3× higher than the theoretical estimate (7.1 GHz using Eq. 6.13). However, it should be noted that this is not a viable way of comparing the theory with the experiments since the nanowire placement process also affects the experimental conditions. It is mainly attributed to the solvents, e.g. acetone and isopropyl alcohol, used to clean the device chip prior to the nanowire placement. These solvents contaminate the microring through adsorption and modify n_{eff} and α_{ring}. This is a known practical issue especially when the lithography resist is of negative tone (ma-N 2403 here). Thus, to eliminate such discrepancies, one should perform the comparison in a better-controlled experiment, e.g. by using the dynamic properties such as g_{om}. This will be evaluated in the following section.

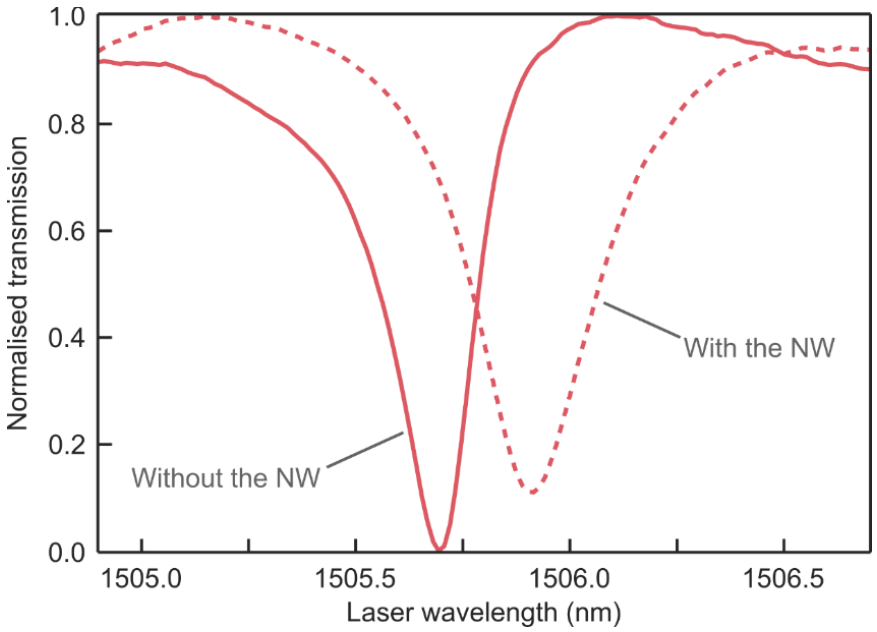


Figure 6.13 Normalised optical cavity transmission before (solid line, critical coupling) and after (dashed line) the nanowire deposition. The nanowire introduces additional optical loss to the microcavity, resulting in linewidth broadening.

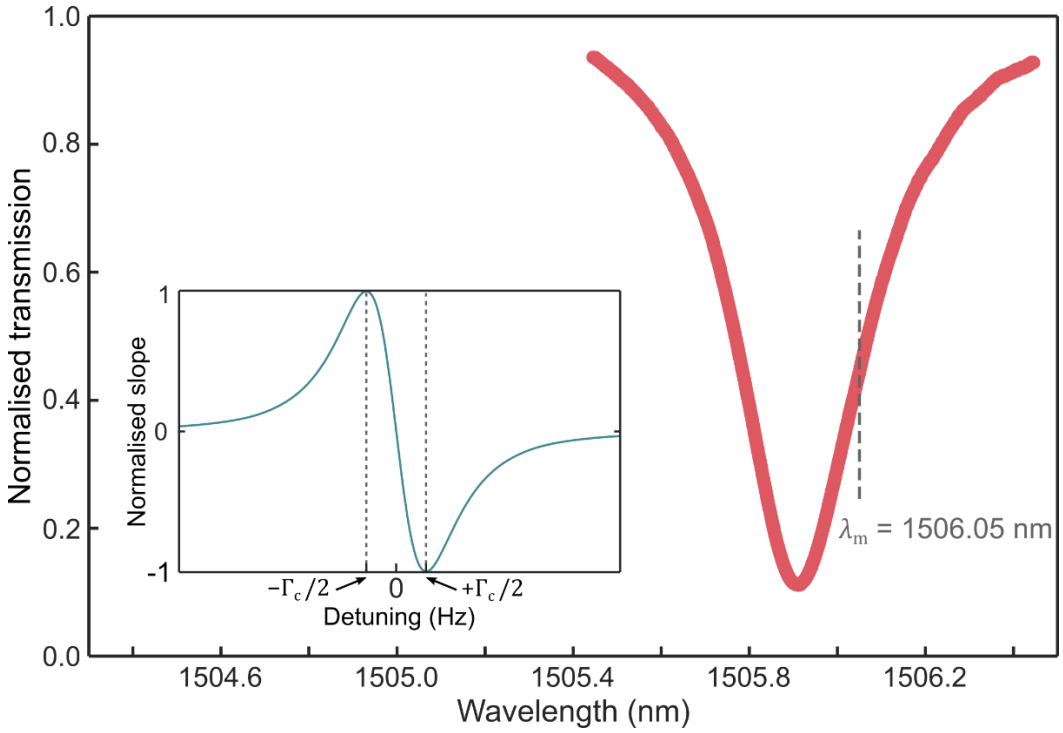


Figure 6.14 Normalised microcavity transmission showing the measurement wavelength λ_m. Inset shows the normalised slope of a microring cavity numerically obtained from Eq. 6.5. Maximum slope is obtained for a detuning of $\pm\Gamma_c/2$.

Using the Lorentzian fit, the variation of the Q factor can also be inspected. The unperturbed cavity has a Q of 6,970. Optical losses introduced by the nanowire (together with the pick-and-place process) further alter the critical coupling condition and reduce the Q down to 4,460. Such linewidth broadening is a result of the additional loss, which modifies α_{ring} from 6.7 dB cm^{-1} to 8.6 dB cm^{-1}. From this Q value, the cavity decay rate can also be calculated as Γ_c = 43.5 GHz using Eq. 6.15. Cavity decay rate is a measure of how fast the field intensity inside the microring resonator responds to perturbations. By choosing $\Gamma_c \gg f_0$, where f_0 is the mechanical resonance frequency of the nanowire, the effects of dynamical back-action such as mechanical amplification or damping (cooling) can be minimised [91], [92]. Given that the mechanical resonance frequencies used in this study are on the order of several MHz, the condition of $\Gamma_c \gg f_0$ is ensured.

$$\Gamma_c = \frac{\omega_c}{2\pi Q} \qquad 6.15$$

To start with, the cavity is excited with a 21 µW probe at a red-detuned wavelength of λ_m = 1506.05 nm, which is approximately at $\omega_c - \Gamma_c/2$. When the laser detuning is $\pm\Gamma_c/2$, one can show from Eq. 6.5 that the transmission spectrum reaches the maximum slope (see Figure 6.14), whereby the readout amplitude can be maximised for a given probe.

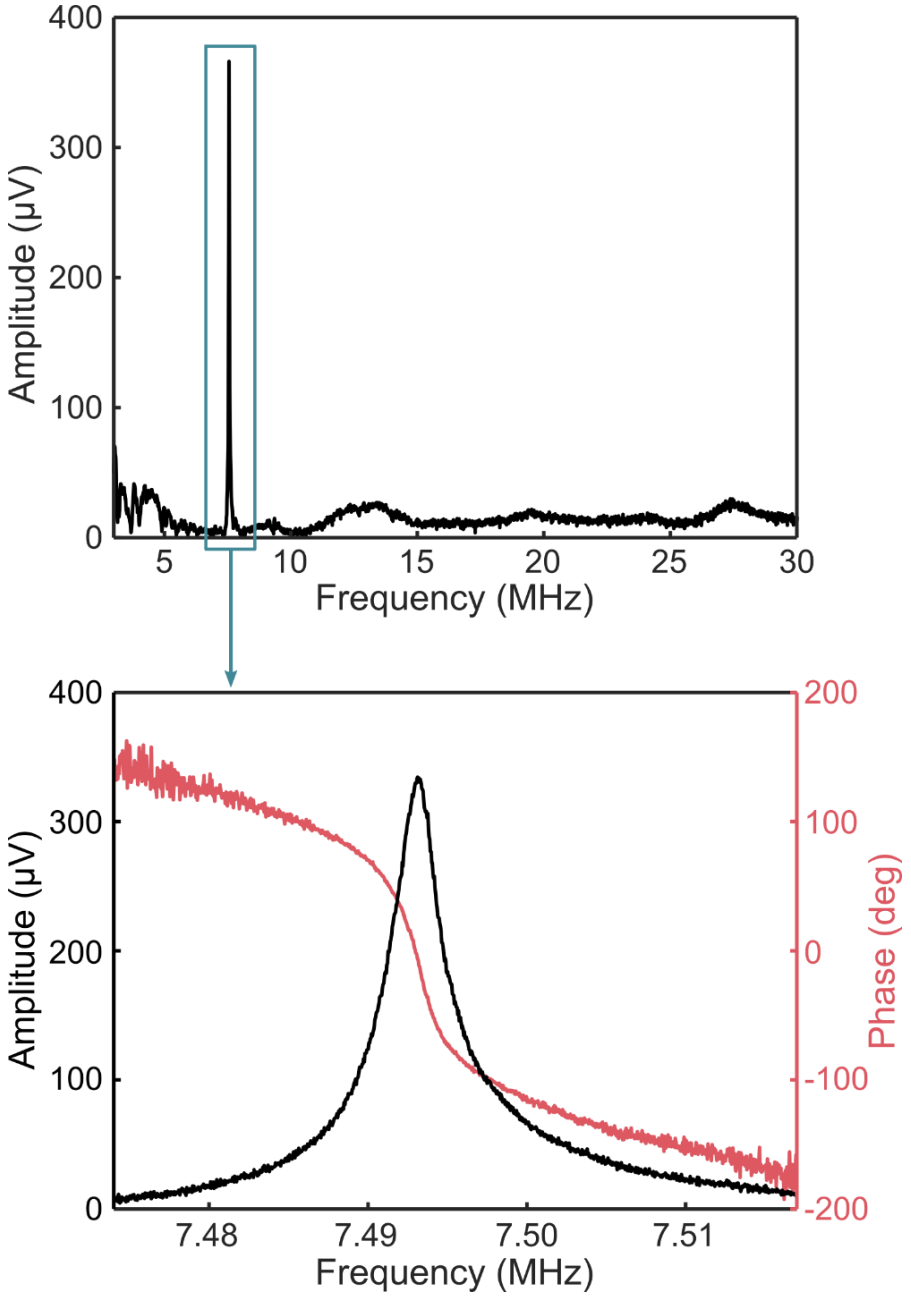


Figure 6.15 Raw experimental data acquired from the InP nanowire with dimensions L = 9.2 µm and D = 150 nm. The finer sweep shows the magnitude and phase response of the resonator.

In order to obtain the resonance spectrum of the InP nanowire, frequency of the drive signal is swept from 3 to 30 MHz (for V_{drive} = 2.5 V). A distinctive resonance peak can be seen from the raw experimental data in Figure 6.15 (top panel). Lower panel in Figure 6.15 displays the magnitude and phase response of the resonator. Remarkably, the readout amplitude is already 10× higher than those obtained via piezoresistive detection (in Chapters 4 & 5) while offering an improved background response owing to the minimal crosstalk between the electrical (actuation) and optical (transduction) domains.

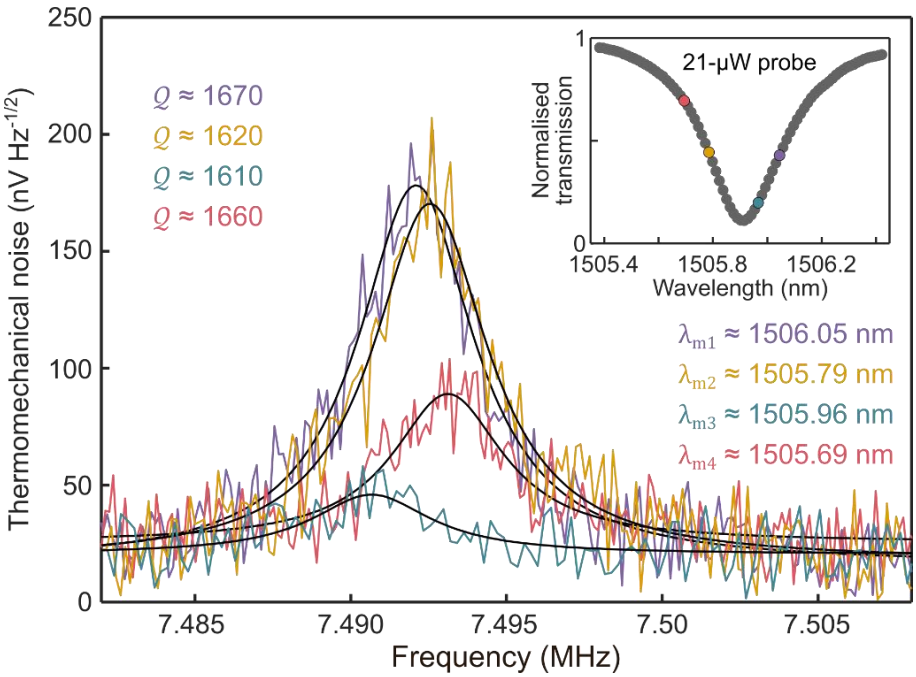


Figure 6.16 Thermomechanical noise spectral density of the resonator with a probe power of 21 μW for various wavelengths. Inset shows the transmission spectrum of the optical cavity with colour-coded wavelength values. Measurement wavelengths and Q factors are further displayed in the same colour as the corresponding readout data, where Lorentzian fits are shown by black solid lines. Goodness of the fits are better than 10%.

Resonance parameters (f_0 and Q) of the nanowire has been determined by capturing its thermomechanical response, i.e. under no actuation. During this experiment, the measurement wavelength has also been varied for the same probe power (21 μW). Figure 6.16 shows the relevant experimental data obtained at different wavelengths. Here, λ_{m1} and λ_{m3} are red-detuned whereas λ_{m2} and λ_{m4} are blue-detuned. It should also be mentioned that λ_{m1} and λ_{m2} are detuned by $-\Gamma_{\mathrm{c}}/2$ and $+\Gamma_{\mathrm{c}}/2$, respectively.

From the Lorentzian fitting results, the resonance frequency and the quality factor of the nanowire are found as f_0 = 7.4920 MHz and Q = 1670 (at λ_{m1}). From this f_0 value, the Young's modulus of InP nanowires can also be estimated as 122 GPa, which is in decent agreement with the literature values [179].

The data in Figure 6.16 suggest that λ_{m1} and λ_{m2} yield the largest readout amplitude owing to the maximum slope at $\pm\Gamma_c/2$ detuning. This is in line with the numerical analysis given in Figure 6.14. Moreover, both resonance peaks have similar amplitude and Q factor. This further validates that mechanical amplification/damping is negligible as predicted previously, i.e. the cavity response time is much faster than f_0. Also note that the resonance frequency reaches its lowest value (7.4909 MHz) at λ_{m3} and highest value (7.4932 MHz) at λ_{m4}. This can be explained by opto-thermo-mechanical effects, meaning that intracavity power leads to electromagnetic heating of the nanowire due to its non-zero imaginary refractive index, which in turn softens the mechanical mode, i.e. stress-softening. This is an expected outcome given that the largest (smallest) intracavity power in this experiment is attained at λ_{m3} (λ_{m4}).

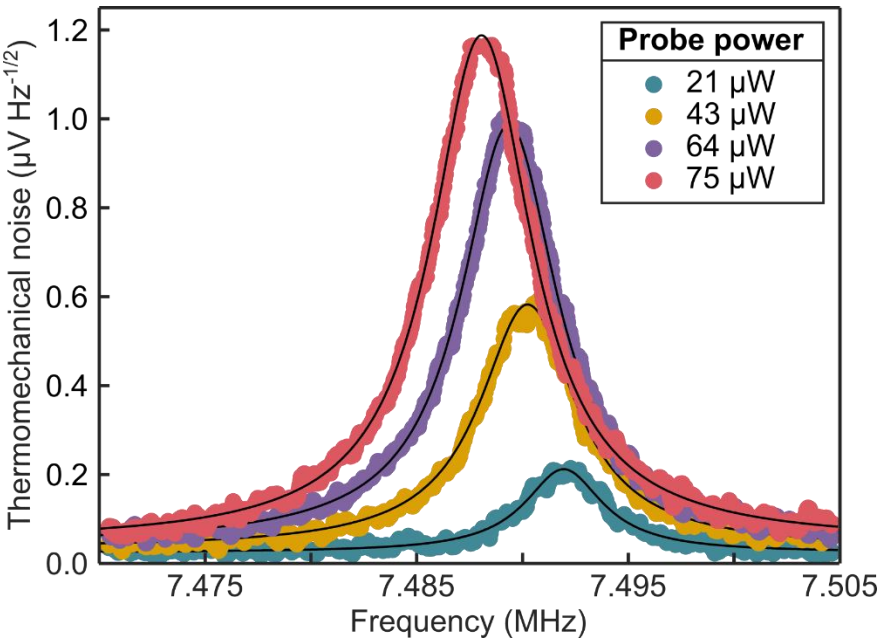


Figure 6.17 Raw thermomechanical noise data (circles) of the nanowire together with the corresponding Lorentzian fits (solid black lines) for various probe powers. Increasing optical field intensity softens the resonator (lower resonance frequency) and improves the transduction gain (larger resonance peak).

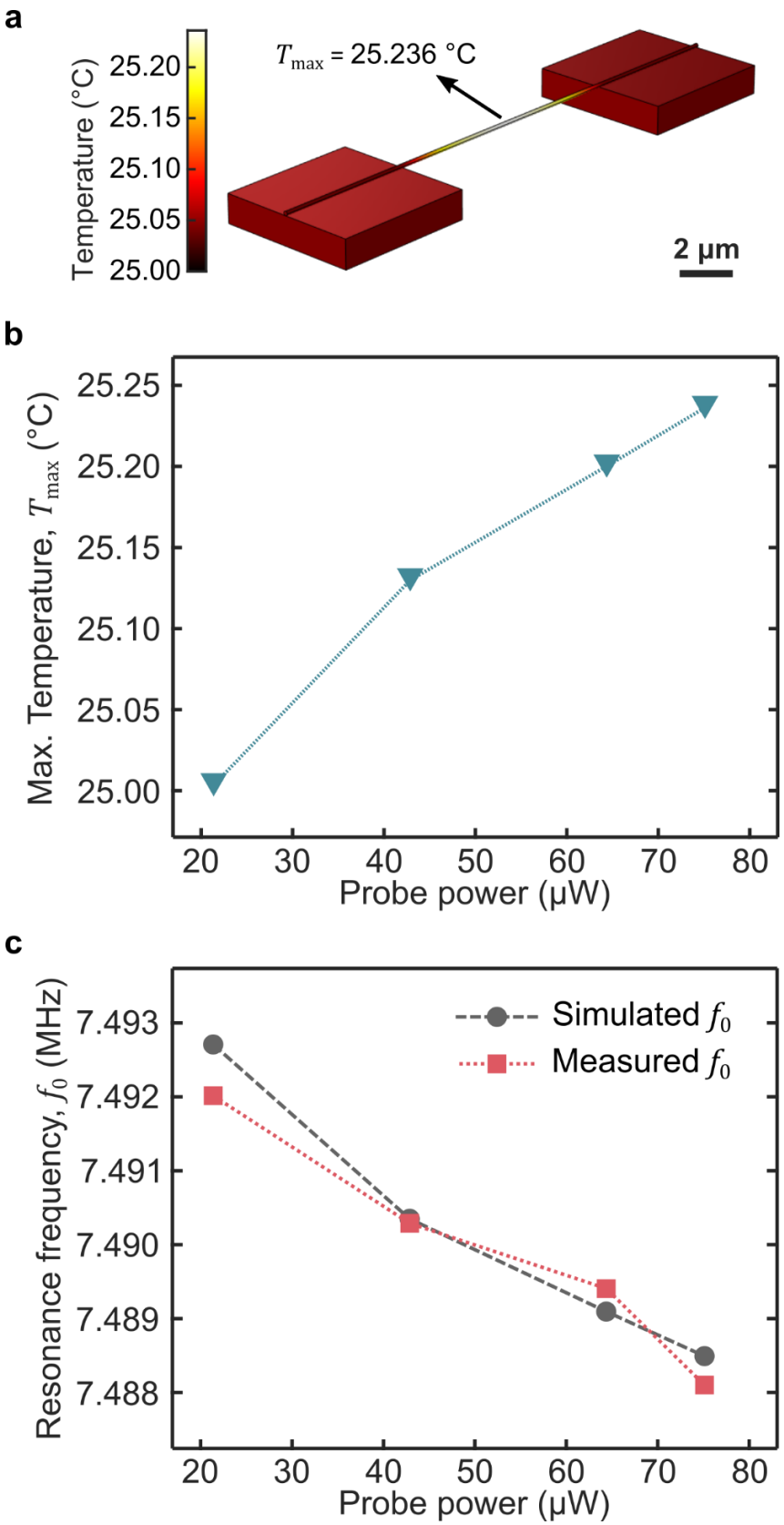


Figure 6.18 Finite element analysis results for the opto-thermo-mechanical effect. **a**, Spatial temperature profile indicating a maximum temperature value of T_{max} = 25.236 ℃ for the 75-μW probe. **b**, Simulated T_{max} values for various probe powers. **c**, Measured and simulated change in the mechanical resonance for different probes. Dashed and dotted lines are guide to the eye.

To further study the opto-thermo-mechanical effect, noise spectrum of the resonator has been obtained for various probe powers at a single wavelength λ_{m1}. As seen in Figure 6.17, the peak noise voltage increases for increasing probe powers. The effect of stress-softening is also evident from the measurement results, indicating a maximum frequency shift of ~3.9 kHz for the 75-μW probe. For this probe power, the spatial temperature profile (simulated in COMSOL Multiphysics®) has been given in Figure 6.18a, suggesting a maximum temperature increase of $\Delta T_{\max}$ = 0.236 ℃.

In detail, the simulations have been performed at room temperature (25 ℃). Initially, the optical power evanescently coupled from the microring cavity into the nanowire is obtained. Here, the electromagnetic radiation generates dielectric currents inside the nanowire (via k_{InP}), which in turn results in Joule heating. Using these results, spatial temperature profile of the nanowire has been computed (e.g. as given in Figure 6.18a). The temperature change causes thermal expansion, exerting a compressive stress on the doubly-clamped nanowire. Subsequently, the thermal expansion results are inserted into the mechanical domain via prestressed eigenvalue analyses, which yield the softened mechanical mode at equilibrium.

As such, the simulations have been performed for different probes. The maximum temperature inside the nanowire ($T_{\max}$) for each case has been provided in Figure 6.18b. Figure 6.18c further shows an excellent agreement of 4% between the simulated and measured f_0 values. Thus, the frequency shift can be considered purely thermal. In addition to the frequency shift, there is also a dramatic increase in the peak amplitude for increasing probe levels as previously mentioned. This is a result of the improved transduction efficiency and will be examined in the next section.

6.3.4 Estimating the displacement sensitivity

As discussed in Section 2.3, displacement sensitivity is an important parameter while assessing a transduction mechanism. Thus, the relevant performance parameters

regarding the optomechanical transduction of the nanowires will be investigated here. Calibration will be performed using the thermomechanical spectra of the resonator following a similar procedure described by Li et al. [83].

Equipartition theorem suggests that noise displacement of a mechanical resonator at thermal equilibrium reaches a resonant peak amplitude of a_{th},

$$a_{\mathrm{th}} = \sqrt{\frac{4k_{\mathrm{B}}TQ}{m_{\mathrm{eff}}(2\pi f_0)^3}\Delta f} \qquad 6.16$$

where k_{B} is the Boltzmann constant, T is the ambient temperature, and Δf is the measurement bandwidth [180]. Note that a_{th} yields the spectral density when Δf is unity. By substituting f_0 = 7.492 MHz, Q = 1670, T = 300 K, and k_{B} = 1.38×10^{-23} J K^{-1} together with m_{eff} = 3.101×10^{-16} kg (estimated by COMSOL Multiphysics®) into Eq. 6.16, one can find a_{th} ≈ 924.83 fm Hz$^{-1/2}$.

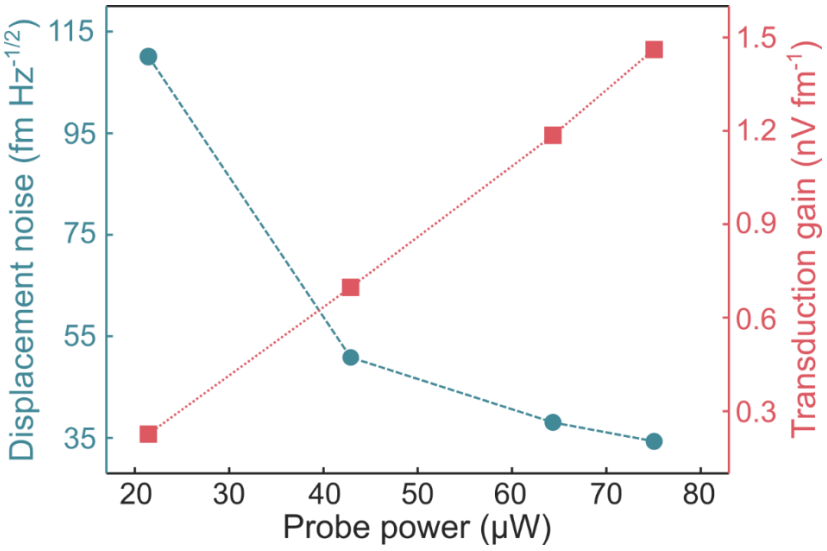


Figure 6.19 Measured displacement noise (left axis) and transduction gain (right axis) for different probes. Dashed and dotted lines are guide to the eye.

For the 21-μW probe, the Lorentzian fit to the noise spectral density yields a peak value of 210.352 nV Hz$^{-1/2}$ and a noise floor of 24.926 nV Hz$^{-1/2}$ (see Figure 6.17). Here, the excess voltage above the noise floor originates from the thermomechanical motion of the nanowire, which is the square root of the difference between their squares and

numerically equal to 208.87 nV $Hz^{-1/2}$. Therefore, the transduction gain can be simply calculated as: G_{TR} = 208.87 nV $Hz^{-1/2}$ / 924.83 fm $Hz^{-1/2}$ ≈ 0.226 nV fm^{-1}. Using this gain value, the minimum resolvable displacement for this configuration can be found by converting the off-resonance voltage noise into the displacement domain as follows: 24.926 nV $Hz^{-1/2}$ / 0.226 nV fm^{-1} ≈ 110.29 fm $Hz^{-1/2}$, which yields the displacement sensitivity.

Using the data in Figure 6.17, this procedure has been repeated for other probe values, as well. The measured displacement noise and transduction gain are plotted in Figure 6.19. Since the ring resonators are linear systems (Eq. 6.2), increasing the probe power linearly increases ΔI_{out}. On the other hand, the noise floor is somewhat invariant of the probe power as it is a parameter that depends on the laser source. This in turn leads to a linear enhancement in the transduction gain for larger probes, as evidenced experimentally. Therefore, the displacement sensitivity improves as the probe power is increased, and the measurement imprecision is consequently reduced. As a result, the displacement sensitivity gets as good as ~34 fm $Hz^{-1/2}$ for the 75-µW probe at a transduction gain of G_{TR} = 1.46 nV fm^{-1} (or 1.46 mV nm^{-1}).

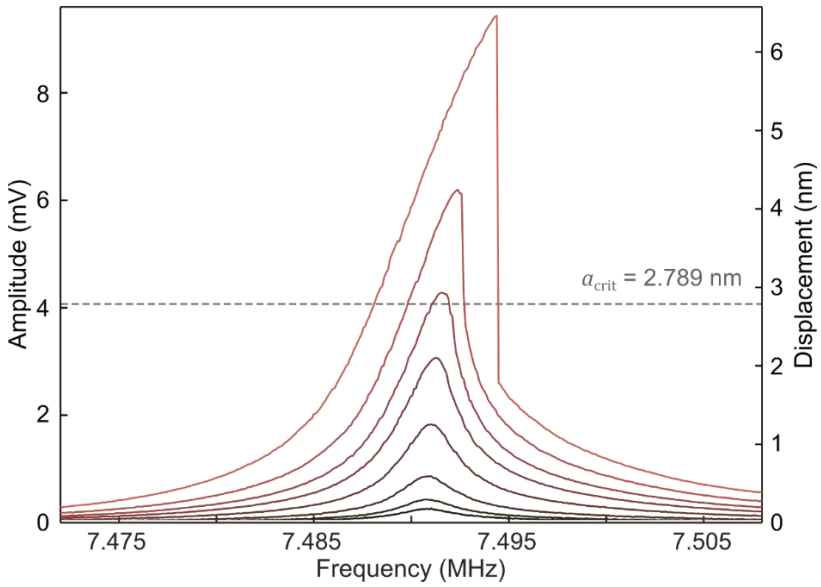


Figure 6.20 Raw experimental data obtained by increasing the piezo drive voltage, using the 75-µW probe. The left axis shows the readout voltage, and the corresponding displacement value is given on the right axis. Dashed line denotes the critical amplitude (a_{crit}), above which the Duffing nonlinearity kicks in. The resonator shows spring-hardening effect.

In oscillator design, the resonators are employed in linear region of operation, whereby the vibrational amplitude remains below a_{crit} (Eq. 4.14). For the InP nanowire in this experiment, the critical amplitude can be computed as a_{crit} = 2.789 nm. Using the transduction gain value for the 75-μW probe, one can find that the attainable signal amplitude within the linear regime becomes larger than 4 mV. The supporting data is given in Figure 6.20, which shows the readout amplitude and the corresponding displacement value for increasing piezo drive levels. As seen, the resonator displays Duffing nonlinearity with spring-hardening effect. Significantly, the voltage level at a_{crit}, i.e. 4 mV, results in at least two orders of magnitude improvement compared to the amplitude levels in the previous chapter as well as in other examples of electrical transduction [73], [79], [82]. This relaxes the gain requirement in real-world applications from 75 dB to less than 35 dB as it was the particular vision and objective for photonic integration.

Once the transduction gain is known, experimental value for g_{om} can also be estimated. To that end, the photodetector gain (G_{PD}) and responsivity ($\mathcal{R}$) has been determined (from the datasheet of Newport 1811-FC) as 40 V/mW and 1.0, respectively, at λ = 1500 nm. Using these values, the grating couplers have been found to have ~7.6% efficiency per coupler. For example, when the input power from the laser source is 275 μW, only 21 μW is coupled into the waveguide, which gives the probe power. At a detuning of $-\Gamma_{\mathrm{c}}/2$ (i.e. λ = 1506.05 nm), one can show from the transmission spectrum in Figure 6.14 that the PD receives a power level of 3.4 μW.

For the 21-μW probe, G_{TR} = 0.226 nV fm^{-1} = 0.226 mV nm^{-1}. Thus, when the resonator reaches a displacement of d_{c} = 1 nm, optical power fluctuations at the PD input will have an amplitude of 5.65 nW (calculated by $d_{\mathrm{c}}G_{\mathrm{TR}}/\mathcal{R}G_{\mathrm{PD}}$). To reach 5.65 nW, the required optical frequency shift has been numerically calculated in MATLAB (using the experimental data in Figure 6.14) as ~75 MHz, which simply yields an optomechanical coupling rate of g_{om} = 75 MHz nm^{-1}. The comparison of this value with the theory and

simulations has further been given in Figure 6.21. Theory and simulations are consistent with the case in Figure 6.10 and compare favourably within 2% of agreement. Experimental value of g_{om} is also in good agreement with the theory, where the theoretical value is ~7% smaller.

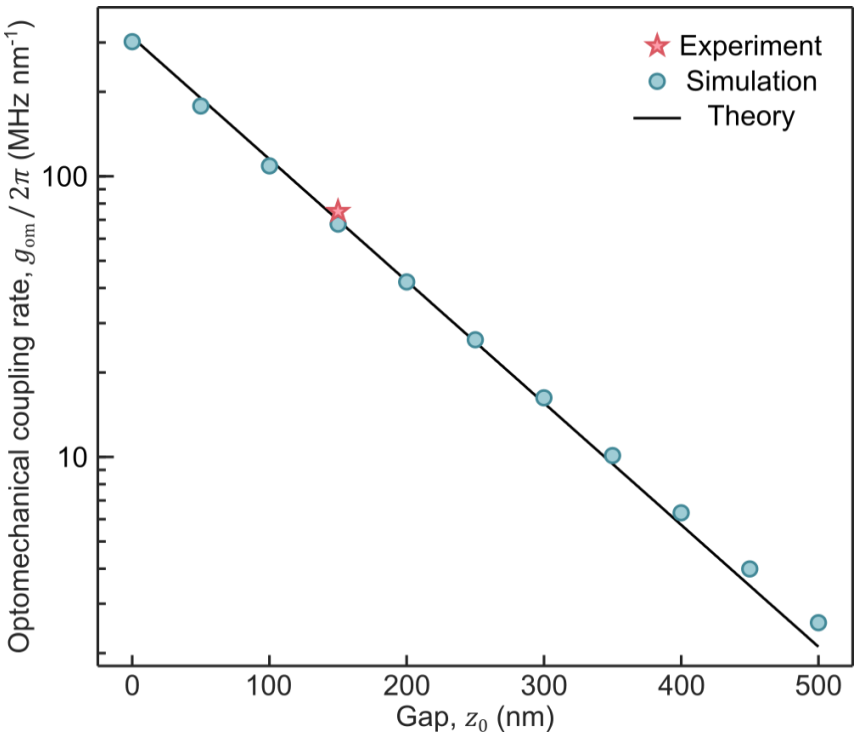


Figure 6.21 Comparison of the experimental g_{om} value with the theory (Eq. 4.14) and simulations (Eq. 6.7). At z_0 = 150 nm, the experiment yields g_{om} ~75 MHz nm^{-1}.

For a given design, i.e. when g_{om} is constant, it has been shown that increasing the probe power can improve the readout amplitude (Figure 6.17). One can also improve the readout by using a cavity with higher Q [92] or improving the coupling efficiency. For the latter case, 3D-printed couplers (in Nanoscribe) can be used as they are fully compatible with the fabrication process in this work and can enhance the coupling efficiency by about 10 dB [175], which in turn increases the readout amplitude by the same amount.

As for the cavity Q, note that the readout amplitude is a linear function of the maximum cavity slope at a detuning of $\pm\Gamma_{\mathrm{c}}/2$. This detuning level further ensures the highest dynamic range in terms of transduction linearity provided that $\Gamma_{\mathrm{c}} \gg a_{\mathrm{crit}} g_{\mathrm{om}}$. For a

given g_{om}, higher cavity Q results in a higher slope, thus improving the readout amplitude. This improvement factor can further be computed numerically using Eq. 6.5, and the relevant computational data for the increasing Q values is provided in Figure 6.22. Here, experimental values have been used as reference for normalisation, where the readout improvement factor is normalised by the maximum amplitude obtained at a_{crit} (i.e. by 4 mV) and the cavity Q by the value after the nanowire deposition (i.e. by 4,460). As can be seen, the improvement factor follows a linear line for small Q, e.g. an improvement in the cavity Q by a factor of 20 will increase the readout amplitude by the same amount. At this point, it is useful to mention that obtaining such Q values in ring resonators are practical with traditional nanofabrication methods [90], [181].

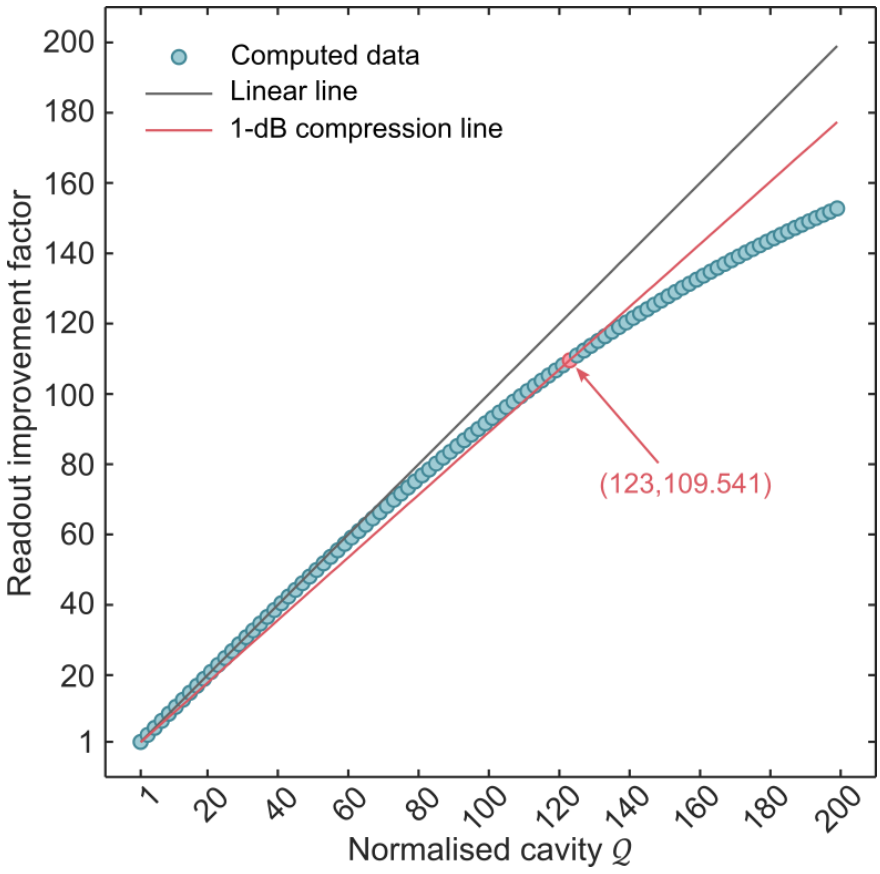


Figure 6.22 Improvement in the readout amplitude for increasing Q values of the optical cavity. Data points (green circles) are numerically computed, and both axes are normalised to the experimental values, i.e. x-axis by Q = 4,460 and y-axis by 4 mV. Gray line shows the linear fit to the first few data points. The pink circle crosses the 1-dB compression line (pink line) where the readout power drops by 1 dB, i.e. 1-dB compression point. The nonlinearity stems from the Lorentzian (second-order) response of the microcavity (Eq. 6.5).

The findings in Figure 6.22 also suggest that the computed values start to deviate from the linear behaviour as the cavity bandwidth gets smaller for larger Q. This is due to the second-order (Lorentzian) nature of the optical transfer function and further imposes an upper limit to the cavity Q, which should satisfy $\Gamma_c \gg a_{crit} g_{om}$ as previously stated. From here, one can also determine the 1-dB compression point, whereby the readout power becomes 1 dB lower than the expected linear behaviour (refer to the 1-dB compression line in Figure 6.22). For this design, it is the point where the Q is improved by 123, which yields a readout improvement factor of 109.541. Note that this parameter becomes especially important in applications where the transduction linearity is of high importance, e.g. mass/force sensing and signal processing.

6.4 Conclusions

In this chapter, a novel way of transducing single-crystal nanowires via integrated photonics has been studied. The main goal of these experiments was to explore the possibility of improving transduction efficiency in nanomechanical systems for the future of mechanical signal processing and telecommunications while still making use of fascinating properties in nanowire systems. These experiments constitute the first instance of fully-integrated optical transduction of exotic nanowires. To that end, an InP nanowire has been interfaced with an ultrasensitive photonic element, i.e. a microring cavity. The relevant theory behind ring resonators and the field of cavity optomechanics have been investigated. An analytical relation for the optomechanical coupling rate has been derived for the first time in the nanowire realm and verified by FEM analysis for such a low-loss material in telecommunication wavelengths as InP. The effect of the optical probe power has also been investigated with the corresponding opto-thermo-mechanical simulations within an agreement of 4%.

Experimental results exhibit around two orders of magnitude improvement in the readout amplitude, i.e. from the typical 10s of microvolts in electrical NEMS to several

millivolts in nano-optomechanical systems. It has been shown that the readout amplitude can be further enhanced by at least 20× by increasing the cavity Q while ensuring a linear transduction. Exploiting the better coupling efficiency of 3D-printed couplers, the readout can be improved by an additional factor of 10, leading to a signal amplitude of ~800 mV (or a power level of 11 dBm on a 50Ω load) at a_{crit}. As anticipated, this completely eliminates the gain requirement for real-world telecommunications and signal processing applications. Adoption of this technique in GeTe nanowires and creating a non-volatile frequency tuner on a chip is the future endeavour, with some preliminary results presented in the next chapter under future work (Section 7.2).

Chapter 7

Conclusions and outlook

7.1 Summary of the results

In this thesis, an entirely new approach for tuning nanomechanical resonances has been reported. Owing to the unique phase transformation properties in phase-change nanowires of GeTe, resonance frequencies can be tuned via electrical pulses within a range of 30% in a non-volatile manner, without affecting their high Q factors. Initially, the transduction has been performed piezoresistively, and an application idea to solve an engineering problem has been shown. However, electrical transduction is not effective enough for real-world applications, thus a transduction method via photonic integration has also been demonstrated for the first time in the nanowire realm.

In order to perform these measurements, a novel way of assembling single nanowires on virtually any platform has been presented in Chapter 3. This method takes its roots from traditional stamp-transfer techniques and further improves them via introducing novel nanoscale tools such as sub-micron polymer tips and dome-shaped stamps. Using this method, a placement precision of below 1 µm has been obtained while only employing manual nanopositioners, with a reproducibility of ~80%. This is limited by the ability of the polymer tip to pick up a single nanowire. Future research for developing a fully-automated system for wafer-scale placement of single nanowires will inexpensively advance nanowire research while enabling mass-produced nanowire devices for the first time.

In Chapter 4, piezoresistive transduction of GeTe nanowire resonators has been performed. The readout scheme makes use of only a battery as a bias source, which offers a simple self-sensing mechanism. Following the derivation of a non-zero phase Lorentzian with frequency-doubling effect, performance metrics of the resonators have been determined, with Q factors above 16,000. The Young's modulus in the crystalline phase is measured as E_{cry} = 86 GPa. By calibrating the actuation method, piezoresistive gauge factors of GeTe nanowires in the crystalline phase have been determined for the first time, reaching a value of γ_{cry} = 19.3.

Chapter 5 summarises a set of experiments to tune the mechanical resonance of GeTe nanowires. Two different approaches of tuning have been reported. One method uses relatively high energy (50-ns) pulses to amorphise the nanowire for the wide-range tuning of f_0, which yields a tuning range over 30% with a spectral tuning performance of 10.6 aJ Hz^{-1}. Such crystalline-to-amorphous phase transition also enhances the gauge factor (γ_{amo} = 1100) while reducing the Young's modulus down to E_{amo} = 41 GPa. In the second method, lower-energy pulses (20 ns) have been used to obtain intermediate frequency states via a dislocation-based amorphization route. In both approaches, the tuned frequency states are non-volatile. Thus, these experiments

constitute the first power-free tuning scheme in NEMS resonators. Excitingly, the Q factors remain intact owing to the phase transformation characteristics, and this enables first-of-its-kind applications in communications electronics as demonstrated in a frequency-hopped radio transmission experiment. However, the readout amplitude levels obtained in these experiments are too low to transmit within a real-world communications system. Thus, improving the readout in electrical domain has always been the holy grail of NEMS researchers.

Finally, in Chapter 6, an alternative way of transducing nanowires has been demonstrated in order to mitigate the amplitude issue. This method makes use of photonic integration, whereby the nanowire is suspended over a microring cavity. Note that this study is the first-time exploitation of a single-crystal nanowire in cavity optomechanics. Thus, the theoretical aspects have been diligently studied. For the sake of simplicity, an InP nanowire has been used for testing due to its low loss at telecommunication wavelengths although the method can be extended to any nanowire system (as will be seen in the next section). Overall, a transduction gain of up to 1.46 mV nm^{-1} have been obtained. This gain value can be further improved by using a higher cavity Q and better fibre-to-chip couplers, which can easily lead to an additional improvement factor of ~200 while maintaining a linear transduction. This can enable the use of nanomechanical resonators of nanowires in IoT systems for the first time, reducing power consumption, cost, and complexity.

7.2 Future work

This thesis has demonstrated novel approaches for tuning and transducing mechanical resonators of single-crystal nanowires. The tuning is based on phase-change materials, and it is power-free. This makes the tuning method suitable for low-power applications in IoT networks as well as mobile and satellite communications. An alternative transduction method using cavity optomechanics has also been

demonstrated with the aim of elevating the potential of nanomechanical resonators in commercial applications by improving the readout quality. This further enables fully-integrated optomechanical resonators of exotic nanomaterials for the first time. If one can combine these two methods on a single chip, i.e. phase-change tuning and fully-integrated optical transduction, the implications of such a device are vast where ultra-low-power requirement is high priority such as in portable wireless and mobile devices. At this point, it is crucial to note that the GeTe nanowires in this thesis cannot handle more than 20 electrical pulses, which requires further investigation to improve the cyclability of these devices for commercial standards, e.g. by exploring other material systems or encapsulating the devices with atomically-thin dielectric layers.

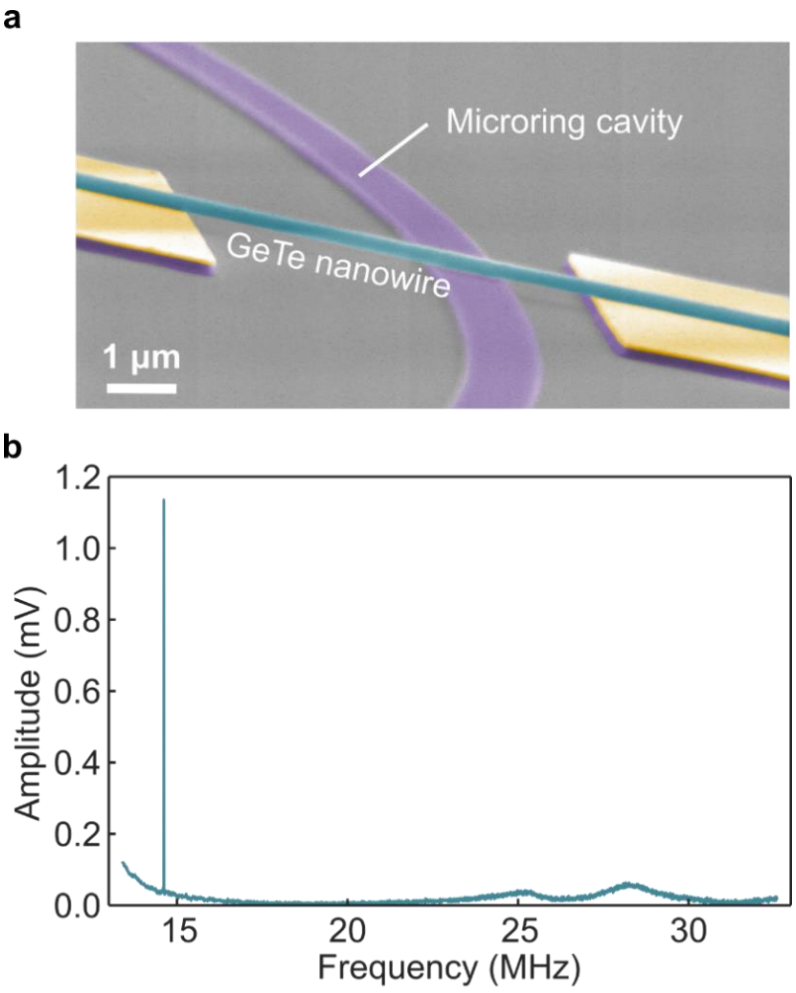


Figure 7.1 Preliminary results regarding the cavity optomechanics of a GeTe nanowire. **a**, False-colour SEM image of the GeTe nanowire (L = 7.5 µm, D = 250 nm) suspended over a microring cavity of Si_3N_4. **b**, Raw experimental data showing the frequency response of the device (f_0 = 14.609 MHz).

To that end, a GeTe nanowire has been interfaced with a microring resonator. SEM image of the free-standing nanowire over the photonic cavity can be seen in Figure 7.1a. Initial results obtained from this device are provided in Figure 7.1b, which suggests a transduction gain of ~2.02 mV nm^{-1} at a probe power of ~70 µW even though the ring resonator and the grating couplers had an inferior performance than the InP case. Yet, this value is relatively higher, and this is attributed to the larger diameter and refractive index of the GeTe nanowire. Vibrations of GeTe also modify the cavity Q to a larger extent due to the non-zero imaginary part of its refractive index, thus cannot be ignored while developing a theory.

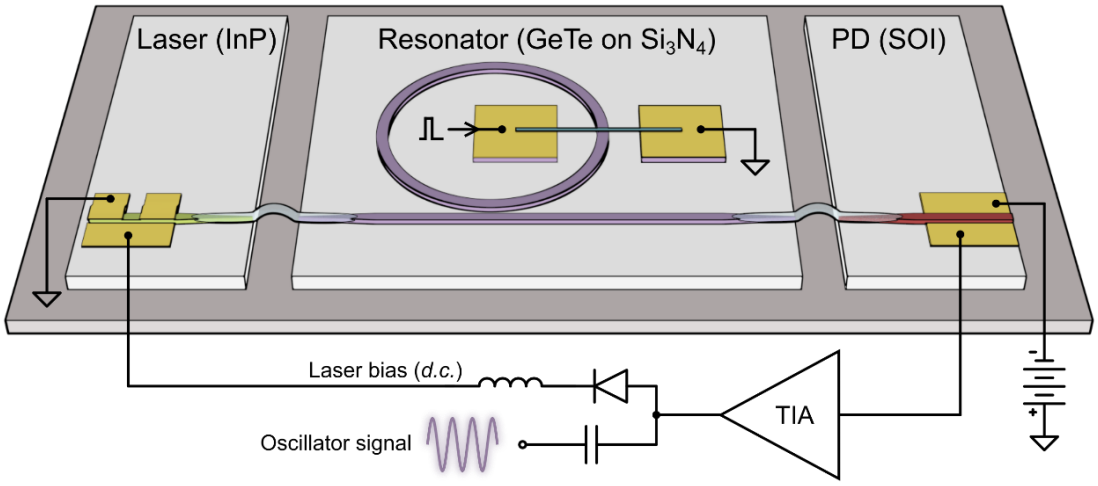


Figure 7.2 Diagram of the proposed device.

Given these promising results, Figure 7.2 schematises the proposed architecture consisting of a GeTe nano-optomechanical resonator on Si_3N_4, an integrated laser on InP, and a photodetector (PD) on SOI. Here, the nanowire is tuned electrically, and different platforms are interfaced with each other via 3D-printed photonic wirebonds [182]. Note that the TIA amplifies the PD signal, and its output is divided into two. The bottom branch is simply the oscillatory signal from the nanowire vibrations. The top branch, on the other hand, generates a *d.c.* current for the laser (via rectification and low-pass filtering) that is proportional to the oscillation amplitude. Combined with the

dynamical backaction from the cavity [92], this can create a positive feedback loop that sustains the oscillations by satisfying the Barkhausen criterion.

Especially with the recent advances of integrated PDs and lasers [182], [183], development of such systems are imminent although further research is needed to optimise the design parameters. Once realised, the concept of fully-integrated optomechanical oscillators that are inherently tunable can transform the telecommunication systems, forming a whole new basis for low-power IoT networks.

Appendix A

Photonic NEMS assembly

The process of gluing the optical fibrearray to the NEMS-carrying chip is summarised in Figure A.1.The two-channel fibrearray is ordered from SQS Vlaknova Optika. In this array, the distance between two fibre cores is 250 μm, thus the same distance has been chosen between the input and output grating couplers of the photonic devices. The fibrearray readily encapsulates two SMF-28 fibres within borosilicate glass ($2.5 \times 2.5 \times 10$ mm^3). Initially, a piece of glass is glued to the fibrearray using epoxy (Araldite Rapid Drying Epoxy Resin) as seen in Step 1 (Figure A.1). The most important step here is to align the bottom of the glass piece with that of the fibrearray as much as possible. If necessary, micromanipulators can be used during this step to precisely control this alignment. Once the parts are aligned, the epoxy should be cured for at least 2 hours.

In Step 2, the fibrearray is attached to a custom-built fibrearray holder (made of aluminium), which is fixed on a micromanipulator. Here, it should be noted that the fibrearray is tilted at an angle of 8° due to the grating coupler parameters. Using the micromanipulator, the fibrearray can then be aligned with the device chip underneath. To facilitate this alignment, external light microscopes are used to roughly determine the location of the device. Simultaneously, the light transmission through the device is monitored in real-time in order to find the exact device location that maximises the transmission. It is also worth noting that there should be a sacrificial area (at least 3 mm in length) on the chip that falls under the glass piece. This is to ensure no devices are damaged in the upcoming steps.

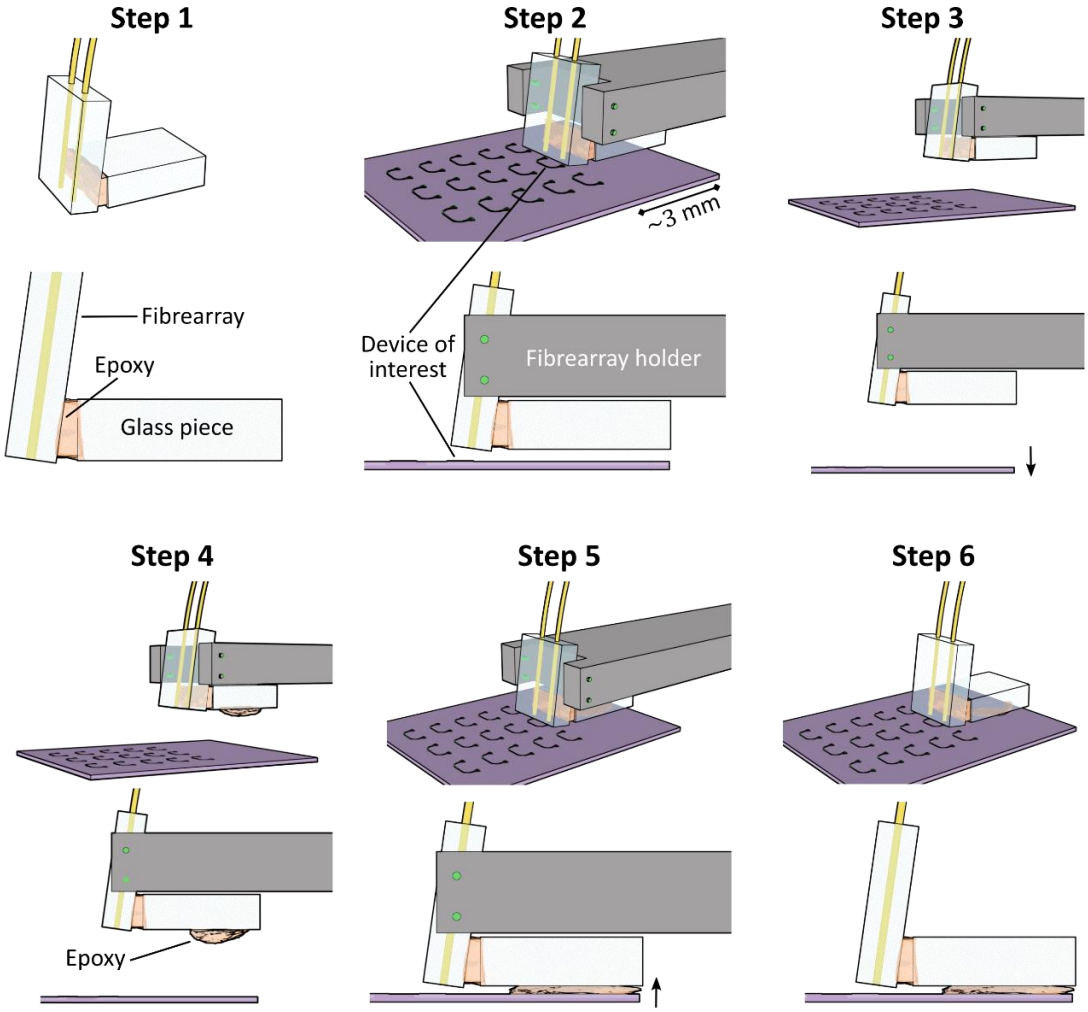


Figure A.1 Fibre gluing process for NEMS measurements in vacuum. **Step 1**: A glass piece is glued to the fibrearray using epoxy. **Step 2**: The fibrearray with the glass piece is attached to a micromanipulator using a custom-built holder and aligned with the device of interest. **Step 3**: The device chip is lowered. **Step 4**: A drop of epoxy is casted on the bottom side of the glass piece. **Step 5**: The device chip is raised back to its initial position. This spreads out the epoxy. At this stage, the epoxy is cured overnight. **Step 6**: The final assembly after the fiberarray holder is removed.

In Step 3, following the alignment, the device chip is lowered such that the vertical distance between the fiberarray and the chip is increased from ~100 μm to at least 1 cm. This facilitates Step 4, where a small drop of epoxy is casted to the bottom side of the glass piece. By bringing the device chip back to its initial vertical position, i.e. back to a vertical gap of 100 μm, the epoxy can be spread out, gluing the empty area on the device chip to the glass piece (Step 5). Once the transmission is maximised by finding the initial the vertical distance, the alignment should be stopped, allowing the epoxy to be cured overnight (> 8 hours). As the grating couplers are sensitive to alignment within a few microns, the whole process should be performed on a table with decent vibration isolation if the optical transmission efficiency is critical for the application. After the curing is completed, the fiberarray with the device chip can be detached from the fiberarray holder. As such, the final assembly can be seen in Step 6 of Figure A.1.

Bibliography

[1] Q. Wu *et al.*, 'Cognitive Internet of Things: A New Paradigm Beyond Connection', *IEEE Internet of Things Journal*, vol. 1, no. 2, pp. 129–143, 2014, doi: 10.1109/JIOT.2014.2311513.

[2] K. Shafique, B. A. Khawaja, F. Sabir, S. Qazi, and M. Mustaqim, 'Internet of Things (IoT) for Next-Generation Smart Systems: A Review of Current Challenges, Future Trends and Prospects for Emerging 5G-IoT Scenarios', *IEEE Access*, vol. 8, pp. 23022–23040, 2020, doi: 10.1109/ACCESS.2020.2970118.

[3] D. Miorandi, S. Sicari, F. De Pellegrini, and I. Chlamtac, 'Internet of things: Vision, applications and research challenges', *Ad Hoc Networks*, vol. 10, no. 7, pp. 1497–1516, 2012, doi: 10.1016/j.adhoc.2012.02.016.

[4] H. G. Barrow, 'Frequency Tunable MEMS-Based Timing Oscillators and Narrowband Filters', Ph.D. dissertation, University of California, Berkeley, 2015.

[5] J. Everard, T. Burtichelov, and K. Ng, 'Ultralow Phase Noise 10-MHz Crystal Oscillators', *IEEE Transactions on Ultrasonics, Ferroelectrics, and Frequency Control*, vol. 66, no. 1, pp. 181–191, Jan. 2019, doi: 10.1109/TUFFC.2018.2881456.

[6] Fox, Adrian, 'PLL Synthesizers | Analog Devices'. https://www.analog.com/en/analog-dialogue/articles/pll-synthesizers.html (accessed Jan. 21, 2021).

[7] S. Zaliasl *et al.*, 'A 3 ppm 1.5 × 0.8 mm 2 1.0 μA 32.768 kHz MEMS-Based Oscillator', *IEEE Journal of Solid-State Circuits*, vol. 50, no. 1, pp. 291–302, 2015, doi: 10.1109/JSSC.2014.2360377.

[8] K. Scott and Azarian, Michel, 'Phase Noise of Integer-N and Fractional-N PLL Synthesizers | Analog Devices'. https://www.analog.com/en/technical-articles/phase-noise-of-integer-n-and-fractional-n-pll-synthesizers.html (accessed Jan. 27, 2021).

[9] M. R. Palattella *et al.*, 'Internet of Things in the 5G Era: Enablers, Architecture, and Business Models', *IEEE Journal on Selected Areas in Communications*, vol. 34, no. 3, pp. 510–527, Mar. 2016, doi: 10.1109/JSAC.2016.2525418.

[10] G. M. Rebeiz *et al.*, 'Tuning in to RF MEMS', *IEEE Microwave Magazine*, vol. 10, no. 6, pp. 55–72, 2009, doi: 10.1109/MMM.2009.933592.

[11] A. M. Elshurafa, P. H. Ho, and K. N. Salama, 'Low voltage RF MEMS variable capacitor with linear C-V response', *Electronics Letters*, vol. 48, no. 7, pp. 392–393, 2012, doi: 10.1049/el.2011.3340.

[12] F. Nabki, K. Allidina, F. Ahmad, P.-V. Cicek, and M. N. El-Gamal, 'A Highly Integrated 1.8 GHz Frequency Synthesizer Based on a MEMS Resonator', *IEEE Journal of Solid-State Circuits*, vol. 44, no. 8, pp. 2154–2168, Aug. 2009, doi: 10.1109/JSSC.2009.2022914.

[13] M. Roukes, 'Nanoelectromechanical systems face the future', *Phys. World*, vol. 14, no. 2, pp. 25–32, 2001, doi: 10.1088/2058-7058/14/2/29.

[14] K. L. Ekinci and M. L. Roukes, 'Nanoelectromechanical systems', *Review of Scientific Instruments*, vol. 76, no. 6, p. 061101, 2005, doi: 10.1063/1.1927327.

[15] S. S. Verbridge, H. G. Craighead, and J. M. Parpia, 'A megahertz nanomechanical resonator with room temperature quality factor over a million', *Appl. Phys. Lett.*, vol. 92, no. 1, p. 013112, 2008, doi: 10.1063/1.2822406.

[16] S. S. Verbridge, D. F. Shapiro, H. G. Craighead, and J. M. Parpia, 'Macroscopic Tuning of Nanomechanics: Substrate Bending for Reversible Control of Frequency and Quality

Factor of Nanostring Resonators', *Nano Lett.*, vol. 7, no. 6, pp. 1728–1735, 2007, doi: 10.1021/nl070716t.
[17] C. Chen *et al.*, 'Graphene mechanical oscillators with tunable frequency', *Nature Nanotechnology*, vol. 8, no. 12, pp. 923–927, 2013, doi: 10.1038/nnano.2013.232.
[18] V. Sazonova, Y. Yaish, H. Üstünel, D. Roundy, T. A. Arias, and P. L. McEuen, 'A tunable carbon nanotube electromechanical oscillator', *Nature*, vol. 431, no. 7006, pp. 284–287, Sep. 2004, doi: 10.1038/nature02905.
[19] F. Ye, J. Lee, and P. X.-L. Feng, 'Electrothermally Tunable Graphene Resonators Operating at Very High Temperature up to 1200 K', *Nano Lett.*, vol. 18, no. 3, pp. 1678–1685, 2018, doi: 10.1021/acs.nanolett.7b04685.
[20] S. C. Jun, X. M. H. Huang, M. Manolidis, C. A. Zorman, M. Mehregany, and J. Hone, 'Electrothermal tuning of Al–SiC nanomechanical resonators', *Nanotechnology*, vol. 17, no. 5, pp. 1506–1511, 2006, doi: 10.1088/0957-4484/17/5/057.
[21] Q. P. Unterreithmeier, E. M. Weig, and J. P. Kotthaus, 'Universal transduction scheme for nanomechanical systems based on dielectric forces', *Nature*, vol. 458, no. 7241, Art. no. 7241, Apr. 2009, doi: 10.1038/nature07932.
[22] R. B. Karabalin *et al.*, 'Piezoelectric nanoelectromechanical resonators based on aluminum nitride thin films', *Appl. Phys. Lett.*, vol. 95, no. 10, p. 103111, Sep. 2009, doi: 10.1063/1.3216586.
[23] R. B. Karabalin, X. L. Feng, and M. L. Roukes, 'Parametric Nanomechanical Amplification at Very High Frequency', *Nano Lett.*, vol. 9, no. 9, pp. 3116–3123, Sep. 2009, doi: 10.1021/nl901057c.
[24] X. L. Feng, C. J. White, A. Hajimiri, and M. L. Roukes, 'A self-sustaining ultrahigh-frequency nanoelectromechanical oscillator', *Nature Nanotechnology*, vol. 3, no. 6, pp. 342–346, Jun. 2008, doi: 10.1038/nnano.2008.125.
[25] M. Wuttig and N. Yamada, 'Phase-change materials for rewriteable data storage', *Nature Materials*, vol. 6, no. 11, pp. 824–832, 2007, doi: 10.1038/nmat2009.
[26] C. Ríos *et al.*, 'Integrated all-photonic non-volatile multi-level memory', *Nature Photonics*, vol. 9, no. 11, pp. 725–732, 2015, doi: 10.1038/nphoton.2015.182.
[27] M. Le Gallo *et al.*, 'Mixed-precision in-memory computing', *Nature Electronics*, vol. 1, no. 4, pp. 246–253, 2018, doi: 10.1038/s41928-018-0054-8.
[28] P. Hosseini, C. D. Wright, and H. Bhaskaran, 'An optoelectronic framework enabled by low-dimensional phase-change films', *Nature*, vol. 511, no. 7508, pp. 206–211, 2014, doi: 10.1038/nature13487.
[29] A. Sebastian, M. Le Gallo, R. Khaddam-Aljameh, and E. Eleftheriou, 'Memory devices and applications for in-memory computing', *Nature Nanotechnology*, vol. 15, no. 7, Art. no. 7, Jul. 2020, doi: 10.1038/s41565-020-0655-z.
[30] N. Farmakidis *et al.*, 'Plasmonic nanogap enhanced phase-change devices with dual electrical-optical functionality', *Science Advances*, vol. 5, no. 11, p. eaaw2687, doi: 10.1126/sciadv.aaw2687.
[31] Y. Won, J. Lee, M. Asheghi, T. W. Kenny, and K. E. Goodson, 'Phase and thickness dependent modulus of $Ge_2Sb_2Te_5$ films down to 25 nm thickness', *Appl. Phys. Lett.*, vol. 100, no. 16, p. 161905, 2012, doi: 10.1063/1.3699227.
[32] H. Nazeer, H. Bhaskaran, L. A. Woldering, and L. Abelmann, 'Young's modulus and residual stress of GeSbTe phase-change thin films', *Thin Solid Films*, vol. 592, pp. 69–75, 2015, doi: 10.1016/j.tsf.2015.08.049.
[33] P. Hosseini, M. Kumar, and H. Bhaskaran, '2-D Materials as a Functional Platform for Phase Change Tunable NEMS', *IEEE Access*, vol. 3, pp. 737–742, 2015, doi: 10.1109/ACCESS.2015.2439572.
[34] S.-W. Nam *et al.*, 'Electrical Wind Force–Driven and Dislocation-Templated Amorphization in Phase-Change Nanowires', *Science*, vol. 336, no. 6088, pp. 1561–1566, Jun. 2012, doi: 10.1126/science.1220119.
[35] P. Nukala *et al.*, 'Inverting polar domains via electrical pulsing in metallic germanium telluride', *Nat Commun*, vol. 8, no. 1, p. 15033, 2017, doi: 10.1038/ncomms15033.

[36] P. Nukala *et al.*, 'Direct Observation of Metal–Insulator Transition in Single-Crystalline Germanium Telluride Nanowire Memory Devices Prior to Amorphization', *Nano Lett.*, vol. 14, no. 4, pp. 2201–2209, Apr. 2014, doi: 10.1021/nl5007036.
[37] P. Nukala, C.-C. Lin, R. Composto, and R. Agarwal, 'Ultralow-power switching via defect engineering in germanium telluride phase-change memory devices', *Nat Commun*, vol. 7, no. 1, p. 10482, Apr. 2016, doi: 10.1038/ncomms10482.
[38] M. Mitra, Y. Jung, D. S. Gianola, and R. Agarwal, 'Extremely low drift of resistance and threshold voltage in amorphous phase change nanowire devices', *Appl. Phys. Lett.*, vol. 96, no. 22, p. 222111, 2010, doi: 10.1063/1.3447941.
[39] S. Park *et al.*, 'Effect of the Thermal Conductivity on Resistive Switching in GeTe and $Ge_2Sb_2Te_5$ Nanowires', *ACS Appl. Mater. Interfaces*, vol. 7, no. 39, pp. 21819–21827, Oct. 2015, doi: 10.1021/acsami.5b05703.
[40] H. Yang *et al.*, 'Nanowire network–based multifunctional all-optical logic gates', *Science Advances*, vol. 4, no. 7, p. eaar7954, doi: 10.1126/sciadv.aar7954.
[41] A. Junk and F. Riess, 'From an idea to a vision: There's plenty of room at the bottom', *American Journal of Physics*, vol. 74, no. 9, pp. 825–830, 2006, doi: 10.1119/1.2213634.
[42] P. Ball, 'Miniature motors', *Nature Materials*, vol. 3, no. 7, p. 428, 2004, doi: 10.1038/nmat1165.
[43] H. C. Nathanson and R. A. Wickstrom, 'A resonant-gate silicon surface transistor with high-q band-pass properties', *Appl. Phys. Lett.*, vol. 7, no. 4, pp. 84–86, 1965, doi: 10.1063/1.1754323.
[44] F. Sy, J. W. Taunton, and E. N. Lightfoot, 'Transient creeping flow around spheres', *AIChE Journal*, vol. 16, no. 3, pp. 386–391, 1970, doi: 10.1002/aic.690160314.
[45] K. Y. Yasumura *et al.*, 'Quality factors in micron- and submicron-thick cantilevers', *Journal of Microelectromechanical Systems*, vol. 9, no. 1, pp. 117–125, 2000, doi: 10.1109/84.825786.
[46] K. Kendall, 'Adhesion: Molecules and Mechanics', *Science*, vol. 263, no. 5154, pp. 1720–1725, 1994, doi: 10.1126/science.263.5154.1720.
[47] Jinling Yang, T. Ono, and M. Esashi, 'Energy dissipation in submicrometer thick single-crystal silicon cantilevers', *Journal of Microelectromechanical Systems*, vol. 11, no. 6, pp. 775–783, 2002, doi: 10.1109/JMEMS.2002.805208.
[48] P. Roura, J. Fort, and J. Saurina, 'How long does it take to boil an egg? A simple approach to the energy transfer equation', *Eur. J. Phys.*, vol. 21, no. 1, pp. 95–100, 2000, doi: 10.1088/0143-0807/21/1/314.
[49] R. Lifshitz and M. L. Roukes, 'Thermoelastic damping in micro- and nanomechanical systems', *Phys. Rev. B*, vol. 61, no. 8, pp. 5600–5609, 2000, doi: 10.1103/PhysRevB.61.5600.
[50] P. A. Truitt, J. B. Hertzberg, C. C. Huang, K. L. Ekinci, and K. C. Schwab, 'Efficient and Sensitive Capacitive Readout of Nanomechanical Resonator Arrays', *Nano Lett.*, vol. 7, no. 1, pp. 120–126, 2007, doi: 10.1021/nl062278g.
[51] K. Y. Billah and R. H. Scanlan, 'Resonance, Tacoma Narrows bridge failure, and undergraduate physics textbooks', *American Journal of Physics*, vol. 59, no. 2, pp. 118–124, Feb. 1991, doi: 10.1119/1.16590.
[52] S. G. Kelly, *Mechanical Vibrations: Theory and Applications, SI Edition*, SI. Stanford, USA: Cengage Learning, 2012. [Online]. Available: https://books.google.co.uk/books?id=Y6Ai9hidEjEC
[53] A. J. Jacobs-Cook, 'MEMS versus MOMS from a systems point of view', *J. Micromech. Microeng.*, vol. 6, no. 1, pp. 148–156, 1996, doi: 10.1088/0960-1317/6/1/035.
[54] R. T. Howe and R. S. Muller, 'Polycrystalline Silicon Micromechanical Beams', *J. Electrochem. Soc.*, vol. 130, no. 6, pp. 1420–1423, 1983, doi: 10.1149/1.2119965.
[55] M. Shimbo, K. Furukawa, K. Fukuda, and K. Tanzawa, 'Silicon-to-silicon direct bonding method', *Journal of Applied Physics*, vol. 60, no. 8, pp. 2987–2989, 1986, doi: 10.1063/1.337750.

[56] W. C. Tang, T.-C. H. Nguyen, M. W. Judy, and R. T. Howe, 'Electrostatic-comb drive of lateral polysilicon resonators', *Sensors and Actuators A: Physical*, vol. 21, no. 1, pp. 328–331, Feb. 1990, doi: 10.1016/0924-4247(90)85065-C.
[57] 'Monolithic Accelerometer ADXL78 Datasheet Analog Devices (Obsolete Product)'. https://www.analog.com/media/en/technical-documentation/obsolete-data-sheets/2044696ADXL50.pdf (accessed May 25, 2019).
[58] L. He, Y. P. Xu, and M. Palaniapan, 'A CMOS Readout Circuit for SOI Resonant Accelerometer With 4-$\mu \rm g$ Bias Stability and 20-$ \mu\rm g/\sqrt\hboxHz$ Resolution', *IEEE Journal of Solid-State Circuits*, vol. 43, no. 6, pp. 1480–1490, 2008, doi: 10.1109/JSSC.2008.923616.
[59] P. Taheri-Tehrani *et al.*, 'Epitaxially-encapsulated quad mass gyroscope with nonlinearity compensation', in *2016 IEEE 29th International Conference on Micro Electro Mechanical Systems (MEMS)*, 2016, pp. 966–969. doi: 10.1109/MEMSYS.2016.7421793.
[60] K. Ikeda *et al.*, 'Silicon pressure sensor integrates resonant strain gauge on diaphragm', *Sensors and Actuators A: Physical*, vol. 21, no. 1, pp. 146–150, Feb. 1990, doi: 10.1016/0924-4247(90)85028-3.
[61] C. T.-C. Nguyen, 'Micromechanical resonators for oscillators and filters', in *1995 IEEE Ultrasonics Symposium. Proceedings. An International Symposium*, 1995, vol. 1, pp. 489–499. doi: 10.1109/ULTSYM.1995.495626.
[62] S. Lee, M. U. Demirci, and C. T.-C. Nguyen, 'A 10-MHz Micromechanical Resonator Pierce Reference Oscillator for Communications', in *Transducers '01 Eurosensors XV*, E. Obermeier, Ed. Berlin, Heidelberg: Springer Berlin Heidelberg, 2001, pp. 1066–1069. doi: 10.1007/978-3-642-59497-7_252.
[63] 'STATUS OF THE MEMS INDUSTRY - MARKET UPDATE 2021'. http://www.yole.fr/Status_Of_The_MEMS_Industry_Market_Update_2021.aspx (accessed Dec. 08, 2021).
[64] C. T.-C. Nguyen, 'MEMS technology for timing and frequency control', *IEEE Transactions on Ultrasonics, Ferroelectrics, and Frequency Control*, vol. 54, no. 2, pp. 251–270, 2007, doi: 10.1109/TUFFC.2007.240.
[65] H. Lee, A. Partridge, and F. Assaderaghi, 'Low jitter and temperature stable MEMS oscillators', in *2012 IEEE International Frequency Control Symposium Proceedings*, 2012, pp. 1–5. doi: 10.1109/FCS.2012.6243704.
[66] M. L. Roukes, 'Yoctocalorimetry: phonon counting in nanostructures', *Physica B: Condensed Matter*, vol. 263–264, pp. 1–15, 1999, doi: 10.1016/S0921-4526(98)01482-3.
[67] J. Chaste, A. Eichler, J. Moser, G. Ceballos, R. Rurali, and A. Bachtold, 'A nanomechanical mass sensor with yoctogram resolution', *Nature Nanotech*, vol. 7, no. 5, pp. 301–304, 2012, doi: 10.1038/nnano.2012.42.
[68] M. Despont *et al.*, 'VLSI-NEMS chip for AFM data storage', in *Technical Digest. IEEE International MEMS 99 Conference. Twelfth IEEE International Conference on Micro Electro Mechanical Systems (Cat. No.99CH36291)*, 1999, pp. 564–569. doi: 10.1109/MEMSYS.1999.746890.
[69] T. Kouh, M. S. Hanay, and K. L. Ekinci, 'Nanomechanical Motion Transducers for Miniaturized Mechanical Systems', *Micromachines (Basel)*, vol. 8, no. 4, p. 108, Apr. 2017, doi: 10.3390/mi8040108.
[70] A. N. Cleland and M. L. Roukes, 'Fabrication of high frequency nanometer scale mechanical resonators from bulk Si crystals', *Appl. Phys. Lett.*, vol. 69, no. 18, pp. 2653–2655, 1996, doi: 10.1063/1.117548.
[71] A. N. Cleland, J. S. Aldridge, D. C. Driscoll, and A. C. Gossard, 'Nanomechanical displacement sensing using a quantum point contact', *Appl. Phys. Lett.*, vol. 81, no. 9, pp. 1699–1701, Aug. 2002, doi: 10.1063/1.1497436.
[72] N. E. Flowers-Jacobs, D. R. Schmidt, and K. W. Lehnert, 'Intrinsic Noise Properties of Atomic Point Contact Displacement Detectors', *Phys. Rev. Lett.*, vol. 98, no. 9, p. 096804, Mar. 2007, doi: 10.1103/PhysRevLett.98.096804.

[73] R. G. Knobel and A. N. Cleland, ‘Nanometre-scale displacement sensing using a single electron transistor’, *Nature*, vol. 424, no. 6946, pp. 291–293, 2003, doi: 10.1038/nature01773.
[74] X. Song, M. Oksanen, M. A. Sillanpää, H. G. Craighead, J. M. Parpia, and P. J. Hakonen, ‘Stamp Transferred Suspended Graphene Mechanical Resonators for Radio Frequency Electrical Readout’, *Nano Lett.*, vol. 12, no. 1, pp. 198–202, 2012, doi: 10.1021/nl203305q.
[75] J. Verd, A. Uranga, G. Abadal, J. Teva, F. Perez-Murano, and N. Barniol, ‘High-sensitivity capacitive sensing interfacing circuit for monolithic CMOS M/NEMS resonators’, *Electronics Letters*, vol. 43, no. 23, 2007, doi: 10.1049/el:20071866.
[76] J. Philippe *et al.*, ‘Fully monolithic and ultra-compact NEMS-CMOS self-oscillator based-on single-crystal silicon resonators and low-cost CMOS circuitry’, in *2014 IEEE 27th International Conference on Micro Electro Mechanical Systems (MEMS)*, Jan. 2014, pp. 1071–1074. doi: 10.1109/MEMSYS.2014.6765830.
[77] D. Garcia-Sanchez *et al.*, ‘Mechanical Detection of Carbon Nanotube Resonator Vibrations’, *Phys. Rev. Lett.*, vol. 99, no. 8, p. 085501, 2007, doi: 10.1103/PhysRevLett.99.085501.
[78] A. Sampathkumar, K. L. Ekinci, and T. W. Murray, ‘Multiplexed Optical Operation of Distributed Nanoelectromechanical Systems Arrays’, *Nano Lett.*, vol. 11, no. 3, pp. 1014–1019, Mar. 2011, doi: 10.1021/nl103823b.
[79] R. He, X. L. Feng, M. L. Roukes, and P. Yang, ‘Self-Transducing Silicon Nanowire Electromechanical Systems at Room Temperature’, *Nano Lett.*, vol. 8, no. 6, pp. 1756–1761, Jun. 2008, doi: 10.1021/nl801071w.
[80] I. Bargatin, I. Kozinsky, and M. L. Roukes, ‘Efficient electrothermal actuation of multiple modes of high-frequency nanoelectromechanical resonators’, *Appl. Phys. Lett.*, vol. 90, no. 9, p. 093116, 2007, doi: 10.1063/1.2709620.
[81] W. P. Mason and R. N. Thurston, ‘Use of Piezoresistive Materials in the Measurement of Displacement, Force, and Torque’, *The Journal of the Acoustical Society of America*, vol. 29, no. 10, pp. 1096–1101, Oct. 1957, doi: 10.1121/1.1908710.
[82] I. Bargatin, E. B. Myers, J. Arlett, B. Gudlewski, and M. L. Roukes, ‘Sensitive detection of nanomechanical motion using piezoresistive signal downmixing’, *Appl. Phys. Lett.*, vol. 86, no. 13, p. 133109, Mar. 2005, doi: 10.1063/1.1896103.
[83] M. Li, H. X. Tang, and M. L. Roukes, ‘Ultra-sensitive NEMS-based cantilevers for sensing, scanned probe and very high-frequency applications’, *Nature Nanotechnology*, vol. 2, no. 2, pp. 114–120, 2007, doi: 10.1038/nnano.2006.208.
[84] E. Mile *et al.*, ‘In-plane nanoelectromechanical resonators based on silicon nanowire piezoresistive detection’, *Nanotechnology*, vol. 21, no. 16, p. 165504, 2010, doi: 10.1088/0957-4484/21/16/165504.
[85] D. W. Carr, L. Sekaric, and H. G. Craighead, ‘Measurement of nanomechanical resonant structures in single-crystal silicon’, *Journal of Vacuum Science & Technology B: Microelectronics and Nanometer Structures Processing, Measurement, and Phenomena*, vol. 16, no. 6, pp. 3821–3824, Nov. 1998, doi: 10.1116/1.590416.
[86] C. Braunsmann, V. Prucker, and T. E. Schäffer, ‘Optical knife-edge displacement sensor for high-speed atomic force microscopy’, *Appl. Phys. Lett.*, vol. 104, no. 10, p. 103101, Mar. 2014, doi: 10.1063/1.4868043.
[87] B. J. Roxworthy and V. A. Aksyuk, ‘Nanomechanical motion transduction with a scalable localized gap plasmon architecture’, *Nat Commun*, vol. 7, no. 1, p. 13746, Dec. 2016, doi: 10.1038/ncomms13746.
[88] M. Li, W. H. P. Pernice, C. Xiong, T. Baehr-Jones, M. Hochberg, and H. X. Tang, ‘Harnessing optical forces in integrated photonic circuits’, *Nature*, vol. 456, no. 7221, pp. 480–484, Nov. 2008, doi: 10.1038/nature07545.
[89] K. Y. Fong, W. H. P. Pernice, and H. X. Tang, ‘Frequency and phase noise of ultrahigh Q silicon nitride nanomechanical resonators’, *Phys. Rev. B*, vol. 85, no. 16, p. 161410, Apr. 2012, doi: 10.1103/PhysRevB.85.161410.

[90] M. Li, W. H. P. Pernice, and H. X. Tang, 'Ultrahigh-frequency nano-optomechanical resonators in slot waveguide ring cavities', *Appl. Phys. Lett.*, vol. 97, no. 18, p. 183110, 2010, doi: 10.1063/1.3513213.
[91] S. K. Roy, V. T. K. Sauer, J. N. Westwood-Bachman, A. Venkatasubramanian, and W. K. Hiebert, 'Improving mechanical sensor performance through larger damping', *Science*, vol. 360, no. 6394, Jun. 2018, doi: 10.1126/science.aar5220.
[92] G. Anetsberger *et al.*, 'Near-field cavity optomechanics with nanomechanical oscillators', *Nature Phys*, vol. 5, no. 12, pp. 909–914, Dec. 2009, doi: 10.1038/nphys1425.
[93] A. W. Barnard, M. Zhang, G. S. Wiederhecker, M. Lipson, and P. L. McEuen, 'Real-time vibrations of a carbon nanotube', *Nature*, vol. 566, no. 7742, pp. 89–93, 2019, doi: 10.1038/s41586-018-0861-0.
[94] K. L. Ekinci, 'Electromechanical Transducers at the Nanoscale: Actuation and Sensing of Motion in Nanoelectromechanical Systems (NEMS)', *Small*, vol. 1, no. 8–9, pp. 786–797, 2005, doi: 10.1002/smll.200500077.
[95] A. Bokaian, 'Natural frequencies of beams under tensile axial loads', *Journal of Sound and Vibration*, vol. 142, no. 3, pp. 481–498, 1990, doi: 10.1016/0022-460X(90)90663-K.
[96] H. S. Solanki *et al.*, 'Tuning mechanical modes and influence of charge screening in nanowire resonators', *Phys. Rev. B*, vol. 81, no. 11, p. 115459, Mar. 2010, doi: 10.1103/PhysRevB.81.115459.
[97] W. Y. Fung, E. N. Dattoli, and W. Lu, 'Radio frequency nanowire resonators and *in situ* frequency tuning', *Appl. Phys. Lett.*, vol. 94, no. 20, p. 203104, May 2009, doi: 10.1063/1.3139750.
[98] I. Kozinsky, H. W. Ch. Postma, I. Bargatin, and M. L. Roukes, 'Tuning nonlinearity, dynamic range, and frequency of nanomechanical resonators', *Appl. Phys. Lett.*, vol. 88, no. 25, p. 253101, Jun. 2006, doi: 10.1063/1.2209211.
[99] S. Manzeli, D. Dumcenco, G. Migliato Marega, and A. Kis, 'Self-sensing, tunable monolayer MoS2 nanoelectromechanical resonators', *Nat Commun*, vol. 10, no. 1, p. 4831, Dec. 2019, doi: 10.1038/s41467-019-12795-1.
[100] K. Schwab, 'Spring constant and damping constant tuning of nanomechanical resonators using a single-electron transistor', *Appl. Phys. Lett.*, vol. 80, no. 7, pp. 1276–1278, Feb. 2002, doi: 10.1063/1.1449533.
[101] J. Rieger, T. Faust, M. J. Seitner, J. P. Kotthaus, and E. M. Weig, 'Frequency and Q factor control of nanomechanical resonators', *Appl. Phys. Lett.*, vol. 101, no. 10, p. 103110, Sep. 2012, doi: 10.1063/1.4751351.
[102] I. Mahboob and H. Yamaguchi, 'Bit storage and bit flip operations in an electromechanical oscillator', *Nature Nanotech*, vol. 3, no. 5, pp. 275–279, May 2008, doi: 10.1038/nnano.2008.84.
[103] S. C. Masmanidis, R. B. Karabalin, I. D. Vlaminck, G. Borghs, M. R. Freeman, and M. L. Roukes, 'Multifunctional Nanomechanical Systems via Tunably Coupled Piezoelectric Actuation', *Science*, Aug. 2007, doi: 10.1126/science.1144793.
[104] Intel, '12th Generation Intel® Core™ Processors Datasheet', Dec. 2021. Accessed: Dec. 26, 2021. [Online]. Available: https://cdrdv2.intel.com/v1/dl/getContent/655258
[105] A. V. Kolobov, M. Krbal, P. Fons, J. Tominaga, and T. Uruga, 'Distortion-triggered loss of long-range order in solids with bonding energy hierarchy', *Nature Chemistry*, vol. 3, no. 4, Art. no. 4, Apr. 2011, doi: 10.1038/nchem.1007.
[106] T. Siegrist *et al.*, 'Disorder-induced localization in crystalline phase-change materials', *Nature Mater*, vol. 10, no. 3, pp. 202–208, Mar. 2011, doi: 10.1038/nmat2934.
[107] M. Wuttig, H. Bhaskaran, and T. Taubner, 'Phase-change materials for non-volatile photonic applications', *Nature Photonics*, vol. 11, no. 8, pp. 465–476, 2017, doi: 10.1038/nphoton.2017.126.
[108] M. Wuttig, 'Towards a universal memory?', *Nature Mater*, vol. 4, no. 4, pp. 265–266, Apr. 2005, doi: 10.1038/nmat1359.
[109] C. A. R. Ocampo, 'Phase-change materials for photonic memories and optoelectronic applications', Ph.D. dissertation, University of Oxford, 2016. [Online]. Available: https://ora.ox.ac.uk/objects/uuid:1c2c3179-ef9f-4fbf-b91c-c4d2f7ee7ed5

[110] N. Youngblood *et al.*, 'Reconfigurable Low-Emissivity Optical Coating Using Ultrathin Phase Change Materials', *ACS Photonics*, vol. 9, no. 1, pp. 90–100, Jan. 2022, doi: 10.1021/acsphotonics.1c01128.
[111] P. Zalden *et al.*, 'Picosecond Electric-Field-Induced Threshold Switching in Phase-Change Materials', *Phys. Rev. Lett.*, vol. 117, no. 6, p. 067601, Aug. 2016, doi: 10.1103/PhysRevLett.117.067601.
[112] G. W. Burr *et al.*, 'Phase change memory technology', *Journal of Vacuum Science & Technology B*, vol. 28, no. 2, pp. 223–262, 2010, doi: 10.1116/1.3301579.
[113] K. Makino, J. Tominaga, and M. Hase, 'Ultrafast optical manipulation of atomic arrangements in chalcogenide alloy memory materials', *Opt. Express, OE*, vol. 19, no. 2, pp. 1260–1270, Jan. 2011, doi: 10.1364/OE.19.001260.
[114] V. V. Poborchii, A. V. Kolobov, and K. Tanaka, 'Photomelting of selenium at low temperature', *Appl. Phys. Lett.*, vol. 74, no. 2, pp. 215–217, Jan. 1999, doi: 10.1063/1.123297.
[115] T. P. L. Pedersen, J. Kalb, W. K. Njoroge, D. Wamwangi, M. Wuttig, and F. Spaepen, 'Mechanical stresses upon crystallization in phase change materials', *Appl. Phys. Lett.*, vol. 79, no. 22, pp. 3597–3599, 2001, doi: 10.1063/1.1415419.
[116] W. K. Njoroge and M. Wuttig, 'Crystallization kinetics of sputter-deposited amorphous AgInSbTe films', *Journal of Applied Physics*, vol. 90, no. 8, pp. 3816–3821, 2001, doi: 10.1063/1.1405141.
[117] J.-K. Ahn, K.-W. Park, N.-J. Seong, and S.-G. Yoon, 'Thermal stability of GeSbTe thin films deposited by layer-by-layer metalorganic chemical vapor deposition', *J. Vac. Sci. Technol. B*, vol. 27, no. 6, p. L54, 2009, doi: 10.1116/1.3253472.
[118] D. Ielmini, A. L. Lacaita, and D. Mantegazza, 'Recovery and Drift Dynamics of Resistance and Threshold Voltages in Phase-Change Memories', *IEEE Transactions on Electron Devices*, vol. 54, no. 2, pp. 308–315, 2007, doi: 10.1109/TED.2006.888752.
[119] M. Rütten, M. Kaes, A. Albert, M. Wuttig, and M. Salinga, 'Relation between bandgap and resistance drift in amorphous phase change materials', *Scientific Reports*, vol. 5, p. 17362, 2015, doi: 10.1038/srep17362.
[120] J. Kalb, F. Spaepen, T. P. Leervad Pedersen, and M. Wuttig, 'Viscosity and elastic constants of thin films of amorphous Te alloys used for optical data storage', *J. Appl. Phys.*, vol. 94, no. 8, p. 4908, 2003, doi: 10.1063/1.1610775.
[121] M. T. Loponen, R. C. Dynes, V. Narayanamurti, and J. P. Garno, 'Measurements of the time-dependent specific heat of amorphous materials', *Phys. Rev. B*, vol. 25, no. 2, pp. 1161–1173, 1982, doi: 10.1103/PhysRevB.25.1161.
[122] H. Gehring, M. Blaicher, W. Hartmann, and W. Pernice, 'gdsHelpers: A simple Python package for creating or reading GDSII/OASIS layout files.'
[123] T. Tsuchizawa *et al.*, 'Microphotonics devices based on silicon microfabrication technology', *IEEE Journal of Selected Topics in Quantum Electronics*, vol. 11, no. 1, pp. 232–240, 2005, doi: 10.1109/JSTQE.2004.841479.
[124] L. Cheng, S. Mao, Z. Li, Y. Han, and H. Y. Fu, 'Grating Couplers on Silicon Photonics: Design Principles, Emerging Trends and Practical Issues', *Micromachines*, vol. 11, no. 7, Art. no. 7, Jul. 2020, doi: 10.3390/mi11070666.
[125] W. Lu and C. M. Lieber, 'Nanoelectronics from the bottom up', *Nature Materials*, vol. 6, no. 11, Art. no. 11, Nov. 2007, doi: 10.1038/nmat2028.
[126] R. Yan, D. Gargas, and P. Yang, 'Nanowire photonics', *Nature Photon*, vol. 3, no. 10, pp. 569–576, Oct. 2009, doi: 10.1038/nphoton.2009.184.
[127] Z. Fan *et al.*, 'Wafer-Scale Assembly of Highly Ordered Semiconductor Nanowire Arrays by Contact Printing', *Nano Lett.*, vol. 8, no. 1, pp. 20–25, Jan. 2008, doi: 10.1021/nl071626r.
[128] Y. Lu *et al.*, 'Mixed-Mode Operation of Hybrid Phase-Change Nanophotonic Circuits', *Nano Letters*, vol. 17, no. 1, pp. 150–155, 2017, doi: 10.1021/acs.nanolett.6b03688.
[129] D. Li, Y. Wu, R. Fan, P. Yang, and A. Majumdar, 'Thermal conductivity of Si/SiGe superlattice nanowires', *Appl. Phys. Lett.*, vol. 83, no. 15, pp. 3186–3188, 2003, doi: 10.1063/1.1619221.

[130] H. Xie, D. S. Haliyo, and S. Régnier, ‘A versatile atomic force microscope for three-dimensional nanomanipulation and nanoassembly’, *Nanotechnology*, vol. 20, no. 21, p. 215301, May 2009, doi: 10.1088/0957-4484/20/21/215301.
[131] M. Bockrath, ‘Single-Electron Transport in Ropes of Carbon Nanotubes’, *Science*, vol. 275, no. 5308, pp. 1922–1925, Mar. 1997, doi: 10.1126/science.275.5308.1922.
[132] R. He *et al.*, ‘Si Nanowire Bridges in Microtrenches: Integration of Growth into Device Fabrication’, *Advanced Materials*, vol. 17, no. 17, pp. 2098–2102, 2005, doi: 10.1002/adma.200401959.
[133] D. Whang, S. Jin, Y. Wu, and C. M. Lieber, ‘Large-Scale Hierarchical Organization of Nanowire Arrays for Integrated Nanosystems’, *Nano Lett.*, vol. 3, no. 9, pp. 1255–1259, Sep. 2003, doi: 10.1021/nl0345062.
[134] I. E. Zadeh *et al.*, ‘Deterministic Integration of Single Photon Sources in Silicon Based Photonic Circuits’, *Nano Lett.*, vol. 16, no. 4, pp. 2289–2294, Apr. 2016, doi: 10.1021/acs.nanolett.5b04709.
[135] B. A. Latella, B. K. Gan, C. J. Barbé, and D. J. Cassidy, ‘Nanoindentation hardness, Young’s modulus, and creep behavior of organic–inorganic silica-based sol-gel thin films on copper’, *Journal of Materials Research*, vol. 23, no. 9, pp. 2357–2365, Sep. 2008, doi: 10.1557/jmr.2008.0315.
[136] D. F. Merchant, P. J. Scully, and N. F. Schmitt, ‘Chemical tapering of polymer optical fibre’, *Sensors and Actuators A: Physical*, vol. 76, no. 1, pp. 365–371, Aug. 1999, doi: 10.1016/S0924-4247(99)00008-4.
[137] A. F. Stalder, G. Kulik, D. Sage, L. Barbieri, and P. Hoffmann, ‘A snake-based approach to accurate determination of both contact points and contact angles’, *Colloids and Surfaces A: Physicochemical and Engineering Aspects*, vol. 286, no. 1, pp. 92–103, Sep. 2006, doi: 10.1016/j.colsurfa.2006.03.008.
[138] R. A. Hemnani *et al.*, ‘2D material printer: a deterministic cross contamination-free transfer method for atomically layered materials’, *2D Mater.*, vol. 6, no. 1, p. 015006, Oct. 2018, doi: 10.1088/2053-1583/aae62a.
[139] D. Rosser, T. Fryett, A. Saxena, A. Ryou, A. Majumdar, and A. Majumdar, ‘High-precision local transfer of van der Waals materials on nanophotonic structures’, *Opt. Mater. Express, OME*, vol. 10, no. 2, pp. 645–652, Feb. 2020, doi: 10.1364/OME.383255.
[140] H. Liang *et al.*, ‘Ultrahigh Numerical Aperture Metalens at Visible Wavelengths’, *Nano Lett.*, vol. 18, no. 7, pp. 4460–4466, Jul. 2018, doi: 10.1021/acs.nanolett.8b01570.
[141] Y. Lu, M. Yang, F. Qu, G. Shen, and R. Yu, ‘Enzyme-functionalized gold nanowires for the fabrication of biosensors’, *Bioelectrochemistry*, vol. 71, no. 2, pp. 211–216, Nov. 2007, doi: 10.1016/j.bioelechem.2007.05.003.
[142] R. He and P. Yang, ‘Giant piezoresistance effect in silicon nanowires’, *Nature Nanotechnology*, vol. 1, no. 1, p. 42, 2006, doi: 10.1038/nnano.2006.53.
[143] R. He, ‘Silicon nanowires for nanoelectromechanical systems’, 2006. Accessed: Dec. 10, 2021. [Online]. Available: https://ui.adsabs.harvard.edu/abs/2006PhDT.....206H
[144] A. H. Edwards *et al.*, ‘Electronic structure of intrinsic defects in crystalline germanium telluride’, *Phys. Rev. B*, vol. 73, no. 4, p. 045210, Jan. 2006, doi: 10.1103/PhysRevB.73.045210.
[145] V. A. Sazonova, ‘A tunable carbon nanotube resonator’, Ph.D. dissertation, Cornell University, 2006. Accessed: Apr. 26, 2020. [Online]. Available: https://ecommons.cornell.edu/handle/1813/3205
[146] M. Belov, N. J. Quitoriano, S. Sharma, W. K. Hiebert, T. I. Kamins, and S. Evoy, ‘Mechanical resonance of clamped silicon nanowires measured by optical interferometry’, *Journal of Applied Physics*, vol. 103, no. 7, p. 074304, Apr. 2008, doi: 10.1063/1.2891002.
[147] X. L. Feng, R. He, P. Yang, and M. L. Roukes, ‘Very High Frequency Silicon Nanowire Electromechanical Resonators’, *Nano Lett.*, vol. 7, no. 7, pp. 1953–1959, Jul. 2007, doi: 10.1021/nl0706695.
[148] J. Molina *et al.*, ‘High Dynamic Range Nanowire Resonators’, *Nano Lett.*, vol. 21, no. 15, pp. 6617–6624, Aug. 2021, doi: 10.1021/acs.nanolett.1c02056.

[149] L. D. Landau, E. M. Lifshitz, A. M. Kosevich, and L. P. Pitaevskii, *Theory of elasticity*, 3rd English ed., rev.enl. By E.M. Lifshitz, A.M. Kosevich, and L.P. Pitaevskii. Oxford [England]: Butterworth-Heinemann, 1986.
[150] T. Nonaka, G. Ohbayashi, Y. Toriumi, Y. Mori, and H. Hashimoto, 'Crystal structure of GeTe and Ge2Sb2Te5 meta-stable phase', *Thin Solid Films*, vol. 370, no. 1, pp. 258–261, Jul. 2000, doi: 10.1016/S0040-6090(99)01090-1.
[151] G. M. Guttmann and Y. Gelbstein, 'Mechanical Properties of Thermoelectric Materials for Practical Applications', in *Bringing Thermoelectricity into Reality*, P. Aranguren, Ed. InTech, 2018. doi: 10.5772/intechopen.75476.
[152] Z. Wang *et al.*, 'Highly sensitive integrated flexible tactile sensors with piezoresistive Ge 2 Sb 2 Te 5 thin films', *npj Flex Electron*, vol. 2, no. 1, pp. 1–6, 2018, doi: 10.1038/s41528-018-0030-4.
[153] H.-P. Phan, D. V. Dao, K. Nakamura, S. Dimitrijev, and N.-T. Nguyen, 'The Piezoresistive Effect of SiC for MEMS Sensors at High Temperatures: A Review', *Journal of Microelectromechanical Systems*, vol. 24, no. 6, pp. 1663–1677, Dec. 2015, doi: 10.1109/JMEMS.2015.2470132.
[154] H. W. Ch. Postma, I. Kozinsky, A. Husain, and M. L. Roukes, 'Dynamic range of nanotube- and nanowire-based electromechanical systems', *Appl. Phys. Lett.*, vol. 86, no. 22, p. 223105, May 2005, doi: 10.1063/1.1929098.
[155] A. N. Cleland and M. L. Roukes, 'Noise processes in nanomechanical resonators', *Journal of Applied Physics*, vol. 92, no. 5, pp. 2758–2769, Aug. 2002, doi: 10.1063/1.1499745.
[156] P. Fons *et al.*, 'Photoassisted amorphization of the phase-change memory alloy Ge 2 Sb 2 Te 5', *Phys. Rev. B*, vol. 82, no. 4, p. 041203, Jul. 2010, doi: 10.1103/PhysRevB.82.041203.
[157] A. Gemant, 'Correlation Between Elastic Moduli and Viscosity of Liquids and Plastics', *Journal of Applied Physics*, vol. 12, no. 9, pp. 680–685, Sep. 1941, doi: 10.1063/1.1712960.
[158] '47 CFR § 15.247 - Operation within the bands 902-928 MHz, 2400-2483.5 MHz, and 5725-5850 MHz.', *LII / Legal Information Institute*. https://www.law.cornell.edu/cfr/text/47/15.247 (accessed Jan. 03, 2021).
[159] R. C. Welch *et al.*, 'Dynamics of Glass Relaxation at Room Temperature', *Phys. Rev. Lett.*, vol. 110, no. 26, p. 265901, Jun. 2013, doi: 10.1103/PhysRevLett.110.265901.
[160] M. J. Lighthill and G. B. Whitham, 'On kinematic waves II. A theory of traffic flow on long crowded roads', *Proceedings of the Royal Society of London. Series A. Mathematical and Physical Sciences*, vol. 229, no. 1178, pp. 317–345, May 1955, doi: 10.1098/rspa.1955.0089.
[161] Z. Hao, A. Erbil, and F. Ayazi, 'An analytical model for support loss in micromachined beam resonators with in-plane flexural vibrations', *Sensors and Actuators A: Physical*, vol. 109, no. 1, pp. 156–164, Dec. 2003, doi: 10.1016/j.sna.2003.09.037.
[162] H. Hosaka, K. Itao, and S. Kuroda, 'Damping characteristics of beam-shaped micro-oscillators', *Sensors and Actuators A: Physical*, vol. 49, no. 1, pp. 87–95, Jun. 1995, doi: 10.1016/0924-4247(95)01003-J.
[163] T. H. Lee and A. Hajimiri, 'Oscillator phase noise: a tutorial', *IEEE Journal of Solid-State Circuits*, vol. 35, no. 3, pp. 326–336, Mar. 2000, doi: 10.1109/4.826814.
[164] 'HF2 User Manual :: Zurich Instruments Documentation'. https://docs.zhinst.com/hf2_user_manual/overview.html (accessed Nov. 25, 2022).
[165] X. L. Feng, R. R. He, P. D. Yang, and M. L. Roukes, 'Phase Noise and Frequency Stability of Very-High Frequency Silicon Nanowire Nanomechanical Resonators', in *TRANSDUCERS 2007 - 2007 International Solid-State Sensors, Actuators and Microsystems Conference*, Jun. 2007, pp. 327–330. doi: 10.1109/SENSOR.2007.4300134.
[166] B. Bahreyni, 'Chapter 7 - Noise', in *Fabrication and Design of Resonant Microdevices*, B. Bahreyni, Ed. Norwich, NY: William Andrew Publishing, 2009, pp. 129–141. doi: 10.1016/B978-081551577-7.50011-0.

[167] N. Tesla, ‘System of signaling’, US725605A, Apr. 14, 1903 Accessed: Jan. 03, 2021. [Online]. Available: https://patents.google.com/patent/US725605/en
[168] A. J. Viterbi, ‘Spread spectrum communications: myths and realities’, *IEEE Communications Magazine*, vol. 40, no. 5, pp. 34–41, May 2002, doi: 10.1109/MCOM.2002.1006970.
[169] C. Yeh, ‘CHAPTER 1 - Introduction’, in *Applied Photonics*, C. Yeh, Ed. Boston: Academic Press, 1994, pp. 1–8. doi: 10.1016/B978-0-08-049926-0.50005-8.
[170] R. Soref and J. Lorenzo, ‘All-silicon active and passive guided-wave components for λ = 1.3 and 1.6 μm’, *IEEE Journal of Quantum Electronics*, vol. 22, no. 6, pp. 873–879, 1986, doi: 10.1109/JQE.1986.1073057.
[171] L. Vivien *et al.*, ‘High speed and high responsivity germanium photodetector integrated in a Silicon-On-Insulator microwaveguide’, *Opt. Express, OE*, vol. 15, no. 15, pp. 9843–9848, 2007, doi: 10.1364/OE.15.009843.
[172] D. Marpaung, J. Yao, and J. Capmany, ‘Integrated microwave photonics’, *Nature Photon*, vol. 13, no. 2, pp. 80–90, Feb. 2019, doi: 10.1038/s41566-018-0310-5.
[173] D. Taillaert *et al.*, ‘An out-of-plane grating coupler for efficient butt-coupling between compact planar waveguides and single-mode fibers’, *IEEE Journal of Quantum Electronics*, vol. 38, no. 7, pp. 949–955, 2002, doi: 10.1109/JQE.2002.1017613.
[174] M. Antelius, K. B. Gylfason, and H. Sohlström, ‘An apodized SOI waveguide-to-fiber surface grating coupler for single lithography silicon photonics’, *Opt. Express*, vol. 19, no. 4, p. 3592, 2011, doi: 10.1364/OE.19.003592.
[175] H. Gehring *et al.*, ‘Low-loss fiber-to-chip couplers with ultrawide optical bandwidth’, *APL Photonics*, vol. 4, no. 1, p. 010801, Jan. 2019, doi: 10.1063/1.5064401.
[176] J. E. Heebner, R. Grover, and T. A. Ibrahim, *Optical microresonators : theory, fabrication, and applications*. London: Springer, 2008.
[177] S. Adachi, ‘Optical dispersion relations for GaP, GaAs, GaSb, InP, InAs, InSb, AlxGa1−xAs, and In1−xGaxAsyP1−y’, *Journal of Applied Physics*, vol. 66, no. 12, pp. 6030–6040, Dec. 1989, doi: 10.1063/1.343580.
[178] J. D. Joannopoulos, S. G. Johnson, N. W. Joshua, and R. D. Meade, *Photonic crystals: Molding the Flow of Light*, 2nd ed. Princeton and Oxford: Princeton University Press, 2008.
[179] M. Dunaevskiy *et al.*, ‘Young’s Modulus of Wurtzite and Zinc Blende InP Nanowires’, *Nano Lett.*, vol. 17, no. 6, pp. 3441–3446, Jun. 2017, doi: 10.1021/acs.nanolett.7b00312.
[180] T. B. Gabrielson, ‘Mechanical-thermal noise in micromachined acoustic and vibration sensors’, *IEEE Transactions on Electron Devices*, vol. 40, no. 5, pp. 903–909, 1993, doi: 10.1109/16.210197.
[181] W. H. P. Pernice, C. Xiong, and H. X. Tang, ‘High Q micro-ring resonators fabricated from polycrystalline aluminum nitride films for near infrared and visible photonics’, *Opt. Express, OE*, vol. 20, no. 11, pp. 12261–12269, May 2012, doi: 10.1364/OE.20.012261.
[182] M. R. Billah *et al.*, ‘Hybrid integration of silicon photonics circuits and InP lasers by photonic wire bonding’, *Optica, OPTICA*, vol. 5, no. 7, pp. 876–883, Jul. 2018, doi: 10.1364/OPTICA.5.000876.
[183] F. Ashtiani, A. J. Geers, and F. Aflatouni, ‘An on-chip photonic deep neural network for image classification’, *Nature*, pp. 1–6, Jun. 2022, doi: 10.1038/s41586-022-04714-0.